THE
ELECTROCHEMICAL BEHAVIOUR
OF
LEAD DIOXIDE
ELECTRODES

by

Jerzy Antoni Bialacki

Supervisor : Professor N.A. Hampson

A Doctoral Thesis submitted in partial fulfilment of the requirements for the award of Doctor of Philosophy of the Loughborough University of Technology, June, 1984

Thomas Hughes.

1822-1896

Life isn't all beer and skittles; but beer and skittles, or something better of the same sort, must form a good part of every Englishman's education.

Tom Brown's Schooldays
|1857|, pt. I, ch. 2.

The work described in this thesis has not been submitted, in full or in part, to this or any other institution for a higher degree.

ACKNOWLEDGEMENTS

I am extremely grateful to my supervisor, Professor N.A. Hampson for his patience, help and guidance throughout the duration of my project. His humour and encouragement has been of great value to me.

Total financial support from Chloride Technical Ltd. is gratefully acknowledged. I wish to acknowledge the advice, encouragement and technical assistance which have been given by Mr. E.J. Pearson, Mr. K. Peters, Dr. K. Julian and Mr. F. Wilson, all of Chloride Technical Ltd.

I thank my fellow research students (and Research Fellows) for their comradeship and help, and the countless minutes of entertainment provided by them.

The technical assistance required throughout this research has been considerable and the help provided by the Chemistry Department, especially by Mr. B. Bower, Mr. M. Coupe and Mr. A. Stevens, is very much appreciated.

I would like to thank Mrs. B. Kowalski for her patience whilst typing this thesis.

ABSTRACT

The electrochemistry of planar and porous lead dioxide electrodes has been investigated using the techniques: linear sweep voltammetry, potentiostatic pulse experiments and Faradaic (a.c.) impedance studies. The first two techniques were digitally controlled and the data were acquired at high speed and could be easily retrieved after storage. A morphological examination on the electrodes was also carried out using scanning electron microscopy.

The electrochemical behaviour of flat lead in sulphuric acid at concentrations in excess of 5 mol dm^{-3} has been studied. Various solid lead alloys in different sulphuric acid concentrations were investigated together with porous PbO_2 on different lead alloy supports. It was found that the acid concentration had a marked effect on the electrochemistry of the electrodes. The current transients obtained from potentiostatic step experiments with the porous PbO_2 electrodes were nearly all of a complex nature and some attempt was made to match the data with established mathematical relationships for electrocrystallisation processes. The alloys used were of industrial importance and they were lead-antimony, lead-tin-calcium and lead-tin-bismuth-calcium. Also various automotive positive pastes were employed to form the porous PbO_2 structure.

A.C. impedance studies were carried out on the porous PbO_2 electrodes. An analogue was found which described the discharge process of PbO_2.

LIST OF SYMBOLS

A	electrode area
A'	nucleation rate constant
b	Tafel slope
C_{ads}	adsorption capacitance
$C_{diffuse}$	capacitance corresponding to a diffuse layer
C_{dL}, C_L	double layer capacitance
C_{ext}	external film capacitance
C_{fixed}	capacitance corresponding to a fixed layer
C_O, C_R	concentrations of species O and R
C^b	bulk concentration
C_O^b, C_R^b	bulk concentrations of O and R
C_O^s, C_R^s	surface concentrations of O and R
D, D_O, D_R	diffusion coefficient, diffusion coefficients of O and R
E	electrode potential on a suitable reference scale
E^o	standard electrode potential
E_p	potential of peak current
E_r	reversible electrode potential (at $i = 0$)
E_{rat}	rational potential
$E_{\frac{1}{2}}$	polarographic half wave potential
f	frequency
F	Faraday's constant
h	height of nucleus
i	current or current density
i_a, i_c	partial anodic and cathodic current densities
i_d, i_t	diffusion controlled current density
i_m, i_p	peak current or current density
i_o	exchange current density

k	nucleation constant
k_1	parallel growth rate constant
k_2	orthogonal growth rate constant
k_a, k_c	potential dependent rate constants for the anodic and cathodic reactions
k_a^o, k_c^o	values of k_a and k_c at the reference potential
k_s	specific rate constant at E.
k_{sh}	standard heterogeneous rate constant
k^o	apparent standard rate constant
M	molar mass
N	number of nuclei at any one time
N_o	initial number of nuclei
O	oxidised species
Q, q	charge on electrode, flux of diffusing species
q_m	maximum charge, monolayer charge
r	radius of nucleus
R	gas constant, reduced species
R_{ads}	adsorption resistance
R_{CT}	charge transfer coefficient
R_{ext}	external film resistance
R_Ω	ohmic resistance of electrolyte
S	area on which material is deposited
S_1	actual area of isolated nucleus
S_{1ex}	top area of isolated nucleus
t	time
t_m	time taken to reach maximum current
T	temperature, tortuosity
u	age of the nucleus
v	alternating voltage
V	volume

W	Warburg impedance
z	number of electrons, mean distance from the electrode
Z	total cell impedance
Z'	real part of electrode impedance
Z"	imaginary part of electrode impedance
α	charge transfer coefficient
η	overpotential
θ	charge transfer resistance, potential dependent constant, porosity
ν	potential sweep rate
ρ	density, specific resistance
σ	Warburg coefficient
ϕ	phase angle
ω	angular frequency

CONTENTS

CHAPTER 1

INTRODUCTION

After Volta's discovery of the galvanic cell principle in 1800 it took approximately another fifty years before Siemens and Sinsteden applied it to the lead/sulphuric acid/lead dioxide system. In 1860 Planté's reported results introduced the lead-acid battery as an electrochemical storage device[1]. Today the lead-acid storage battery is the most widely used secondary, electrochemical power source in the world. The applications of these lead-acid cells vary from small sealed batteries of a few watt-hours capacity in consumer uses (e.g. motor vehicles) to large batteries of many megawatt-hours capacity in submarines, emergency-lighting and other utilities.

The theory of operation of the rechargeable lead-acid battery is based on the so-called double sulphate principle[2]. It explains the fact that the electrolyte in solution, sulphuric acid, is not only an ion-transport medium but a reactant as well. The discharge product of both the lead anode electrochemical oxidation reaction and the lead dioxide cathode reduction reaction is lead sulphate, hence the term "double sulphate". The reactions are:

Cathode: $$PbO_2 + SO_4^{2-} + 4H^+ + 2e^- \underset{\text{charge}}{\overset{\text{discharge}}{\rightleftarrows}} PbSO_4 + 2H_2O \qquad (1.1)$$

$E = +1.69V$

Anode: $$Pb + SO_4^{2-} \underset{\text{charge}}{\overset{\text{discharge}}{\rightleftarrows}} PbSO_4 + 2e^- \qquad (1.2)$$

$E = -0.36V$

Overall reaction:

$$PbO_2 + 2H_2SO_4 + Pb \quad \underset{\text{charge}}{\overset{\text{discharge}}{\rightleftarrows}} \quad 2PbSO_4 + 2H_2O \qquad (1.3)$$

$E = +2.04V$

The theory of double sulphation has been confirmed thermodynamically by Craig and Vinal [3,4].

The life-limiting component of any lead-acid battery system is the lead dioxide electrode. Due to the complex nature of charge, discharge and self-discharge occurring at the positive plate, various studies and reviews have been published concerning these phenomena [5-10]. Various metals, and even their oxides and sulphates [11], have been added to the material of the support grids of lead-acid batteries in order to impart many desirable properties, such as, longer service life, improved castability, etc. Antimony in automotive positive grids extends the life of the battery by producing further resistance to deep cycling and extensive overcharge. This is probably due to the corrosion layer, formed by the Pb-Sb alloy, adhering well to the active material and not causing an intergranular attack on the crystallites in the grid alloy. The only technical disadvantage of the addition of Sb is that the hydrogen overvoltage of the cell is lowered because the additive deposits itself on the negative plate resulting in a decrease in the potential of hydrogen evolution at that electrode. It has also been discovered that at low antimony concentrations the retention characteristics of the positive paste in the support grids are usually observed to be poor.

Other materials have been used instead of antimony, such as, calcium, tin, aluminium, magnesium, titanium and bismuth [12]. The introduction of alloys based on lead-tin-calcium has led to the development of low-cost, low-maintenance batteries of high capacity. These maintenance-free batteries have been used successfully in standby and telephone batteries, as well as for starting, lighting and ignition applications. Although the additives tin and calcium seem to supress markedly the hydrogen evolution reaction, however, removing antimony from the positive grids results in rather inferior cycle lives.

This thesis contains the results of an investigation of the effects that the lead-alloy support, positive paste and H_2SO_4 concentration have on the PbO_2 electrode using electrochemical techniques.

CHAPTER 2

THEORETICAL PRINCIPLES

2.1 The Electrode-Electrolyte Interphase

When a metal is placed in an electrolyte an electrical double layer exists at the metal-solution interphase. The interphase is defined as a three dimensional transition region between two phases in which the properties have not yet reached the bulk of either phase. The structure of the electrode-electrolyte interphase is of fundamental importance in establishing the way electrode reactions proceed in this region. The electrical double-layer, or just "double layer", is the arrangement of two layers of charges and oriented dipoles which are less than a nanometre apart so producing a potential difference across the interfacial region.

The earliest model of the double layer was given by Helmholtz [13] in 1879 who suggested that it was a layer of ions at the solid surface and a rigidly held layer of oppositely charged ions in the solution. The Helmholtz double layer is equivalent to a simple parallel-plate capacitor. However, in order for the model of the double layer to be viable the following assumptions have to be made:

a) the separated charges at the interphase are in electrostatic equilibrium

b) there is no transfer of charge in either direction across the interphase with changes in electrode potential

c) the charge in the solution near the electrode interphase varies with changes in electrode potential.

Therefore the electrical behaviour of the double layer should be purely capacitive and that it has no parallel resistive components.

However, 'ideally polarisable' electrodes are ones which closely obey the above conditions, for example, the mercury electrode in KCl solution (1 mol dm^{-3}). The Helmholtz model of the double layer is basically inadequate because the thermal motions of liquid molecules would not sustain a rigid array of charges at the interphase.

Gouy [14] and Chapman [15] proposed the theory of a diffuse double layer with a statistical distribution of ions in the electric field. However, a serious defect of the Gouy-Chapman theory is that it treats the ions as point charges. This leads to very high values for the charge concentration in the immediate neighbourhood of the interphase. Stern [16] provided a suitable correction in the form of an adsorbed layer of ions which have finite sizes and approach the electrode only to within a certain critical distance. Hence the double layer can be divided into two regions; next to the electrode there is a region of high field and low dielectric constant with a row of firmly held ions beyond which a diffuse layer extends from the plane of closest approach to the bulk solution.

Grahame [17] postulated that the Helmholtz fixed plane is divided into two regions. As Fig. 2.1 shows, the inner Helmholtz plane consists of specifically adsorbed ions and it is assumed that they have lost some of their water of hydration and so are closest to the electrode surface. The outer Helmholtz plane consists of normal hydrated ions at their distance of closest approach to the surface. The double layer model can be treated as two capacitors connected in series:

$$\frac{1}{C_L} = \frac{1}{C_{\text{fixed}}} + \frac{1}{C_{\text{diffuse}}} \qquad (2.1)$$

where C_L = overall double-layer capacitance

C_{fixed} = capacitance corresponding to a fixed layer

C_{diffuse} = capacitance corresponding to a diffuse layer

Fig. 2.1 Grahame Model of the Double Layer

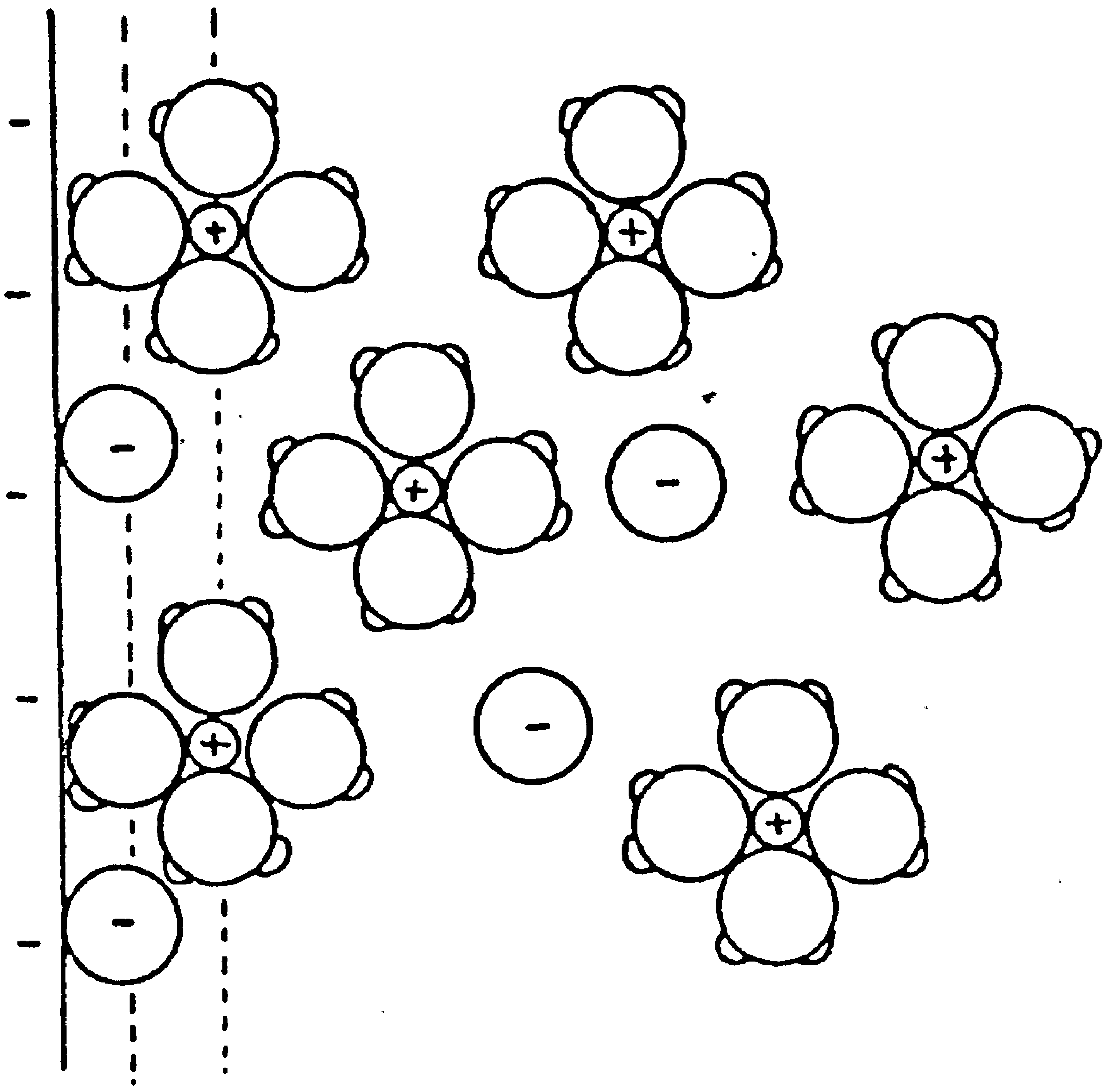

Variation of Potential with Distance through the Interphase predicted by the Grahame Model.

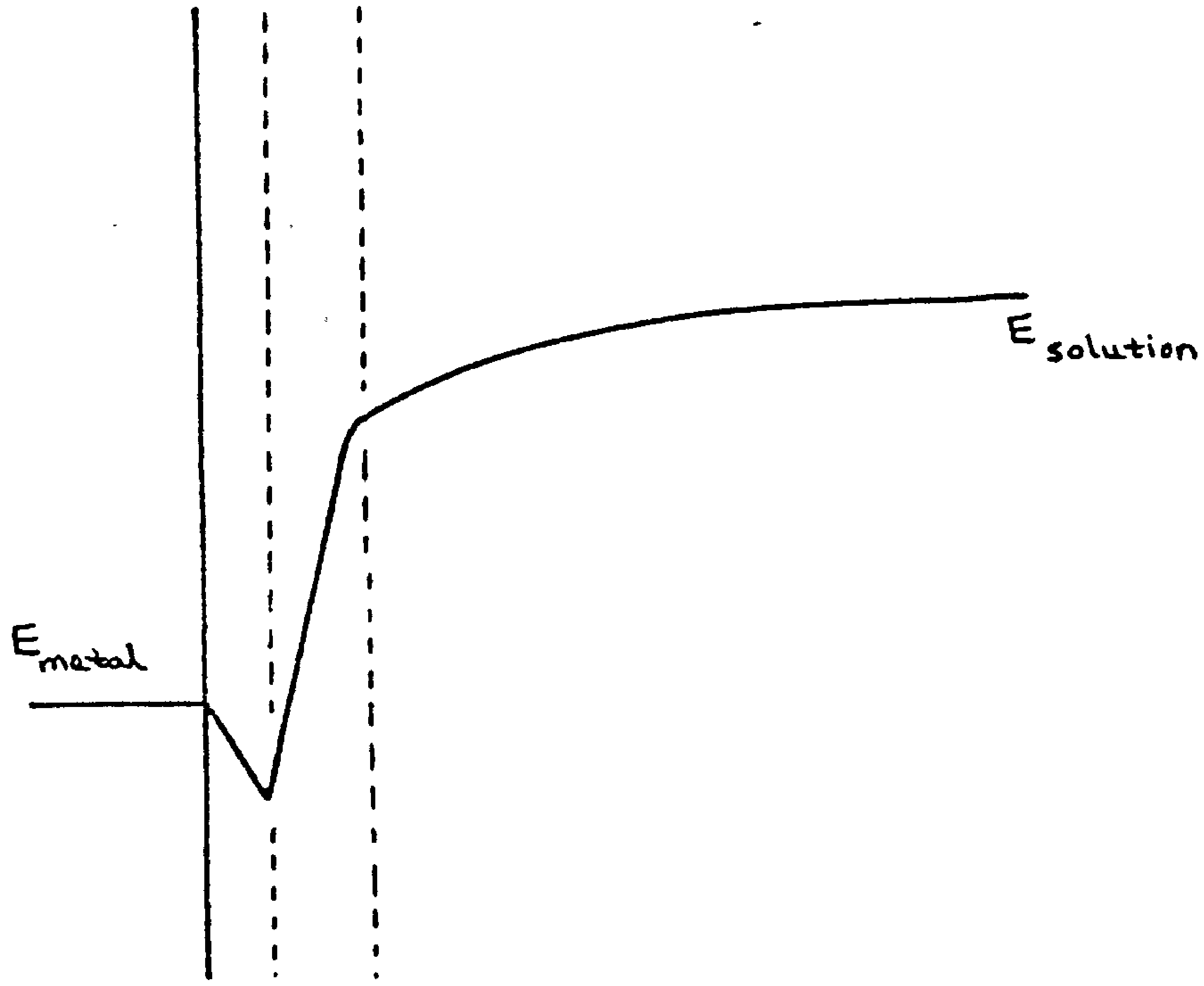

The diffuse layer component becomes significantly larger than the capacitance associated with the fixed layer, as the electrolyte becomes more dilute and C_L becomes virtually independent of C_{fixed}. At very low concentrations a sharp minimum is obtained on a C_L versus potential plot. This minimum is associated with the point of zero charge (p.z.c.) on the electrode.

Devanathan et al [18] proposed that adsorbed solvated cations remained outside a layer of strongly orientated solvent dipoles. The inner solvent layer is penetrated by specifically adsorbed anions and the water molecules are thought to be adsorbed with their negative poles pointing either towards or away from the metal surface, depending on the potential. A schematic diagram of this model is shown in Fig. 2.2.

The importance of the potential of zero charge was discussed by Frumkin [19,20] who explained that for anion adsorption, the p.z.c. moves to more negative potentials and for cation adsorption the reverse applies. The direction of p.z.c. can be reversed by concentration changes when anion and cation adsorption occur. Hence the quantity of charge on the electrode can be found out by using E_{rat} (rational potential). At positive E_{rat}, adsorption of negative ions is favoured and at negative E_{rat}, adsorption of positive ions occurs readily. When the size of E_{rat} is small, that is, very little charge on the electrode the adsorption of neutral molecules competes favourably with ionic adsorption.

More recently the work done on the interphase structure has been mainly concerned with the orientation of the water dipoles in the fixed layer [21-23]. Cooper and Harrison [24-28] have reservations about dividing the double layer into a concentration dependent compact layer and a diffuse region and, particularly with regard to the structure and properties of individual solvent molecules within the compact layer. Instead, the idea was put forward that the double layer should be treated as a single entity with no usage of the concepts of compact layer,

Fig. 2.2 Model of the electrical double layer.

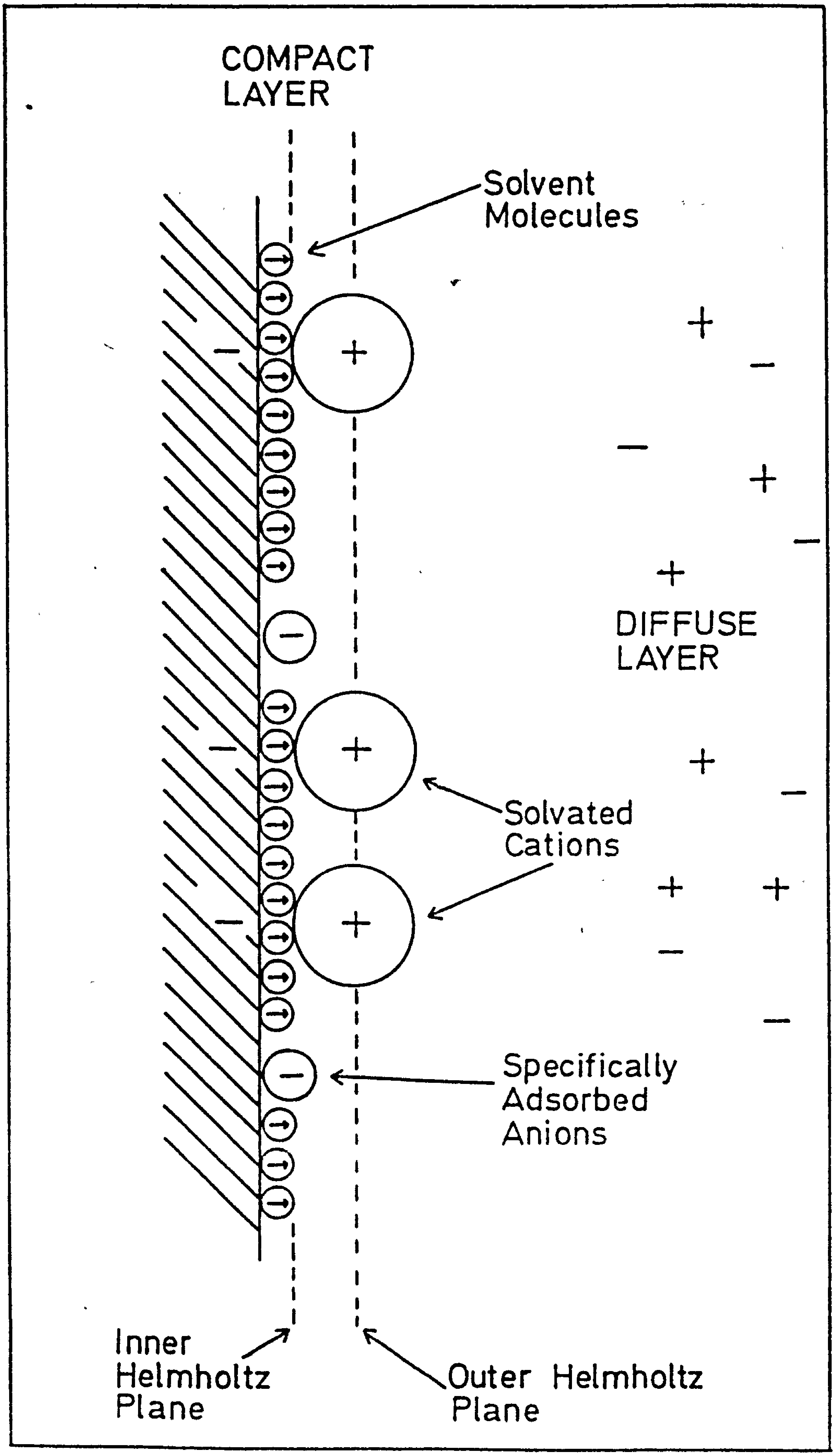

inner or outer Helmholtz planes, or contact adsorption. The structure of the double layer is considered to arise specifically from the known differences between anions and cations in aqueous solution and the net distributed charge acts at a mean distance, z, from the electrode.

In conclusion, the statistical theories for the distribution of ions in the interphase, as well as, the study of the differential capacitance and p.z.c. are vital in understanding experimental data and looking at reactions at the electrode-electrolyte interphase.

2.2 The Charge Transfer Process

An electrode process is a heterogeneous chemical reaction involving the transfer of charge to or from an electrode which may be an electronic conductor, such as a metal, or a semi-conductor. Consider the redox reaction:

$$O + ze \underset{k_a}{\overset{k_c}{\rightleftharpoons}} R \qquad (2.2)$$

At the equilibrium potential charge is simultaneously being donated and accepted by the electrode in a dynamic equilibrium. The overall current (per unit electrode area) flowing at a given potential can be expressed as the difference between the forward and reverse rates:

$$i = zF(k_c C_O{}^s - k_a C_R{}^s) \qquad (2.3)$$

$C_O{}^s$ and $C_R{}^s$ are the surface concentrations of O and R, whilst k_c and k_a are the potential dependent rate constants given by:

$$k_c = k_c{}^o \exp\left(\frac{-\alpha zFE}{RT}\right) \qquad (2.4)$$

and $$k_a = k_a^{o} \exp\left(\frac{(1-\alpha)zFE}{RT}\right) \tag{2.5}$$

where α is the charge transfer coefficient

E is the electrode potential

k_c^{o} is the value of k_c at the reference potential

and k_a^{o} is the value of k_a at the reference potential

By substituting (2.4) and (2.5) into equation (2.3) we get:

$$i = zF\left[k_c^{o} C_O^{s} \exp\left(\frac{-\alpha zFE}{RT}\right) - k_a^{o} C_R^{s} \exp\left(\frac{(1-\alpha)zFE}{RT}\right)\right] \tag{2.6}$$

At the reversible potential (E_r) the net current is zero and

$$i_c = i_a = i_o \tag{2.7}$$

i_o is defined as the exchange current density and it follows from (2.7) that

$$\begin{aligned} i_o &= zFk_c^{o} C_O^{s} \exp\left(\frac{-\alpha zFE_r}{RT}\right) \\ &= zFk_a^{o} C_R^{s} \exp\left(\frac{(1-\alpha)zFE_r}{RT}\right) \end{aligned} \tag{2.8}$$

By solving (2.8) for $zFk_c^{o} C_O^{s}$ and $zFk_a^{o} C_R^{s}$ and substituting into (2.6) we obtain

$$i = i_o\left[\exp\left(\frac{-\alpha zF(E-E_r)}{RT}\right) - \exp\left(\frac{(1-\alpha)zF(E-E_r)}{RT}\right)\right] \tag{2.9}$$

where $(E-E_r)$ is defined as the charge transfer overpotential, η_D [29].

Equation (2.9) is known as the Erdey-Gruz and Volmer equation [30].

a) Low Overpotentials

This is when $|\eta_D| \ll \frac{RT}{\alpha zF}$ or $|\eta_D| \ll \frac{RT}{(1-\alpha)zF}$

A linear overpotential-current curve is obtained. Differentiation of (2.9) and putting $\eta_D = 0$ gives

$$\left(\frac{di}{d\eta_D}\right)_{\eta_D \rightarrow 0} = \frac{-zF}{RT}.i_o \tag{2.10}$$

Since the current-overpotential relationship is of the form of Ohm's law, the reciprocal of the left-hand side of (2.10) is defined as the charge transfer resistance R_{CT} [31,32] so that

$$R_{CT} = \frac{RT}{zF} \cdot \frac{1}{i_o} \tag{2.11}$$

b) High Overpotentials

$|\eta_D| \gg \frac{RT}{\alpha zF}$ or $|\eta_D| \gg \frac{RT}{(1-\alpha)zF}$

and one of the exponential terms in equation (2.9) can be missed out.

The Tafel [33] relationship at cathodic overpotentials is obtained:

$$\eta_D = \frac{2.303RT}{\alpha zF} \log i_o - \frac{2.303RT}{\alpha zF} \log i \tag{2.12}$$

and at anodic overpotentials:

$$\eta_D = \frac{2.303RT}{(1-\alpha)zF} \log i_o + \frac{2.303RT}{(1-\alpha)zF} \log i \tag{2.13}$$

The exchange current density, i_o, can be determined from the values of charge transfer resistance (R_{CT}) at low overpotentials, and from measurements taken at high overpotentials by extrapolating η_D vs. log i plots to the equilibrium potential.

The dependence of the exchange current density on the reactant concentration has been shown by Vetter[34] to be

$$i_o = zF\, k^o\, C_O^{(1-\alpha)} \cdot C_R^{\alpha} \qquad (2.14)$$

where k^o is the apparent standard rate constant first introduced by Randles[35].

The above theory is only applicable to reactions in which all electrons are transferred simultaneously. In a review by Losev[36] it deals with electrode reactions which proceed via successive electron transfers with a single rate determining step, and others with comparable rate constants for successive steps.

Recently Levich[37], Marcus[38] and Dogonadse[39] have further developed the theory for simple electrode reactions using a quantum mechanical approach. Instead of the reaction occurring in one smooth step over a single energy barrier it proceeds in stages. The reactant first diffuses to the electrode followed by an arrangement of the ionic atmosphere and the orientation of the solvent molecules to form a transition state. Lastly the electron which is transferred, only this step is treated kinetically whilst the first stages of the process are all in equilibrium and can be solved by thermodynamics. After the electron transfer, the ligand bond distances are changed and the solvent dipoles and ion atmosphere are reorientated. There is no change in energy when an electron is transferred which is a mainstay in the Marcus and Levich theories. Finally, Levich and Dogonadse[40] have worked out a detailed theory for the process of solvent reorganisation.

2.3 Mass Transport Processes

The electrode process represented by equation (2.2)

$$O + ze \rightleftharpoons R$$

may be considered to be made up of the following individual processes:

$$O_{bulk} \longrightarrow O_{electrode} \qquad (2.15)$$

$$O_{electrode} + ze \longrightarrow R_{electrode} \qquad (2.16)$$

$$R_{electrode} \longrightarrow R_{bulk} \qquad (2.17)$$

The overall flow of electrons can be controlled by either process (2.15) or process (2.16). If the first step, given by equation (2.15), is the slowest then the overall reaction is limited by mass transfer of the oxidised species (O) to the electrode, that is, the overall process is mass transfer controlled. If, however, (2.16) has a slower rate than (2.15) the reaction proceeds under charge transfer control. Sometimes neither of the above processes are as slow as a chemical transformation involving the electroactive species, in which case the chemical transformation is the rate determining process.

Three modes of mass transfer are normally encountered: migration, convection and diffusion.

a) Migration

Mass transfer by migration is the result of the forces exerted on charged particles by an electric field. In the presence of a large excess of support electrolyte the migration of electroactive material is minimised to such an extent that it can be neglected.

b) Convection

In any solution undergoing electrolysis, free or natural convection occurs spontaneously as a result of density differences which occur near the electrode and may also originate from thermal or mechanical disturbances. Forced convection can be caused by stirring the solution, rotating the electrode, bubbling gas near the electrode and so forth.

c) Diffusion

Diffusion occurs whenever concentration differences are set up. As soon as electrolysis is started a concentration gradient develops showing that diffusion arises to some extent in every practical electrode reaction. If a planar electrode is immersed in an electrolyte solution containing the species O which is reduced according to equation (2.2) then the number of moles of O which diffuse past a given area (Acm^{-2}) in a time dt, is proportional to the concentration gradient of the diffusing species.

$$\frac{dN}{Adt} = D_O \cdot \frac{\partial C_O}{\partial x} \qquad (2.18)$$

This is Fick's first law. The term $\frac{dN}{A.dt}$ is called the flux (q) and is the number of moles diffusing per unit time through unit area. D_O is the diffusion coefficient, defined as the number of molecules per second crossing unit area under unit concentration gradient. If electrolysis proceeds over a period of time, C_O and hence $\frac{\partial C_O}{\partial x}$ must decrease with time because O is being consumed at the electrode.

Fick's second law shows how C_O varies with time and is summarised in the following manner

$$\frac{\partial C_O}{\partial t} = D_O \cdot \frac{\partial^2 C_O}{\partial x^2} \qquad (2.19)$$

By solving equation (2.19) in terms of C_0 (x,t), equation (2.20) is obtained

$$C_0(x,t) = C_0^b \frac{2}{\pi^{\frac{1}{2}}} \int_0^{x/2\sqrt{(D_0 t)}} e^{-y^2} . \, dy \tag{2.20}$$

The conditions for the solution of (2.19) are

at $t = 0$ $\qquad C_0^s = C_0^b$

at $t > 0$ $\qquad C_0^s = 0$

also $C_0 \rightarrow C_0^b$ as $x \longrightarrow \infty$

where C_0^s and C_0^b correspond to the concentrations of O at the electrode surface and in the bulk solution respectively. The instantaneous current, i_t, is proportional to the flux at $x = 0$, so

$$i_t = zFAq\ (0,t) = \left(zFA\ D_0 \frac{\partial C_0}{\partial x} \right)_{0,t} \tag{2.21}$$

The value of $\left(\frac{\partial C_0}{\partial x}\right)_{0,t}$ is determined by differentiating equation (2.20) and putting $x = 0$.

The final expression for the instantaneous current at a planar electrode under diffusion control becomes

$$i_t = \frac{zFA\ D_0^{\frac{1}{2}}\ C_0^b}{\pi^{\frac{1}{2}}\ t^{\frac{1}{2}}} \tag{2.22}$$

This equation is sometimes called the Cottrell equation.

2.4 Porous Electrode Theory

a) Introduction

A porous body consists of a framework of material traversed by interconnected capillaries. Electrodes with a porous structure change the electrochemical characteristics of the reactions drastically in comparison to flat surfaces because the effective surface is about 10^3 to 10^5 times greater than the geometric surface. In addition, higher limiting current densities can be obtained. However, due to mass transfer and ohmic hindrances the current distribution over the internal surface is mostly non-uniform. Hence coupled effects of concentration changes in the pores and changes in current distribution during discharge have to be considered when analyzing the transient discharge behaviour of the porous electrode. Also, with the porous PbO_2 electrode further difficulty arises due to lead sulphate precipitating and gradually insulating the electrode surface and plugging up the pores.

Various mathematical models have been derived for the analysis of the discharge behaviour of porous electrodes. De Levie [41] published a comprehensive review on the work done in this area. It treats the porous electrode by considering only one single pore with uniform cross-section which is homogeneously filled with electrolyte and that the resistance of the electrode material is assumed to be negligible. Also by neglecting any curvature of the equipotential surfaces within the pore the three dimensional structure can be transformed into an one-dimensional body, hence simplifying the mathematics. There are three main groups of models for flooded electrodes:

i) the pore model,

ii) the analogue model,

and iii) the macrohomogeneous - or continuous-model

b) The Pore Model

The basis of this model is that the porous structure is represented by cylindrical pores, each with a constant radius, parallel to each other and perpendicular to the surface. Winsel [42] has developed this model thoroughly and the derivation obtained takes into account the pore size distribution and deviations from the cylindrical shape.

For redox reactions Austin [43] was able to derive whether the porous electrode underwent a reaction which was controlled by diffusion (concentration gradients, Fick's Law), or by one which was controlled by resistance (potential gradients, Ohm's Law) using the equation:

$$\Phi = \frac{\alpha\rho\, Dz^2F^2C_0}{RT} \qquad (2.23)$$

Φ is a dimensionless constant

ρ is the specific resistance (resistivity)

D is the diffusion constant for the free electrolyte

C_0 is the electrolyte concentration at the outer surface

For a porous electrode an effective diffusion coefficient D^* and an effective specific ionic resistance ρ^* have to be employed.

Using ρ^*, for example

$$\rho^* = \rho \cdot \frac{T}{\theta} = \rho \cdot \frac{\text{tortuosity}}{\text{porosity}} \qquad (2.24)$$

Electrode processes which are resistance-controlled have values of $\Phi > 5$ whereas $\Phi < 0.5$ for diffusion-controlled reactions.

For a charged lead storage battery $\Phi = 0.7$. Although these equations were derived for redox systems with soluble reactants at inert electrodes, they can still be applied to the lead storage battery. Low Φ values are obtained with these batteries showing that the reactions at the electrodes are affected by diffusion of acid which agrees with experimental results obtained by Dolezaek [44] and Burbank et al [5]. However, the pore model cannot be applied to cylindrical electrodes or ones which can be thought of as two-dimensional because then the direction of the pores have to be taken into account.

c) The Analogue Model

This model was established by Euler and Nonnenmacher [45,46] and is represented by electrical equivalent circuits. Therefore a network of ohmic and charge-transfer resistances can be used to simulate the behaviour of porous electrodes. What limits this model is that non-linear resistances must be used when the overvoltage does not very linearly with current density and it is difficult to take into account the influence of diffusion.

d) The Macrohomogeneous Model

This model was introduced by Newman and Tobias [47] and it eliminates the drawbacks posed by the abovementioned models. The whole electrode-electrolyte system is regarded as the superposition of two continua : the electrode matrix and the electrolyte which occupies the voids within the matrix. In the two phases, variables, such as, potential and current are continuous functions of time and distance. The model is based upon equations describing mass transfer, ionic and electronic currents, electrode kinetics and conservation equations for each dissolved species. However, this model does not take into account structural changes when the porous electrodes undergo electrochemical reactions.

Alkire et al [48] investigated flooded porous metal electrodes undergoing structural change by anodic dissolution. Equations were derived to represent the pseudo-steady state which remains intact after the concentration gradients within the pores have become fully established. Later Alkire and Place [49] used the steady-state approach again to investigate the transient behaviour of porous electrodes when a limited quantity of solid reactant is depleted.

Dunning et al [50] put forward a model for the analysis of porous electrodes with sparingly soluble reactants. The model is based on the solution of a set of coupled partial differential equations representing the various applicable laws of transport and conservation. Non-uniform current distribution were considered together with variation in the distribution of reactants and products although the effect of pore-plugging was neglected.

Micka and Rousar [51-53] applied the model to the lead-acid cell. Partial differential equations were derived to describe the transport of mass and charge through the porous lead electrode and equations for the lead dioxide plate, as well as, extending their model to the lead-acid cell as a whole. It was found that the positive PbO_2 plate always limits the capacity of the standard lead-acid battery.

Simonsson [54-57] investigated the discharge behaviour of the positive plate in some detail. Using computational methods pseudo-steady state equations were solved numerically, showing that at high current densities the discharge capacity is limited by both structural and mass-transport effects. At low discharge currents the current distribution is initially uniform but gradually becomes uneven due to changes in electrode porosity and electrolyte concentration. Other workers [58-60] have also used the steady state approach to predict the discharge behaviour of lead-acid cells.

CHAPTER 3

THEORIES OF RELEVANT ELECTROCHEMICAL TECHNIQUES

3.1 Linear Potential Sweep/Cyclic Voltammetry

The method involves the application of a linear potential/time function to an electrode and observing the subsequent voltammogram. If only a single sweep (anodic or cathodic) is carried out the technique is known as linear sweep voltammetry (LSV), but if the sweeps are repetitive, the method is called cyclic voltammetry.

The abovementioned methods were first introduced by Matheson and Nichols [61] and the fundamental equations which describe linear sweep/cyclic voltammetry have been developed by Delahay [62], Shain [63, 64] and others [65-68]. The two techniques have been fully utilised, for example, obtaining detailed description of charge transfer systems and examining reaction mechanisms. Also, cyclic voltammetry has been effective in the study of surface processes, such as, the formation and reduction of oxide layers on metal surfaces.

The basic feature of a voltammogram (that is, a current-potential plot during the sweep) is the formation of a current peak at a potential characteristic of the electrode reaction taking place. The position and shape of current peaks obtained depend on many factors, such as, sweep-rate, electrode material, temperature, solution composition and the concentration of the reactants. The slow sweep rates are employed to study steady-state reactions whereas fast sweep rates are used to test the existence of short-lived intermediates. Only the linear potential sweep can give accurate kinetic parameters because the equations derived apply only if there are no concentration gradients in solution just before the start of the sweep. Cyclic voltammetry causes complex concentration gradients to appear near the electrode surface, hence this technique is best suited to identifying steps in the overall reaction and, new species which occur during electrolysis. Although cyclic voltammetry has limitations, it is used extensively in evaluating, on a qualitative basis, intermediates formed in complex reaction processes.

For a simple electron transfer process, increasing the sweep rate (ν) increases the peak current density (i_p) at the corresponding potential (E_p). If the electron transfer rate is very high then reversible conditions prevail and the peak current density for the process (both reactants and products are soluble) is given by:

$$|i_p| = 2.72 \times 10^5 z^{3/2} D.^{\frac{1}{2}} C_0 \nu^{\frac{1}{2}} \text{ (at } 25^\circ\text{C)} \qquad (3.1)$$

where z is the number of electrons transferred in overall electrode process,

D is the diffusion coefficient ($cm^2 s^{-1}$)

C_0 is the concentration in solution ($mol\ cm^{-3}$)

i_p is measured in Acm^{-2}

and ν is in Vs^{-1}

The peak potential is independent of sweep rate and is related to the polarographic half-wave potential by:

$$E_p = E_{\frac{1}{2}} - 1.109 \frac{RT}{zF} \qquad (3.2)$$

Under totally irreversible conditions,

$$|i_p| = 3.01 \times 10^5 z \left(\frac{2.303\ RT}{bF}\right) D^{\frac{1}{2}} C_0 \nu^{\frac{1}{2}} \qquad (3.3)$$

where b is the Tafel slope and the peak potential in this case is given by:

$$E_p = E_{\frac{1}{2}} - b\left[0.52 - \tfrac{1}{2}\log\left(\frac{b}{D}\right) - \log k_s + \tfrac{1}{2}\log \nu\right] \qquad (3.4)$$

where k_s is the specific rate constant.

The dependence of E_p on ν indicates the departure of the system from equilibrium. Provided that D is known, k_s at the standard potential and b can be calculated from a plot of E_p vs. log ν.

The described equations apply quantitatively only to first order charge transfer reactions with no kinetic or catalytic complications.

3.2 The Potential Step Method

3.2.1 Introduction

This technique is used in studying such processes as electrocrystallisation, corrosion, passivation and so forth which are of technological importance.

The method involves an instantaneous change of the working electrode potential, from a point where its state is well defined, to a new potential where the reaction of interest takes place. The current-time response is recorded as the system relaxes to the steady-state. The transient appears as a sharp rise in current initially (due to double layer charging) followed by a current decay as a result of the reactant near the electrode surface.

When the diffusion is much faster than the electron charge transfer or any other reaction in the sequence, the current will be independent of time except for the charging current. At high overpotentials where electron transfer is fast, and current always determined by the rate of diffusion, the whole transient gives a linear plot of i vs. $t^{-\frac{1}{2}}$.

Under mixed control, the rates of diffusion and the other processes are similar, and a falling transient is observed once more. The decay curve, however, falls less sharply because the diffusion is only partially determining the rate of the electrode process. This situation applies to low overpotentials. Thus mass transfer is fastest at short times whilst at long times diffusion controls the current decay. In the intermediate case the current density can be expressed by the equation [69] :

$$i = zFk_cC_0^{\,b} \exp\left(\frac{k_c + k_a}{D}\right)^2 t \ \mathrm{erfc}\left(\frac{k_c + k_a}{D^{\frac{1}{2}}}\right) t^{\frac{1}{2}} \tag{3.5}$$

The expression has the limiting forms,

i) at short times the equation approximates to:

$$i = zFk_cC_0^{\,b} \left[1 - \frac{2(k_c + k_a)}{\pi^{\frac{1}{2}} \ D^{\frac{1}{2}}} .t^{\frac{1}{2}}\right] \tag{3.6}$$

and ii) at long times it approximates to:

$$i = \frac{zFk_c \ C_0^{\,b}D^{\frac{1}{2}}.t^{-\frac{1}{2}}}{\pi^{\frac{1}{2}} \ (k_c + k_a)} \tag{3.7}$$

Equation (3.6) shows that an i vs. $t^{\frac{1}{2}}$ relationship gives a linear plot and by extrapolating to t = 0 for short times, kinetic data can be extracted. Equation (3.7) for long times should be linear if i is plotted against $t^{-\frac{1}{2}}$.

3.2.2 Electrocrystallisation

A. Two-dimensional model.

The potential step method is used to investigate nucleation and growth of an electrochemical process which occurs at the surface of the electrode. The crystal formation process proceeds via two distinct stages. First, there is the incorporation of an atomic species into the crystal lattice. In order for this phase to occur a kink site must be available for the species to adsorb on to. Furthermore, an edge is first required for the formation of nuclei. The second stage involves the thickening of the deposited layer, this happens by growth occurring at the peripheries of the formed nuclei.

Fleischmann and Thirsk [70] have thoroughly studied the deposition of a new phase under controlled potentiostatic conditions and interpreted potentiostatic transients. The following discussion is concerned with the nucleation and growth model with no edge effects.

a) Without diffusion

i) Growth of Isolated Centres

When a pulse is started nuclei form as discreet centres, either instantaneously or progressively with time, and grow [71]. The characteristic current-time curves in the early stages before the nuclei overlap are calculated on the basis of simple geometric arguments for one nucleus:

$$i = zFk\ S \qquad (3.8)$$

where k is the rate constant (mol m^{-2} sec^{-1}) and S is the area on which material is deposited. The current (rate of growth) is also equal to the rate of change of accumulated charge with time on the surface. Hence using Faraday's Law,

$$i = zFkS = \frac{\rho\ zF}{M}\left(\frac{dV}{dt}\right) \qquad (3.9)$$

where ρ and V are the density and volume, respectively, of the deposited phase of molecular weight M. By expanding the derivative ${}^{d}V/dt$ with respect to the radius r, equations (3.8) and (3.9) give:

$$\frac{dr}{dt} = \frac{MkS}{\rho\,({}^{d}V/dr)} \qquad (3.10)$$

using a cylinder as a model for the growth of a single two-dimensional nucleus, the height of the nucleus is taken as h and

$$S = 2\pi r\,h \qquad (3.11)$$

$$V = \pi r^2\,h \qquad (3.12)$$

By substituting for S and V equation (3.10) becomes

$$\frac{dr}{dt} = \frac{Mk}{\rho} \qquad (3.13)$$

Assuming that r = 0 at t = 0, equation (3.13) is integrated with respect to time to yield the time dependence of the radius of a single nucleus,

$$r = \frac{Mkt}{\rho} \qquad (3.14)$$

Substitution for r in equation (3.11) followed by insertion of S into equation (3.8) gives the current for the growth of a single centre as a function of time

$$i = \frac{2\pi zFk^2hMt}{\rho} \qquad (3.15)$$

However, a large number of nuclei will exist at a given time on the electrode surface. Hence, the factor N_0 is introduced which is the total number of nuclei for the simplest case of instantaneous nucleation. It is assumed that no new growth centres occur after the imposition of the pulse, hence equation (3.15) for the total current becomes

$$i = 2\pi z\, N_0\, Fk^2 h\, \frac{M}{\rho}\, t \quad \text{(instantaneous nucleation)} \qquad (3.16)$$

which predicts a linear dependence between i and t.

The expression for progressive nucleation can be calculated given that the number of nuclei at any time is given by:

$$N = N_0\, (1-(\exp - A't)) \qquad (3.17)$$

where N is the number of nuclei at any one time, N_0 is the initial number of nuclei and A' is the nucleation rate constant. Differentiating equation (3.17) with respect to t followed by the fact that at short times $N \ll N_0$ then the differential dN/dt is given by

$$\frac{dN}{dt} = N_0 A' \qquad (3.18)$$

As nucleation and growth occur simultaneously the resulting current at time t after the start of deposition can be shown by equation (3.19)

$$i = \int_0^t i(u) \left(\frac{dN}{dt}\right)_{t-u} du \qquad (3.19)$$

where u is the age of the nucleus. By substituting equations (3.15) and (3.18) into equation (3.19) the total current due to simultaneous growth and nucleation is obtained:

$$i = \frac{\pi zFk^2h M N_o A't^2}{\rho} \quad \text{(progressive nucleation)} \qquad (3.20)$$

Similar equations for other geometries are listed by Harrison and Thirsk [71].

ii) Overlap of Growth Centres

Equations (3.16) and (3.20) predict that the current is infinite with time, which is unacceptable because at some point during the deposition neighbouring centres overlap. Hence the area available for growth decreases as overlap increases.

When the growing centres overlap randomly, Avrami[72]has shown that

$$S_1 = 1 - \exp(-S_{1ex}) \qquad (3.21)$$

where $S_{1ex} = \pi r^2$, is the top area of an isolated nucleus and S_1 is the actual area when considering overlap.

For instantaneous nucleation S_{1ex} will be

$$S_{1ex} = N_o \pi r^2 \qquad (3.22)$$

and for progressive nucleation

$$S_{1ex} = \pi \int_0^t r(u)^2 \left(\frac{dN}{dt}\right)_{t-u} du \qquad (3.23)$$

substituting for r with $r = Mkt/\rho$ from (3.14) gives

$$S_{1ex} = \pi N_o k^2 \frac{M^2}{\rho^2} t^2 \quad \text{(instantaneous)} \qquad (3.24)$$

$$S_{1ex} = \pi N_o A'k^2 \frac{M^2}{3\rho^2} t^3 \qquad \text{(progressive)} \qquad (3.25)$$

Substitution into equation (3.21) yields

$$S_1 = 1-\exp(-\pi N_o k^2 \frac{M^2}{\rho^2} t^2) \qquad \text{(instantaneous)} \qquad (3.26)$$

and

$$S_1 = 1-\exp\left(-\pi N_o A'k^2 \frac{M^2}{3\rho^2} t^3\right) \qquad \text{(progressive)} \qquad (3.27)$$

For circular two dimensional nuclei, the volume per unit area of total surface is $V = S_1 h$ and if equation (3.9) is introduced then the following expressions for potentiostatic transients are produced:

$$i = \left(2zF\pi . N_o h \, k^2 \frac{M}{\rho} t.\right) \exp\left(-\pi N_o k^2 \frac{M^2}{\rho^2} t^2\right) \text{(instantaneous)} \quad (3.28)$$

$$i = \left(zF . \pi N_o A'h \, k^2 \frac{M}{\rho} t^2\right) \exp\left(-\pi N_o A' \, k^2 \frac{M^2}{3\rho^2} t^3\right) \text{(progressive)} \quad (3.29)$$

Equations (3.28) and (3.29) have the characteristic shapes shown in Fig. 3.1 when plotted in non-dimensional form. The experimental i-t plots sometimes, have a similar shape. The maximum current (i_m) and time(t_m) are given by differentiating (3.28) and (3.29).

At very short times the current increases linearly with t (instantaneous nucleation) or t^2 (progressive nucleation) because the exponential terms in both cases are approximately equal to 1. However, at long times ($t > t_{max}$) the exponents dominate, and ln i varies linearly with t^2 (instantaneous) or t^3 (progressive).

Another current/time relationship can be achieved by dividing both the above equations by t and t^2 respectively. By taking logarithms of both sides of the equations the following expressions occur,

$$\ln (i/t) = a - bt^2 \text{ (instantaneous)} \tag{3.30}$$

$$\ln (i/t^2) = a' - b't^3 \text{ (progressive)} \tag{3.31}$$

Only in a few situations, for example, deposition on amalgams the formation of a true monolayer is found. In most cases though, the production of successive layers of deposit is observed. Hence different transients are obtained and this multilayer deposition has been studied by many workers [73-75], including the numerical work by Armstrong and Metcalfe [76] who considered the contributions to the transient from the formation of 50 two-dimensional layers. Fig. 3.2 shows the contributions from the first 5 monolayers together with the total current observed; it was discovered that the limiting value for the current was reached after four or five monolayers.

b) With diffusion

Using the nucleus in the previous section, it is considered here to grow by diffusion, two-dimensionally and without overlap. The radius (r) at time t was shown [77] to obey the equation

$$r = \theta\ (Dt)^{\frac{1}{2}} \tag{3.32}$$

where θ is a constant controlled by the potential, M and ρ, and D is the solution diffusion coefficient.

Using Avrami's treatment [72] the following expressions are obtained,

Fig. 3.1 Theoretical current-time curves according to:

(a) equation (3.28)

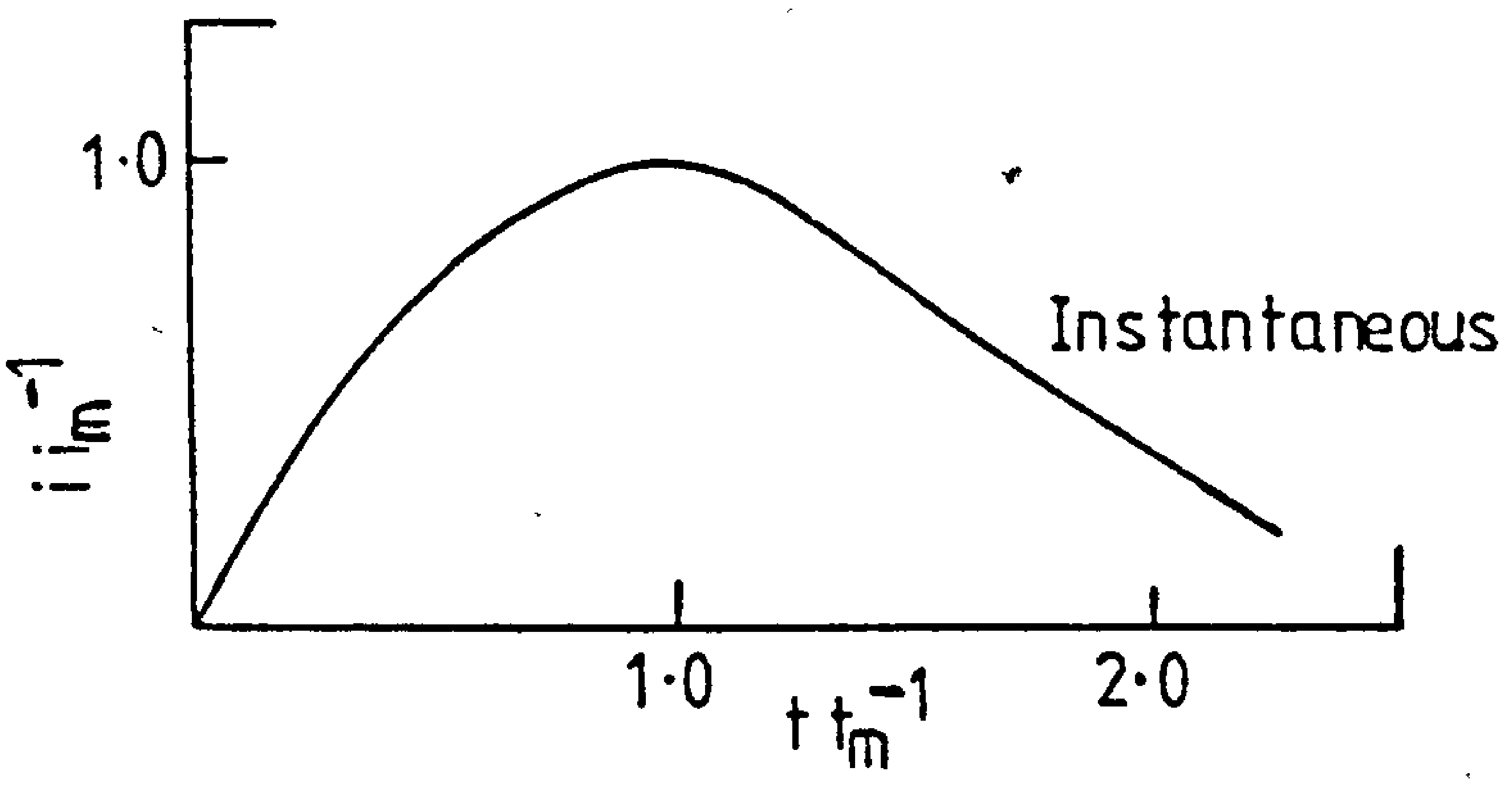

(b) equation (3.29)

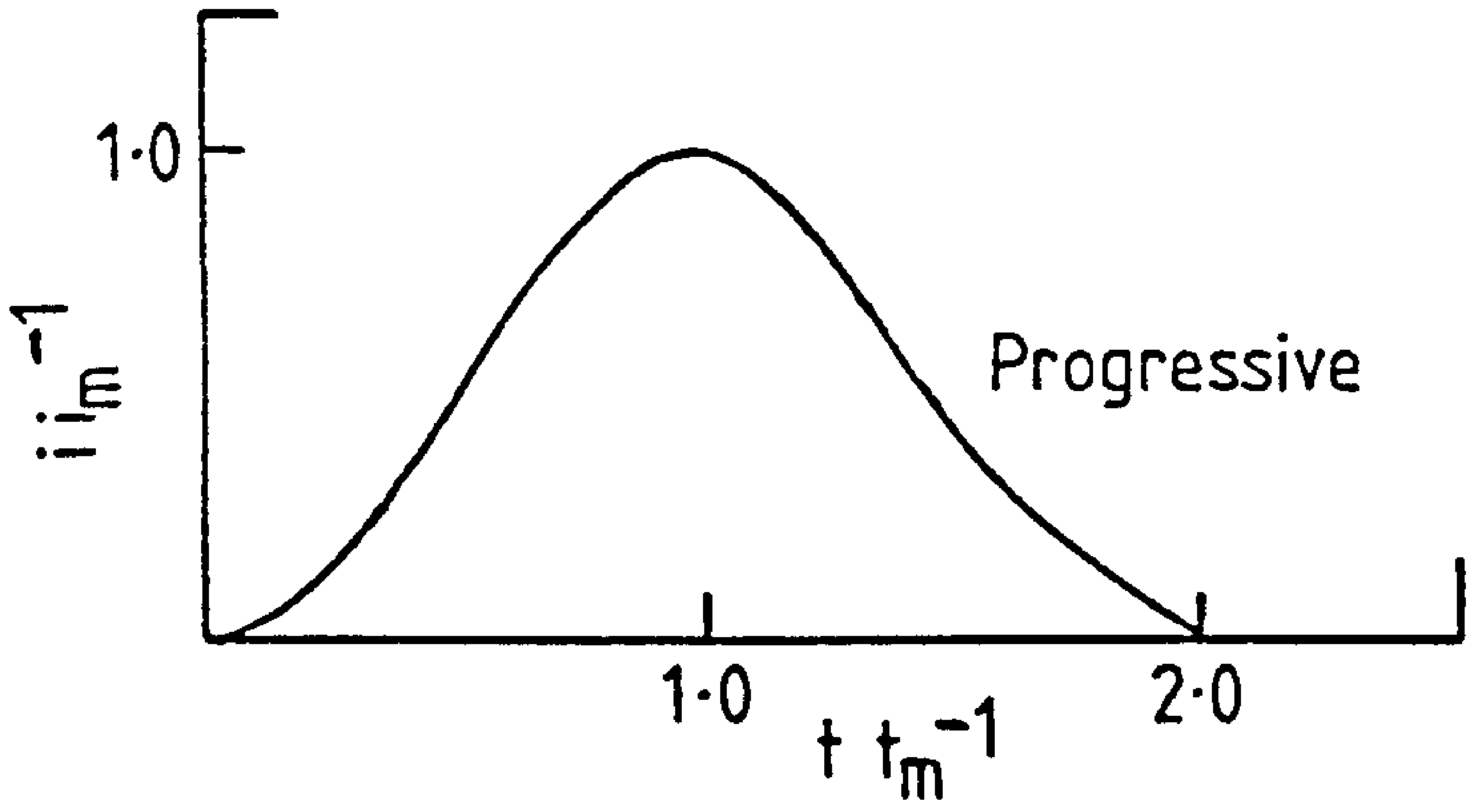

Fig. 3.2 Total current transient for layer by layer growth showing contribution from individual layers

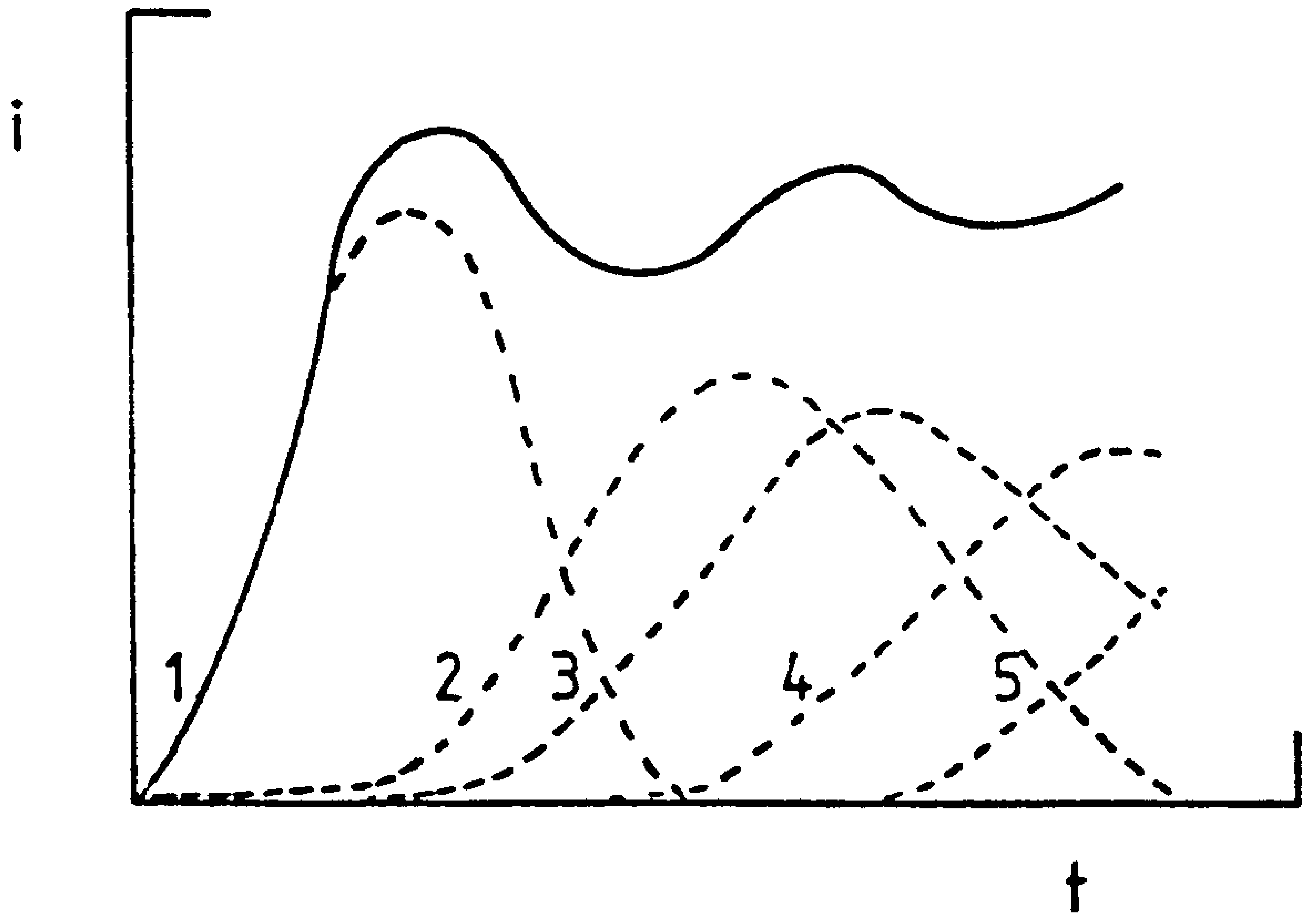

$$i = q_m \pi \theta^2 D \exp(-\pi \theta^2 D N_0 t) \quad \text{(instantaneous nucleation)} \qquad (3.33)$$

$$i = q_m \pi \theta^2 D N_0 A't \exp\left(\frac{-\pi \theta^2 D N_0 A't^2}{2}\right) \quad \text{(progressive nucleation)} \qquad (3.34)$$

where q_m is the charge for the monolayer.

B. Three-dimensional model

Three-dimensional growth is basically obtained by layer-by-layer growth. As shown in Fig. 3.3, Armstrong et al [78] have used a three-dimensional model of growth of right circular cones where the rates of advance are defined as V_1, V_2, V_3. Considering a slice x from the surface and height dx growing out horizontally, assuming that the nuclei are randomly distributed on the surface and that the Avrami equation can be employed to describe the interaction of slices at a height x, then finally the current due to a layer comprising all the cylinders of height dx can be written as

$$di = f(x)dx = 2zF N_0 M k_1^2 \left(t - \frac{x}{V_2}\right) \exp\left[\frac{-\pi N_0 k_1^2 M^2}{\rho^2} \left(t - \frac{x}{V_2}\right)^2\right] dx \qquad (3.35)$$

for the case of instantaneous nucleation, where V_2 is the growth velocity perpendicular to the plane and k_1 is the rate constant parallel to the plane. Integration and substitution of V_2 by the related rate constant k_2 gives

$$i = zFk_2 \left[1 - \exp\left(-\frac{\pi N_0 k_1^2 M^2 t^2}{\rho^2}\right)\right] \qquad (3.36)$$

At short times the current is given by

$$i = \frac{zFk_1^2 k_2 \pi N_0 M^2 t^2}{\rho^2} \qquad (3.37)$$

Fig. 3.3 Three-dimensional models

(a) growth of circular cones on an inert substrate (metal deposition)

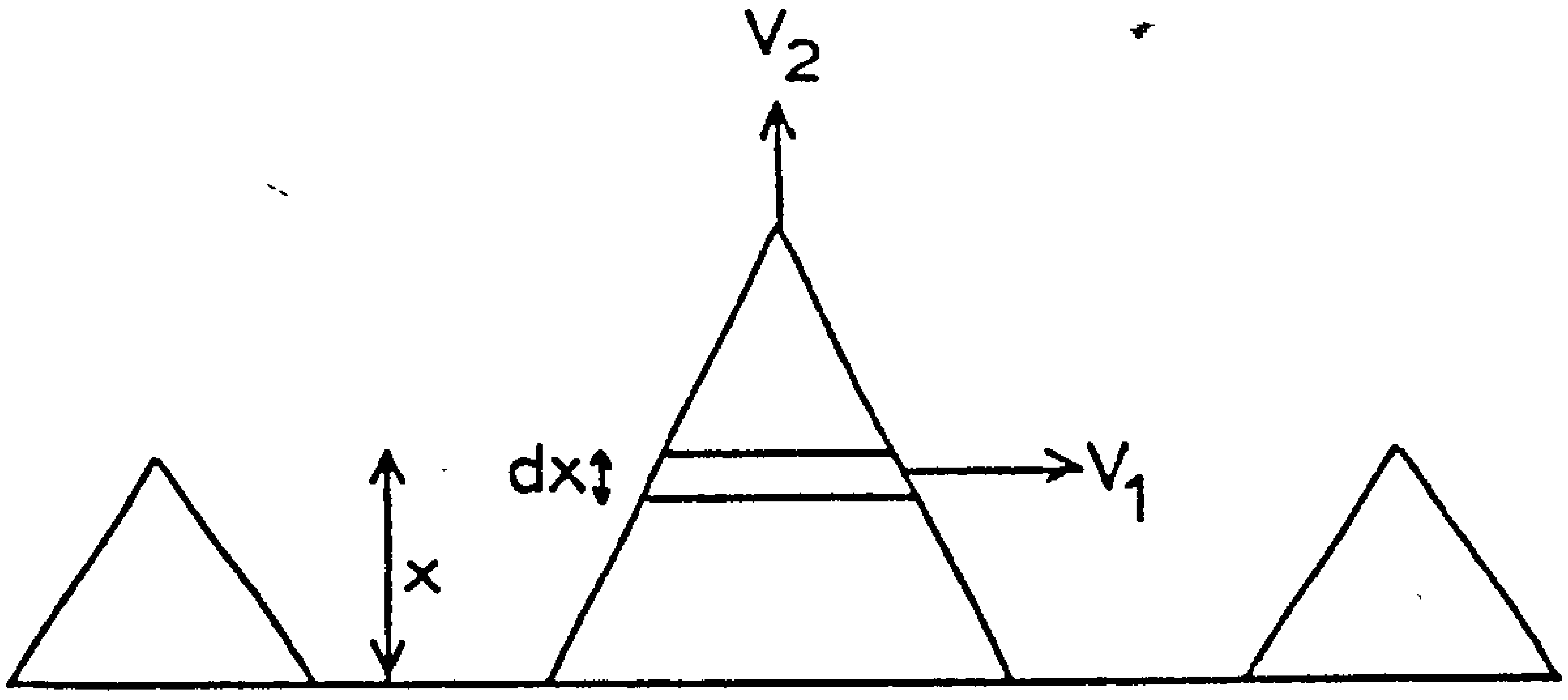

(b) growth of circular cones on a substrate of the same material, the base plane moves with velocity V_3 (metal deposition)

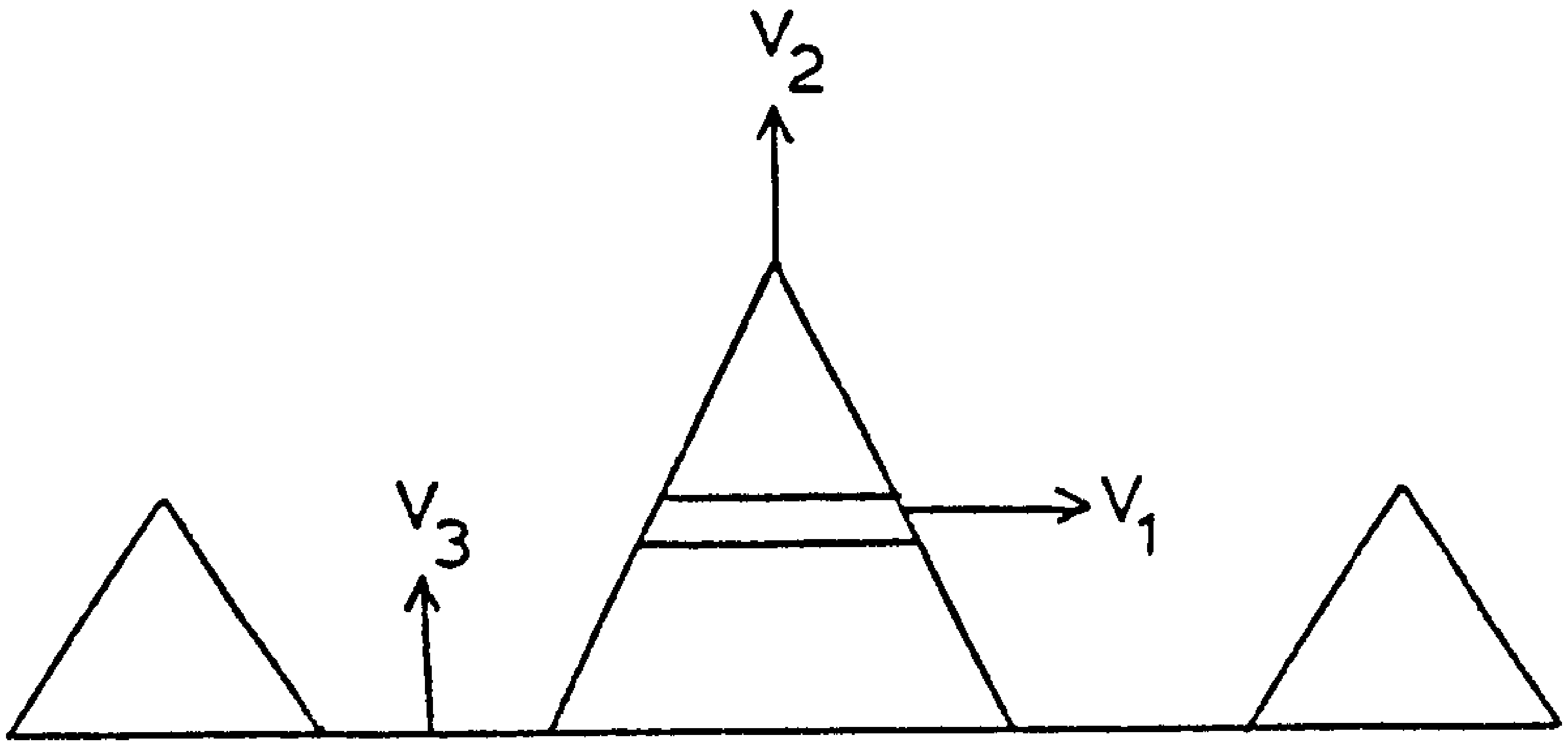

(c) current only flows into the uncovered area (passivation)

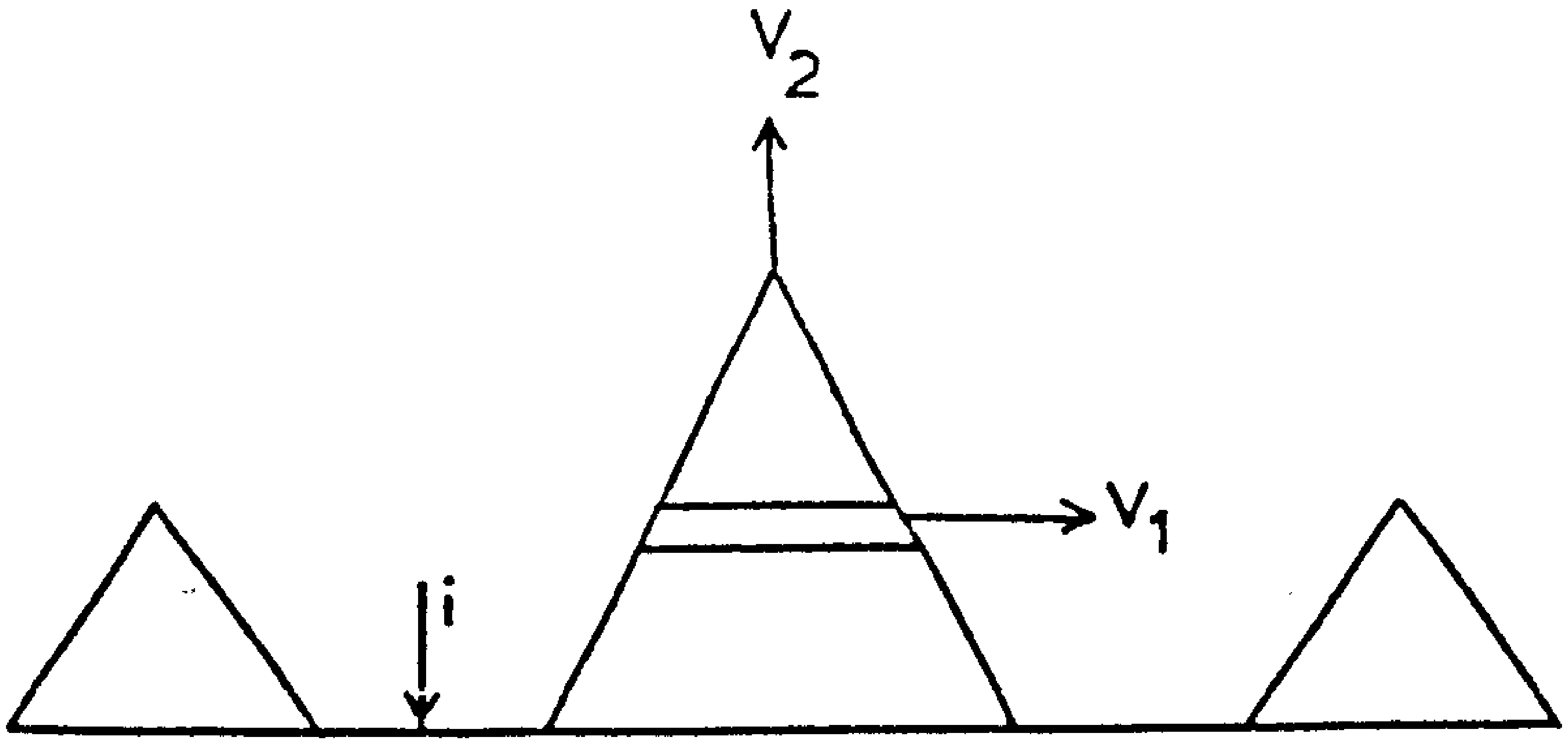

The following expression is obtained when considering progressive nucleation:

$$i = zFk_2 \left[1 - \exp\left(\frac{-\pi M^2 k_1^2 N_o A' t^3}{3\rho^2} \right) \right] \qquad (3.38)$$

The model can be used to explain passivation. Here the species must spread from the electrode to the nucleation centres in order to increase expansion. If the species is considered to go through only the uncovered electrode area, hence as time approaches infinity, the current reaches zero. By assuming that the velocity of advance (V_2) (perpendicular to the electrode) is proportional to the uncovered surface area, then equation (3.38) is obtained for progressive nucleation.

$$i = zFk_2 \left[1 - \exp\left(\frac{- \pi M^2 k_1^2 N_o A' t^3}{3\rho^2} \right) \right] \exp\left(\frac{- \pi M^2 k_1^2 N_o A' t^3}{3\rho^2} \right) \qquad (3.39)$$

Equation (3.39) describes a maximum in the i-t curve given by

$$i_m = \frac{zFk_2}{4} \qquad (3.40)$$

and

$$t_m = \left(\frac{3\rho^2 \ln 2}{\pi M^2 k_1^2 N_o A'} \right)^{1/3} \qquad (3.41)$$

Also $i_m t_m = 0.208\, zFk_2 \left(\frac{3\rho^2}{\pi M^2 k_1^2 N_o A'} \right)^{1/3}$ (3.42)

hence k_1, k_2 and A' can be eliminated if the above values are substituted into equation (3.39) and Fig. 3.4 shows the resulting reduced plot. Fig. 3.5 exhibits two i-t transients, one for equation (3.38) corresponding to progressive-three dimensional growth without passivation and the other

Fig. 3.4 Theoretical plot for 3-D progressive nucleation corresponding to eq. (3.39)

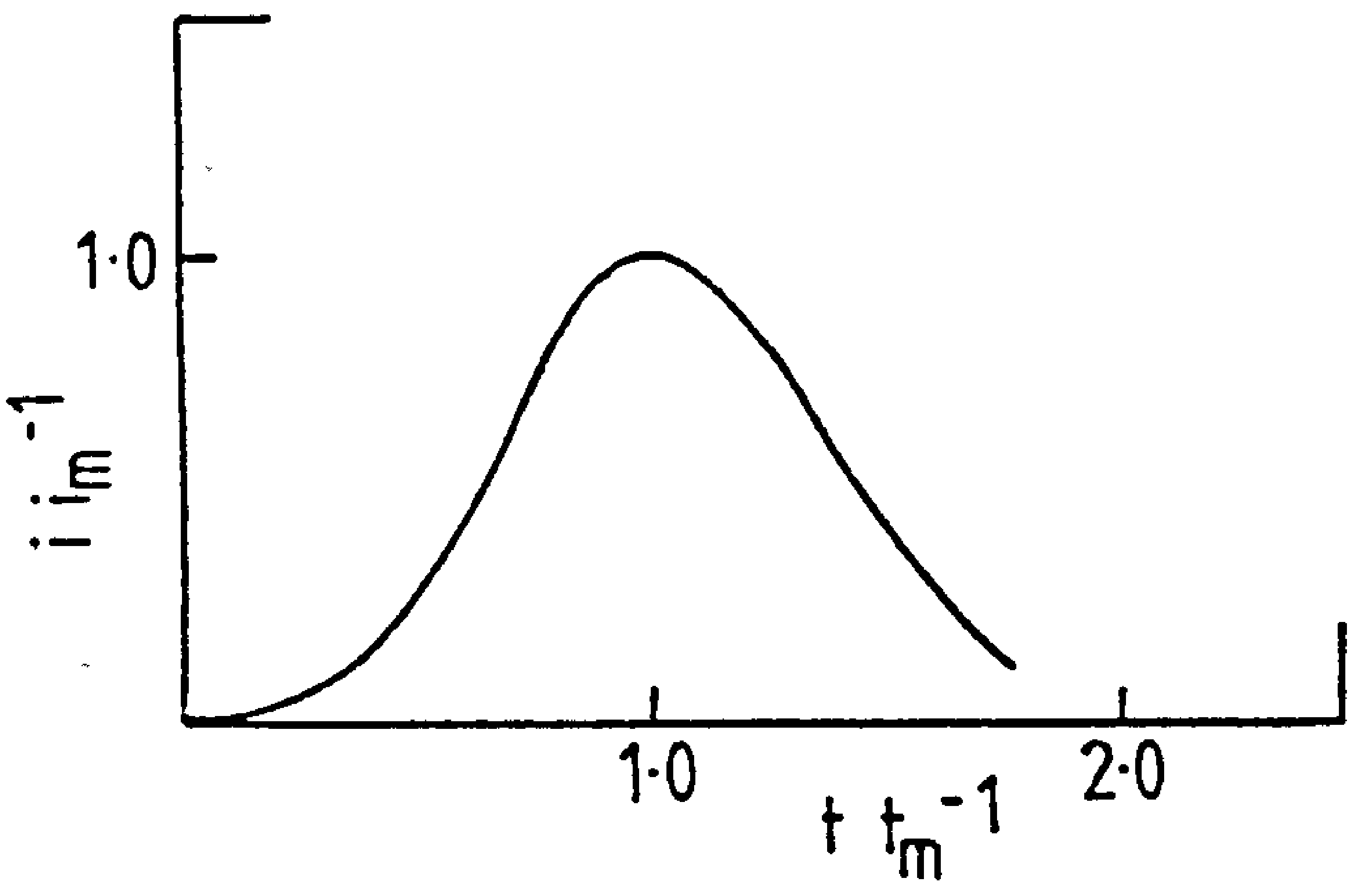

Fig. 3.5 Predicted $i - t$ curves for 3-D progressive nucleation :
(A) without passivation, eq.(3.38)
(B) with subsequent passivation, eq.(3.39)

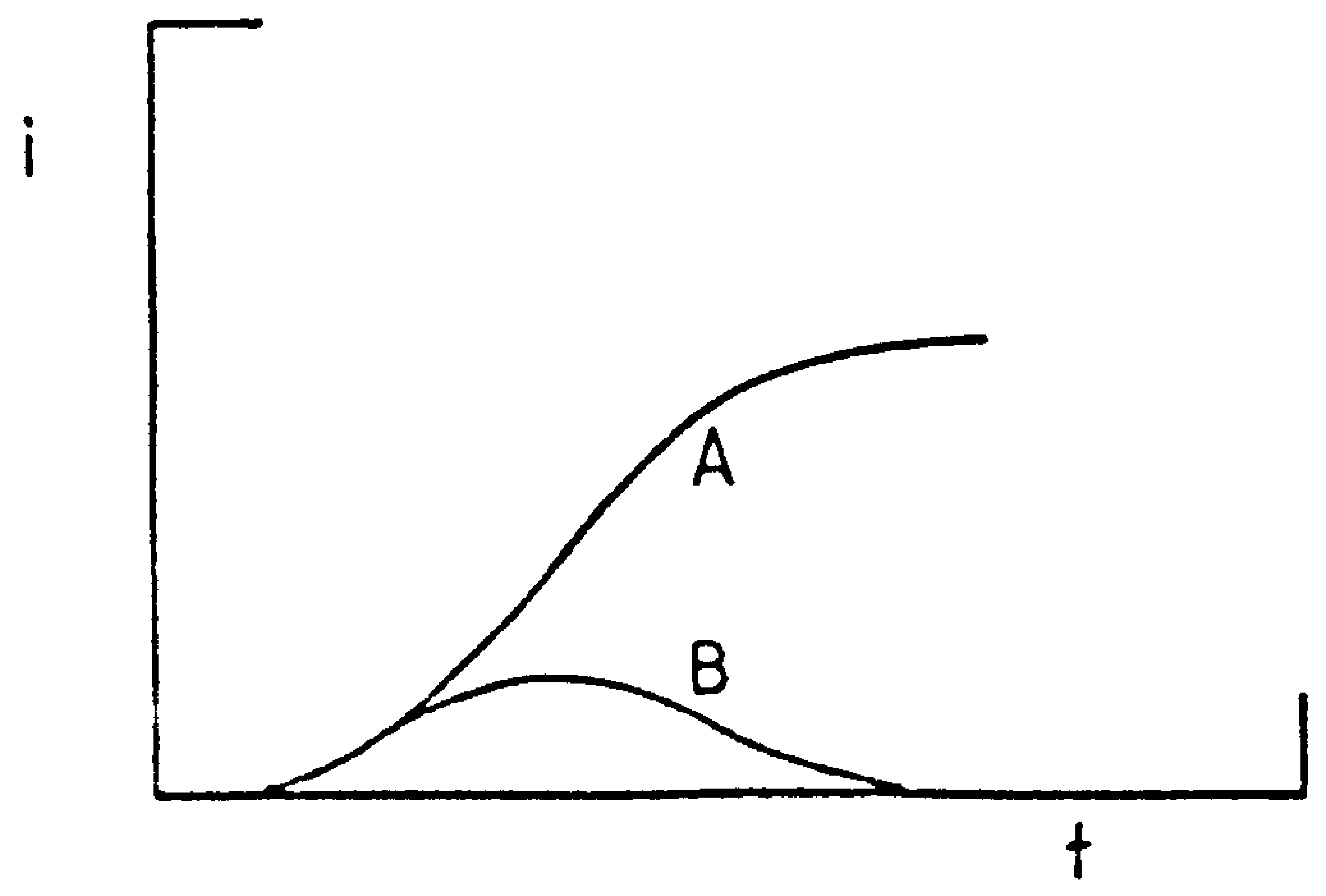

equation (3.39), where subsequent passivation occurs.

3.3 The A.C. Impedance Technique

3.3.1 Introduction

This method is used to study the a.c. impedance characteristics of an electrochemical system. Kinetic parameters related to the electrode concerned can be evaluated to give a better understanding of the reaction mechanisms occurring at it. With this technique it is possible to examine simple charge transfer processes and more complex ones which involve specific adsorption of reactants or products, as well as, chemical reactions preceding or following the charge transfer process.

There has been some industrial application of the a.c. impedance method to fuel cells, batteries, electrochemical synthesis, electrolysis, electroplating, etc. Also, in some cases, the state of charge of primary and secondary cells have been determined.

In normal electrochemical techniques, the voltage applied to the two electrodes in the cell is kept constant during the current measurement. For the alternating current method, an alternating voltage (v) of relatively small amplitude (3mV) is superimposed on the potential difference, and the current contains an alternating component of amplitude i. When the amplitude of v varies sinusoidally with time (t), and with frequency (f), the following expressions are obtained:

$$\omega = 2\pi f \tag{3.43}$$

$$v = V_{max} \sin . \omega t \tag{3.44}$$

$$i = I_{max} \sin (\omega t - \phi) \tag{3.45}$$

$$\text{and} \quad Z_{cell} = \frac{V_{max}}{I_{max}} \quad \arg(\phi) = \left| Z_{cell} \right| \arg \phi \qquad (3.46)$$

where Z_{cell} is the impedance of the cell and ϕ is the phase angle between the current and voltage.

In electrochemistry the reactances most often observed are capacitive, giving a negative quantity on the Argand diagram. However, it is normal practice to use the first quadrant of the complex plane to display them (Sluyters Plot). Also the Randles Plot allows the impedance to be resolved into resistive and capacitive components which are plotted against $\omega^{-\frac{1}{2}}$.

3.3.2 The Cell Impedance

Warburg [79]first calculated the faradaic impedance of a cell although double layer capacitance was neglected. Next, Randles [80]described the impedance for fast electrode reactions in a galvanic cell with a simple one step redox reaction, the rate of which is controlled only by charge transfer and diffusional mass transfer processes. Fig. 3.6 shows a network [81, 82] of resistances and capacitors which represents the impedance of an electrolytic cell and is usually described as a Randles Circuit. R_Ω is the ohmic resistance of the electrolyte solution between the electrodes and C_{dL} is the double layer capacitance which varies with d.c. potential, and is dependent on the concentration and nature of the electrolyte. Θ is the charge transfer resistance which represents the activation polarisation of the electrode reaction, (also related to the rate of reaction).

The Warburg impedance W ($W = R_d + C_d$) is the impedance to a.c. current due to the charged species diffusing to and from the electrode.

Solution of Fick's second law of diffusion, taking into account the appropriate boundary conditions, allows the Warburg impedance to be represented by a series combination of resistive and capacitive reactance:

$$W = \sigma\omega^{-\frac{1}{2}} - i\,\sigma\omega^{-\frac{1}{2}} \qquad (3.47)$$

where σ is the Warburg coefficient.

ω is the angular frequency of the alternating current. The charge transfer resistance Θ, and the Warburg coefficient σ, at the equilibrium potential are given by:

$$\Theta = \frac{RT}{z^2F^2\, k_{sh}\, C_O^{\ \alpha}\, C_R^{\ (1-\alpha)}} \qquad (3.48)$$

and

$$\sigma = \frac{RT}{z^2F^2 2^{\frac{1}{2}}} \left(\frac{1}{C_O D_O^{\frac{1}{2}}} + \frac{1}{C_R D_R^{\frac{1}{2}}} \right) \qquad (3.49)$$

At potentials other than the equilibrium potentials, Θ and σ can be expressed in terms of bulk concentrations providing equations (3.48) and (3.49) are accordingly modified [83].

Sluyters [84]and Sluyters-Rehbach [85]managed the interpretation of the total cell impedance in terms of R_Ω, C_{dL}, Θ and σ, and represented the frequency dependent impedance of the simple electrode, by plotting the impedance as a vector in the complex plane. The procedure involved plotting the real component Z' against the imaginary Z" of the cell impedance, as a function of some varied parameter, e.g. frequency, concentration or d.c. potential.

Using Randles circuit (Fig. 3.6) the cell impedance is given by:

$$Z = R_\Omega + \frac{1}{i\omega C_{dL} + \left(\frac{1}{\Theta + \sigma\omega^{-\frac{1}{2}} - i\sigma\omega^{-\frac{1}{2}}} \right)} \qquad (3.50)$$

After separation of the real and imaginary parts of Z the following is obtained:

Fig. 3.6 Electrical analogue of the electrode interphase

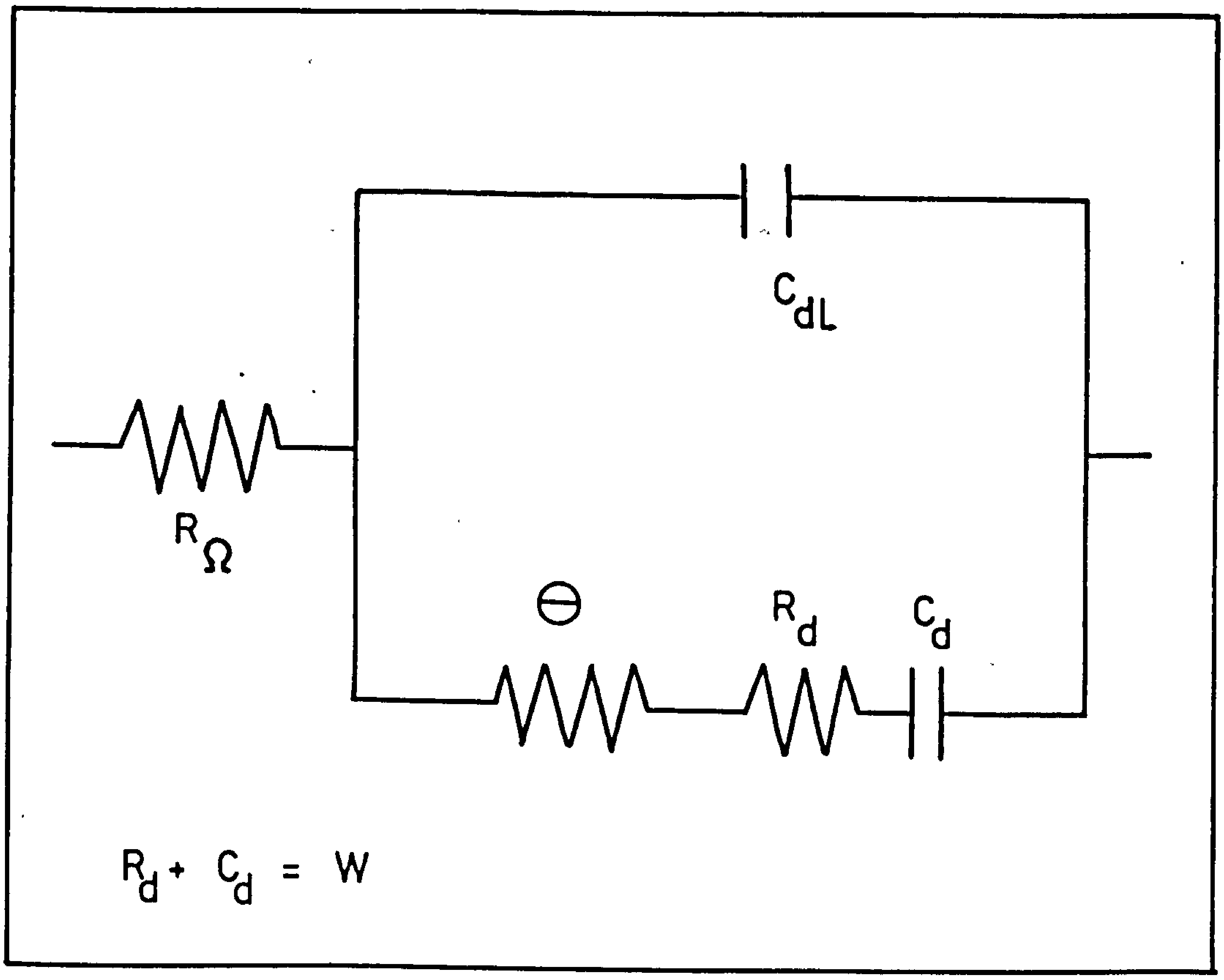

Fig. 3.7 Complex plane display – diffusion control

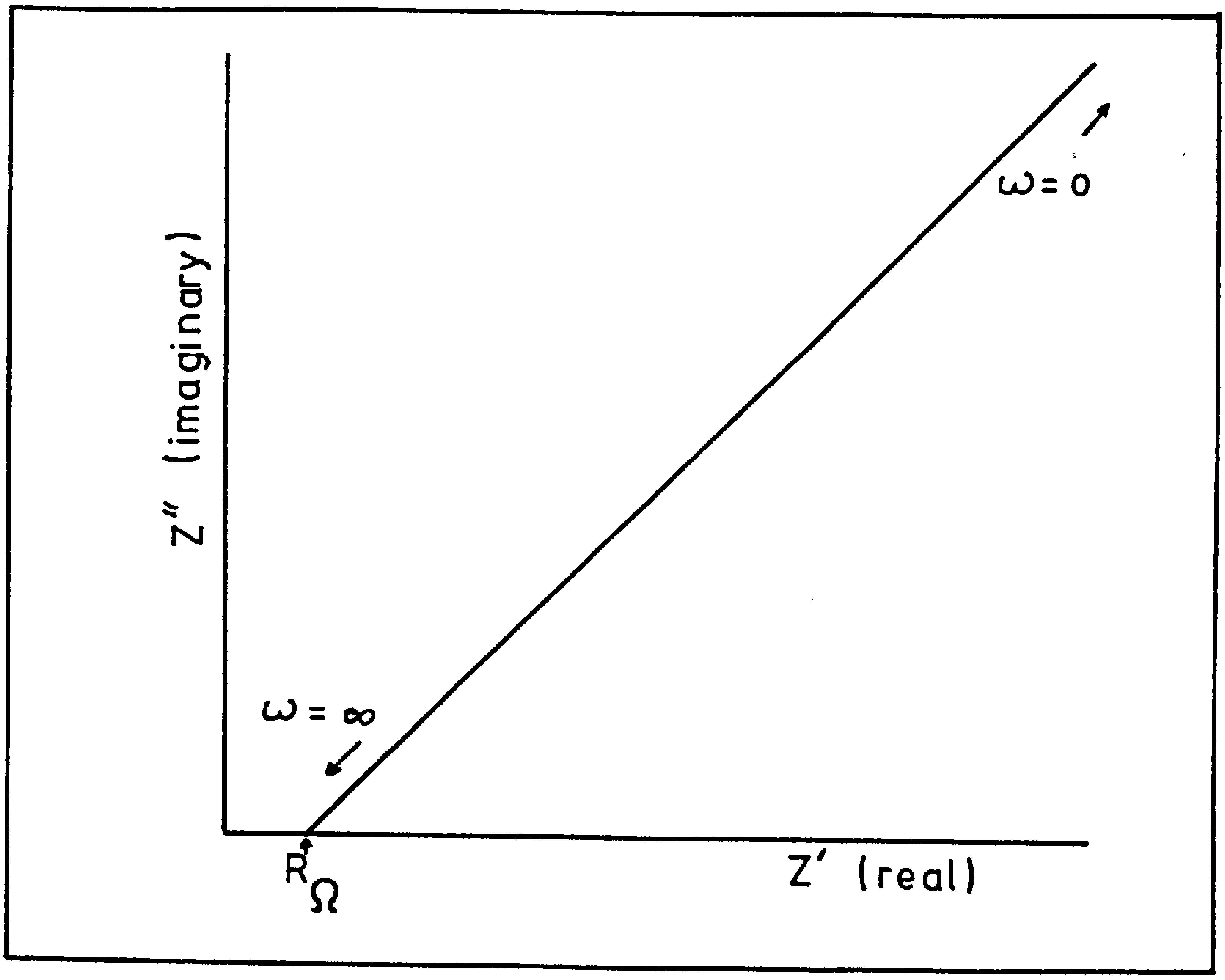

$$Z = Z' - iZ'' \qquad (3.51)$$

where Z' and Z" are given by:

$$Z' = R_{\Omega} + \frac{\Theta + \sigma\omega^{-\frac{1}{2}}}{(\sigma\omega^{\frac{1}{2}}C_{dL}+1)^2+\omega^2C_{dL}^2(\Theta+\sigma\omega^{-\frac{1}{2}})^2} \qquad (3.52)$$

and

$$Z'' = \frac{\omega\, C_{dL}(\Theta+\sigma\omega^{-\frac{1}{2}})^2 + \sigma^2C_{dL} + \sigma\omega^{-\frac{1}{2}}}{(\sigma\omega^{\frac{1}{2}}C_{dL}+1)^2 + \omega^2C_{dL}^2\ (\Theta+\sigma\omega^{-\frac{1}{2}})^2} \qquad (3.53)$$

At low frequencies, the effects of the double layer capacitance can be neglected and the impedance Z from equation (3.51) reduces to:

$$Z = R_{\Omega} + \Theta + \sigma\omega^{-\frac{1}{2}} - i\ (\sigma\omega^{-\frac{1}{2}} + 2\sigma^2C_{dL}) \qquad (3.54)$$

The impedance tends to W and Fig. 3.7 shows a plot on the Argand diagram which is a straight line of 45° slope.

At higher frequencies and with a fairly irreversible reaction, the concentration polarisation can be neglected, and equation (3.51) becomes:

$$Z = R_{\Omega} + \frac{\Theta}{1+\omega^2C_{dL}^2\Theta^2} - \frac{i\omega C_{dL}\Theta^2}{1+\omega^2C_{dL}^2\theta^2} \qquad (3.55)$$

Fig. 3.8 shows a Sluyters plot. A semicircle is displayed which is due to Θ and C_{dL} acting as a parallel resistance and capacitance, and shunted along the real axis from the origin by the ohmic resistance of the electrolyte (R_{Ω}). Also, C_{dL} can be calculated using the frequency at the top of the semicircle:

$$\omega = \frac{1}{\Theta\ C_{dL}} \qquad (3.56)$$

Fig. 3.8 Complex plane display - charge transfer control

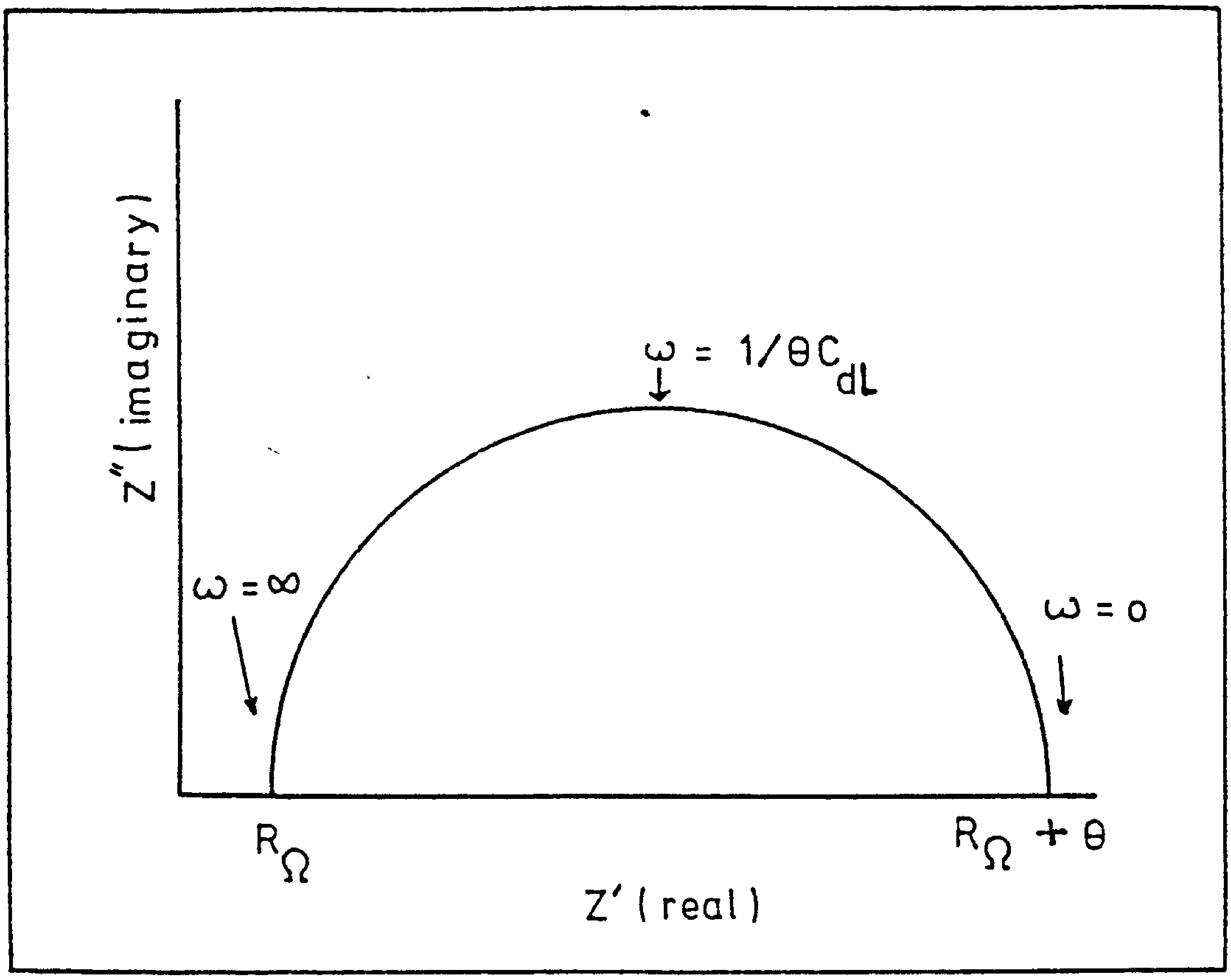

Fig. 3.9 Complex plane display - mixed control

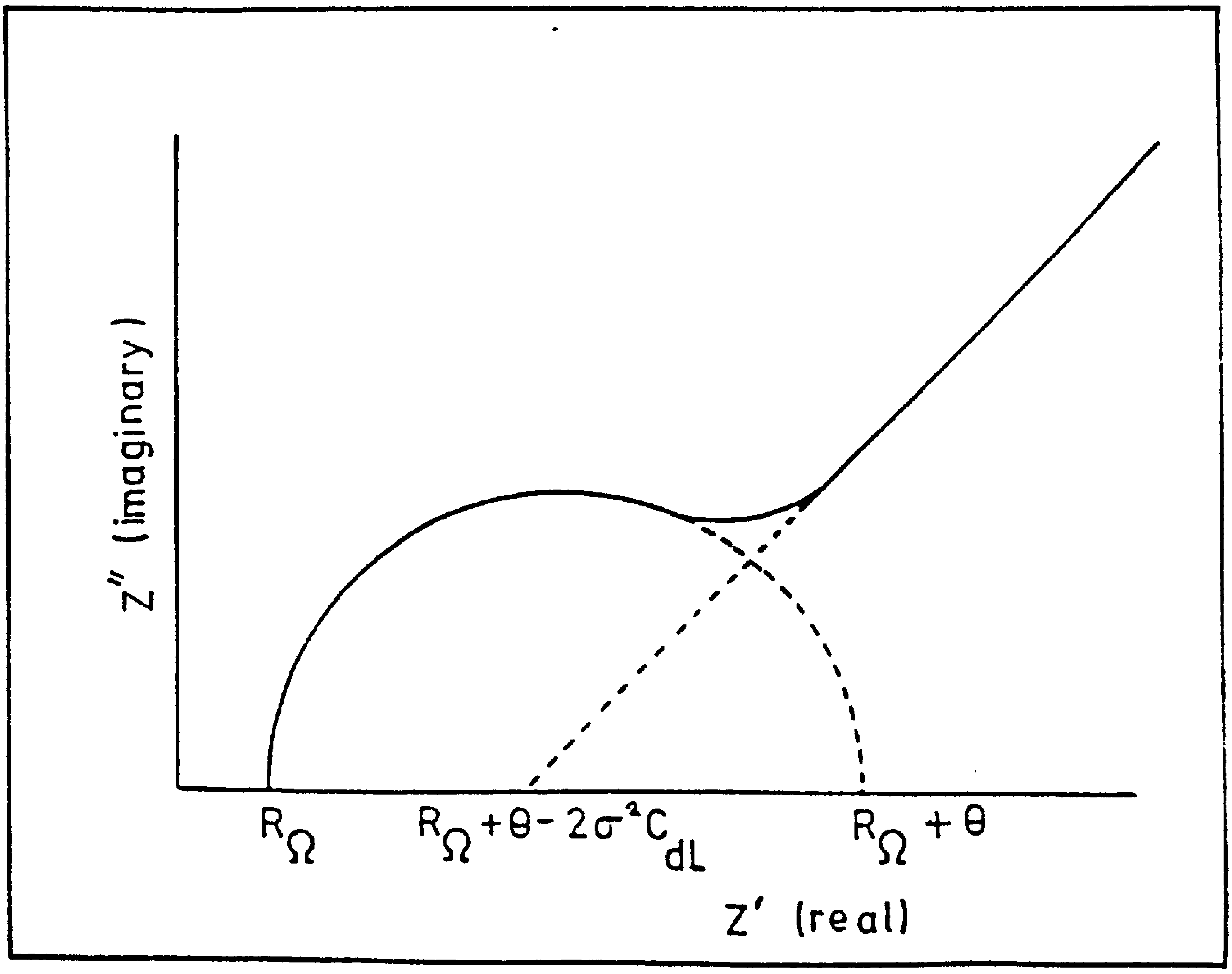

At lower frequencies the diffusion polarisation distorts the semicircle. Fig. 3.9 highlights a 45^{0} slope at low frequency.

3.3.3 Practical Considerations

The simple electrochemical process has been extended to incorporate the effects of surface processes by Grahame [86]and Sluyters [85].

The use of extra resistances and capacitances in the simple electrode analogue are used to represent the adsorption of species. If the adsorbed species are able to undergo a redox reaction, then extra components are added to the analogue, in effect, shunting the double layer [87]. The review by Armstrong et al [88]extends the discussion of complex reactions to passivity, nucleation and growth processes. It was shown that differences in the impedance spectra can be used to distinguish between cases of two-dimensional nucleation and growth, and adsorbed intermediates.

Impedance measurements are being carried out on complete cells [89, 90]. As the cells are discharged the impedance spectra vary and hence a state-of-charge test can be developed based on a frequency-response experiment. Thus, the existing impedance theory can be extended so that the behaviour of commercial cells can be better understood. However, difficulties occur due to the fact that for planar electrodes, the current lines are perpendicular to the surface whereas for porous electrodes they are effectively parallel to it. As a consequence, the Warburg impedance for the porous electrode is dependent on terms proportional to $\omega^{-\frac{1}{4}}$ rather than $\omega^{-\frac{1}{2}}$ in equation (3.47). Also, the high-frequency semicircle which cuts the real axis normally for the planar electrode, comes off at $^{\pi}/4$ in the case of the porous one. The usual method of dealing with the porous electrode is to use the method of "squaring"[41]. This involves doubling the phase angle of the impedance locus and the amplitude is squared.

Darby [91] and Gutmann [92] have described inductive impedances in some detail, however, with the work done on porous PbO_2 described in later chapters, the impedance plots contain no inductive parts, especially at high frequencies.

CHAPTER 4

REVIEW OF WORK DONE ON PbO_2 IN H_2SO_4 AT LOUGHBOROUGH UNIVERSITY (1975-1981) IN CONJUNCTION WITH CHLORIDE TECHNICAL LTD.

The work carried out by P. Casson (1975-1978) was concerned with the electrochemistry of solid β-lead dioxide and porous lead dioxide electrodes. Techniques, such as, linear sweep voltammetry, potentiostatic pulse experiments and a.c. impedance measurements were employed in studying the electrochemistry of the lead dioxide. The data gained from these methods enabled a model to be put forward to explain the reduction of β-PbO_2 to $PbSO_4$ in 5M H_2SO_4. The discharge process is controlled by charge transfer and terminated by a blocking film of $PbSO_4$ which conducts only by a high field process. In other words, the current through the $PbSO_4$ is due to high field ion conduction and is small compared with the current at the uncovered areas of the electrode. The current through the uncovered areas of the surface is charge transfer controlled. Also the reduction of the porous electrode was not diffusion-controlled (via the electrolyte) and there was no evidence for a nucleation process. Scanning electron microscopy (SEM) was used to confirm the electrochemical data obtained from the above experiments carried out.

A variety of alloy supports have been investigated concerning the effect that the solid/porous material interphase has on the electrode behaviour. Additives used in lead were, for example, antimony, aluminium, bismuth, cadmium, tin, barium, arsenic and copper. It was discovered that the porous lead/antimony (6%) alloy was far superior to the other porous alloys because it could be cycled quite extensively with no disastrous loss in charge output in the reduction. Bismuth was the only additive to enhance the porous electrode behaviour whereas the other additives all had marked detrimental effects.

Kelly (1978-1981) used the same techniques as mentioned earlier when investigating the formation of lead dioxide on both the flat lead/ lead alloy electrode and the porous electrode. (The latter electrode was produced by oxidation of a standard automotive positive paste on a lead/ lead alloy base). The electrochemistry of the pure lead and lead alloy electrodes (flat and porous) were studied. The alloys used were lead-antimony, lead-bismuth, lead-tin-calcium and, lead-tin-bismuth-calcium at various levels of bismuth addition. The impedance studies have shown the appearance of an inductive loop in the impedance loci of PbO_2 layers on Pb-Sb alloy, which was absent in the same experimental range with other alloys. An analogue was produced which describes the discharge process of the PbO_2 electrode. The reaction is controlled by charge transfer and diffusion in solution in series with a leaky capacitance representing the sulphate layer.

It was again found that addition of antimony to lead in the positive grids resulted in them having a greater retention of active material. Also a certain concentration range of bismuth displayed some useful significant effect on both lead and lead-tin-calcium alloys.

As yet the importance of antimony is not fully understood, especially the mechanism by which the metal in the grid alloy delays the onset of positive plate failure is unknown. However, cells containing antimonial lead grids have a larger cycle life than similar cells with pure lead and lead-tin-calcium grids. The Pb-Ca alloy is used extensively in the maintenance-free battery because it reduces the float current, hydrogen evolution and water consumption quite considerably when compared with the lead-antimony alloy. If the Pb-Ca cell discharges too deeply, however, recharging is very difficult.

Adding bismuth, in the range 0.1-0.4% [12], does not seem to harm the maintenance-free characteristics of lead-tin-calcium alloys. However, a detailed study of introducing bismuth in batteries showed that it caused an increase in the amount of positive shedding and gave rise to grid growth.

CHAPTER 5

EXPERIMENTAL TECHNIQUES

5.1 Electrolytic Systems

5.1.1 Electrolyte Solutions

The electrolyte solutions were prepared from Analar grade chemicals and water tri-distilled from dionised stock. Any dissolved oxygen was removed from solutions by the passage of white spot nitrogen, which was deoxygenated by passing over copper at 400°C and prehumidified for at least three days prior to measurement.

5.1.2 Electrolytic cells

All the cells were made from borosilicate glass and cell fittings were attached via lubrication-free ground glass joints. The cells together with all glassware were cleaned by total immersion in a 50 : 50 mixture of nitric and sulphuric acids for a minimum period of three days. The acid mixture was removed by thoroughly washing with tri-distilled water.

A conventional three-limb cell, shown in Fig. 5.1, was used for both cyclic voltammetry and potentiostatic pulse experiments. For the a.c. impedance measurements, both the working and counter electrodes were in the same compartment with the large surface area counter electrode surrounding the working electrode.

Using the cell depicted in Fig. 5.2 galvanostatic charging was carried out in an upward-facing position to prevent oxygen remaining in the porous matrix.

Fig. 5.1

Three compartment cell

A - Counter

B - Working

C - Reference

D - Luggin Capillary

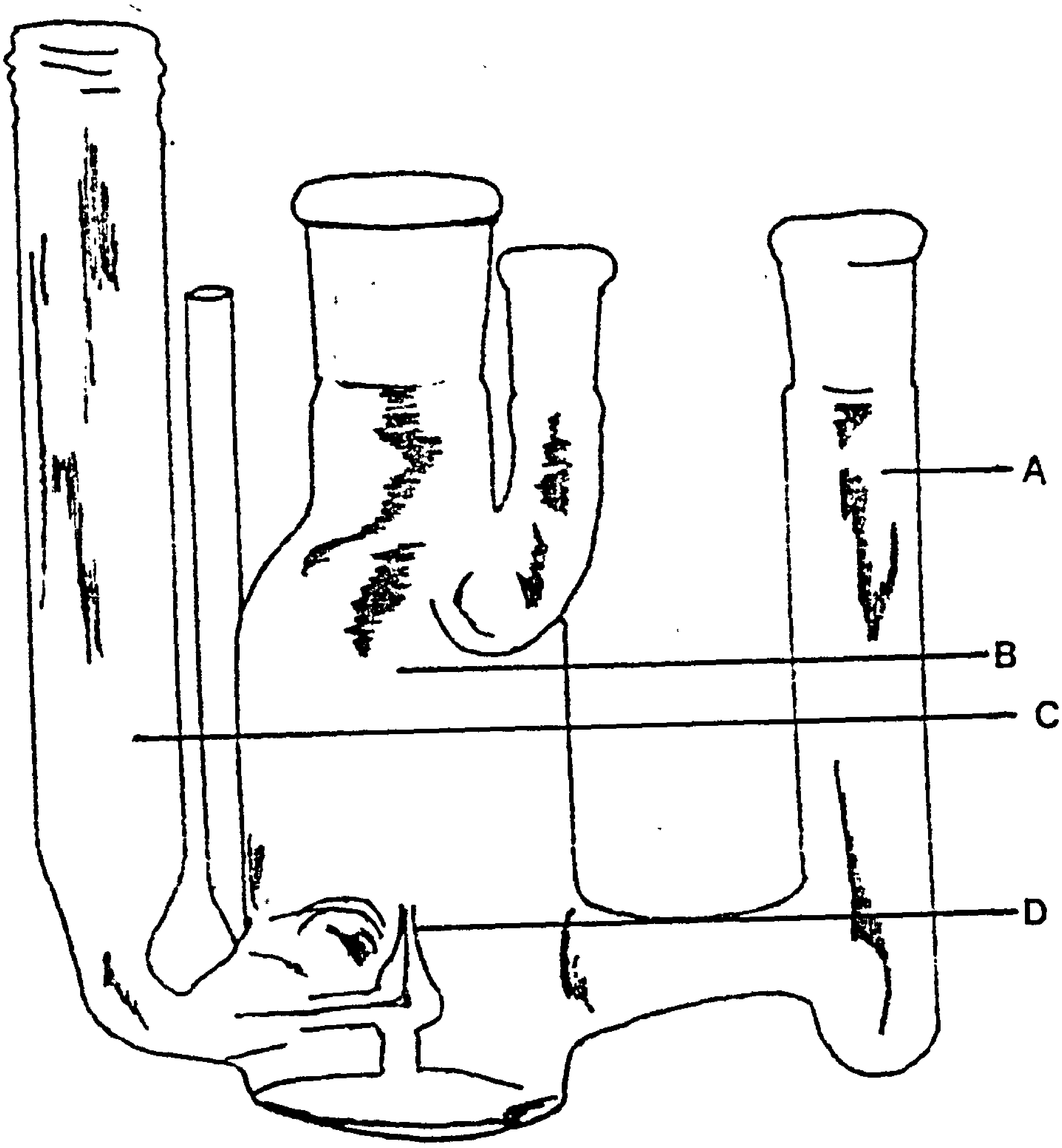

Fig. 5.2

Formation Cell

A - Provision for the reference electrode

B - Counter electrode

C - Working electrode

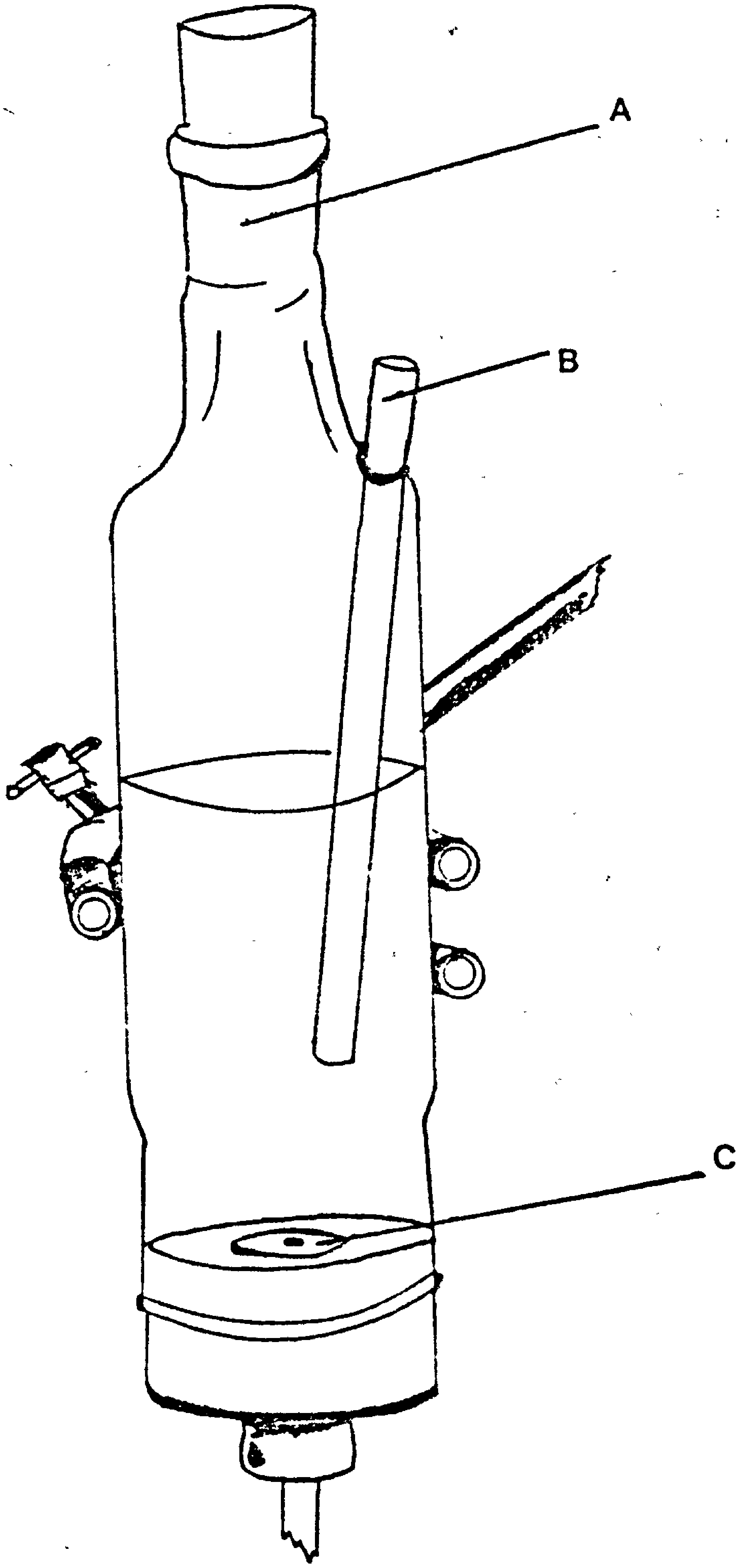

5.1.3 Planar electrodes

These electrodes were made as rotating disc electrodes (RDE) as shown in Fig. 5.3. The lead and lead-alloys were machined to produce electrodes of cross-sectional area 0.071 cm^2 which were set in Teflon receptors. A stout steel spring was then soldered onto the back of the electrode, ensuring good electrical contact with the shaft of the RDE assembly, and the receptor was screwed into a hollow Teflon holder. This arrangement allowed the simple removal of the working electrode for scanning electron microscopy (SEM) examination. A mercury pool provided the contact between the rotating electrode and the external circuit.

The preparation of the electrode surface consisted of a polish on roughened glass followed by a chemical etch (10% nitric acid solution for 10 sec) and a thorough rinse with tri-distilled water.

5.1.4 Porous electrodes

The porous electrodes were constructed by arranging the solid support (lead or various lead alloys) to lie beneath the level of the Teflon shrouding. By forcing the positive paste into the cavity, a porous layer was produced (3 mm diameter, 0.76 mm deep) which terminated the lead electrode. Following the pasting of the recess, the electrode was allowed to stand in a humid atmosphere for three days and then dried at room temperature (23 ± 1°C) for one day.

The porous matrix was converted to lead dioxide by galvanostatic oxidation (0.3 M H_2SO_4; ~ 25 mA cm^{-2}) which was continued until the potential was steady (1250 mV vs. Hg/Hg_2SO_4 in 0.3 M H_2SO_4), and oxygen was freely evolved from the porous matrix. The electrode was converted to lead dioxide in the upward-facing position to effectively release

Fig. 5.3 Working electrode

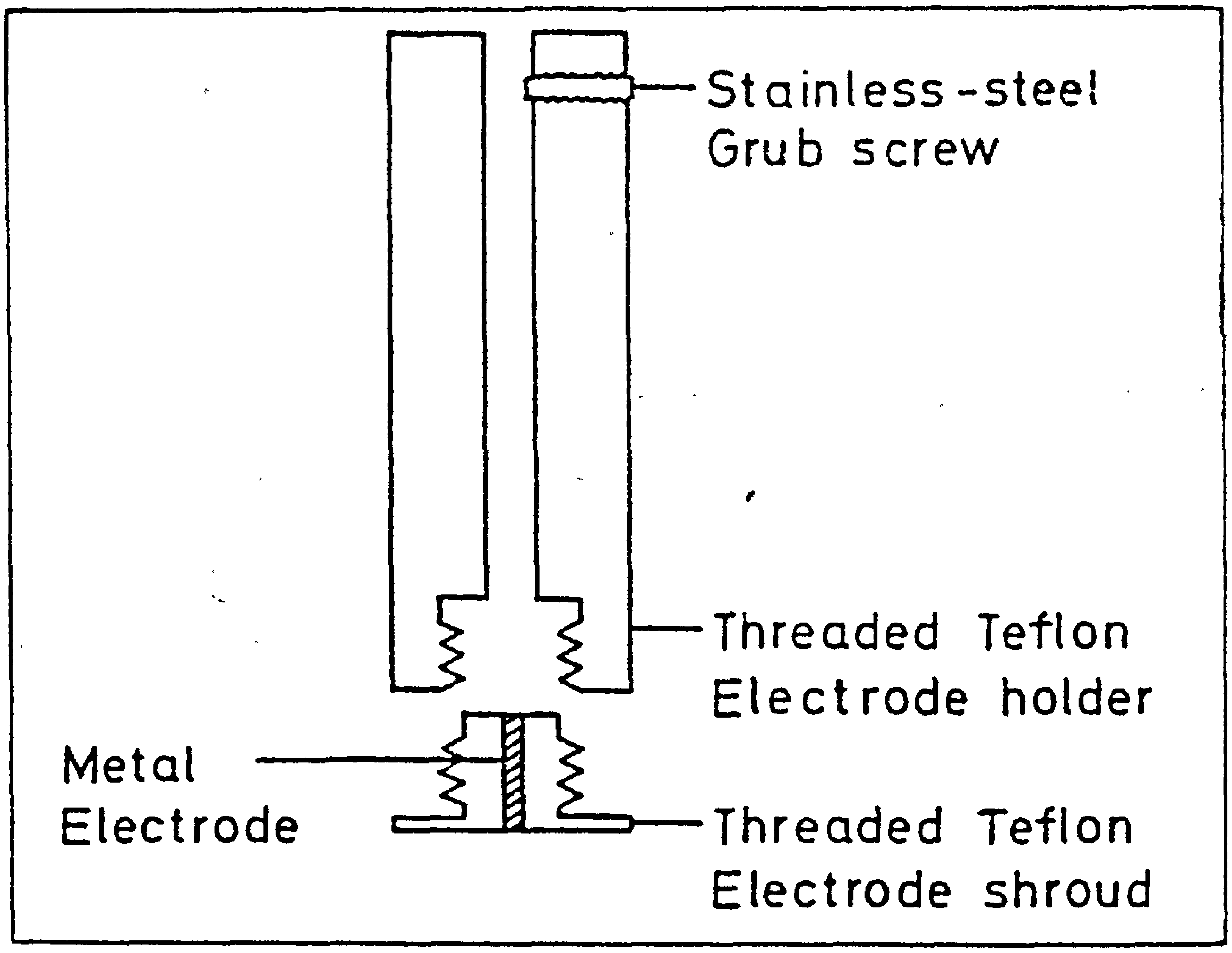

Fig. 5.4 Reference Electrode

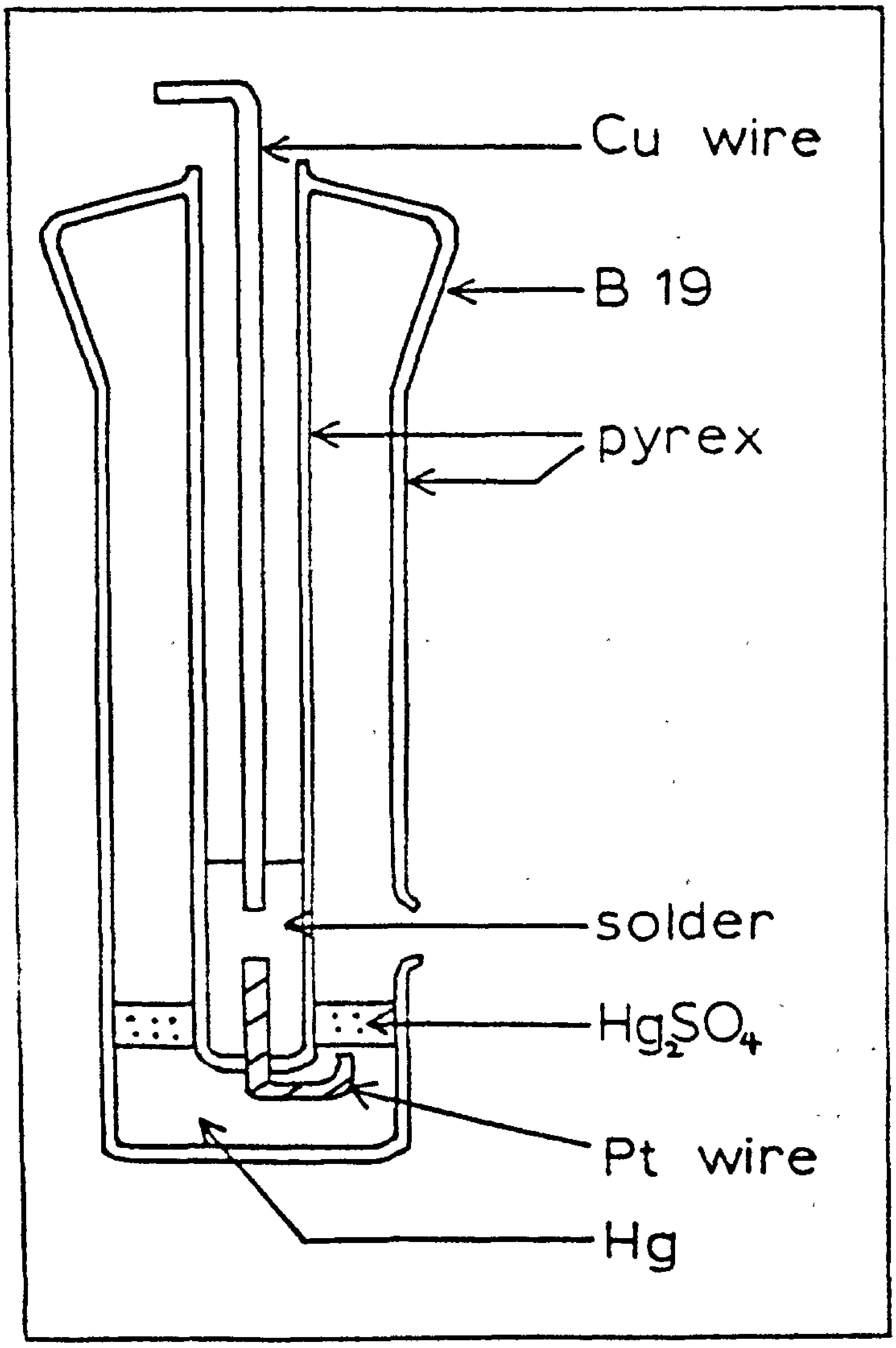

oxygen because otherwise it would saturate the matrix and interfere with the oxidation.

5.1.5 Counter and Reference electrodes

For the cyclic voltammetry and potentiostatic pulse experiments the counter electrode was a pure lead rod (99.99%).

In the a.c. impedance experiments a large surface area pure lead-sheet, which surrounded the working electrode, was employed.

The potentials were always measured with reference to a Hg/Hg_2SO_4 electrode in H_2SO_4 of the same concentration as the working solution. Fig. 5.4 shows the construction of the wick-type reference electrode.

5.2 Electrical Circuits

5.2.1 Linear sweep/cyclic voltammetry

Fig. 5.5 shows a schematic diagram of the experimental arrangement. A Z-80 microprocessor-based 64 K system (Kemitron 3000) with a twin-floppy disc access facility equiped with D/A (digital to analogue) and A/D (analogue to digital) interfaces was used [93]. The voltage ramp needed to perturb the electrochemical system was obtained by generating a set of the corresponding digital potentials and transmitting them via the D/A converter. Following the potential sweep the current response of the system was immediately transmitted to the computer memory via the A/D converter. The numbers representing the outgoing voltage ramp and the resulting current response were filed on discs and were either printed out or shown graphically using a digital plotter (Watanabe WX4671). The output part of the computer was connected to the external input of a potential (Hi-Tek, Type DT 2101 or Kemitron POT.03) and the potential of the working electrode was varied potentiostatically from any desired

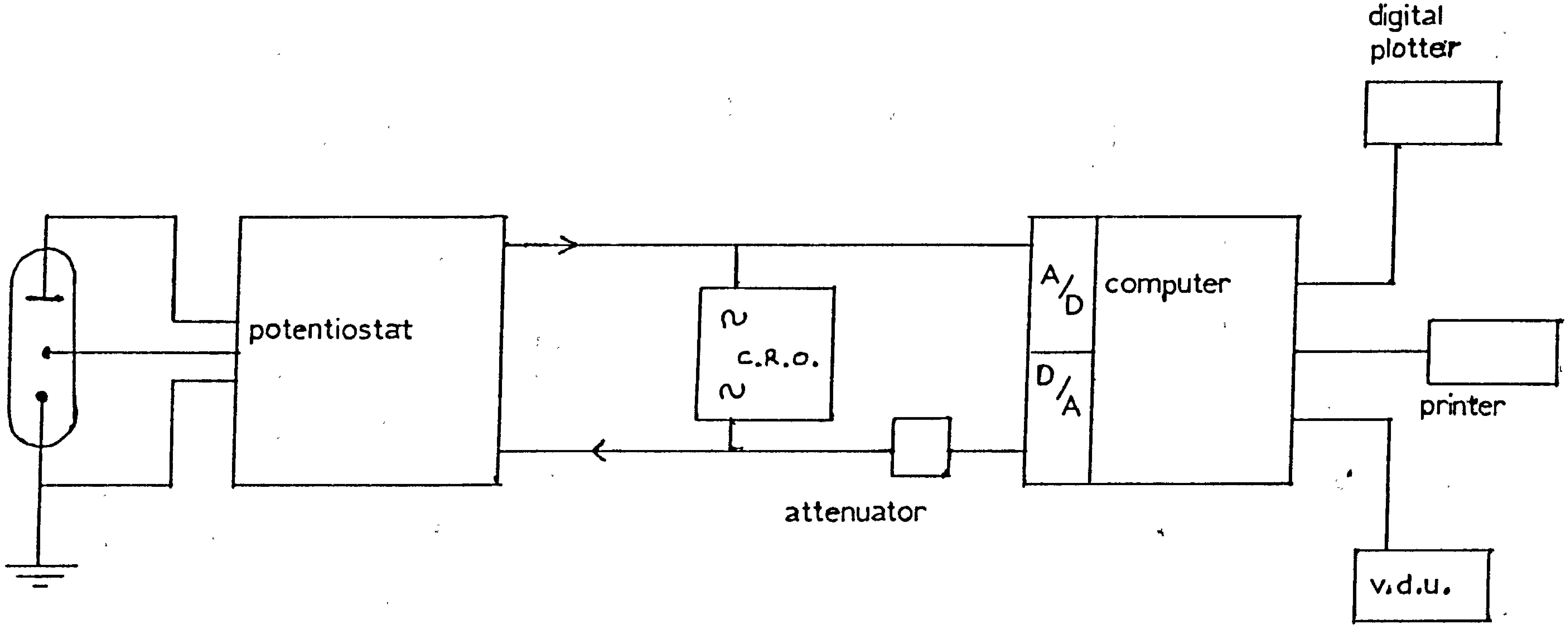

L.S.V. CIRCUIT.

FIG.5.5

value. The voltage output from the potentiostat corresponded to the current flowing through the cell and was transmitted to the input part of the computer. The programs needed to drive the experiments, to plot and process data were written in Microsoft BASIC language operating in a Digital Research CP/M 2.2 environment. The output and input signals of the computer were monitored on a dual channel oscilloscope (Hameg HM 512).

5.2.2 Potentiostatic pulse experiments

The arrangement used is very similar to the one in Fig. 5.5. However, as Fig. 5.6 shows, the computer (via the D/A converter) can instantaneously impose a potential on the working electrode via the potentiostat. The data from the potentiostat were captured by a transient recorder (Datalab, DL 905) which in turn was transferred to the computer via a 8255 P.P.I. (programmable peripheral interface) chip. An oscilloscope was used to display the data recorded by the transient recorder.

5.2.3 Faradaic Impedance Measurements

Fig. 5.7 shows the experimental set-up used for a.c. impedance measurements. It is based on the Solartron 1170 Frequency Response Analyser (F.R.A.) with an 1186 Solartron Electrochemical Interphase to control the potential. The F.R.A. consists of a programmable generator which delivers the perturbing signal, measures the system response, analyses the result with the aid of a correlator, and displays it.

The F.R.A. can reject all harmonics present in the output of the system and minimises the effect of random noise. The generator can be programmed to choose a frequency and measure the response at that frequency, or more often to scan through a range of frequencies from the highest

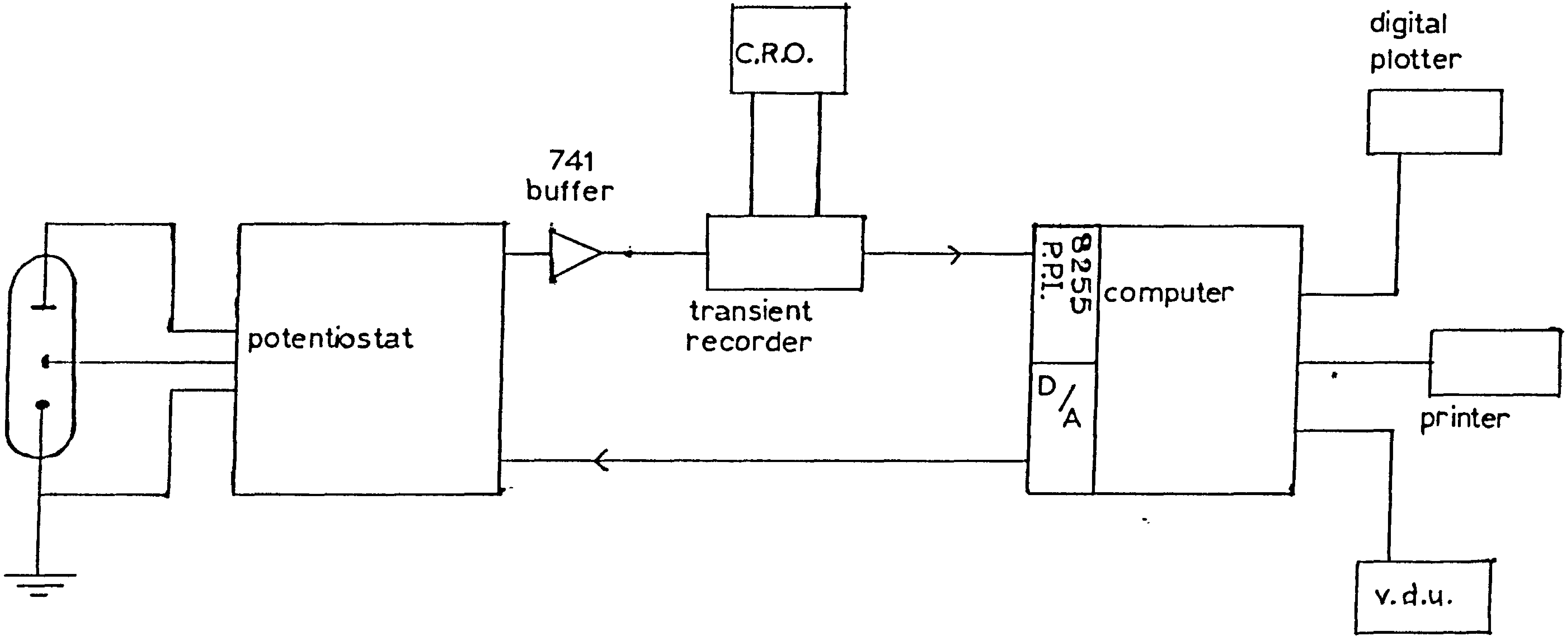

FIG.5.6

POTENTIOSTATIC PULSE CIRCUIT.

FIG. 5.7

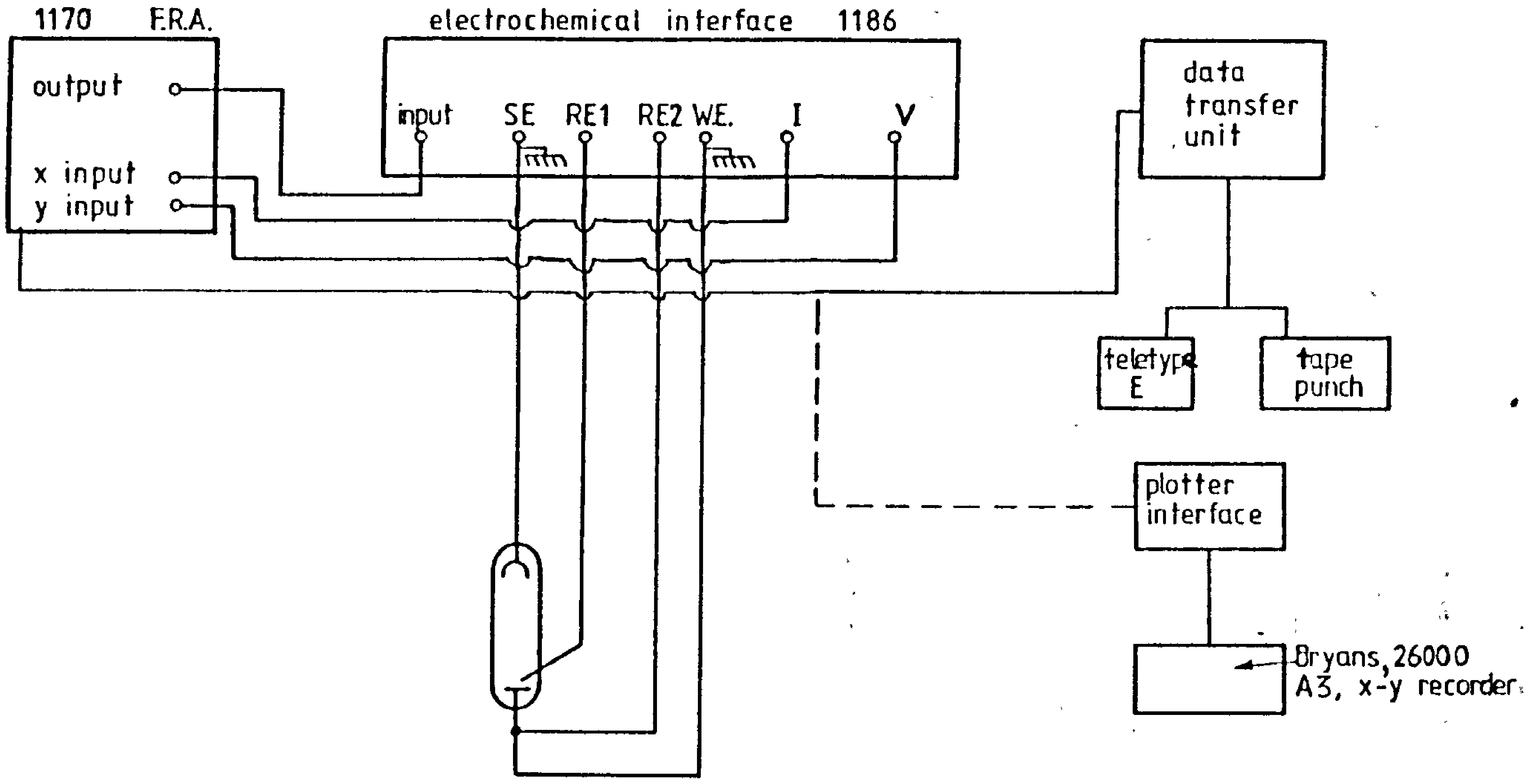

CELL IMPEDANCE MEASUREMENT SYSTEM.

10 kHz to 1 mHz. The equipment can scan sequentially in either direction. At each frequency the response is averaged over a number of cycles and then displayed in one of three possible ways: resultant impedance (R) and phase angle (ϕ), log (R) and ϕ, or the real and imaginary parts of the impedance. The Solartron Data Transfer Unit is used to store the results and can be printed out on a teletype printer or paper punch tape, and simultaneously plotted using a Solartron 1180 Plotter Interface and X-Y recorder (Bryans 26000, A3).

The paper punch tape facility allows the data to be fed into the Honeywell Multics DPS8/M University computer. A graphics terminal (TEKTRONIX) was then employed to obtain the complex plane (Sluyters) plots and Randles plots.

This facility enabled the use of a computer program to obtain theoretical model fits to the experimental data as will be seen in later chapters.

CHAPTER 6

THE BEHAVIOUR OF PbO_2 IN CONCENTRATED SULPHURIC ACID

6.1 Introduction

Traditionally the concentration of sulphuric acid in lead acid cells is about 5 mol dm^{-3} in the fully-charged condition. Automotive batteries with the requirement of generating high engine cranking capability are furnished with electrolyte solution at a somewhat higher final concentration (sg. = 1.280) and standby batteries with the requirement of low loss due to local action at the negative plate contain a rather lower concentration (maybe as low as sg. = 1.210). With the introduction of fully-sealed lead cells containing a static phase on which the electrolyte is absorbed the concentrations within the cell may exceed 5 mol dm^{-3}. There is surprisingly little in the literature regarding the behaviour of the two lead cell electrodes in sulphuric acid concentrations greater than 5 mol dm^{-3}. Consequently it was considered timely to examine the behaviour of PbO_2 at these higher concentrations.

6.2 Experimental procedure

The electrometric experiments were made using the micro-computer described in Chapter 5. In the present case, the computer commanded the potentiostat (Hi-tek, Type DT 2101) and the output was monitored on the dual channel oscilloscope (Hameg HM 512).

Electrodes were prepared with lead (99.999%, Koch-Light) as the control working surface (0.071 cm^2) of a rotating disc electrode. The reference electrode was Hg/Hg_2SO_4 in the same H_2SO_4 electrolyte solution as the working electrode. All measurements were made at a room temperature of 22 ± 1°C.

6.3 Results and Discussion

At each sulphuric acid concentration the lead electrode was cycled between the limits 550 and 1550 mV at the appropriate rate of potential sweep to a constant response. This was found to require about 1.5h potential cycling.

Fig. 6.1 shows a typical current response corresponding to a cyclic linear sweep between the limits 600 - 1450 mV. For the cases with no interference from gaseous evolution, e.g. as in Fig. 6.3, the anodic and cathodic charges balanced to within experimental limits. Well-defined oxidation and, a rather shallow, reduction peaks are obvious. These are similar to previously reported data [94] and the effects of potential sweep rate on the peak oxidation currents (i_p) are shown in Fig. 6.2 for the various acid concentrations investigated. It is clear that the expected $i_p - \nu^{\frac{1}{2}}$ (ν = potential scan rate) relationship is observed, although at the low concentrations the lines do not extrapolate back through the origin in agreement with the work of Hampson <u>et al</u> [94]. The peak currents found for the oxidation of the lead used in that work [94] were significantly smaller than those observed in the present study. This is apparently the influence of the low level impurities in the lead on the earlier work. This is confirmed by work reported in Chapter 8 with similar antimony/lead binary alloys when results agreed to within 5%. The lead in the earlier work [94] contained Ag (0.0025 wt%), Cu (0.0026 wt%), Ti (0.0025 wt%) and Bi (0.010 wt%) and further work will clearly be needed in order to decide which of these materials is exerting the protective effect or whether there is any synergism.

It is clear from Fig. 6.2 that there is a large decrease in the peak currents in passing from 5 mol dm^{-3} to 10 mol dm^{-3} H_2SO_4 the greatest relative change occurring in the region around 5 mol dm^{-3}. At concentrations around 7 mol dm^{-3} the recoverable charge was ~ 25% of

Fig. 6.1 : Constant response curve for pure Pb for the range 600 → 1450 mV after cycling for 1.5 hours. Sweep rate, 100 mV s^{-1}.

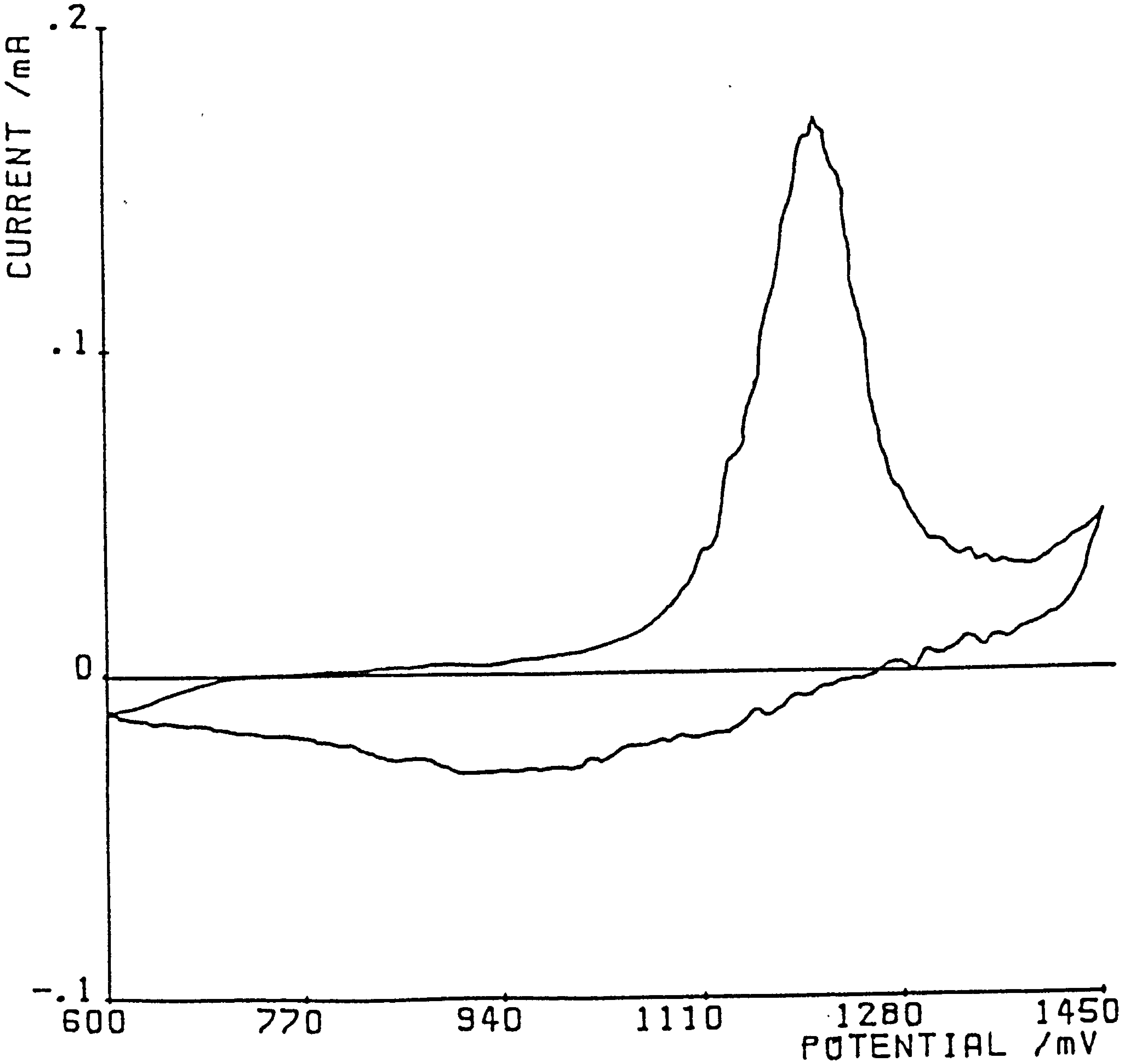

Fig. 6.2 : Plot of i_p versus $\sqrt{\nu}$ in the range 10 - 100 mVs^{-1} for various concentrations of H_2SO_4:

● ; 5.0M H_2SO_4
◇ ; 5.5M H_2SO_4
⊡ ; 6.0M H_2SO_4
△ ; 6.5M H_2SO_4
X ; 7.0M H_2SO_4
◆ ; 10.0M H_2SO_4

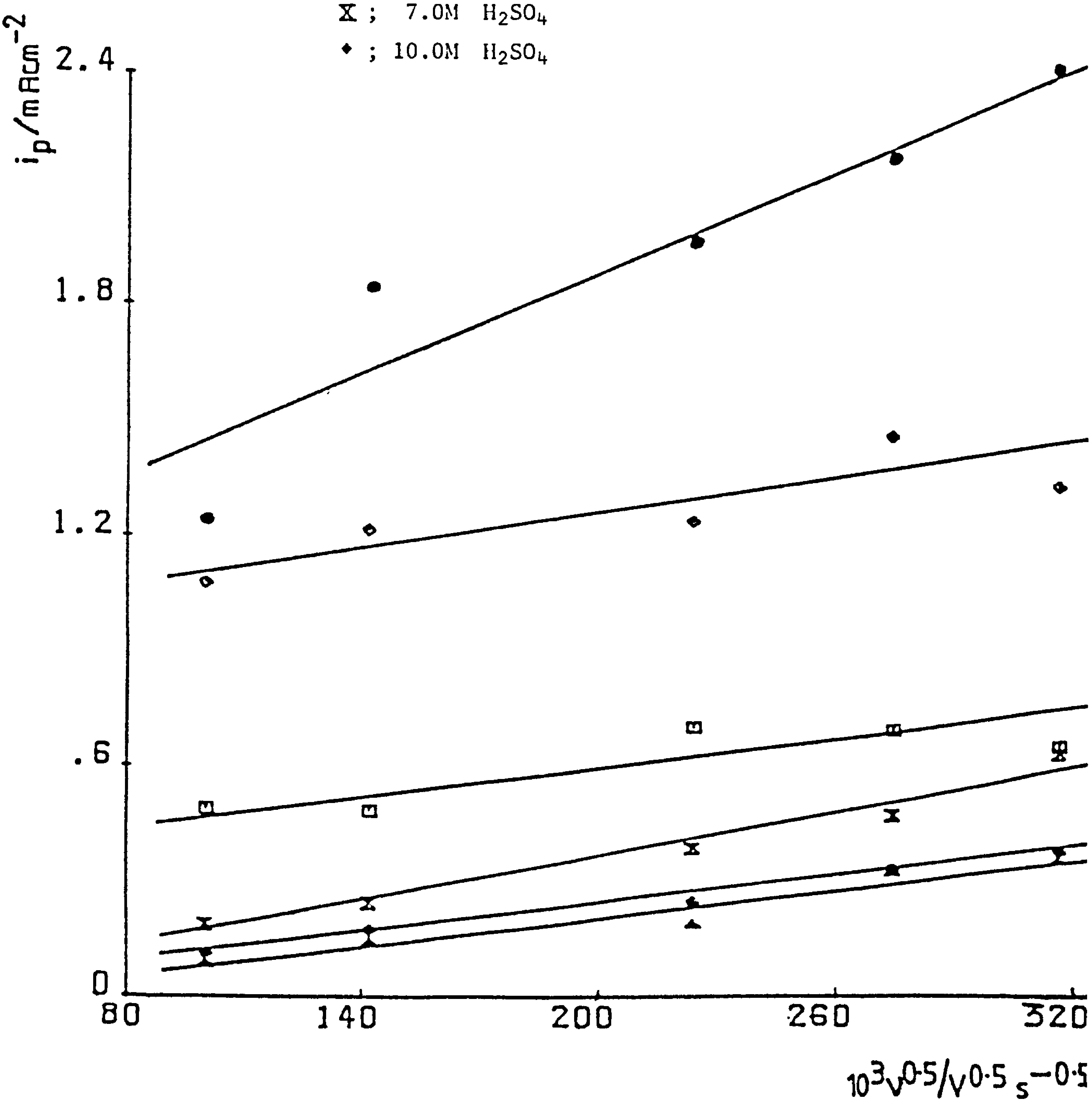

that obtainable at 5 mol dm^{-3} as shown by Table 6.1 which contains data obtained by direct integration of the anodic current in the stabilized voltammogram. This was done by utilising the on-line computer using the 'extended Simpson's rule technique' [95]. Table 6.1 shows a maximum at 7.0 mol dm^{-3}. This local maximum is maintained at all rates of potential sweeping in replicate experiments. It can be concluded that as the concentration of sulphuric acid is increased, the form of the lead sulphate film becomes passivating at a smaller deposit thickness. If the reaction is controlled by a film as is clear from earlier work that if the film is more mechanically sound at high concentrations the i_p-$\nu^{\frac{1}{2}}$ relationship will clearly be justified. Hence it seems that a mechanically sounder film is being produced at the higher concentrations. An alternative explanation is possible in terms of the change in peak potentials producing a $PbSO_4$ film which is tighter on the electrode. However, at the formation potentials corresponding to the higher concentrations, this explanation does not seem to be tenable in view of the local charge maximum at ~ 7 mol dm^{-3}.

6.3.1 Note on the stability of PbO_2 in H_2SO_4

In the course of this investigation an attempt was made to use PbO_2 as a reference electrode. This was done by forming a thick deposit of PbO_2 on a lead rod (99.999%, Koch-Light) by employing the Planté formation process [96] using perchlorate ion as the aggressive ion. The conventional thickness of PbO_2 was generated on the lead base according to practice established over many years in the lead-acid industry.

It was found that the electrode could be used satisfactorily up to a concentration of 6 mol dm^{-3} with the well-defined peaks occurring at the expected overpotentials. A typical voltammogram is shown in Fig. 6.3 for 5 mol dm^{-3} H_2SO_4 solution.

TABLE 6.1

Charge ($mCcm^{-2}$) contained in the positive-going sweep in various concentrations of H_2SO_4.

Concentration of H_2SO_4 (mol dm^{-3})	Sweep rate ν (mVs^{-1})		
	100	75	50
5.0	3.333	4.532	8.490
5.5	2.238	2.965	5.010
6.0	1.355	1.942	2.546
6.5	0.976	0.191	1.226
7.0	1.402	1.543	1.926
10.0	0.950	0.970	1.137

Fig. 6.3 : Constant response curve for pure Pb for the range −300 → 200 mV after cycling for 1.5 hours. Sweep rate, 100 mVs^{-1}.

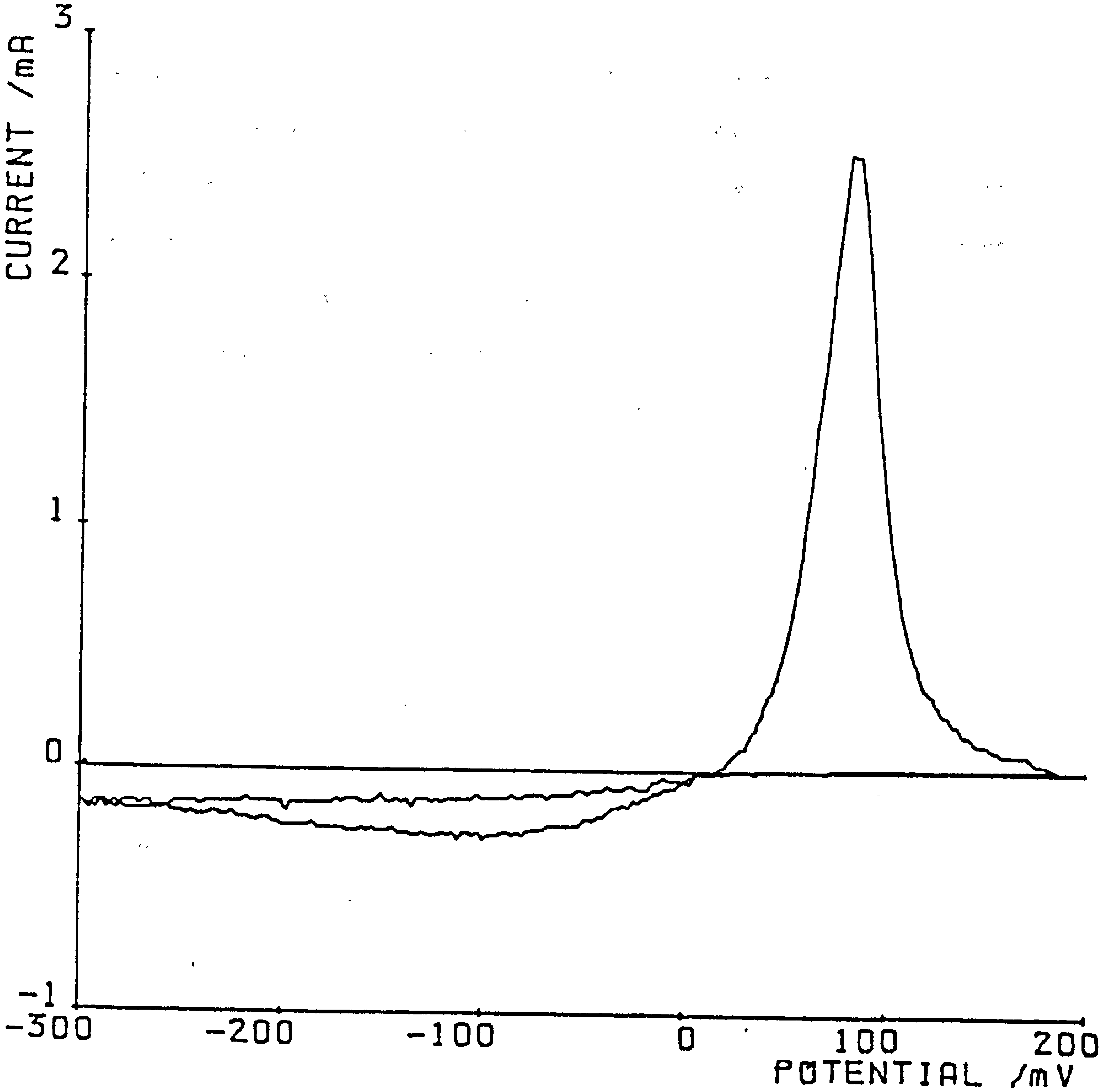

For concentrations in excess of 6 mol dm^{-3} the form of the voltammogram was a gradually rising line in the anodic direction. The only feature occurred at - 1000 mV (working electrode vs. 'PbO_2 reference') where on the cathodic sweep the current rose abruptly and fell progressively to - 1400 mV. An examination of the reference electrode indicated that it had been transformed to $PbSO_4$ presumably by the reaction between the PbO_2 on the surface and the underlying Pb

$$Pb + PbO_2 + 2H_2SO_4 \longrightarrow 2PbSO_4 + 2H_2O$$

The implication is that the strong H_2SO_4 solution is able to penetrate the barrier between the PbO_2 and the Pb whereas the more dilute (5 mol dm^{-3}) solution could not. It would appear that the PbO_2 produced on Pb in concentrated (7 mol dm^{-3}) H_2SO_4 forms a barrier layer sufficiently passivating for penetration by the electrolyte solution. The barrier layer between Pb and PbO_2 for the case of PbO_2 produced on Pb in dilute electrolyte is not so effective in excluding the molecules of H_2SO_4 from concentrated electrolyte solution and the self-discharge reaction occurs. No chemical evidence was found for the development of peroxodisulphuric acid via a reaction of the type:

$$3H_2SO_4 + PbO_2 \longrightarrow H_2S_2O_8 + PbSO_4 + 2H_2O$$

This is an important technological point for it implies that in certain cell situations recharging in dilute electrolyte which ultimately increased in concentration considerably above 5 mol dm^{-3} (possibly in the contemporary static electrolyte phase battery) could give rise to undue positive cell self-discharge and enhanced positive plate corrosion.

6.4 Conclusions

1. Increases in H_2SO_4 concentration above 5M results in decreased charge output of the PbO_2 electrode.
2. The self-discharge of positives is increased in H_2SO_4 at concentrations greater than 6M.

CHAPTER 7

MORPHOLOGY OF $PbSO_4$ FORMED ON SOLID Pb IN CONCENTRATED SULPHURIC ACID

7.1 Introduction

In Chapter 6 the behaviour of PbO_2, in concentrations of H_2SO_4 in excess of 5M was investigated. This was approached by carrying out linear sweep voltammetry (LSV) on pure solid lead in different high concentrations of sulphuric acid at a series of sweep rates (10-100 mVs^{-1}). It was found that the maximum peak current values (i_p), and hence the charge values, decreased dramatically in passing from 5 mol dm^{-3} to 10 mol dm^{-3} H_2SO_4. This indicated that as the concentration of sulphuric acid was increased the form of the lead sulphate film became passivated at a smaller deposit thickness.

In this chapter photographic evidence in support of the electrochemical data is shown.

7.2 Experimental procedure

The computer-controlled experimental set-up and electrode preparation have been described in Chapter 6. The linear sweep experiments were carried out at 23 ± 1°C with a Hg/Hg_2SO_4 reference electrode which was in the same H_2SO_4 electrolyte solution as the working electrode. The pure lead electrodes were cycled to a constant response between the limits 550 mV and 1550 mV, finally being held in the $PbSO_4$ region (550 mV). Again, the time needed for constancy was approximately 1.5h. The sweep-speed, ν was kept constant, that is $\nu = 100$ mVs^{-1}.

The experiments were performed in 5.0, 7.0 and 10.0 mol dm^{-3} sulphuric acid on pure lead rods (diameter = 0.3 cm) shrouded in Teflon in the form of stubs which screwed into the end of the rotating disc electrode [97]. After the electrochemistry had been carried out at the solid electrode, the electrodes were washed with tri-distilled water, rinsed with acetone and stored in a vacuum desiccator. For SEM observations the stubs were coated with a thin layer of gold by diode sputtering and examination was performed using a Jeol JSM 35 scanning electron microscope.

7.3 Results and Discussion

Fig. 7.1 shows the surface morphology of a pure lead electrode after redox cycling for 1.5h in 5.0 mol dm^{-3} H_2SO_4. The final potential was 550 mV ($PbSO_4$ region). The prismatic $PbSO_4$ crystals are clearly visible and are dispersed on the surface of the electrode in an irregular fashion. Fig. 7.2 displays the effect of increasing the concentration of the sulphuric acid electrolyte on the $PbSO_4$ crystals formed on the Pb electrode. Hence at 7 mol dm^{-3} H_2SO_4 the crystals become smaller, deformed and more compact, producing a tighter layer on the surface of the electrode. This is in accordance with what was reported in the previous chapter suggesting that the $PbSO_4$ film becomes mechanically sound and tighter on the electrode.

At 10 mol dm^{-3} H_2SO_4 Fig. 7.3 shows that the $PbSO_4$ crystals become even smaller and are packed much closer together to give a very densely packed film of lead sulphate. Hence the charge output of the PbO_2 electrode is drastically reduced in concentrated sulphuric acid because the mechanically sound film of $PbSO_4$ becomes very passivating and effectively resists oxidation to PbO_2 on cycling potentiodynamically between the PbO_2 and $PbSO_4$ regions.

The important conclusion of this chapter is that in H_2SO_4 concentrations > 5 mol dm^{-3} the $PbSO_4$ crystals become much smaller forming a tighter and passivating film.

Fig. 7.1

Pure Pb 5M H_2SO_4.
LSV (550-1550 mV for 1.5h, ending at 550 mV) ν = 100 mVs^{-1}.

a) Magnification x 10000

b) Magnification x 20000

Fig. 7.2

As Fig. 7.1, but in 7M H_2SO_4 electrolyte.

a) Magnification x 10000

b) Magnification x 20000

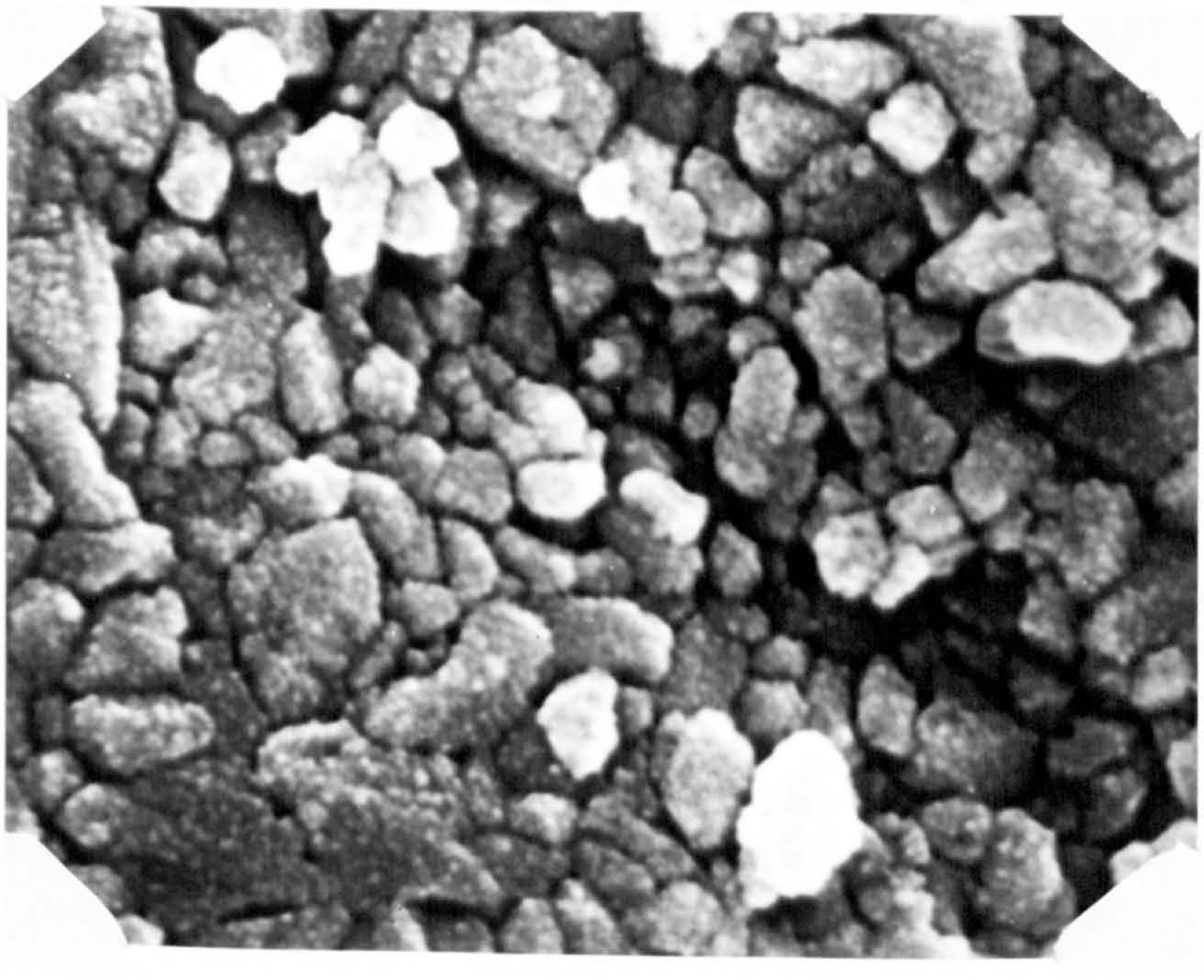

Fig. 7.3

As Fig. 7.1, but in 10M H_2SO_4 electrolyte.

a) Magnification x 10000

b) Magnification x 20000

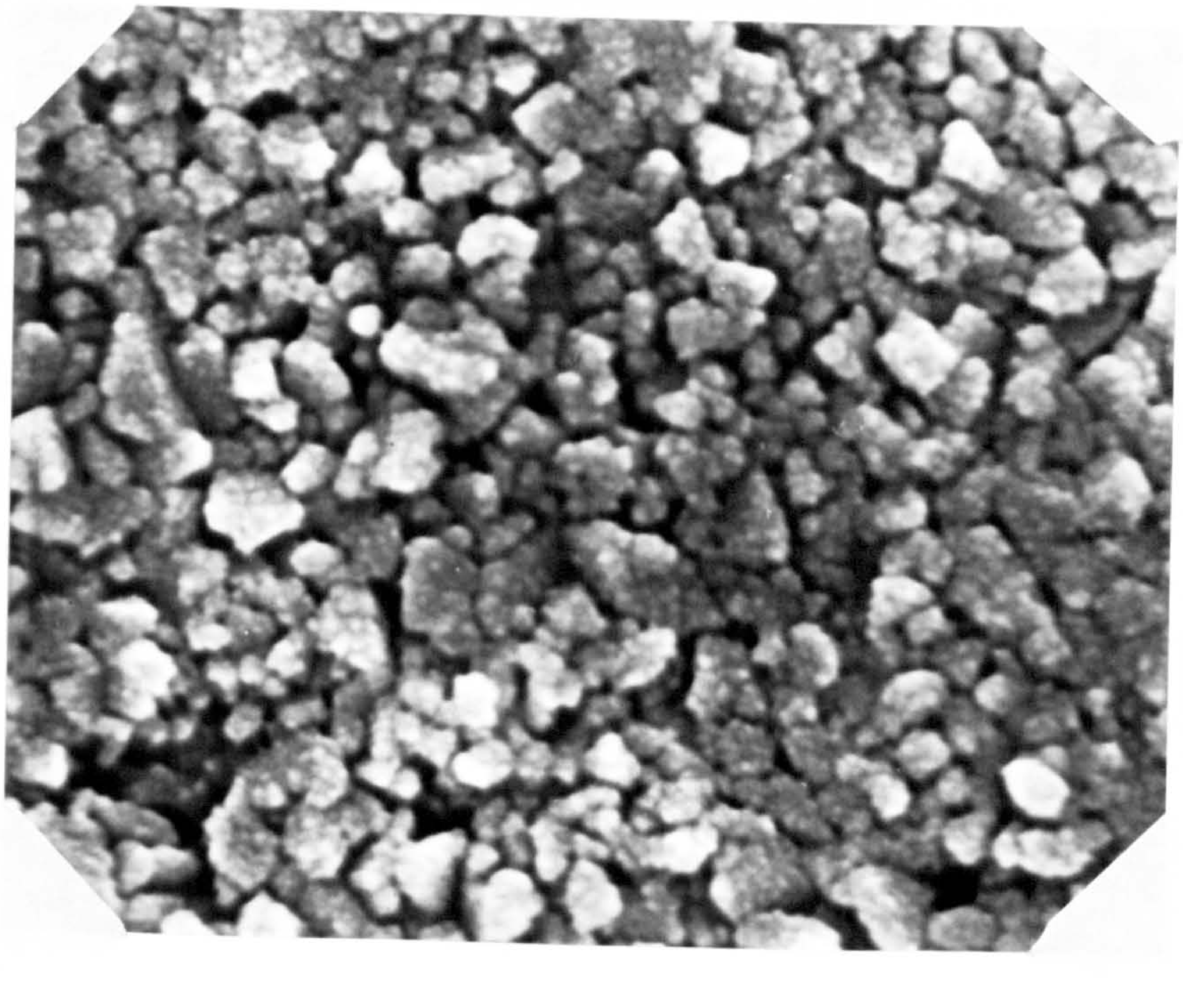

CHAPTER 8

THE EFFECT OF ALLOYING WITH Sb and Sn/Ca ON THE ELECTROCHEMICAL PROPERTIES OF SOLID LEAD

8.1 Introduction

As explained in Chapter 1 different metals are added to the lead grids in lead-acid batteries in order to impart many useful properties, such as, longer service life, improved castability, etc. This chapter records the LSV measurements carried out, and compares the data obtained on pure lead and various lead alloys in two different H_2SO_4 concentrations, that is, 5.0 and 5.5M (the range of maximum operative concentration). However, it should be noted that in industry, battery discharge techniques are carried out at rates equivalent to extremely slow sweeps whereas here a faster cycle range is employed.

8.2 Experimental procedure

The working electrodes were prepared from pure and alloy lead rods (CTL-metals, diameter = 0.3 cm) shrouded in Teflon which could be rotated at a known constant speed. The linear sweep experiments were performed using the computer controlled potentiostat referred to in Chapter 6.

All potential measurements were made at 23°C with a Hg/Hg_2SO_4 reference electrode which was in the same H_2SO_4 electrolyte solution as the working electrode.

The alloys used contained:

	Analysis, weight per cent			
Code	Sb	Sn	Ca	Pb
A	-	-	-	99.999
B	0.58	-	-	Remainder
C	1.88	-	-	Remainder
D	4.18	-	-	Remainder
E	-	0.34	0.086	Remainder
F	-	0.75	0.076	Remainder

The experiments consisted of cycling to a constant response between 500-1500 mV at a series of sweep rates (10-100 mVs^{-1}) in both H_2SO_4 concentrations. The time needed for constancy was approximately 1.5h.

8.3 Results and Discussion

Fig. 8.1 shows stabilised current response curves for pure lead and varying degrees of antimonial lead in 5.0M H_2SO_4. As can be seen, pure lead undergoes greater anodic attack than the other antimonial alloys showing that the presence of antimony or other impurities exert a protective effect. Alloy D is corroded the least, and the PbO_2 peak corresponding to it occurs at a lower potential. Alloys B and C have very similar maximum peak current values (i_p) which are highlighted in Table 8.1, although in the case of the former, the peak potential (E_p) appears at a higher value than for pure lead. The peaks appear broad, comparable to those obtained by Kelly <u>et al</u> [94], indicating that the PbO_2 formed on the electrodes is quite porous and thus the reaction can be driven deeper into the porous layer as the potential is increased.

Fig. 8.2 displays the potential curves for the same alloys used for Fig. 8.1 but in 5.5M H_2SO_4. This reveals that although pure lead undergoes more anodic attack than the other alloys, the effect is not so prominent

Fig. 8.1 : 5.0M H_2SO_4 electrolyte. Digitally drawn voltammograms of A, pure Pb; B, Pb-Sb (0.58%); C, Pb-Sb (1.88%); D, Pb-Sb (4.18%). (500-1500 mV, ν = 100 mVs^{-1}) after cycling for 1.5 h.

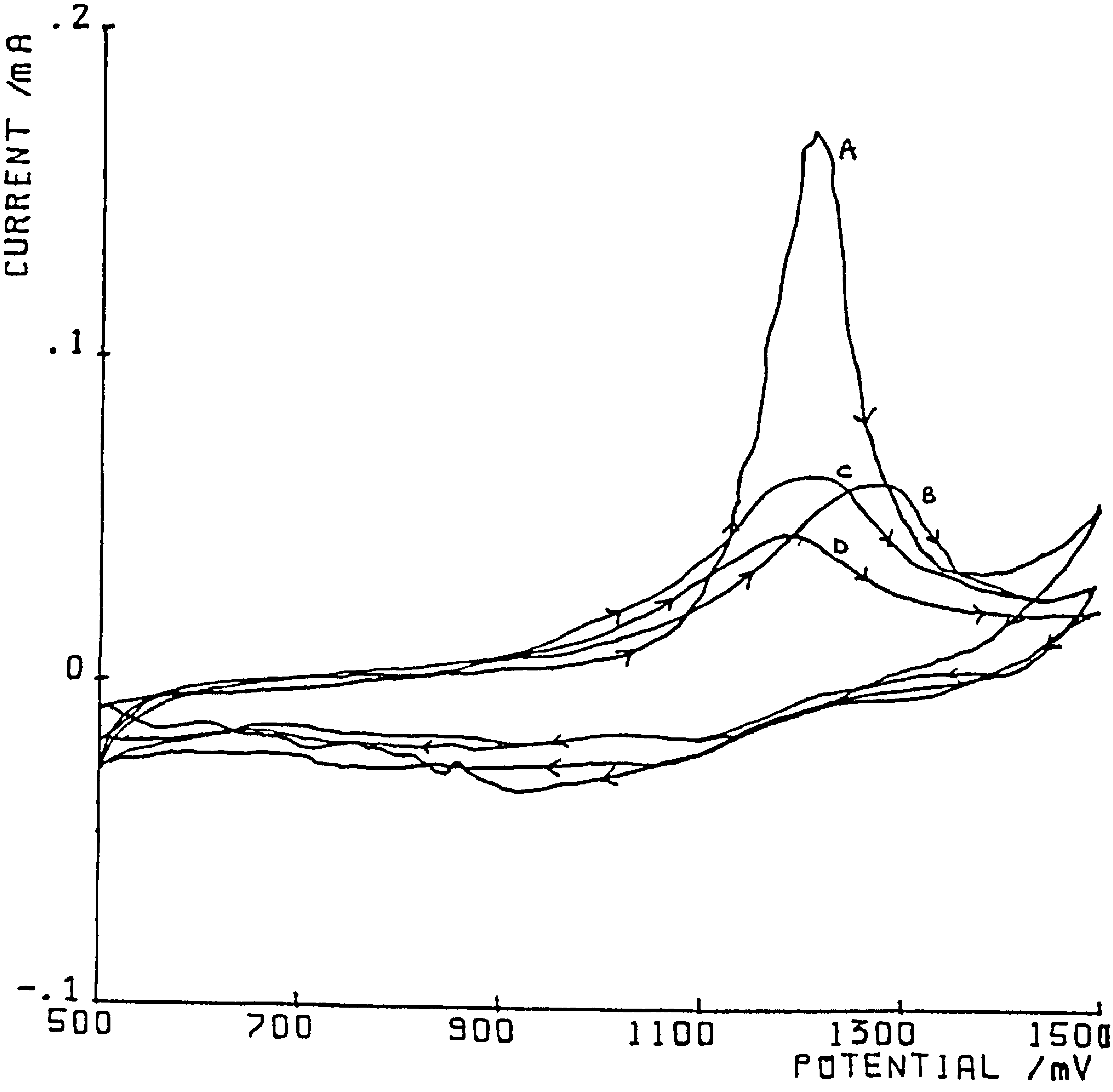

Fig. 8.2 : The same conditions as in Fig. 8.1, but LSV's carried out in 5.5M H_2SO_4.

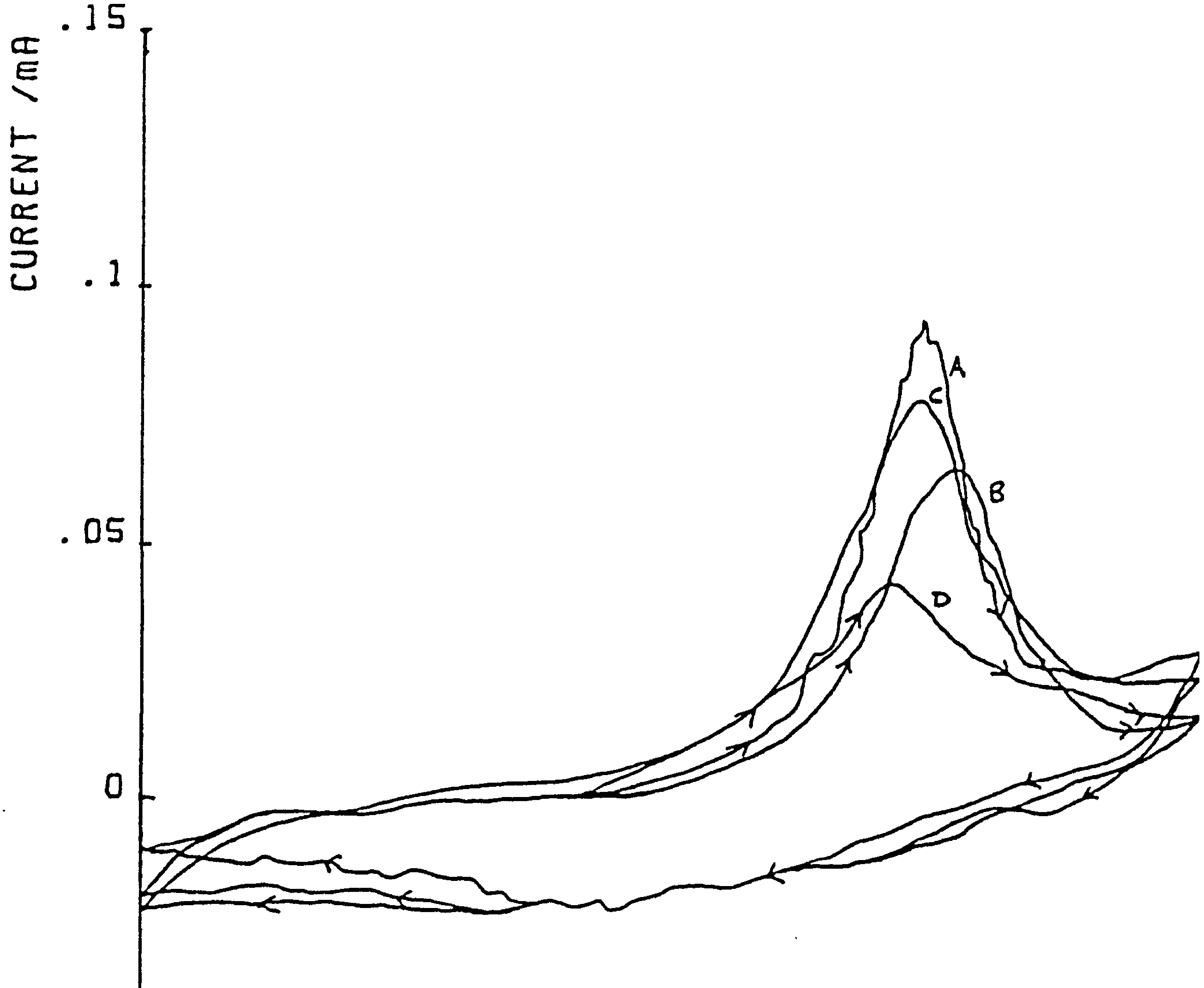

and again the placing of the antimonial alloy peaks is similar to those in Fig. 8.1. However, as described in Chapter 6, the amount of charge contained in the positive-going sweep (sweep rate, $\nu = 100\ \mathrm{mVs^{-1}}$) for all the alloys (A-F) decreases dramatically in 5.5M H_2SO_4 when compared with the charge values in 5.0M H_2SO_4. (See Tables 8.1 and 8.2).

Fig. 8.3 exhibits the LSV curves for pure lead and ternary alloys (Pb-Sn-Ca) in 5.0M H_2SO_4; Fig. 8.4 corresponds to the same metals employed in 5.5M sulphuric acid.

In Fig. 8.3 the ternary alloys undergo more corrosive attack than pure Pb, especially alloy E. This highlights the point mentioned earlier that the reduction of Sb, or even lack of it in the positive grids results in rather poor cycle life. Hence, adding Sn/Ca to pure Pb produces a PbO_2 deposit which is more analogous to that of a freshly plated more reactive electrode as described by Fleischmann (whose research used lead freshly electroplated onto massive lead [98]) than to the deposit produced on flat lead and Pb/Sb electrodes.

Fig. 8.4 shows that alloy E has a lower i_p value than pure lead and alloy F, thus varying the acid concentration has a marked effect on the formation of the PbO_2 deposit on these Pb-Sn-Ca alloys.

The relationship between peak potential (E_p) in the oxidation of $PbSO_4$ to PbO_2 and sweep rate (ν) in the form of E_p vs. $\log_{10}$ (sweep rate) is displayed in Fig. 8.5 for the 5.0M H_2SO_4 case. The equation for this relationship was developed by Canagaratna et al [99] for the production of a single layer on an electrode. As can be seen from the straight line plots in Fig. 8.5, for alloys D and F, the formation of PbO_2 occurs at a much less positive potential than on the pure metal. In 5.5M sulphuric acid when E_p is plotted against $\log_{10}$ (sweep rate), all the alloys (B-F) form PbO_2 at a much less positive potential than pure Pb.

Fig. 8.3 : 5.0M H_2SO_4 electrolyte. Digitally drawn voltammograms of A, pure Pb; E, Pb-Sn (0.34%) - Ca (0.086%); F, Pb-Sn (0.75%) - Ca (0.076%). (500-1500 mV, ν = 100 mVs^{-1}) after cycling for 1.5 h.

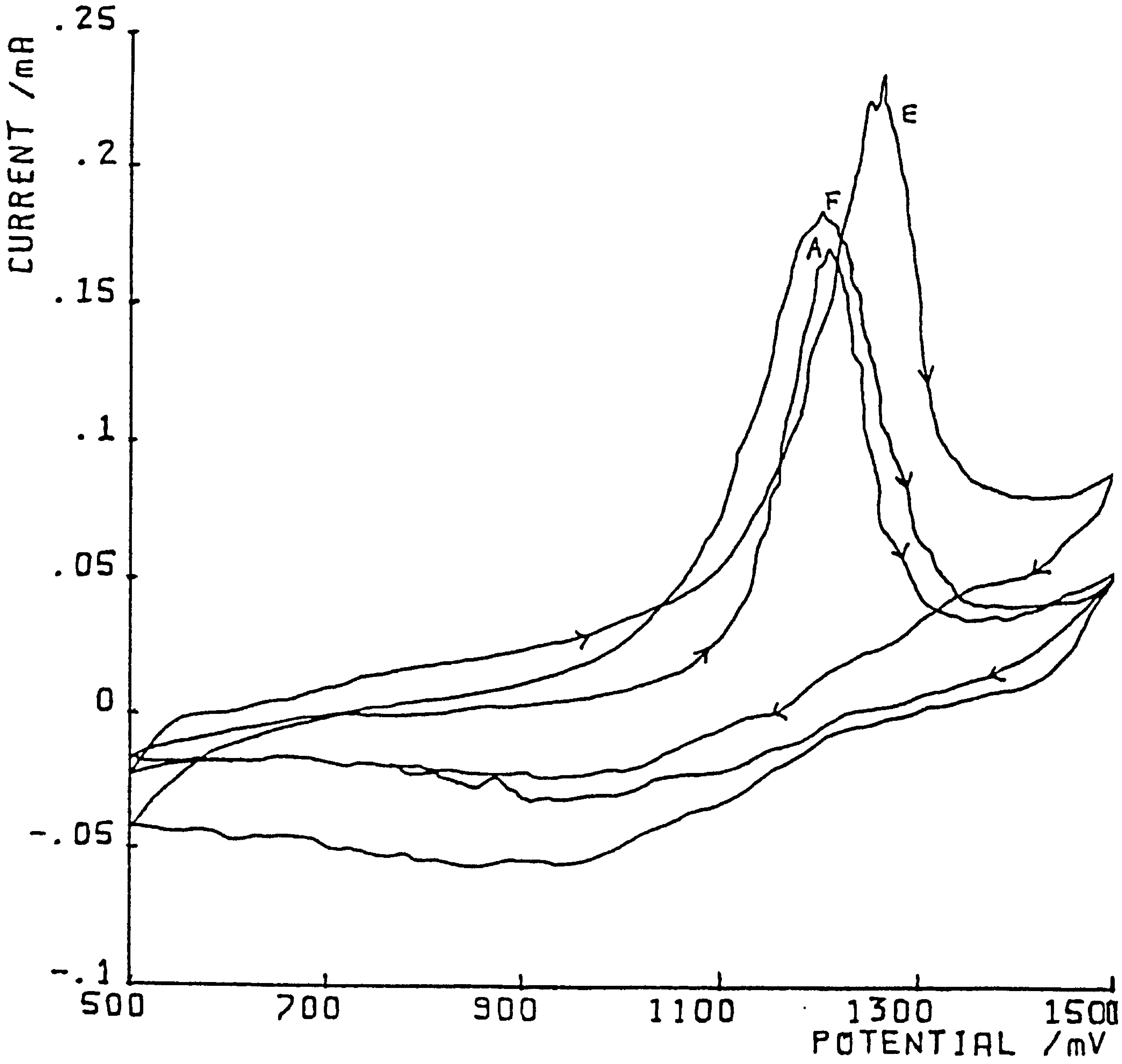

Fig. 8.4 : The same conditions as in Fig. 8.3, but LSV's carried out in 5.5M H_2SO_4.

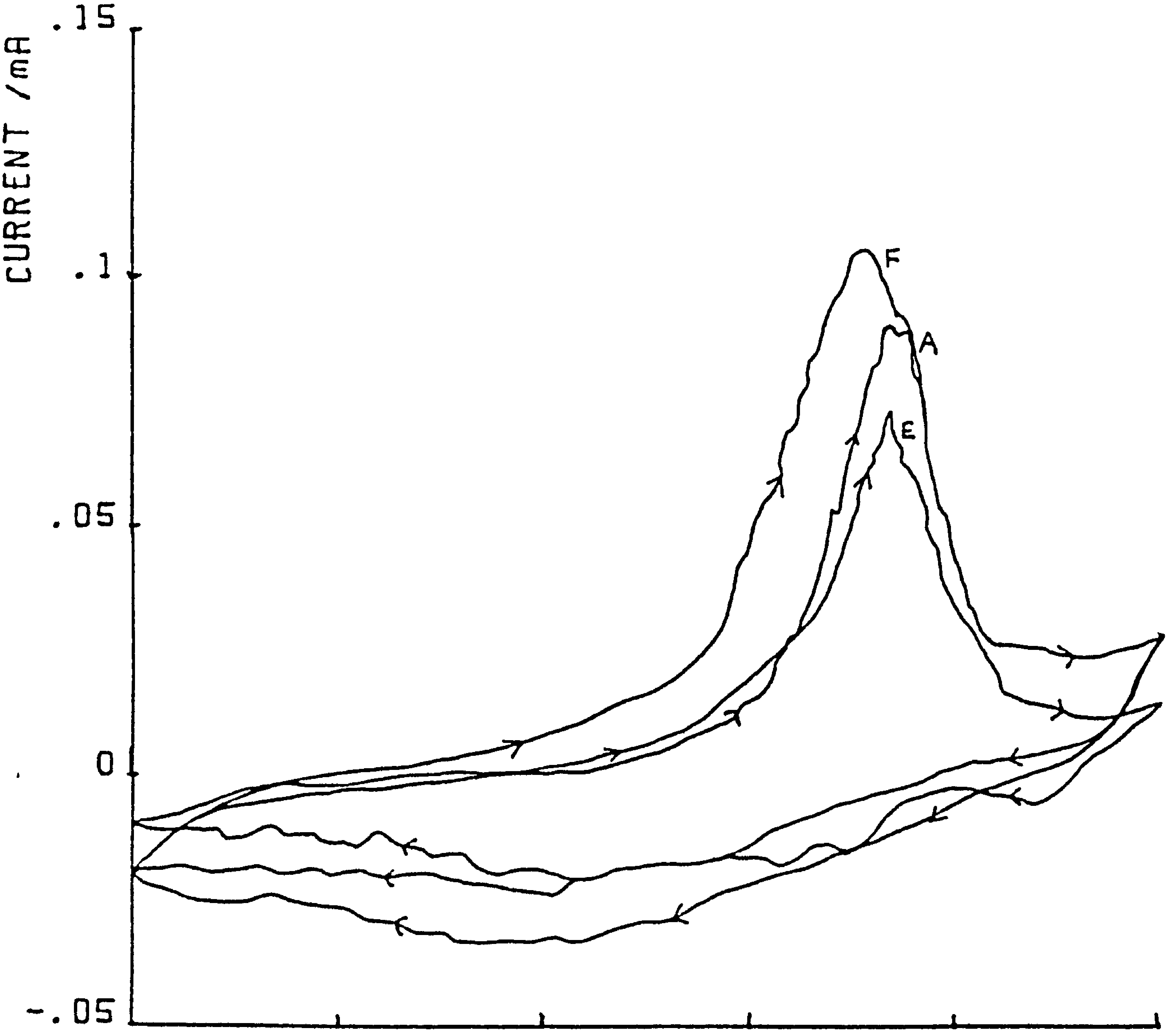

Fig. 8.5 : Plot of E_p versus $\log_{10}\nu$ for:

- ● ; A, pure Pb
- ◈ ; B, Pb-Sb (0.58%)
- ⊡ ; C, Pb-Sb (1.88%)
- △ ; D, Pb-Sb (4.18%)
- ⧗ ; E, Pb-Sn (0.34%) - Ca (0.086%)
- ⊠ ; F, Pb-Sn (0.75%) - Ca (0.076%)

in the range 10 - 100 mVs^{-1}.

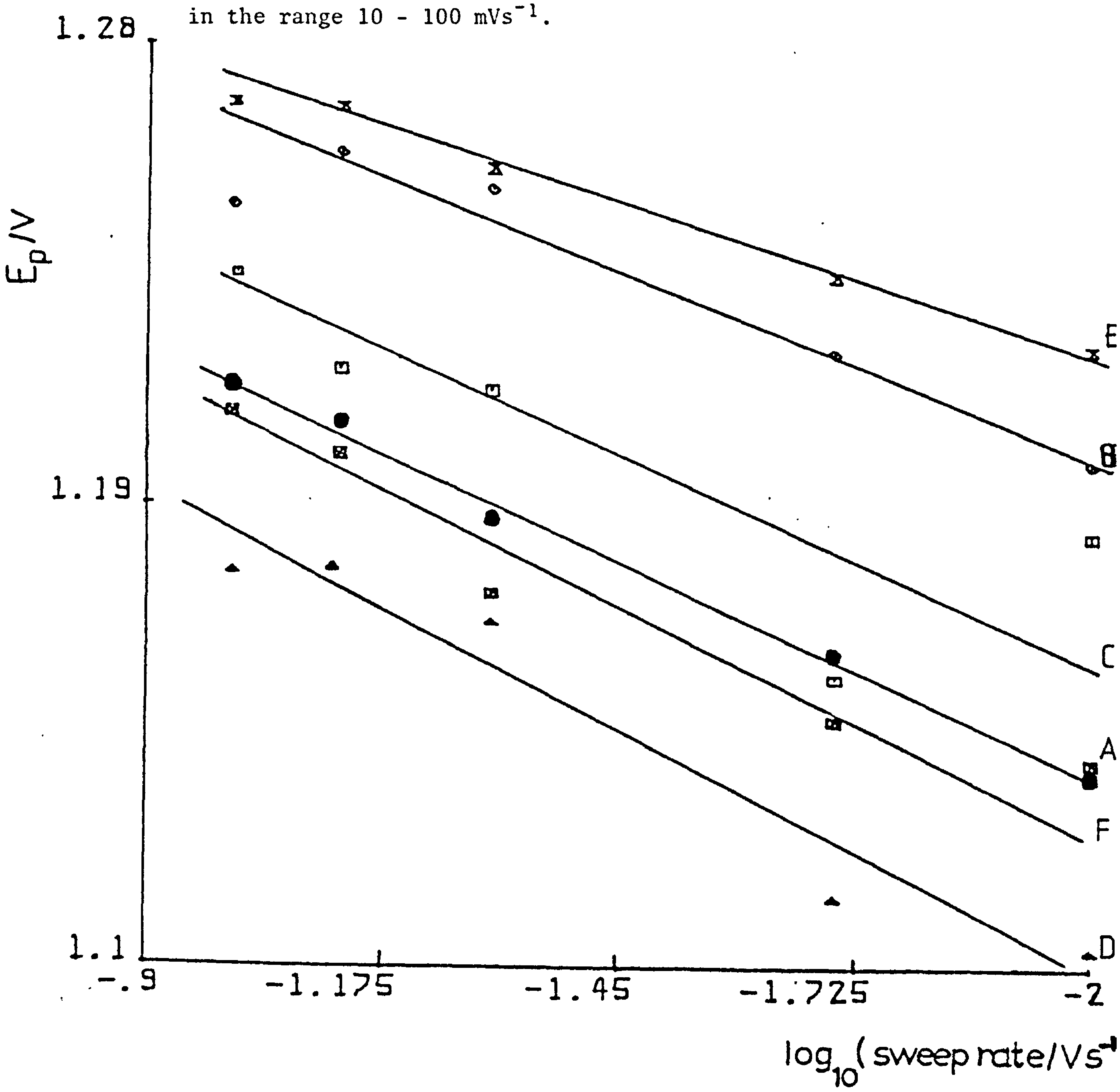

Fig. 8.6 : Plot of i_p versus $\nu^{\frac{1}{2}}$ for:

● ; A, pure Pb
◊ ; B, Pb-Sb (0.58%)
⊡ ; C, Pb-Sb (1.88%)
△ ; D, Pb-Sb (4.18%)
⧗ ; E, Pb-Sn (0.34%) - Ca (0.086%)
▲ ; F, Pb-Sn (0.75%) - Ca (0.076%)

in the range 10 - 100 mVs^{-1}.

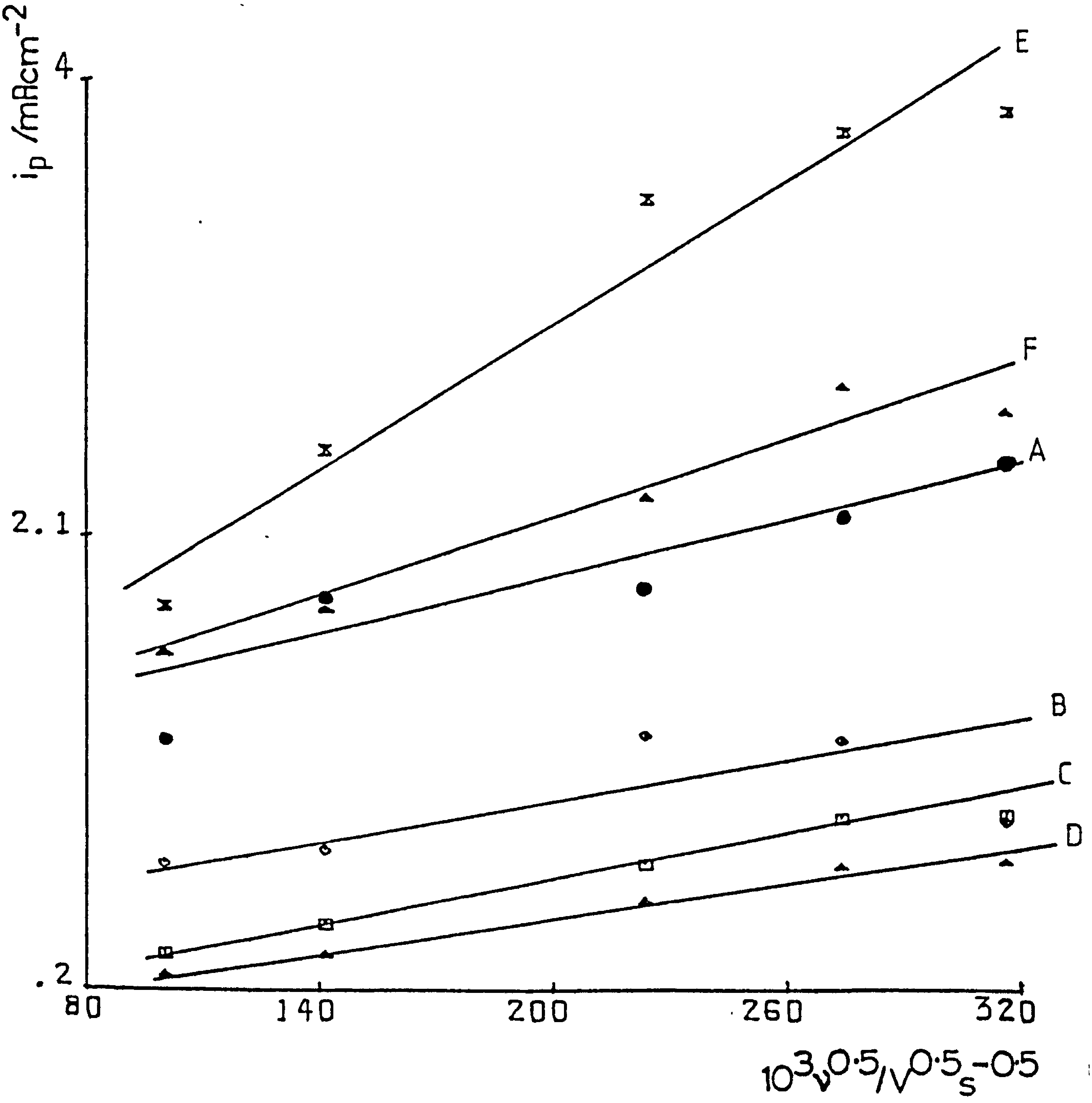

Fig. 8.6 exhibits the i_p - (sweep speed, $\nu)^{\frac{1}{2}}$ relationship in 5.0M H_2SO_4, and straight lines were obtained with the pure lead and the alloys in the range ν = 10 - 100mVs^{-1}. The linearity of the plots indicate that the process for each alloy and pure Pb is a simple first order charge transfer reaction. The i_p vs. $\nu^{\frac{1}{2}}$ relationship still remained intact for most of the alloys in 5.5M sulphuric acid.

Tables 8.1 and 8.2 show that the i_p values corresponding to the sweep rate, ν = 100mVs^{-1} were higher in 5.0M H_2SO_4 for pure Pb and alloys D, E and F. Alloys B and C had higher i_p values in 5.5M H_2SO_4. However, in 5.0M H_2SO_4 more charge was obtained with the ternary alloys.

In 5.0M sulphuric acid, using pure Pb (99.999%, Koch-Light) instead of precast lead (contains many minute impurities and is thus < 99.999% pure) which Kelly et al [94] used, it would seem that more charge is obtained than with the antimonial alloys. This may be due to the fact that the PbO_2 deposited on the pure Pb metal is more porous than the antimony/lead binary alloys and does not produce a passivating layer which is tight and mechanically sound [94]. Even at slower sweep rates, the pure metal still produced more charge in the LSV curves, although it was expected that the antimonial alloys would undergo more anodic attack since it has been observed that some stationary batteries containing Pb-Sb components exhibit a large amount of corrosion. In the author's experiments in 5.5M sulphuric acid, however, only 1.88% antimonial lead displayed higher charge content in the linear sweep voltammogram than the pure metal.

In these experiments the pure lead undergoes more anodic attack than the Pb-Sb alloys. This is probably due to the lack of impurities because, as mentioned in Chapter 6, additives such as Ag, Cu, Ti and Bi in lead metal can exert a protecting effect and considerably reduce corrosion. Also, as reasoned earlier, the pure Pb may produce a PbO_2 layer which is more porous than with the antimonial alloys, thus resulting in a greater

TABLE 8.1

A comparison of i_p, E_p, and anodic charge values for pure Pb (A) and the alloys (B-F) at $\nu = 100\ mVs^{-1}$ in 5.0M H_2SO_4.

Alloys	$i_p/mAcm^{-2}$	E_p/V	Charge, $Q/mCcm^{-2}$
A	2.394	1.213	3.333
B	0.901	1.248	2.554
C	0.930	1.191	2.828
D	0.730	1.177	2.190
E	3.296	1.260	7.087
F	2.592	1.200	5.412

TABLE 8.2

Repeat of Table 8.1, but in 5.5M H_2SO_4.

Alloys	$i_p/mAcm^{-2}$	E_p/V	Charge, $Q/mCcm^{-2}$
A	1.324	1.248	2.238
B	0.963	1.251	1.711
C	1.155	1.209	2.279
D	0.675	1.202	1.608
E	1.037	1.230	1.889
F	1.577	1.209	3.430

degree of corrosion evidenced by voltammograms containing more charge for the pure lead. These results may be considered at variance with those of an earlier investigation [94]; however, the number of sweeps taken to obtain steady states for each alloy and the sweep speed range were comparable with those reported by Kelly et al [94]. However, the potential limits were different; in this case, they were 500-1500 mV, whereas Kelly [94] used the limits of 400-1520 mV.

8.4 Conclusions

1) In 5.0M H_2SO_4, the Pb-Sn-Ca alloys are more susceptible to anodic attack than either pure lead or (0.58-4.18%) antimonial lead.
2) There was more charge in the voltammogram corresponding to pure lead in 5.0M H_2SO_4 than with the Pb-Sb alloys.
3) In 5.5M H_2SO_4, more charge was obtained with electrode C than with pure lead and the other two Pb-Sb electrodes.
4) In 5.0M and 5.5M H_2SO_4, the i_p values corresponding to pure lead were higher than those obtained with the lead/antimony binary alloys.

CHAPTER 9

THE ELECTROCHEMICAL CYCLING OF PASTED Sb and Sn/Ca LEAD ELECTRODES (POSITIVES)

9.1 Introduction

Antimony is employed as the grid alloying additive for the lead-acid positive plate in automotive batteries as described in Chapter 1. However, a technical disadvantage of the metal's presence in the cell is that antimony released from the positive electrode deposits itself on the negative plate resulting in a reduction of the hydrogen overvoltage at that electrode. The use of calcium (< 0.09 weight per cent) [100-102] and tin as alloying agents in lead-acid cells were especially developed for float service; they increase the tensile strength of lead without introducing harmful side reactions into the cells. During float periods, the small overvoltage applied to the cell results in a current which is just sufficient to prevent internal self-discharge processes. At the same time, this low current keeps the loss of water by electrolysis to a minimum. With antimonial grids, because the hydrogen overvoltage is depressed by the presence of antimony on the negative electrode, the float current increases during service. However, removal of antimony from the positive grids gives rise to very poor cycle lives [94].

The LSV experiments were carried out on all the pasted lead alloy electrodes in 5.0M and 5.5M sulphuric acid; the reason for the latter value was discussed in the previous chapter. Also, the base lead alloys used here are the same as those employed and which were reported in Chapter 8.

9.2 Experimental procedure

The computer controlled experimental set-up have been described in the previous chapters. The porous electrodes were prepared by arranging a solid support (various lead-based alloys) to lie beneath the level of a Teflon shrouding. By forcing the positive paste into the cavity, a porous layer was produced (3 mm diameter; 0.76 mm deep) which terminated the lead electrode. The density of the high capacity positive paste used here was 4.2 gcm^{-3} and the composition of it was as follows:

Grey oxide		85.7% (40% Pb and 60% PbO)
Red lead		14.3%
H_2SO_4	1.4 s.g.	53.49 $cm^3\ kg^{-1}$
H_2O		123.57 $cm^3\ kg^{-1}$

The charging of the electrodes was performed in 0.3 M H_2SO_4 as reported in Chapter 5.

For each concentration of sulphuric acid a Hg/Hg_2SO_4 reference electrode was used and all the experiments were carried out at 23 ± 1^oC.

The base lead alloys used in the LSV experiments were:

	Analysis, weight per cent			
Code	Sb	Sn	Ca	Pb
B	0.58	-	-	Remainder
C	1.88	-	-	Remainder
D	4.18	-	-	Remainder
E	-	0.34	0.086	Remainder
F	-	0.75	0.076	Remainder

9.3 Results and Discussion

The linear sweep experiments were carried out between the limits of 1240mV (PbO_2) and 700mV ($PbSO_4$), the sweep speed being always $10mVs^{-1}$.

Fig. 9.1 : Digitally drawn voltammograms for B, pasted Pb-Sb (0.58%) positive in 5.0M H_2SO_4. (1240-700 mV, ν = 10 mV sec^{-1}, nominal surface area = 0.07 cm^2). a, first cycle; b, second cycle; c, third cycle; d, fourth cycle.

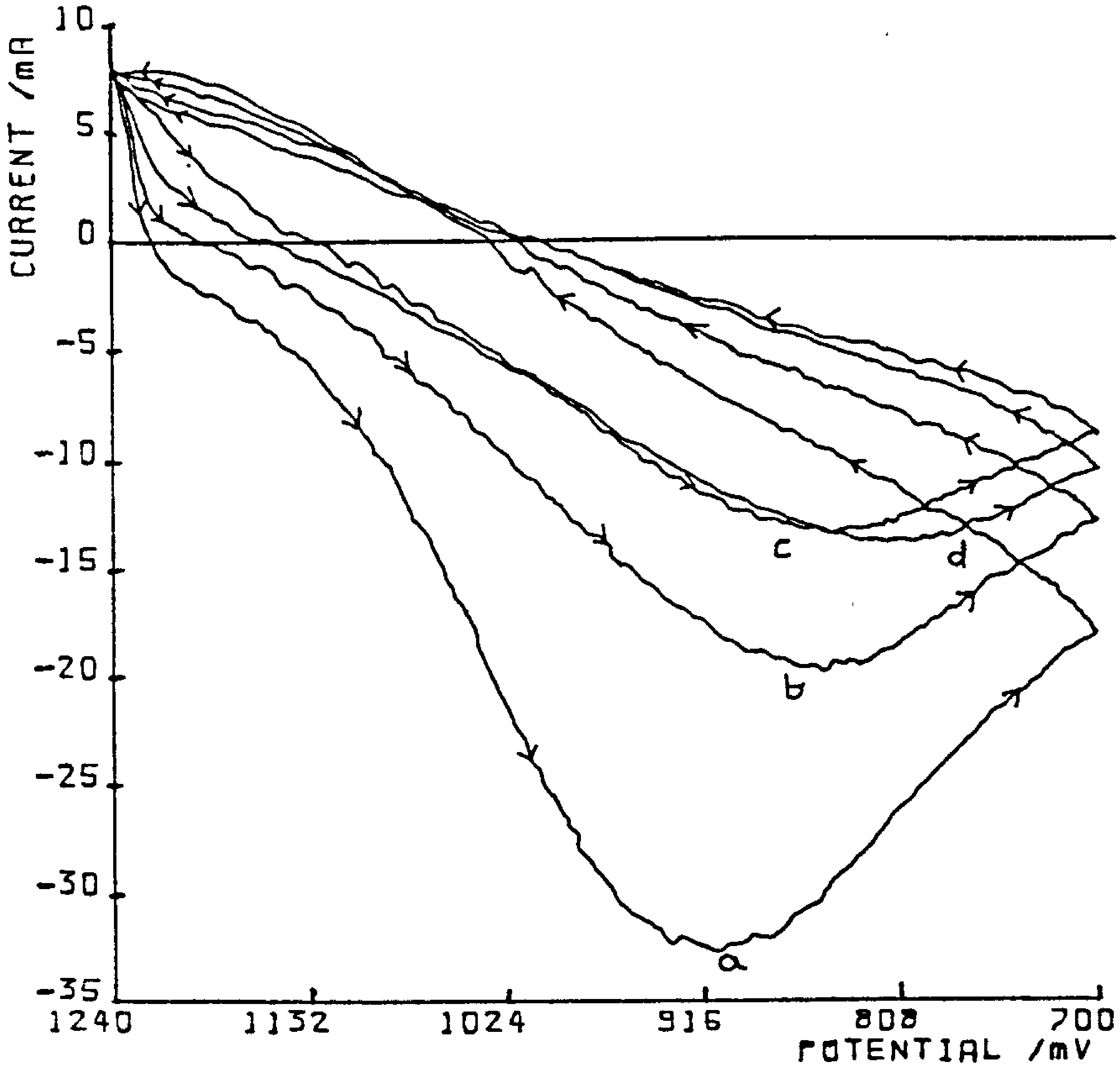

Fig. 9.2 : As in Fig. 9.1, but for C; pasted Pb-Sb (1.88%) positive

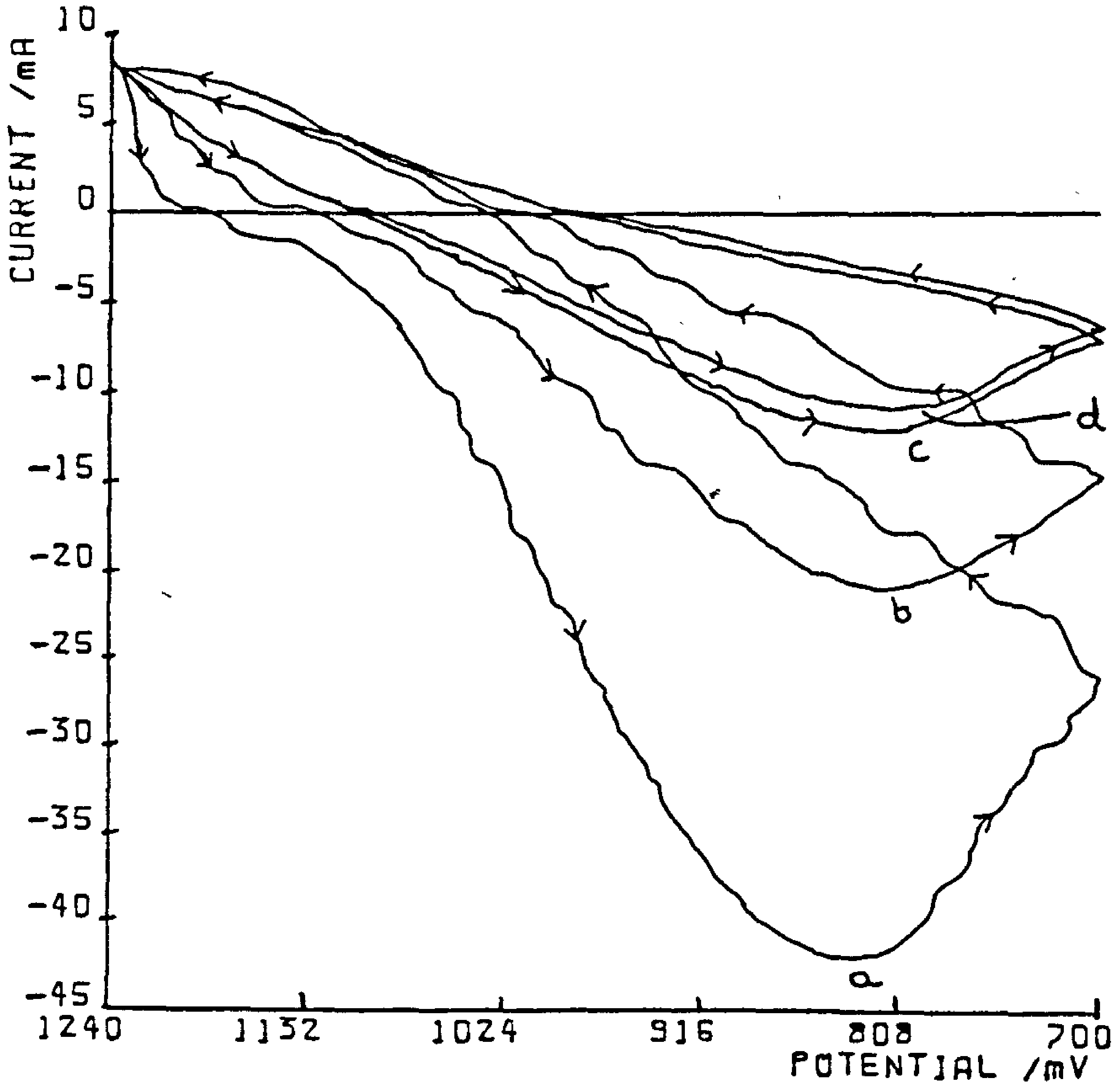

Fig. 9.3 : As in Fig. 9.1, but for D; pasted Pb-Sb (4.18%) positive

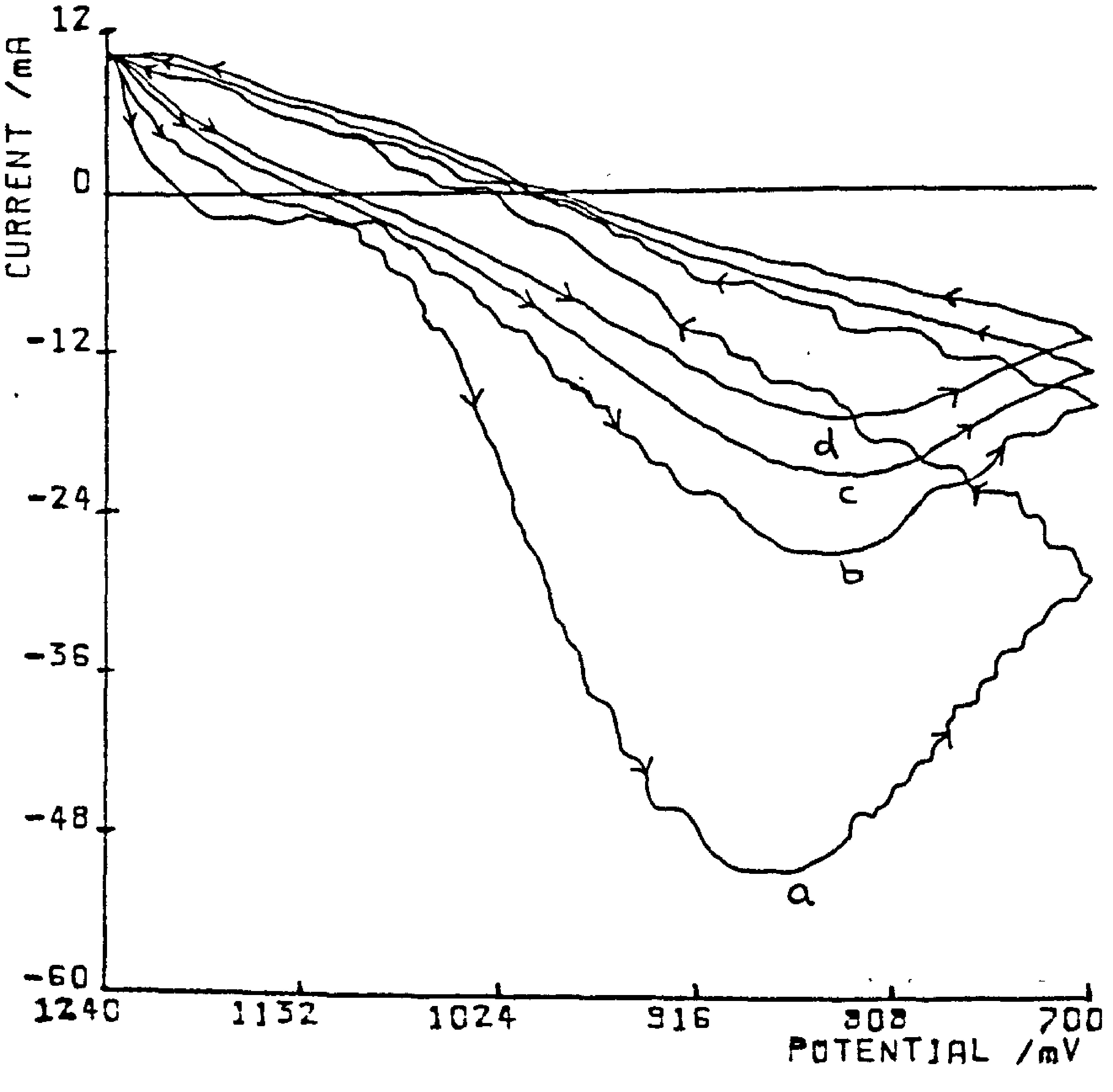

Fig. 9.4 : As in Fig. 9.1, but for E; pasted Pb-Sn (0.34%) - Ca (0.086%) positive.

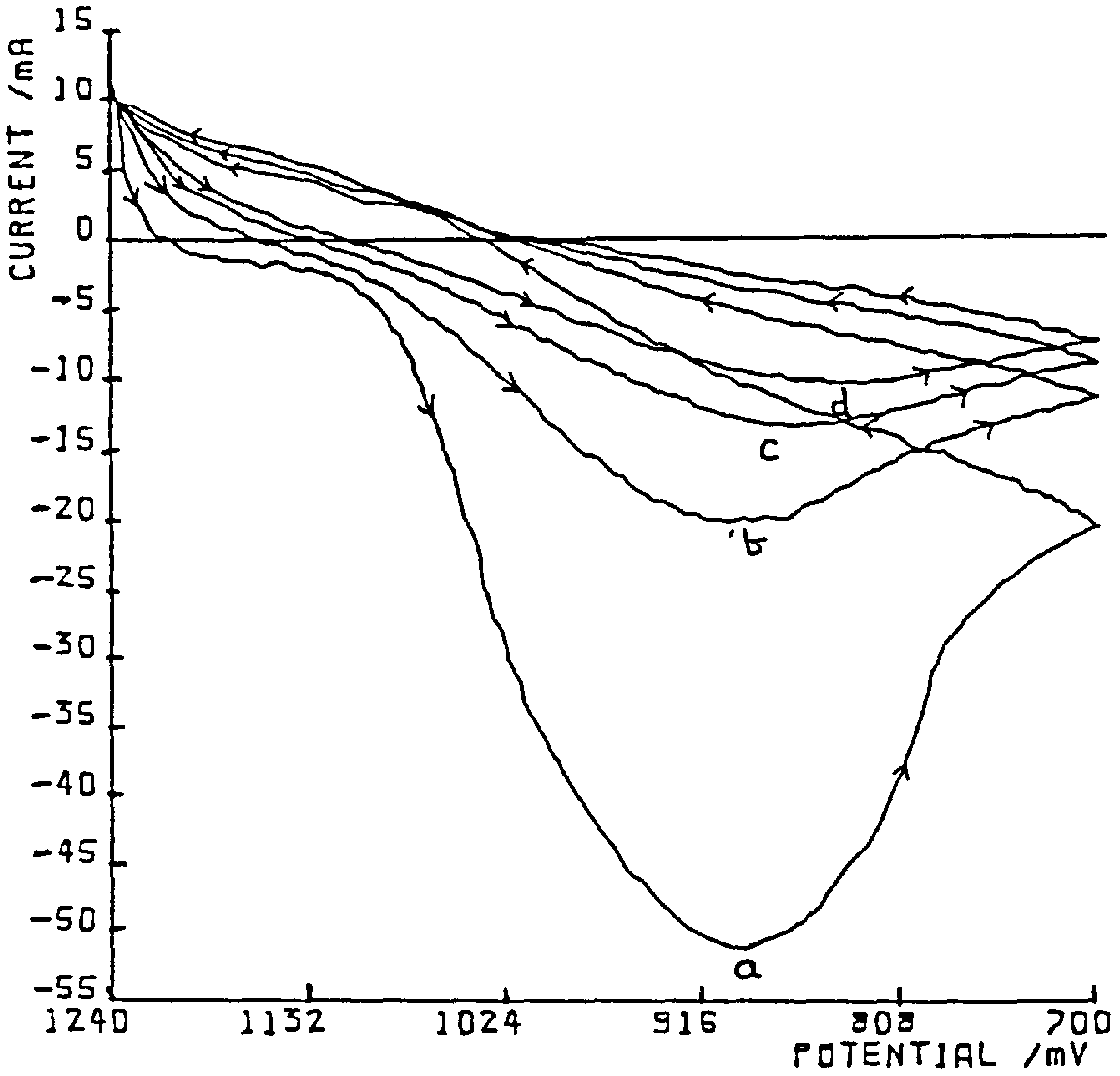

Fig. 9.5 : As in Fig. 9.1, but for F; pasted Pb-Sn (0.75%) - Ca (0.076%) positive.

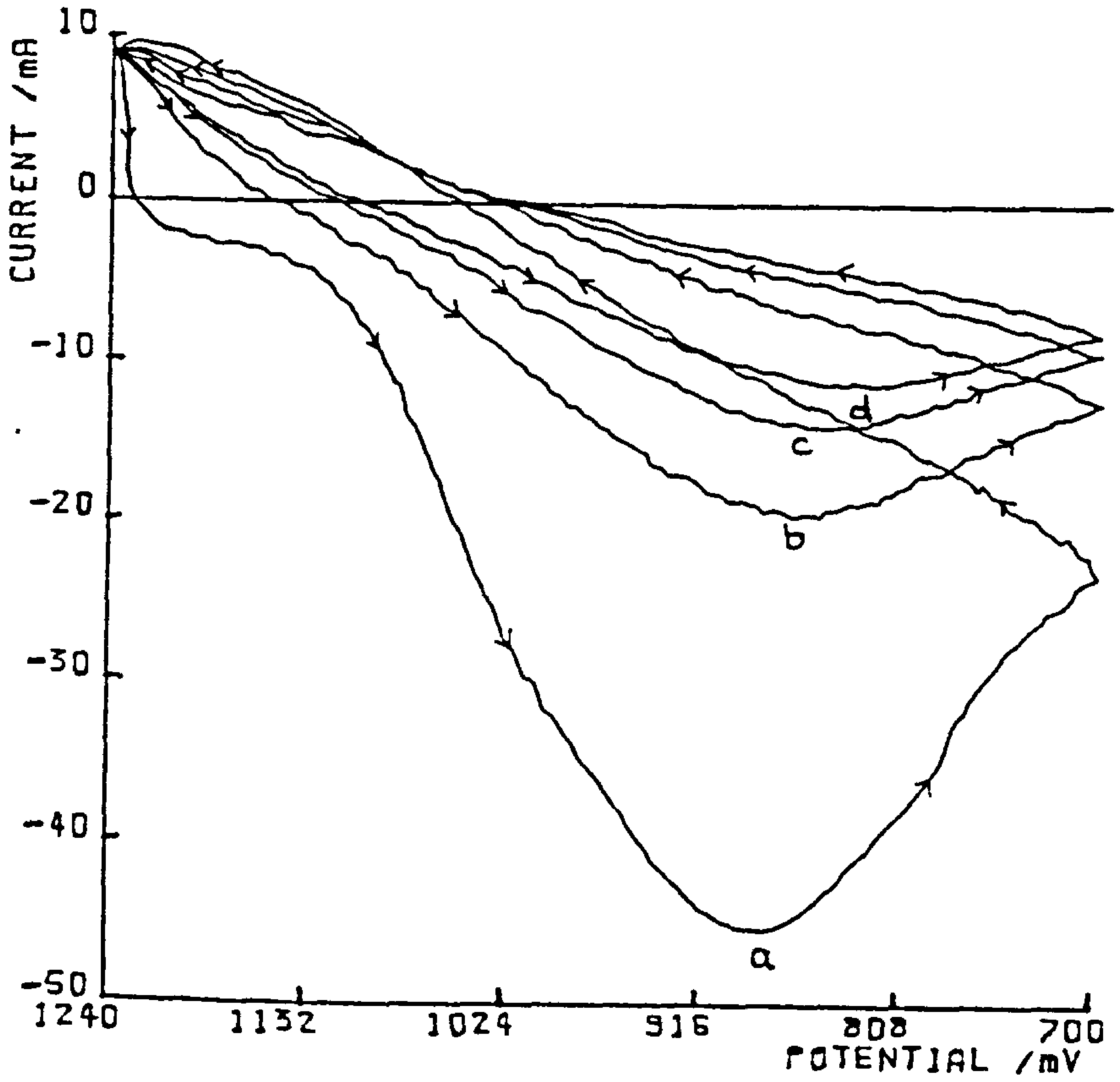

TABLE 9.1

A comparison of i_p with linear sweep cycling of the porous Pb-alloy electrodes (1240-700 mV, 10 mVs^{-1}) in 5.0M H_2SO_4.

Alloys	Cycle Number	Reduction peak current, i_p/mA	Position of i_p, E_p/mV
B	1	32.79	912
	2	20.00	851
	3	13.53	844
C	1	42.00	842
	2	20.00	824
	3	15.40	821
D	1	50.00	873
	2	26.00	840
	3	21.00	833
E	1	50.80	894
	2	20.60	891
	3	13.80	866
F	1	45.13	882
	2	20.55	862
	3	13.90	848

Figs. 9.1-9.5 correspond to a series of voltammograms for the early cycle histories of each pasted Pb-alloy electrode, that is, B-F, all in 5.0 M H_2SO_4. Figs. 9.6-9.10 correspond to the same electrodes, but the potentiodynamic cycling experiments were performed in 5.5 M sulphuric acid.

As can be seen from the ten figures, there is a decrease in peak current values (i_p) with cycling ($PbO_2 \rightarrow PbSO_4$ reduction peak). The major differences is between the i_p values for the first and second cycles for all the electrodes as highlighted by Tables 9.1 and 9.2. The large initial reduction current is due to a passivated form of $PbSO_4$ being produced which resists oxidation to PbO_2 during the anodic sweep [103]. If the higher potential limit is raised above 1240mV, oxygen bubbles are formed in the electrode matrix which would interfere with the charging/discharging operation.

The electrodes had to be reoxidised galvanostatically (25mA cm^{-2} in 0.3 M H_2SO_4) in an upward-facing position after a series of cycles. This is because the layer of passivated lead sulphate crystals formed on the Pb electrodes is such that in order to reproduce lead dioxide a large overpotential is needed : galvanostating ensures this.

Table 9.1 shows that in 5.0 M H_2SO_4, the pastedalloy-D electrode has a larger initial i_p value than that of the other porous Pb-Sb electrodes. Also, the pasted alloy positive attains a constant response after approximately 15 cycles, the i_p and position of i_p (E_p) values remaining constant. Pasted alloys B and C reach constant responses after 11 and 14 cycles respectively. However, the pastedalloy-E electrode discharges more deeply on the first cycle than the porous antimonial lead electrodes as highlighted by Table 9.1. This may be attributed to the fact that a more reactive PbO_2 deposit is produced on Pb-Sn-Ca alloys (see Chapter 8) than the deposit formed on pure lead and most Pb-Sb alloys. Hence, the porosity of the pasted Pb-Sn-Ca electrode matrix when charged may have

Fig. 9.6 : Digitally drawn voltammograms for B in 5.5M H_2SO_4. (1240-700 mV, ν = 10 mV sec^{-1}, nominal surface area = 0.07 cm^2). a, first cycle; b, second cycle; c, third cycle; d, fourth cycle.

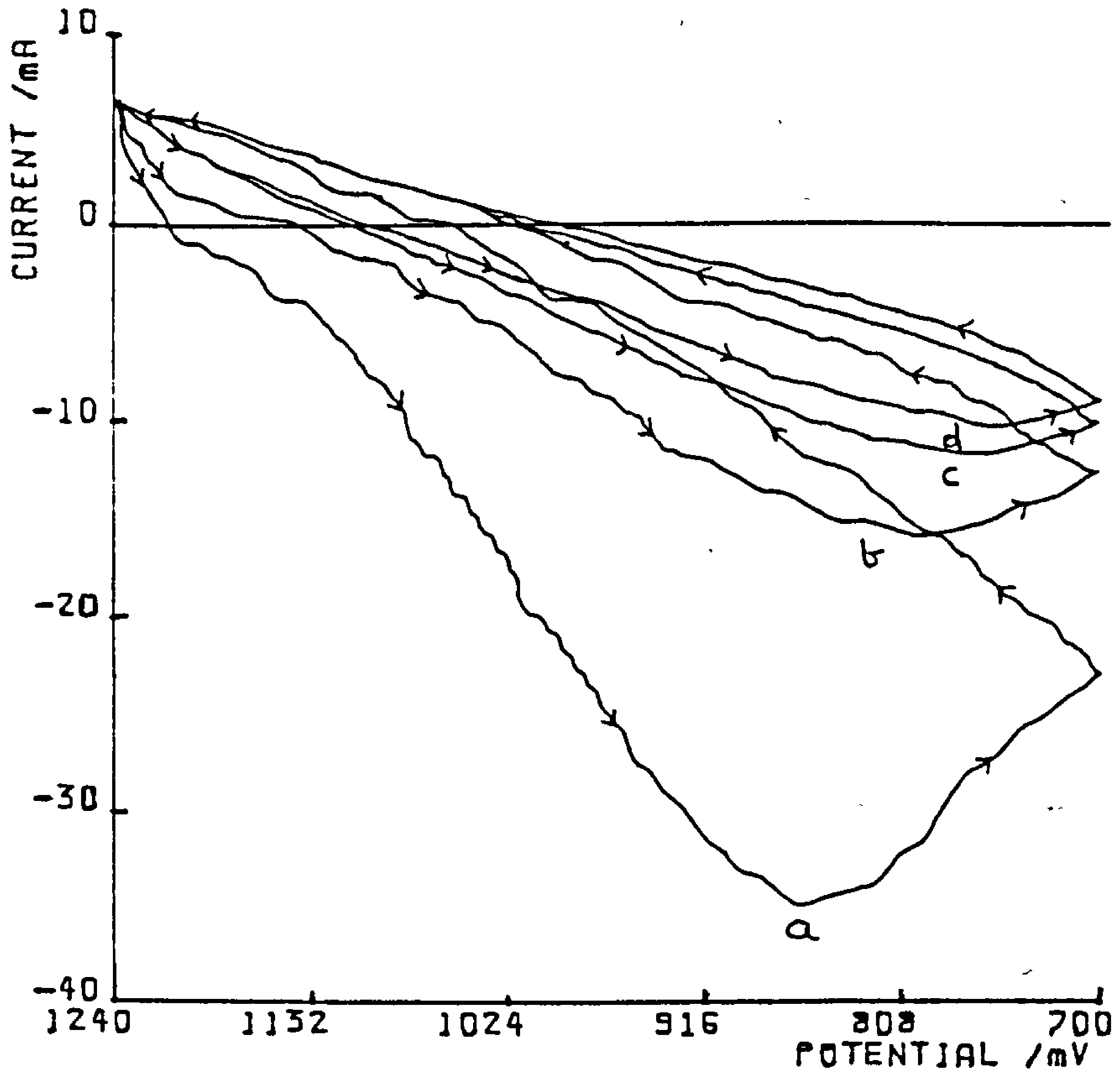

Fig. 9.7 : As in Fig. 9.6, but for C.

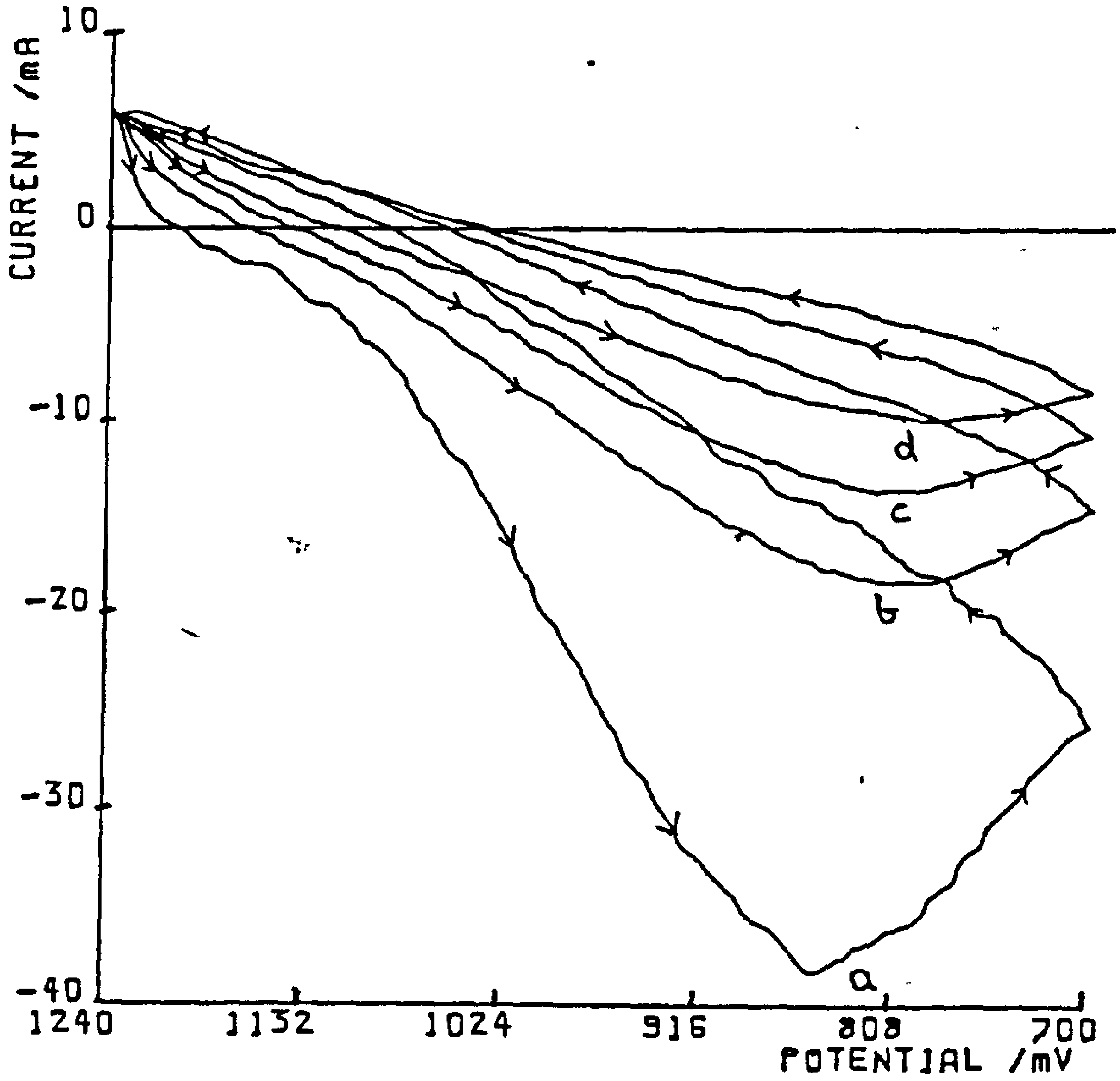

Fig. 9.8 : As in Fig. 9.6, but for D.

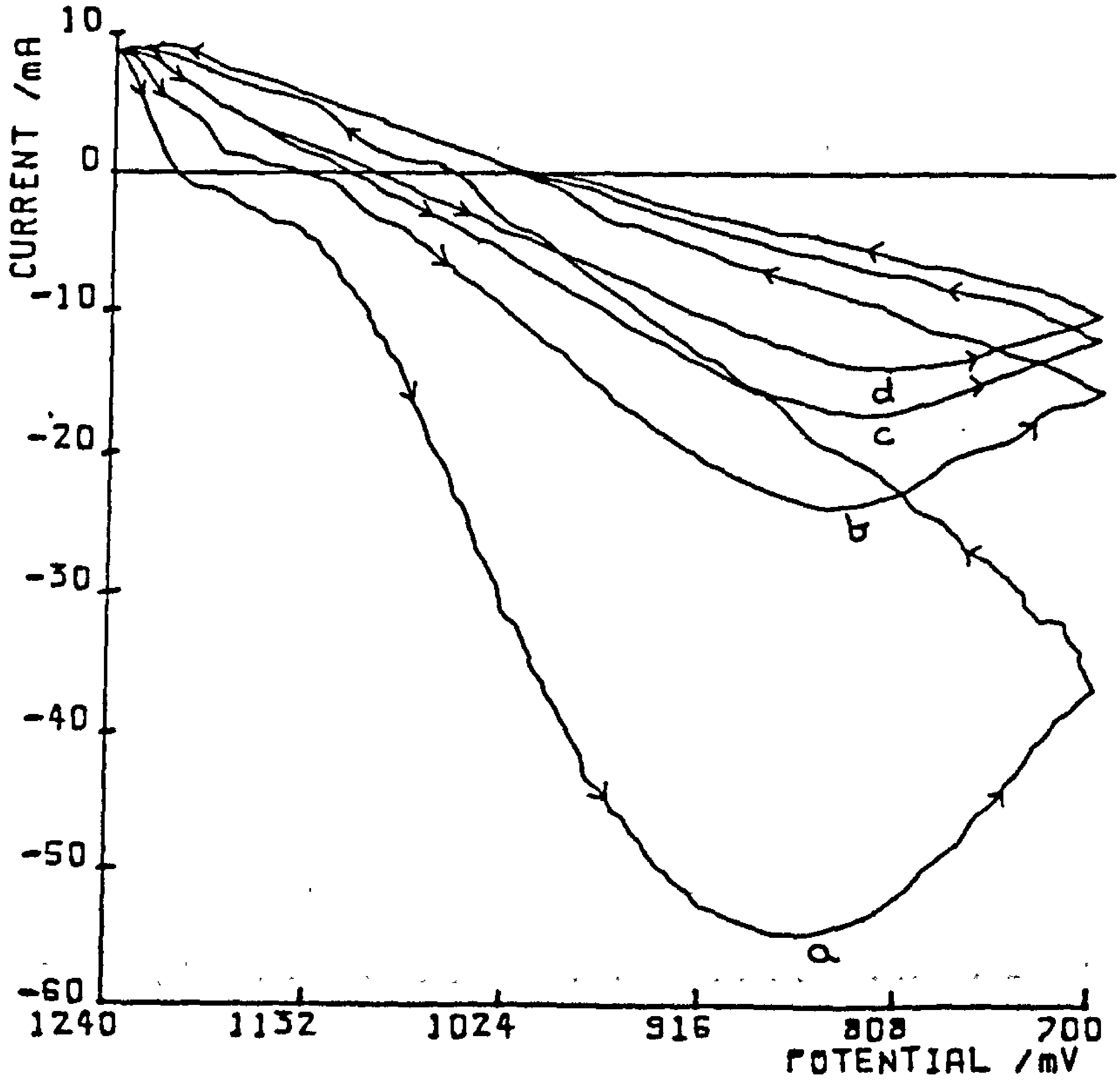

Fig. 9.9 : As in Fig. 9.6, but for E.

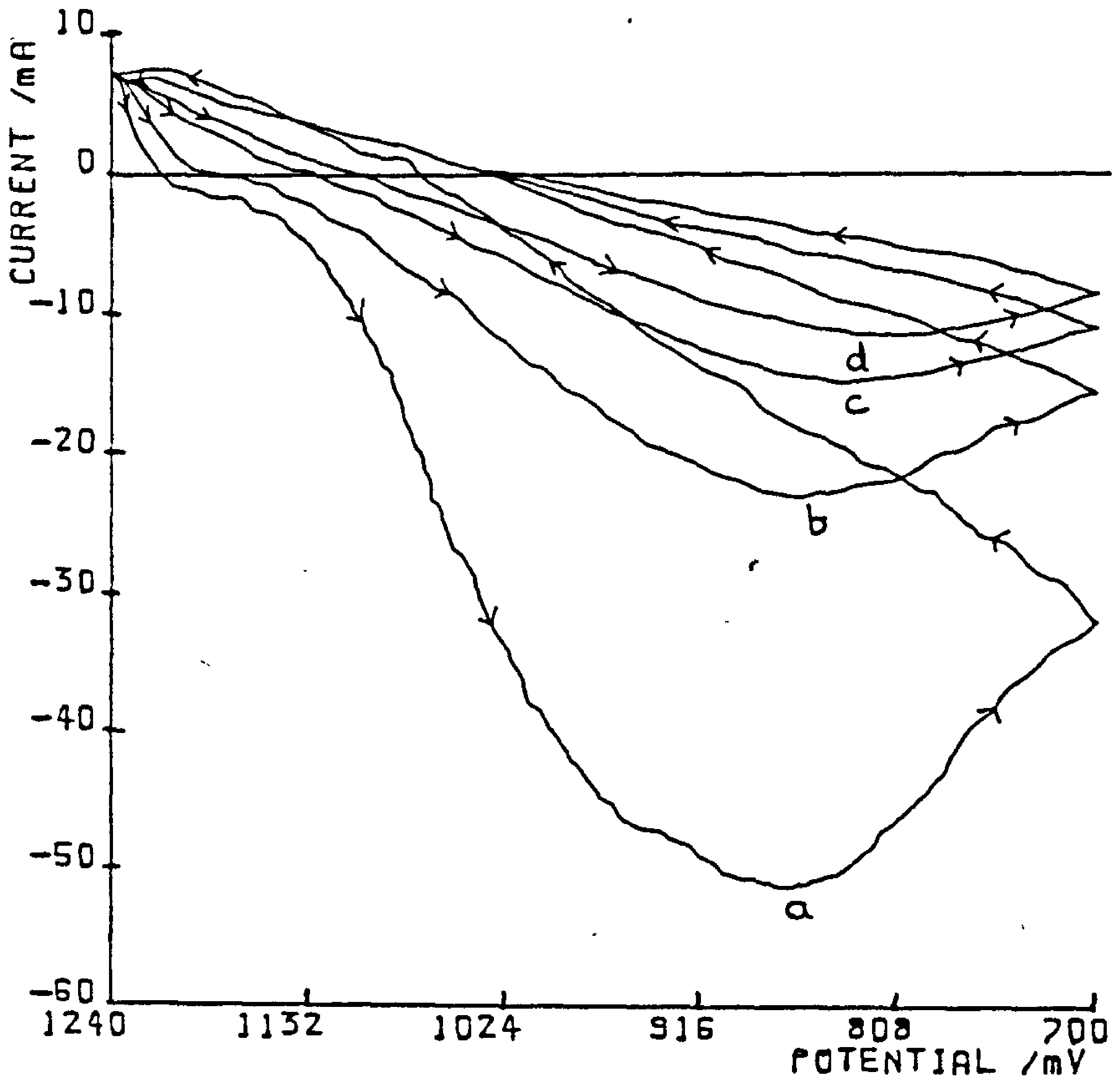

Fig. 9.10 : As in Fig. 9.6, but for F.

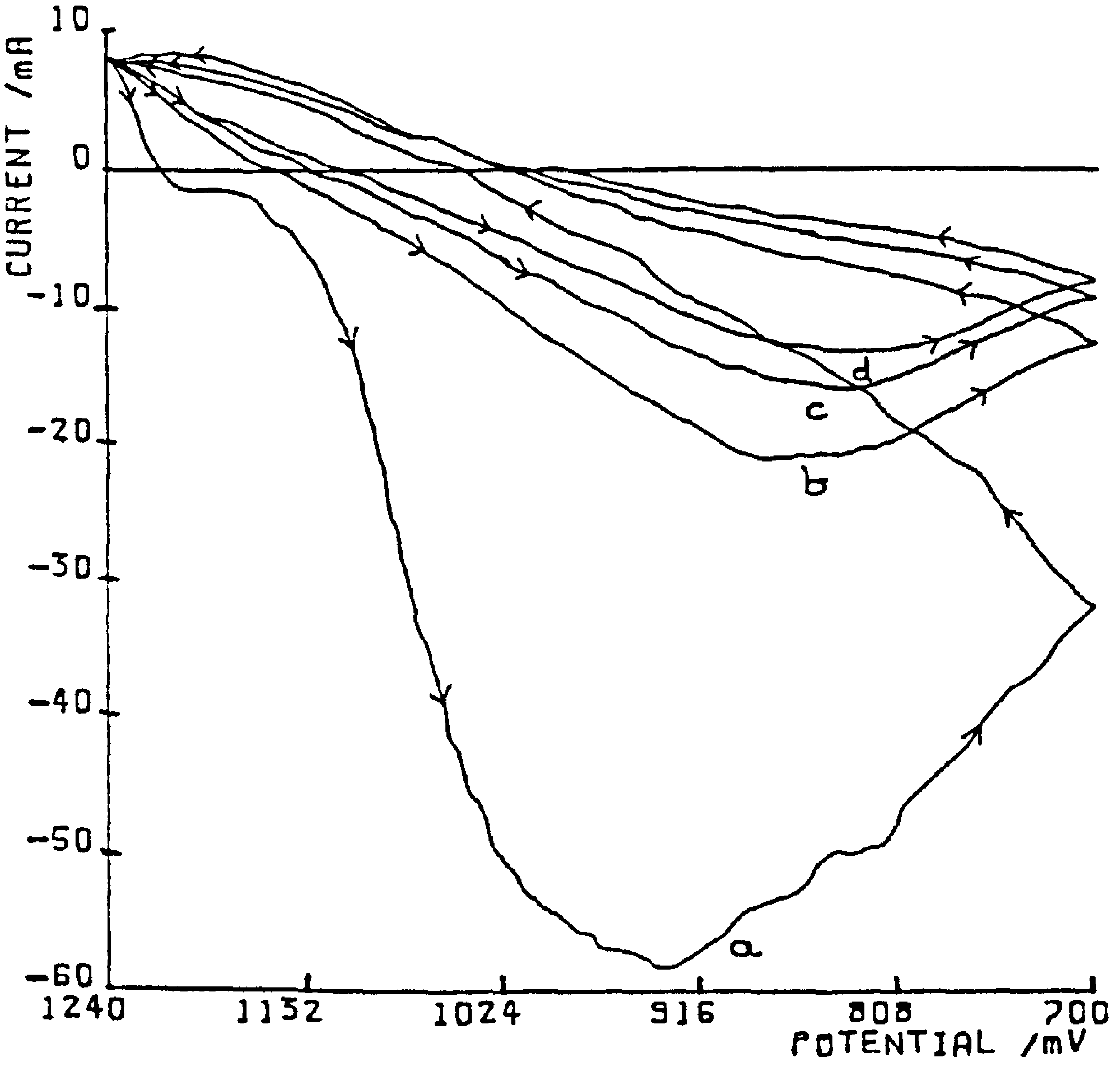

TABLE 9.2

Repeat of Table 9.1, but in 5.5M H_2SO_4.

Alloys	Cycle Number	Reduction peak current, i_p/mA	Position of i_p E_p/mV
B	1	35.00	858
	2	16.00	786
	3	11.60	776
C	1	38.00	850
	2	18.40	813
	3	13.40	808
D	1	55.00	866
	2	24.00	848
	3	17.40	826
E	1	51.17	869
	2	23.00	858
	3	15.00	835
F	1	58.00	950
	2	21.40	861
	3	16.00	840

been further increased. Porous alloy-E positive has a higher initial i_p value than the porous alloy-F electrode, and they obtain a constant response after 11 cycles no matter what subsequent cycling experiments are carried out. (This applies to the previous pasted Pb-Sb positives). It would seem, as described by Hampson et al [103], that the $PbSO_4$ produced reaches an equilibrium form with some of the "unpassivated" lead sulphate present in the porous matrix which can be oxidised (to PbO_2) and reduced (back to $PbSO_4$) by sweeping potentiodynamically.

Table 9.2 shows that in 5.5 M sulphuric acid the pasted alloy-D positive has a greater initial i_p value than that of the other two porous Pb-Sb electrodes but is in turn lower than the initial i_p value of the positive-F electrode. A strange feature of the higher concentration of H_2SO_4 (i.e. 5.5 M) is that the pasted alloy-C electrode undergoes partial ohmic control after 10 cycles. With the other porous electrodes, their voltammograms reach constancy after a larger number of cycles than the corresponding electrodes in 5.0 M H_2SO_4. The pasted Pb-Sn-Ca electrodes discharge more initially in 5.5 M H_2SO_4 than in 5.0 M sulphuric acid, whereas the situation is completely the opposite with the pasted Pb-Sb positives. It would seem that varying the acid concentration has a marked effect on the PbO_2 porous matrix on the base Pb-Sn-Ca metals.

Comparing the data reported in Chapter 8 on flat, unpasted electrodes to these exhibited here, one notices a few major differences. With the flat, unpasted electrode the PbO_2 peak is dominant and the data obtained corresponds to the production of a single layer on an electrode with no thickening of the deposit occurring. With the porous electrode, the prominent PbO_2 formation peak is absent because the lead dioxide produced grows in layers [104], and thus a broad band is observed made up of many different oxidation peaks overlapping with each other. Another significant difference between the two electrodes is that with the porous one larger current and hence charge values are obtained.

A look at the voltammograms of the flat and pasted electrodes shows that the reduction peaks ($PbO_2 \rightarrow PbSO_4$) are clearly different. With the flat electrode, the reduction "peak" is hardly visible; for the pasted electrode, a long "reduction tail" [103] is displayed which is indicative of newly produced porous PbO_2, where the discharge is being driven deep into the porous matrix.

The i_p and hence charge values obtained for the pasted Pb-Sb electrodes, are higher than those reported by Kelly et al [103]. This is due to the fact that the paste used here was such that it could sustain more charge than the standard automotive paste employed by them [103].

9.4 Conclusions

1) The Pb-Sn-Ca electrodes initially discharge more deeply than the Pb-Sb electrodes in 5.0 and 5.5 M H_2SO_4 although electrode D (containing 4.18% Sb) performs very similarly to electrodes E and F.

2) After the first cycle the reduction peak current values (i_p) for the porous Pb-Sb electrodes were higher in 5.0 M H_2SO_4 than in 5.5 M H_2SO_4.

3) The porous Pb-Sn-Ca electrodes had higher reduction peak current values (i_p) in 5.5 M H_2SO_4 than in 5.0 M H_2SO_4.

CHAPTER 10

POTENTIOSTATIC STEP EXPERIMENTS ON PASTED Pb-Sb and Pb-Sn-Ca ELECTRODES

10.1 Introduction

During the last decade it has been realised that positive electrodes prepared on antimony-free grids were inferior in both cycle life span and performance after cycling duty. This shortcoming appeared to be a positive effect of antimony on that of the basic pure lead rather than a detrimental effect of tin and calcium on the basic behaviour. There was also considerable industrial evidence that the grid effects (as they ought to be called) was dependent on the amount and character of the cycling to which the electrodes were subjected; a newly formed positive electrode exhibits a behaviour independent of the grid whereas as few as 10 cycles would show up gross differences in behaviour.

With the present intense interest in the fully-sealed low-loss battery it was considered important to identify the specific grid effects attributable to the alloys Pb-Sb and Pb-Sn-Ca of the relevant commercial compositions. This chapter presents the results of such an investigation in which the specific effects as functions of cycle number were investigated.

10.2 Experimental procedure

The electrochemical stepping experiments were performed using a micro-computer as described in Chapter 5 controlling a potentiostat (Kemitron POT.03); the data obtained from the pulse experiments were captured by a transient recorder (Datalab, DL 905) which in turn transferred back to the computer. An oscilloscope (Hameg HM 512) was used to display the data recorded by the transient recorder.

The electrodes in which a porous PbO_2 phase (derived from the same battery paste described in Chapter 9) overlays the desired base alloy shrouded in Teflon and forming the working face of an RDE electrode have already been described (see Chapter 5). The initial oxidation of paste to PbO_2 was carried out and has also been described in Chapter 5. When formed the working porous electrode was a cylinder (0.07 cm^2 area, 0.076 cm deep; of equivalent electrical charge ∿ 16C).

The base lead alloys used for the porous PbO_2 supports were:

Code	Analysis, wt%			
	Sb	Ca	Sn	Pb
A	-	-	-	99.999
B	0.58	-	-	Remainder
C	1.88	-	-	"
D	4.18	-	-	"
E	-	0.086	0.34	"
F	-	0.076	0.75	"

10.3 Results and Discussion

10.3.1 Uncycled Electrodes

Fig. 10.1 shows the current-time responses of the porous antimonial-lead electrodes (compared with a pasted pure lead electrode) as the potential* is instantaneously stepped from the lead dioxide region (1240 mV) to the lead sulphate region (700 mV). As can be seen B which contains the least amount of antimony, discharges very quickly and gives the highest current output, that is, i_{max} = 140 mA. The low Sb content probably gives rise to more β-PbO_2 being produced compared to α-PbO_2. Burbank et al [5] have discussed that in a mixture of the two polymorphs α-PbO_2 and β-PbO_2

---

*Footnote

A Hg/Hg_2SO_4 reference electrode was used throughout and all potentials are quoted on this scale (23 ± 1°C).

TEXT CUT
OFF IN
ORIGINAL

FIG.10.1. Potentiostatic pulse experiments from 1240 mV to 700 mV on porous Pb and Pb-Sb electrodes.

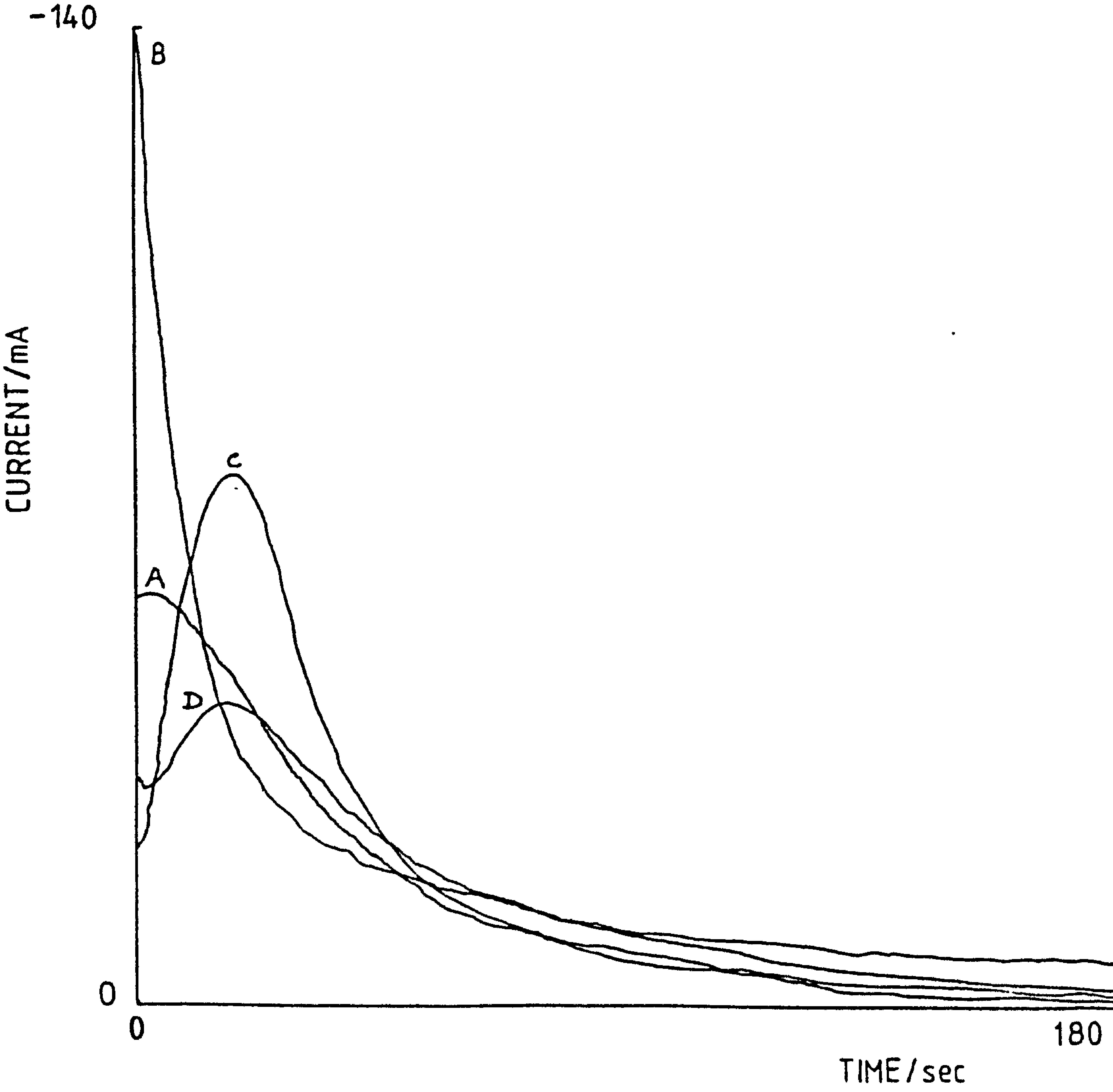

FIG.10.2. Potentiostatic pulse experiments from 700 mV to 1240 mV on the electrodes used in FIG.10.1. following full discharge.

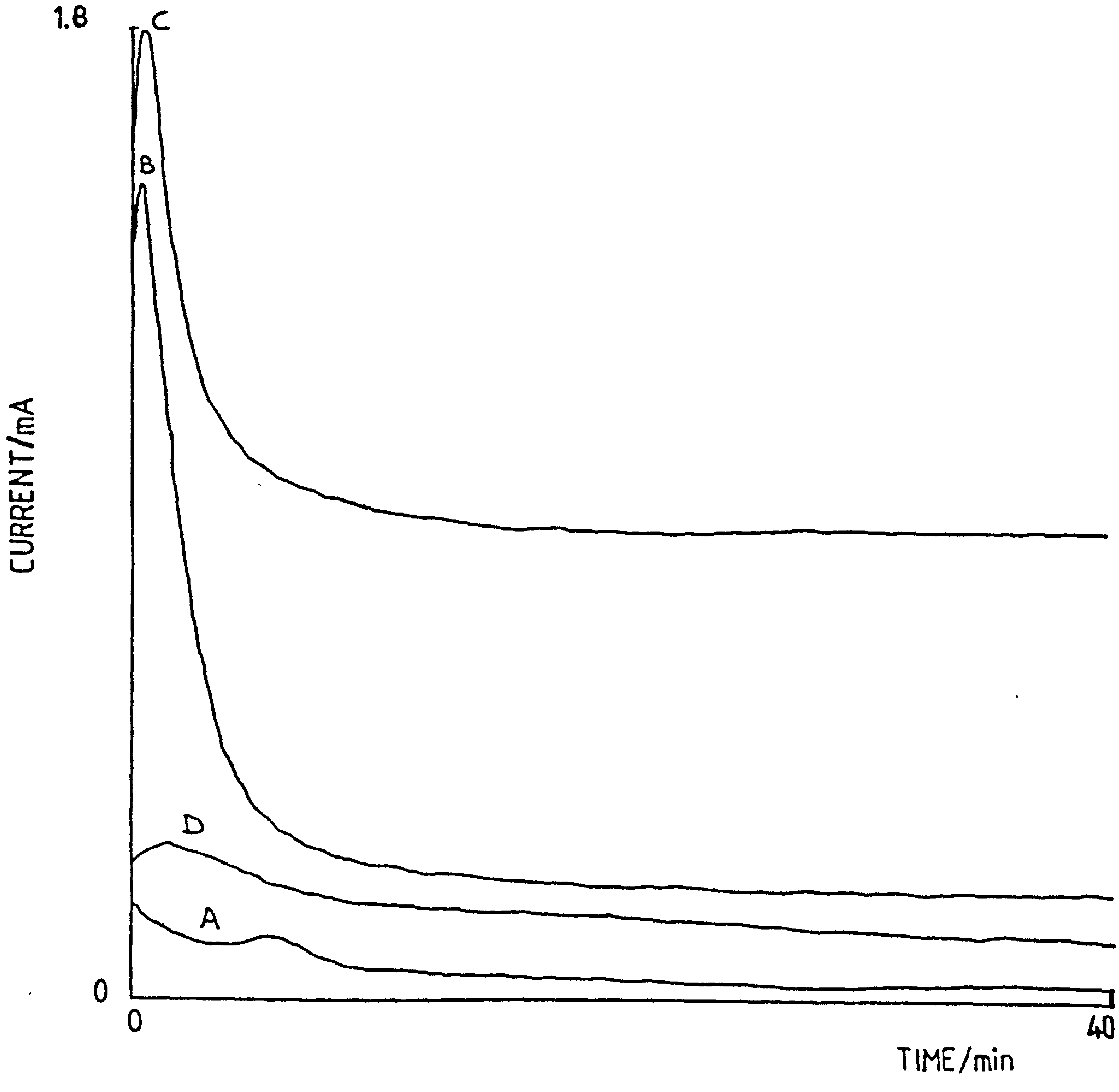

FIG.10.3. The same conditions as in FIG.10.1., but on porous Pb and Pb-Sn-Ca electrodes.

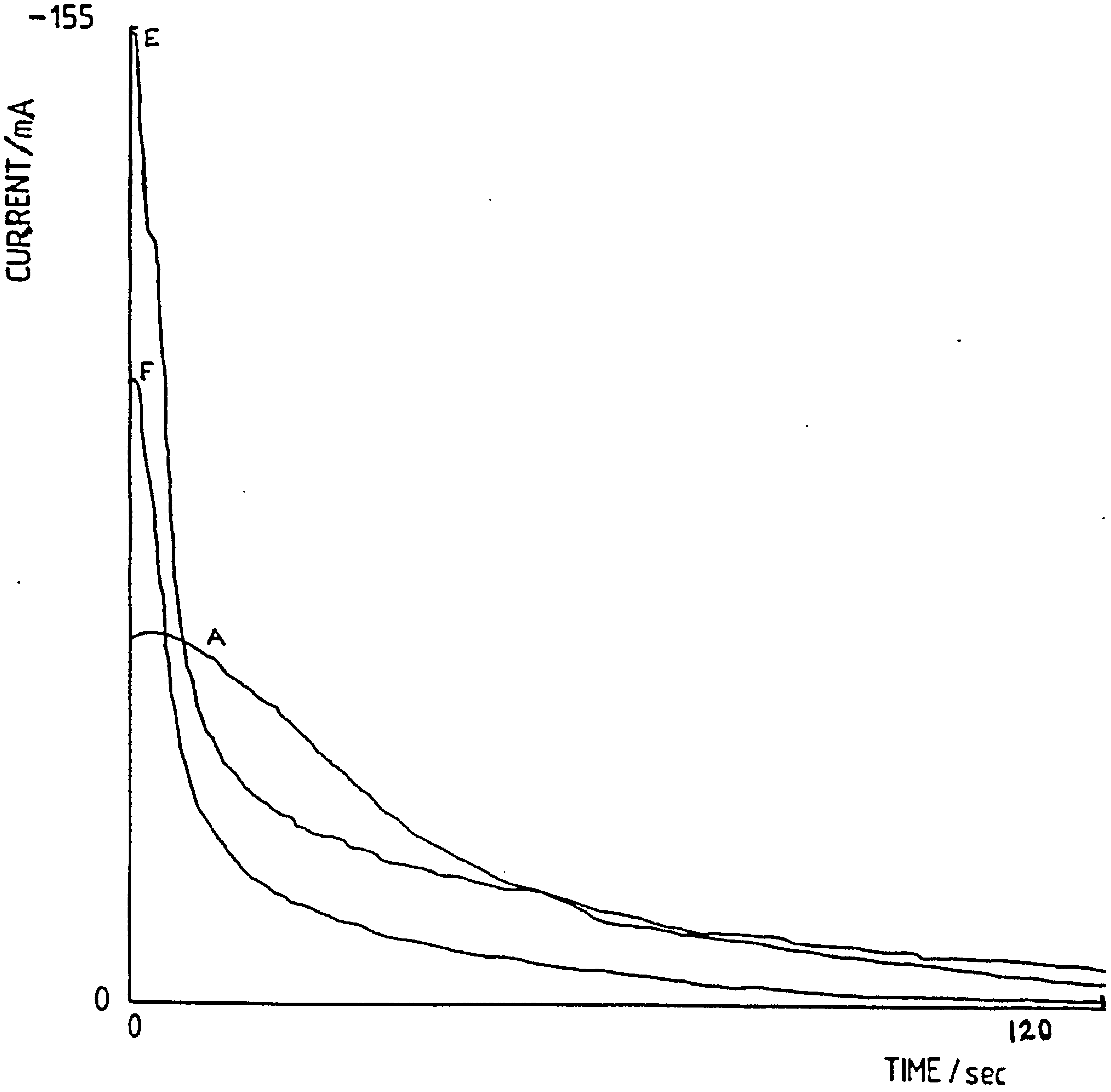

FIG.10.4. Potentiostatic pulse experiments from 700mV to 1240mV on the electrodes used in FIG.10.3. following full discharge.

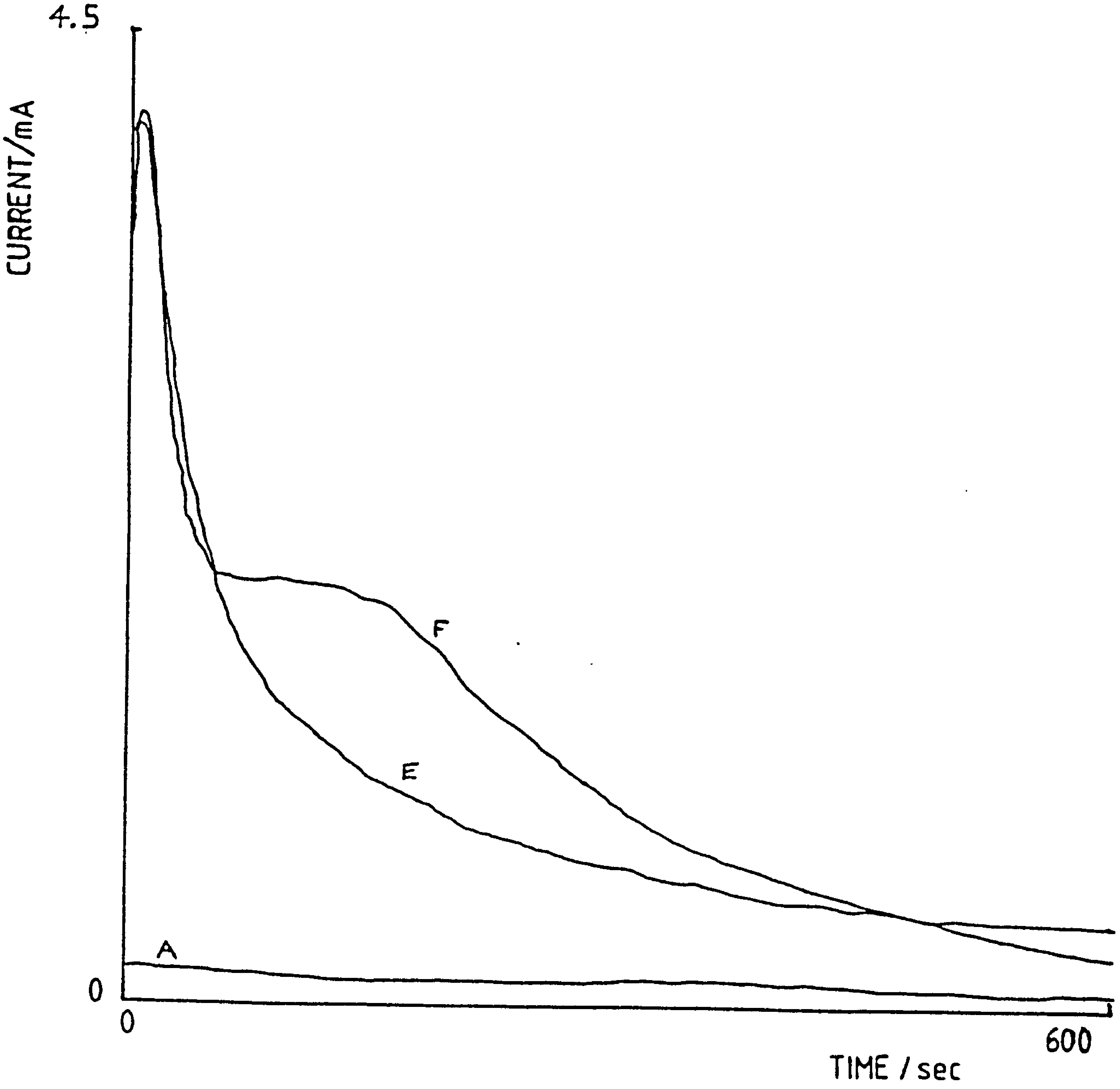

the β-PbO_2 contributes more to the electrochemical capacity of the positive battery plate. Consequently, the higher the Sb content, the less β-PbO_2 is formed on galvanostatic oxidation and hence a lower peak current output is obtained. The pure Pb electrode A gives an appreciable amount of β-PbO_2, intermediate in quantity between the contents of C and D. This results in an i_{max} which lies between the values obtained with C and D. It may be that the particular i_{max} value obtained for pure Pb is a result of enhanced acid availability at the reaction site due in some way to the greater resistance to oxidative corrosion of pure Pb vis a vis antimonial lead. In Fig. 10.1 only the D electrode shows signs of another reaction occurring which is represented by the initial dip before the peak.

The electrodes were then stepped back into the lead dioxide region (1240 mV) from the fully reduced state. Fig. 10.2 displays the current-time responses as the electrodes were subjected to this oxidation. The initial double layer charging spike is followed by an increase in the current due to the formation and growth of nucleation centres. The following decrease in the current flow is the result of subsequent overlap of these growth centres. However, the peaks are followed by constant current outputs over a fairly long time period, especially with the electrodes B and C. This indicates that the current flow is partly due to oxygen evolution since the lead dioxide and oxygen regions overlap. The D electrode accepts less charge than the other two pasted antimonial-lead electrodes. This result is interesting in view of that obtained by Kelly et al [103] and it should be noted that the potential step used here was different, in our case, 700-1240 mV and the paste employed had a density of 4.2 gcm^{-3}. Kelly et al used a paste which contained 100% grey oxide and its density was 4.1 gcm^{-3}.

Fig. 10.3 shows the current-time responses of the porous PbO_2 electrodes on Pb-Sn-Ca bases corresponding to a potentiostatic reduction pulse of the same magnitude as with the Pb-Sb based electrodes. E has the highest i_{max}

value compared with the other five positives, however, Table 10.1 shows that the discharge capacity of E is less than that obtained with A, B and D. Fig. 10.4 shows the current-time responses for the porous PbO_2 electrodes on Pb-Sn-Ca bases after each one was oxidised potentiostatically by stepping from 700 mV to 1240 mV. It seems unusual that electrode F accepts more charge (700 → 1240 mV) than the other electrodes since it discharges the least (1240 → 700 mV). Also the resultant curve obtained for F suggests that another layer of PbO_2 has been formed.

All the pasted alloy electrodes investigated exhibited a very slow (i.e. low current) charge acceptance as can be seen from Table 10.1 which shows oxidation current still flowing after 4h. Kelly et al [103] considered that this effect was due to the reluctance of certain crystals of lead sulphate ("passive" $PbSO_4$) to oxidise to lead dioxide. The electrode is never fully charged potentiostatting at 1240 mV and thus a higher potential is required to fully form PbO_2. Hence before each experiment the electrode was galvanostatically oxidised [103] to ensure that it was fully charged. Figs. 10.2 and 10.4 show that the magnitude of the peak currents for the Pb-Sn-Ca based electrodes are higher than those for the Pb-Sb positives. Also, Table 10.1 shows there is an imbalance between reductive and oxidative charge with all the electrodes. This imbalance remaining after 4h reoxidation was investigated in the cases of C and E, which were of special interest to CTL, using scanning electron microscopy (SEM) and X-ray diffraction (see Chapter 11). It was found that there was clear unambigious evidence for $PbSO_4$ crystals remaining amongst the PbO_2. These crystals are the inactive $PbSO_4$, as mentioned earlier. The absence of such crystals on the completion of the galvanostatic oxidation was confirmed immediately before the reduction by direct examination of the electrodes by SEM. Morphological examination of the electrodes C and E after potentiostatically oxidising for 4h at 1240 mV showed that the

FIG.10.5. ln i vs. $t^{0.5}$ for falling part in FIG.10.1. for uncycled pasted alloy C 'positive'.

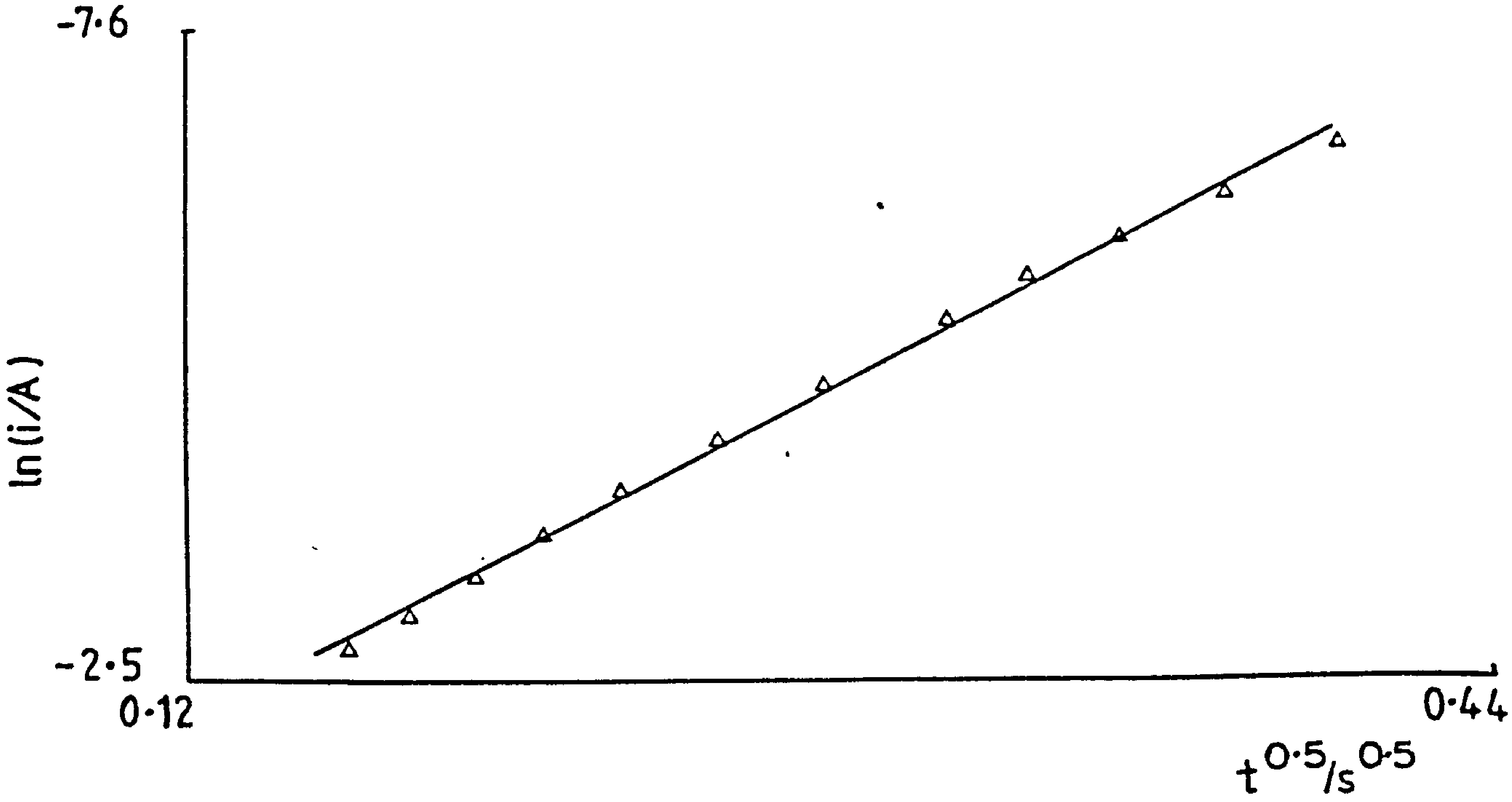

FIG.10.6. As above, but in FIG.10.3. for uncycled pasted alloy E 'positive'.

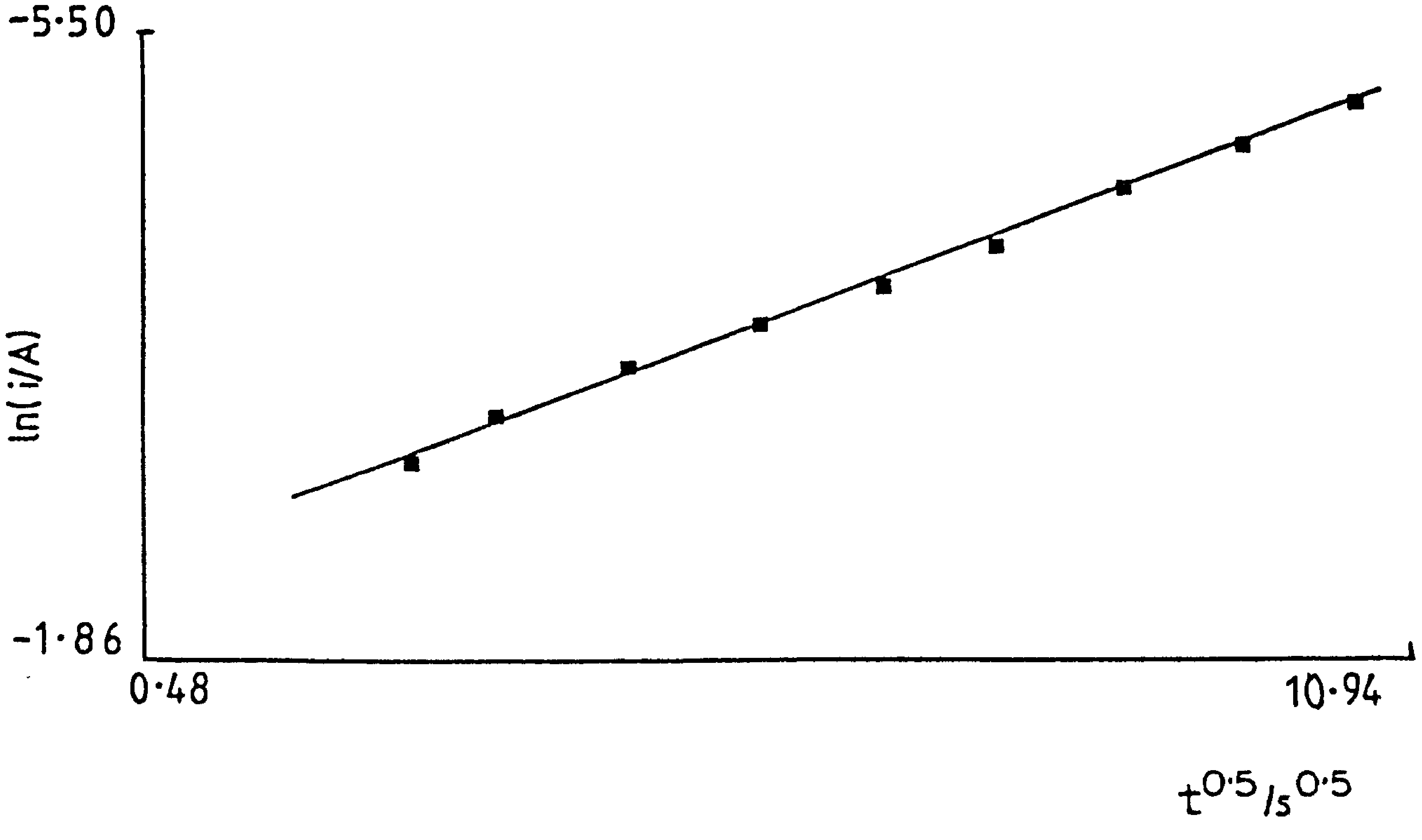

Pb-Sn-Ca electrode contained a high proportion of β-PbO_2 whereas the Pb-Sb positive contained a high proportion of α-PbO_2. It seems that the better charge acceptance of the Pb-Sn-Ca electrode is a result of the higher proportion of the β-polymorph in the final electrode state, however, this is not conclusive.

A number of established current-time relationships for electrocrystallisation processes [105] were used to match the falling parts of the transients in Figs. 10.1-10.4. Using the Least Squares Fit method, via the on-line computer, a variety of straight line plots were obtained and the 'best' straight line identified by the correlation coefficient. From the data of Figs. 10.1 and 10.3 it was found that all the electrodes followed a ln i vs. $t^{\frac{1}{2}}$ relationship as typified in Figs. 10.5 and 10.6 for electrodes C and E respectively.

10.3.2 Cycled Electrodes

10.3.2.1 Electrodes subjected to 20 preparatory cycles

Before potentiostatic stepping experiments the porous electrodes were subjected to a series of cycles using (digital) linear sweep voltammetry. Freshly prepared electrodes were cycled for 20 cycles of discharge and charge from 1240 to 700 mV at 10 mVs^{-1} and back again, the step experiment is therefore to be performed on a pre-conditioned electrode containing an "equilibrium" amount of $PbSO_4$ arising from the out-of-balance of the extents of the oxidation/reduction processes under these conditions. (Before a pulse was performed, care was taken to ensure that the electrode was in a steady state at 1240 mV, that is, the current output was low (1 μA) and constant). After cycling a potentiostatic reduction pulse (1240 → 700 mV) was then performed. Figs. 10.7 and 10.8 show the current-time responses

FIG.10.7. Current-time transients for potentiostatic pulse experiments(1240–700mV) on cycled (20 cycles) porous Pb and Pb-Sb electrodes.

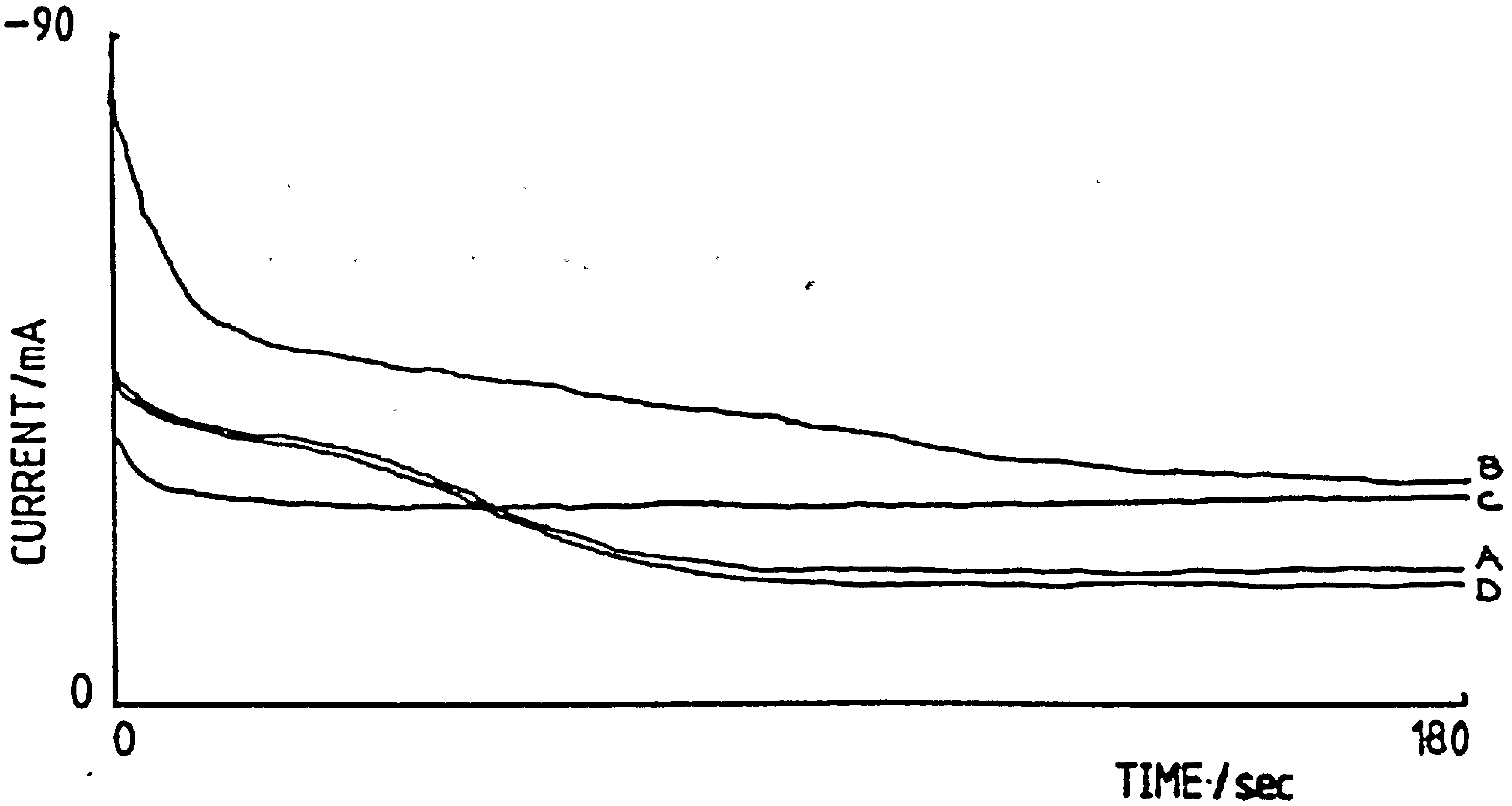

FIG.10.8. As above, but for porous Pb and Pb-Sn-Ca electrodes.

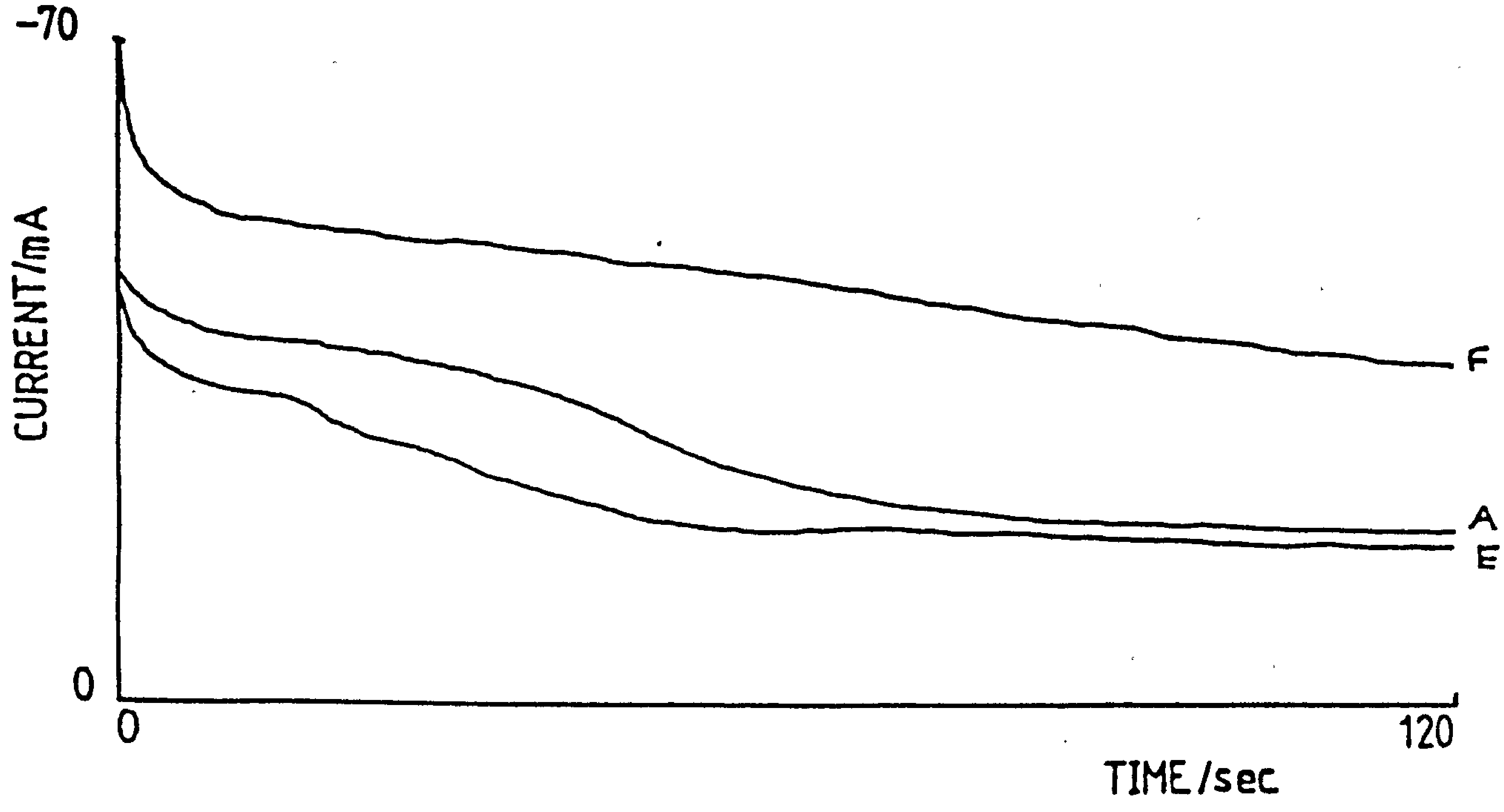

for the porous electrodes corresponding to the potentiostatic reduction. The peak current output decreases as a consequence of the cycling process. Table 10.2 shows that the discharge capacities of the electrodes, as well as the times taken, are lower compared with those values corresponding to the uncycled electrodes. The decrease in the discharge capacity with cycling is apparently due to the production of inactive lead sulphate [103] during the preparatory linear sweep voltammetry since no Pb material was observed to leave the electrode. The conclusion is that on the anodic sweep of the cycle relatively inactive lead sulphate crystals remain unoxidised reducing the amount of PbO_2 available for subsequent reduction in the potentiostatic reaction.

With continued redox cycling the capacities of all the electrodes, judged by the peak current output, on reduction were reduced. In Figs. 10.7 and 10.8 the curvature of the transients are somewhat reduced probably because some 'passivated' lead sulphate has already been formed during cycling, so that less PbO_2 is present before the potentiostatic reduction pulse to $PbSO_4$.

Figs. 10.9 and 10.10 show the current-time responses of the porous electrodes after 20 cycles of linear sweep voltammetry and stepping from the lead sulphate region to the lead dioxide region after fully discharging. The peak current output has increased compared with the uncycled pasted electrodes although the charge acceptance after 4 hours is less. (See Tables 10.1 and 10.2). As can be seen the alloy D electrode (with the highest antimony content) has the highest peak current output compared with other pasted Pb-Sb electrodes. With the alloy B electrode more than one process is occurring as a consequence of the potential step to PbO_2 (1240 mV), hence possibly a more porous form of PbO_2 structure is being produced. Fig. 10.10 shows that alloy F electrode has a higher peak current output than the alloy E electrode. However, Table 10.2 highlights the fact that electrode E accepts more charge than the other electrodes. It is less

FIG.10.9. Current-time transients for potentiostatic pulse experiments (700–1240mV) on cycled (20 cycles) porous Pb and Pb-Sb electrodes, following a full discharge.

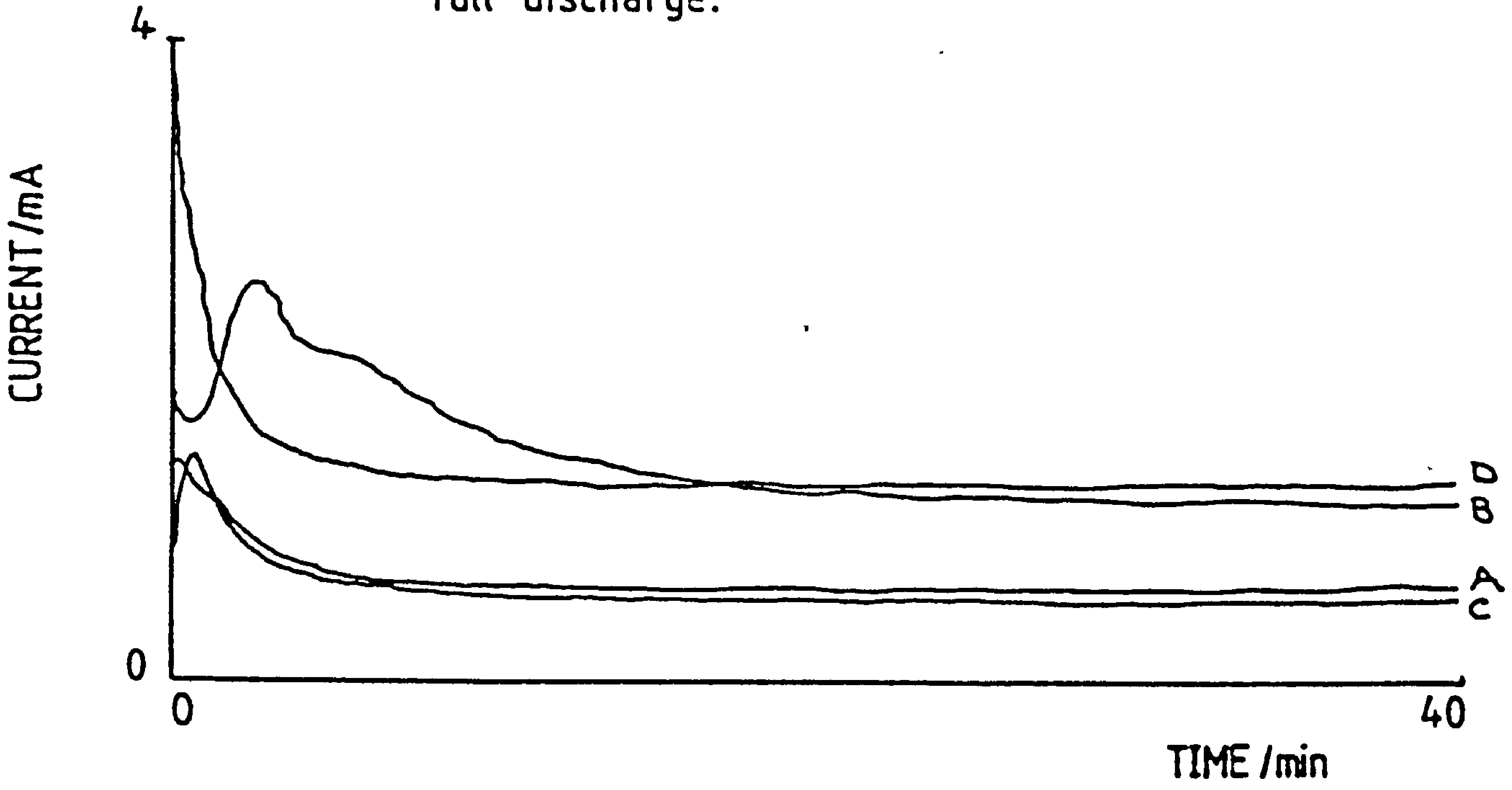

FIG.10.10. As above, but for porous Pb and Pb-Sn-Ca electrodes following a full discharge.

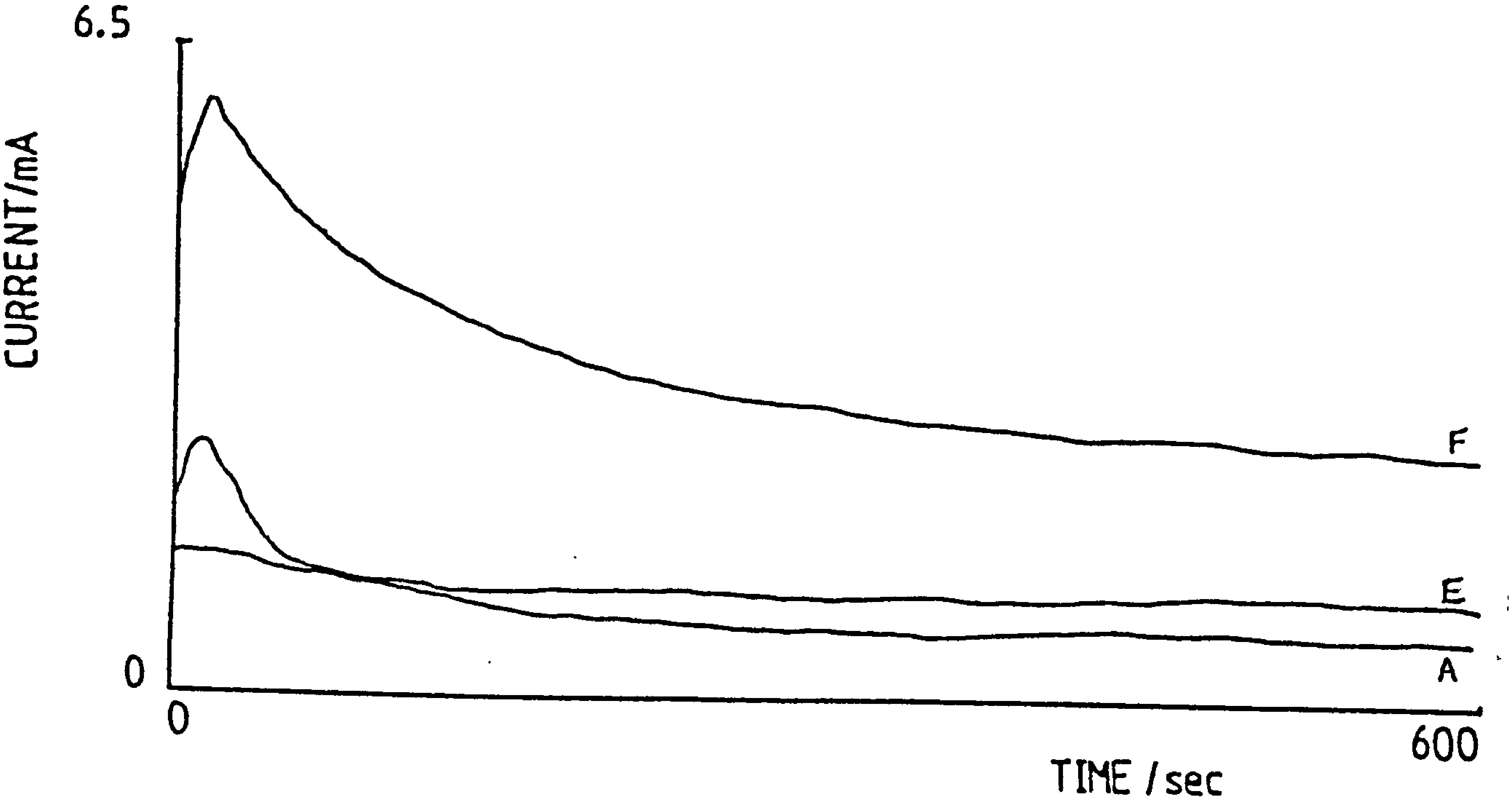

FIG.10.11. i vs. $t^{-0.5}$ for falling part in FIG.10.7. for cycled (20 cycles) porous alloy C electrode.

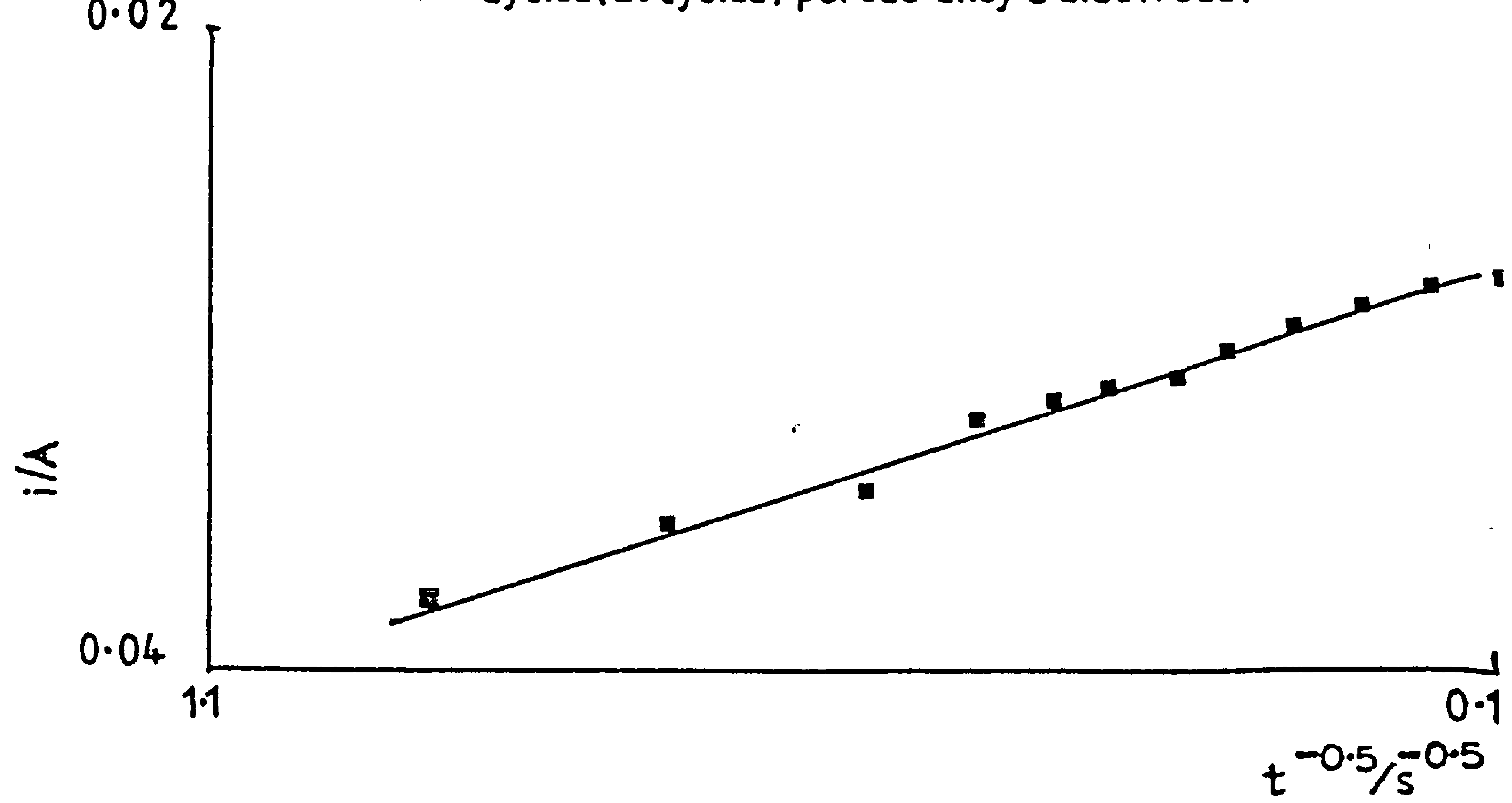

FIG.10.12. ln i vs. $t^{0.5}$ for falling part in FIG.10.8. for cycled (20 cycles) porous alloy E electrode.

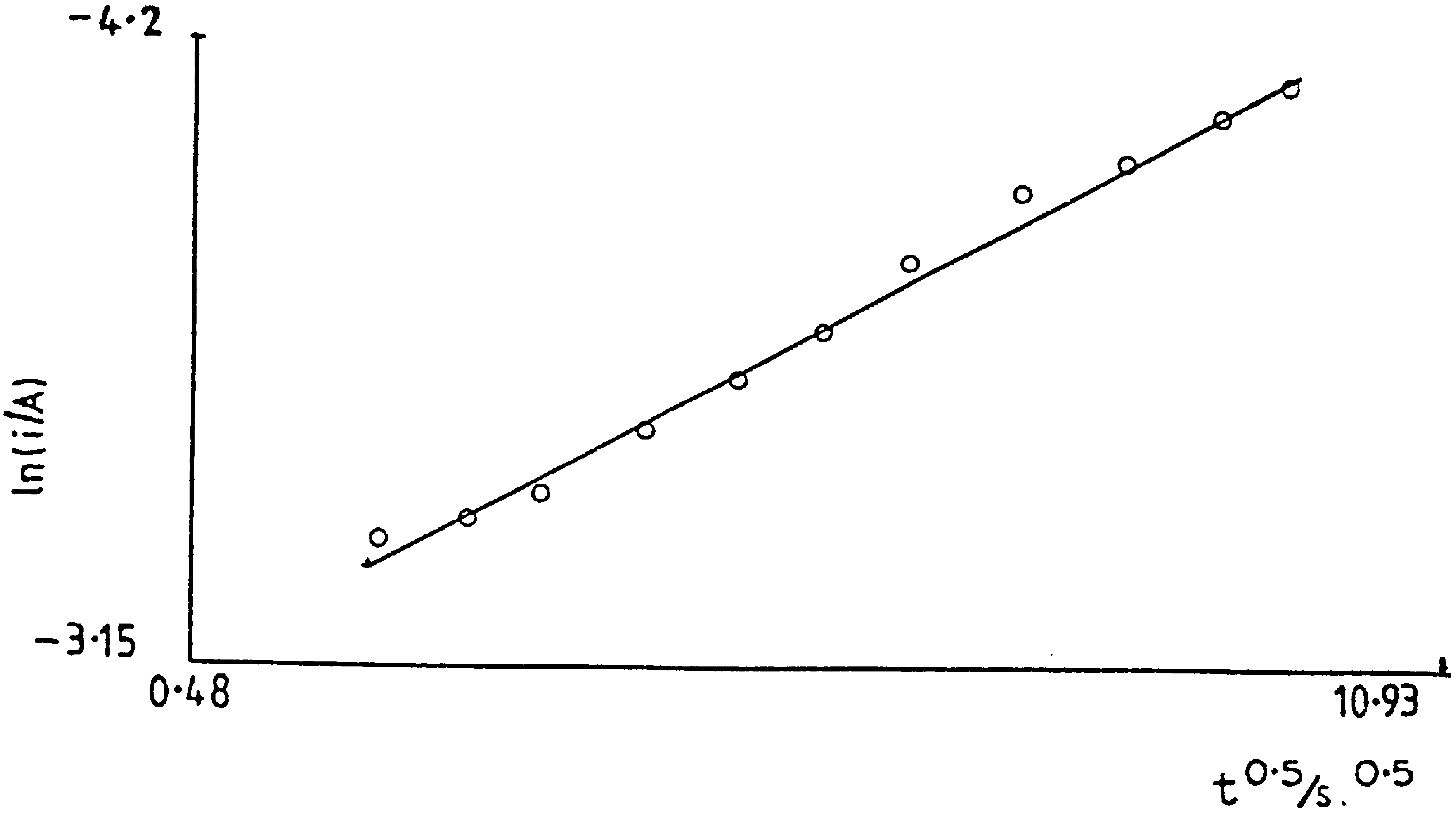

TABLE 10.1

Capacities for the porous electrodes subjected to potentiostatic reduction followed by oxidation.

Alloys	Discharge capacity /C	Time to reach full discharge capacity /min	Recharge capacity after 4 hours /C
A	11.54	150	0.97
B	8.52	180	1.21
C	7.55	145	0.78
D	10.50	210	0.66
E	7.87	150	1.12
F	4.53	85	1.67

TABLE 10.2

As Table 10.1 but for cycled (20 cycles) porous electrodes.

Alloys	Discharge Capacity/C	Time to reach full discharge capacity/min	Recharge capacity after 4 hours/C
A	3.52	40	0.24
B	2.88	30	0.43
C	2.30	5	0.61
D	2.46	15	0.33
E	2.96	10	0.72
F	0.77	30	0.25

than the corresponding value obtained in the uncycled condition. Also, the intermediate Sb content electrode (C) accepts more charge than the other two Pb-Sb positives. As yet no reason can be found to explain these results: a synergistic explanation is a possibility.

Again, using the Least Squares Fit method, for the falling parts of the transients in Figs. 10.7, 10.8, 10.9 and 10.10 the porous electrodes, except alloy C, after a reductive pulse (1240 → 700 mV), follow a ln i vs. $t^{\frac{1}{2}}$ relationship, Fig. 10.12 being an example for the electrode E. Electrode C, however, when subjected to a reductive pulse followed a process for which $i \propto t^{-\frac{1}{2}}$, as shown in Fig. 10.11. This agrees with Dawson et al [106] who found that the discharge of β-lead dioxide occurs by two mechanisms; a diffusion controlled outer layer discharge by a dissolution-precipitation mechanism i vs. $t^{-\frac{1}{2}}$. Within the pores of the growing $PbSO_4$ layer diffusion occurs together with an electrocrystallisation reaction of the inner layer of PbO_2, and under certain conditions, a solid state electrocrystallisation process of i vs. t^2 occurs when PbO_2 reduces to PbO and $PbSO_4$.

10.3.2.2 Variation in number of preparatory cycles

A number of experiments were made in order to explain the variation of current output with cycling. Electrodes C and E of considerable industrial importance were used. The electrodes were initially galvanostatically oxidised [103] to ensure that a fully recharged state had been obtained followed by a reductive pulse (1240 → 700 mV). Figs. 10.13 and 10.14 show the results. The peak current output decreases with the number of linear sweep cycles. This is to be expected following the work of Kelly et al [103]. An unusual feature in Fig. 10.13 is that with the alloy C, after 5 cycles, the peak current output is higher than that obtained with the uncycled case. This is probably due to the fact that the initial few

FIG. 10.13. Potentiostatic pulse experiments from 1240mV to 700mV on porous alloy C electrode following a series of cycles.

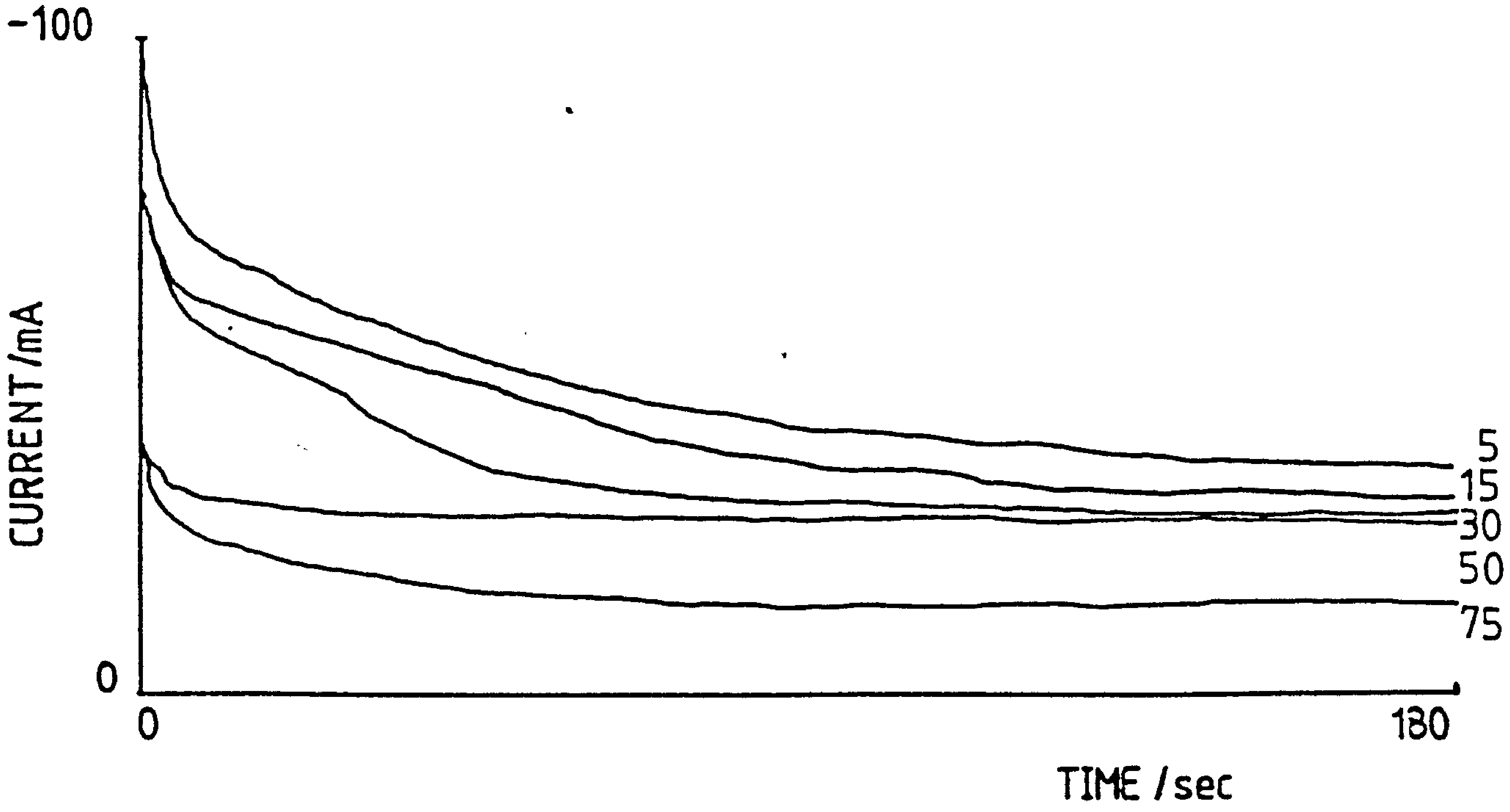

FIG. 10.14. As above, but for porous alloy E electrode following a series of cycles.

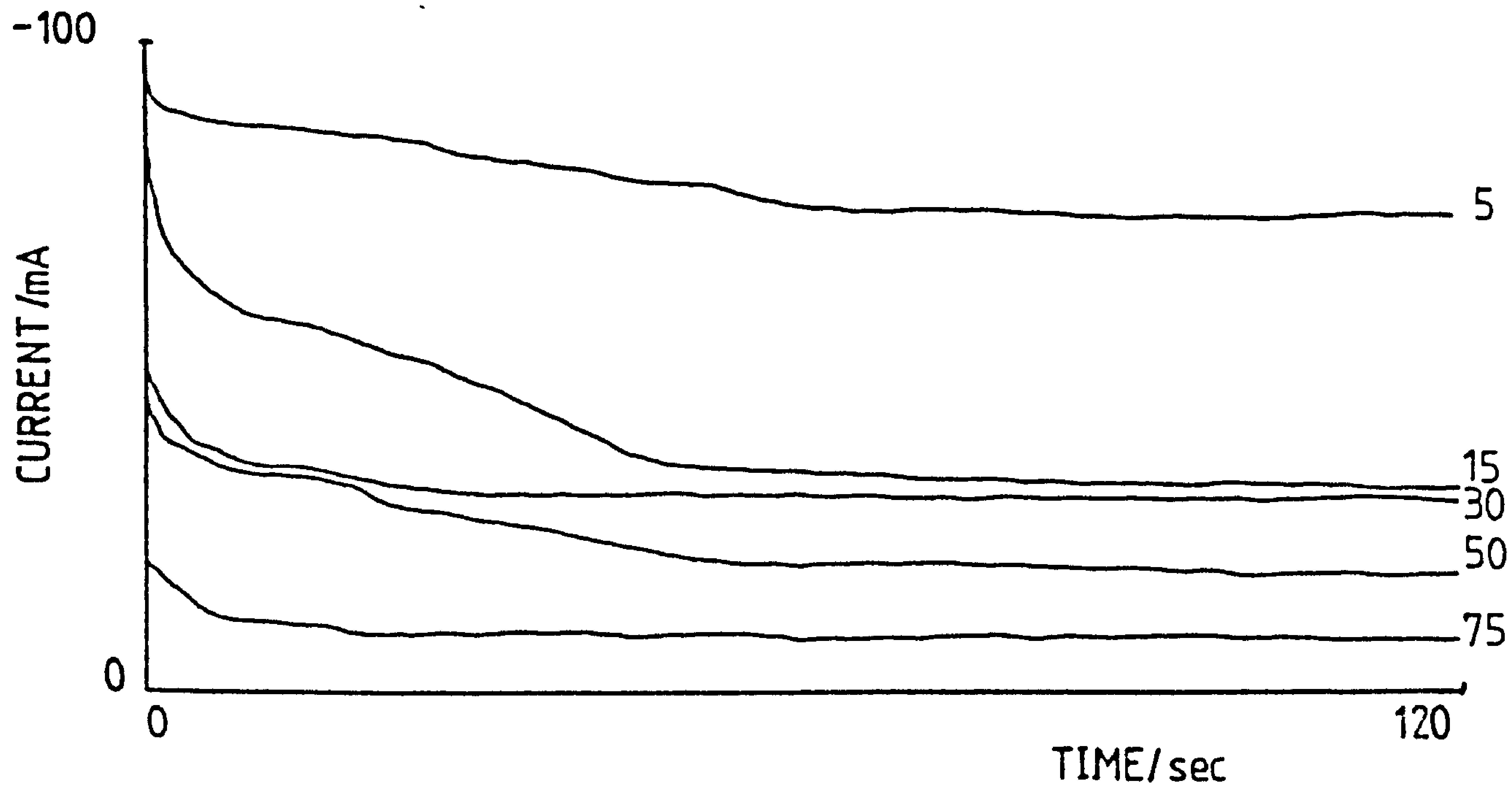

FIG.10.15. Potentiostatic pulse experiments from 700 mV to 1240 mV (details as in FIG.10.13.) following a full discharge.

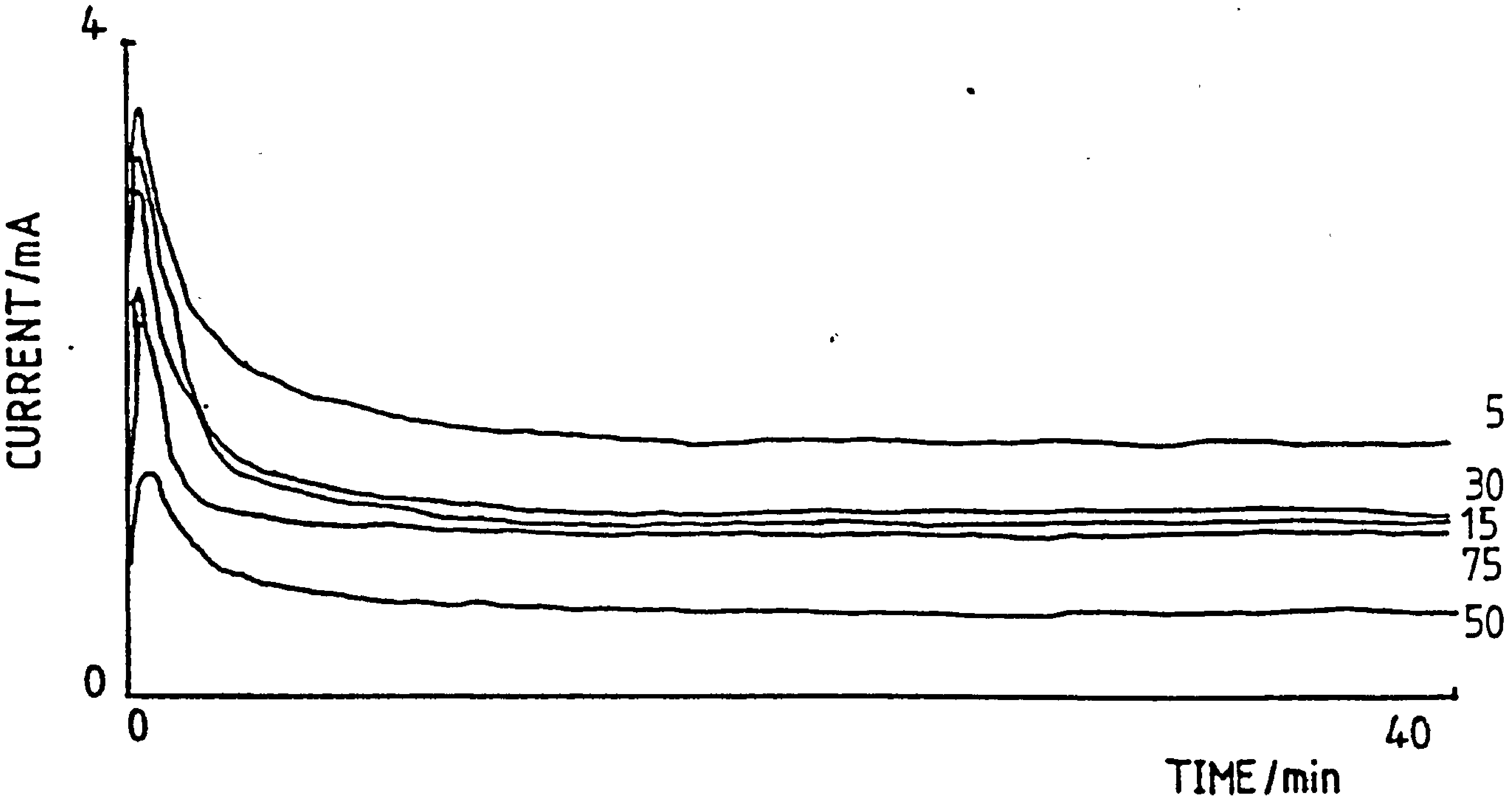

FIG.10.16. As above (details as in FIG.10.14.) after a full discharge.

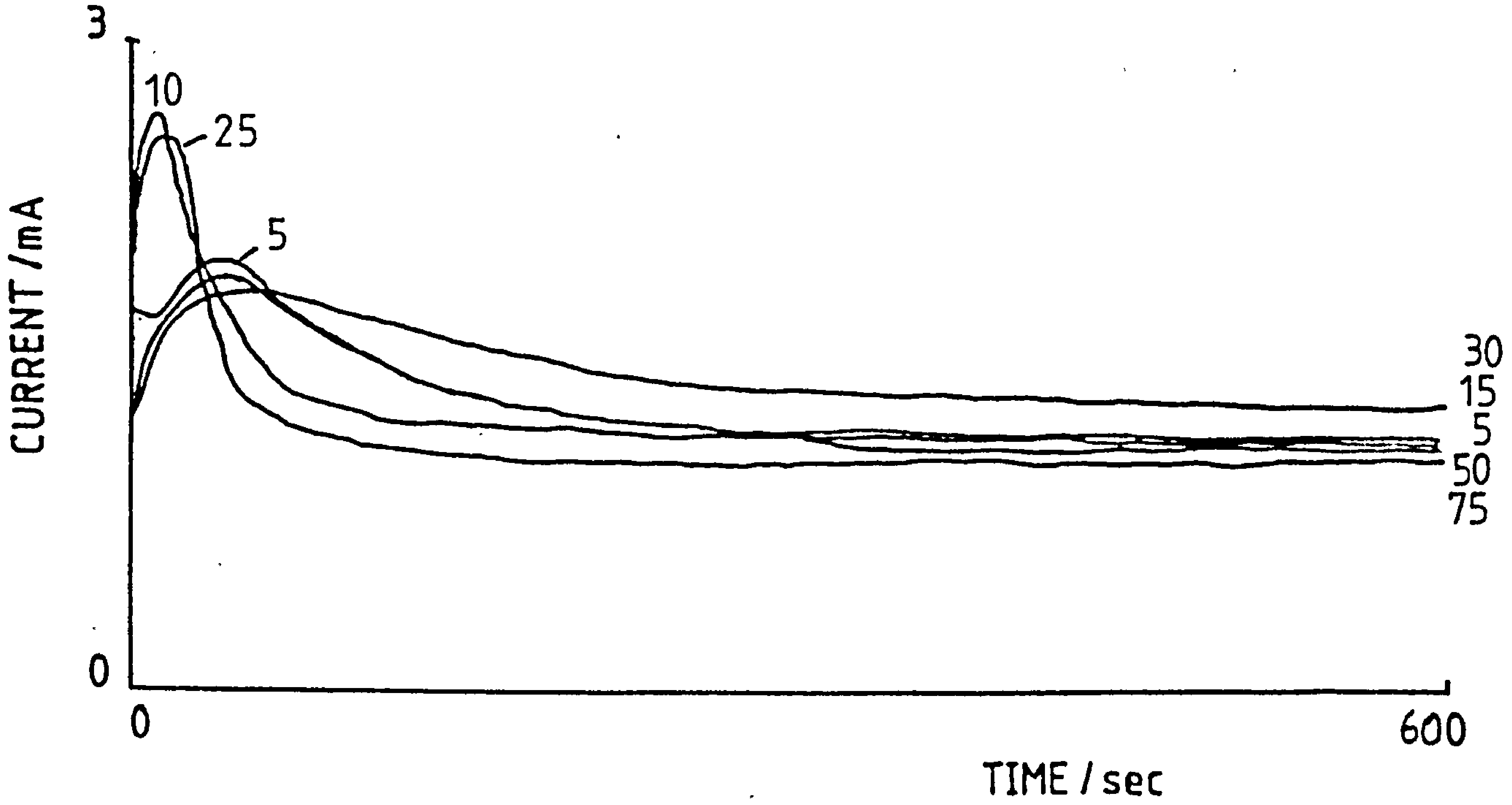

cycles helps to improve the porosity of the PbO_2 matrix. However, with the alloy E although the peak current output, and hence charge, decreases with number of cycles as would be expected the uncycled 'positive' discharges most efficiently. Thus it seems quite significant that for a Pb-Sb electrode, a few preparatory cycles before a potentiostatic reduction pulse can increase the peak current output quite considerably whereas with the Pb-Sn-Ca case, cycling beforehand has no significant effect.

Figs. 10.15 and 10.16 show the current-time responses for alloys C and E electrodes respectively after they had been subjected to a series of cycles, fully discharged by a potentiostatic reduction pulse, as in the case for Figs. 10.13 and 10.14 and finally oxidised back into the PbO_2 region. As can be seen there is no significant difference between the Pb-Sn-Ca positives.

We again used the Least Square Fit method to match the falling parts of the transients in Figs. 10.13-10.16 but none of them followed an established current-time relationship for electrocrystallisation reactions. However, after a potentiostatic oxidation pulse, with both electrodes, all the different preparatory cycle cases gave an i vs. $t^{-\frac{1}{2}}$ relationship. It seems that only after sufficient cycles had been given is the porous matrix transformed into an extensively uniform phase.

10.4 Conclusions

Although the porous nature of the electrode results in a lack of control of the surface (and solution) pre-electrode condition of these experiments certain tentative conclusions can be drawn about the behaviour of these electrodes in these experimental conditions. These conditions are equivalent to high rates of operation (and recharge) of the order of the minute rate. It should be recognised that these conclusions may not apply to other modes of operation.

1. The uncycled pasted Pb-Sn-Ca electrodes discharge at a faster rate than the Pb-Sb electrodes.
2. All the electrodes accept charge very slowly after a complete discharge.
3. Initial cycling for the Pb-Sb positive results in a higher peak current output.
4. As the number of cycles increase, the peak current output of the electrodes, after a reductive pulse, decrease.
5. The imbalance between the charge output and input for the high rate potentiostatic cycling of lead-acid cells clearly indicates the need for periodic galvanostatic conditioning charges.

CHAPTER 11

MORPHOLOGICAL STUDY OF POROUS PbO_2 FORMED IN H_2SO_4 ON Pb-Sb and Pb-Sn-Ca ALLOYS

11.1 Introduction

In Chapter 10 the electrochemical responses of pasted Pb-Sb and Pb-Sn-Ca electrode "positives" in 5 M H_2SO_4 were investigated. Using potentiostatic pulse experiments together with some (digital) linear sweep voltammetry, it was found that the current output from the Pb-Sn-Ca electrodes, after a reductive pulse (from 1240 to 700 mV) was much higher than with pasted pure lead and Pb-Sb electrodes. Also the charge acceptances after a complete discharge for all the electrodes were poor because of the formation of inactive $PbSO_4$ [103].

On potentiostatic reduction, the current output from electrodes which had been subjected to a number of linear sweep cycles before a reductive pulse decreased compared with the uncycled electrodes. In this chapter morphological evidence is presented to support the earlier electrometric investigation (see Chapter 10) and to show a significant difference between the two electrodes when re-stepped back into the PbO_2 region.

11.2 Experimental procedure

The electrical set-up and electrode preparation have been described in previous chapters (see Chapters 5 and 10). The support alloys used were Pb-Sb (1.88%) and Pb-Sn (0.34%)-Ca (0.086%). The electrodes were formed in 0.3 M H_2SO_4 and were subsequently cycled in 5 M H_2SO_4. This relates to common industrial practice.

The porous PbO_2 on the alloy supports were shrouded in Teflon in

Fig. 11.1

Front of pasted Pb-Sb electrode following galvanostatic oxidation ($25\ mAcm^{-2}$) to PbO_2 in 0.3M H_2SO_4.

Magnification x 8500

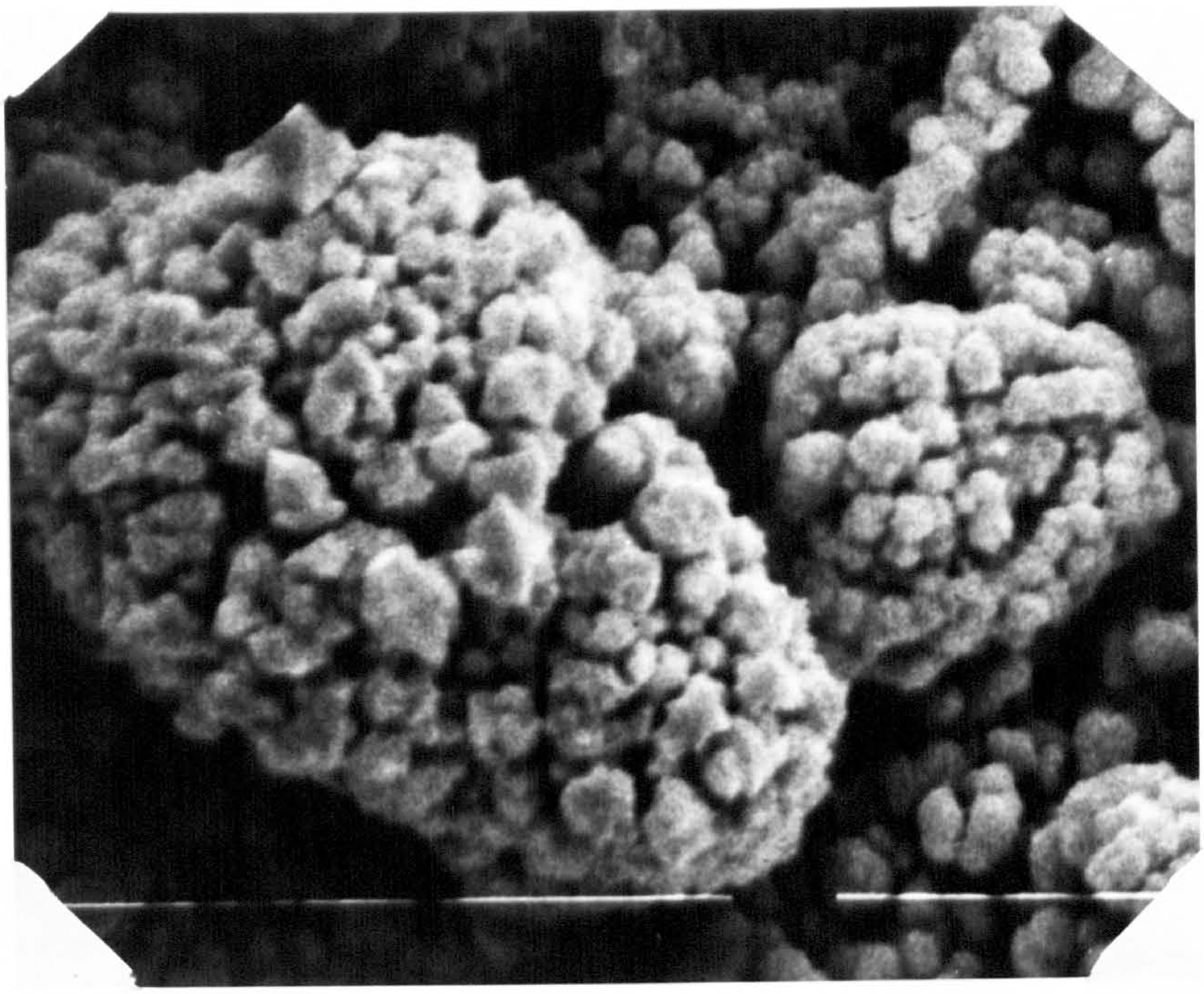

Fig. 11.2

Electrode as in Fig. 11.1, followed by a reductive pulse (from 1240 to 700 mV) in 5M H_2SO_4.

Magnification x 10000

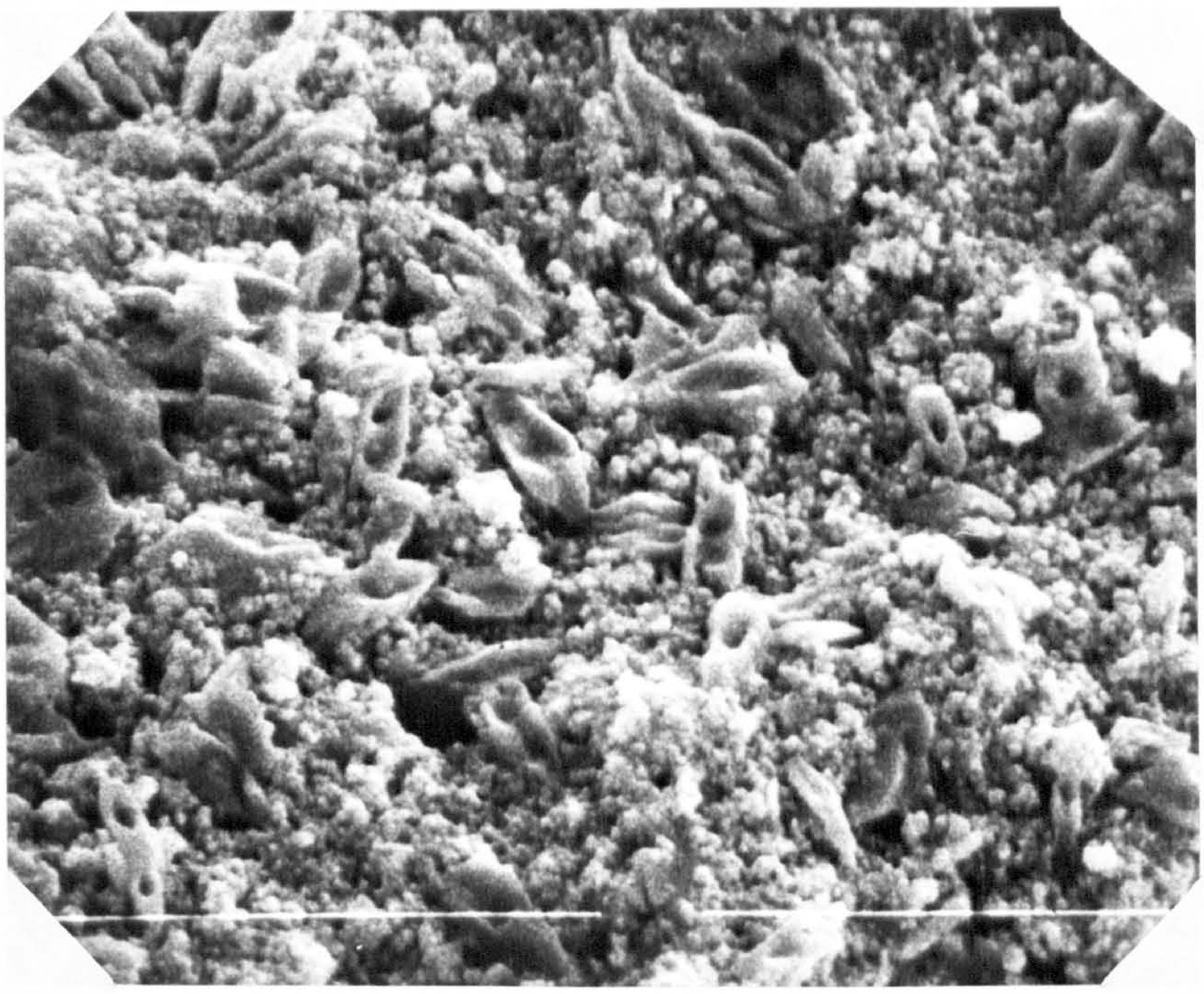

Fig. 11.3

Electrode as in Fig. 11.1, but remaining in the $PbSO_4$ region in 5M H_2SO_4 for 3 min.

Magnification x 10000

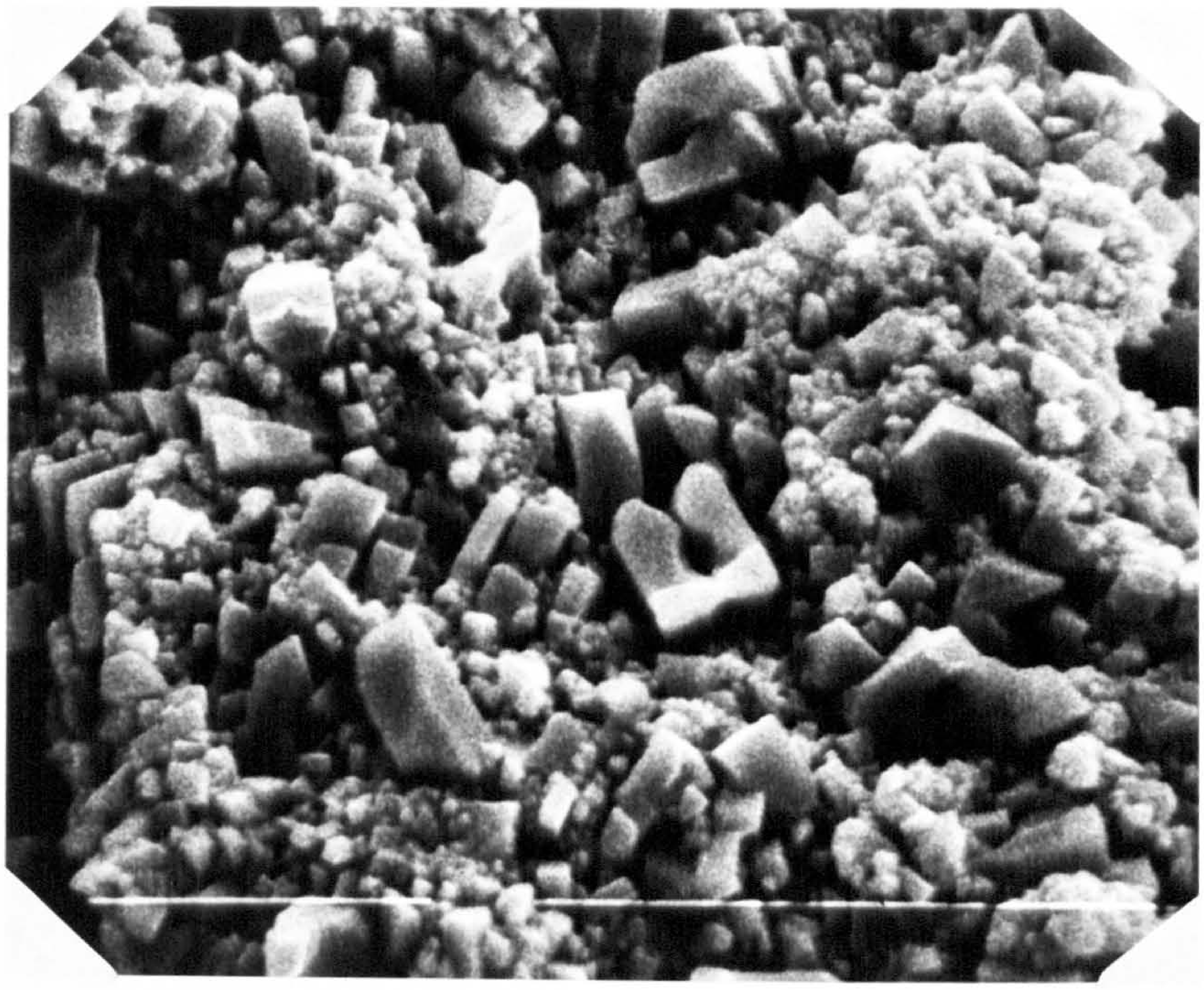

Fig. 11.4

Electrode as in Fig. 11.1, but after it has been fully discharged in 5M H_2SO_4.

Magnification x 8500

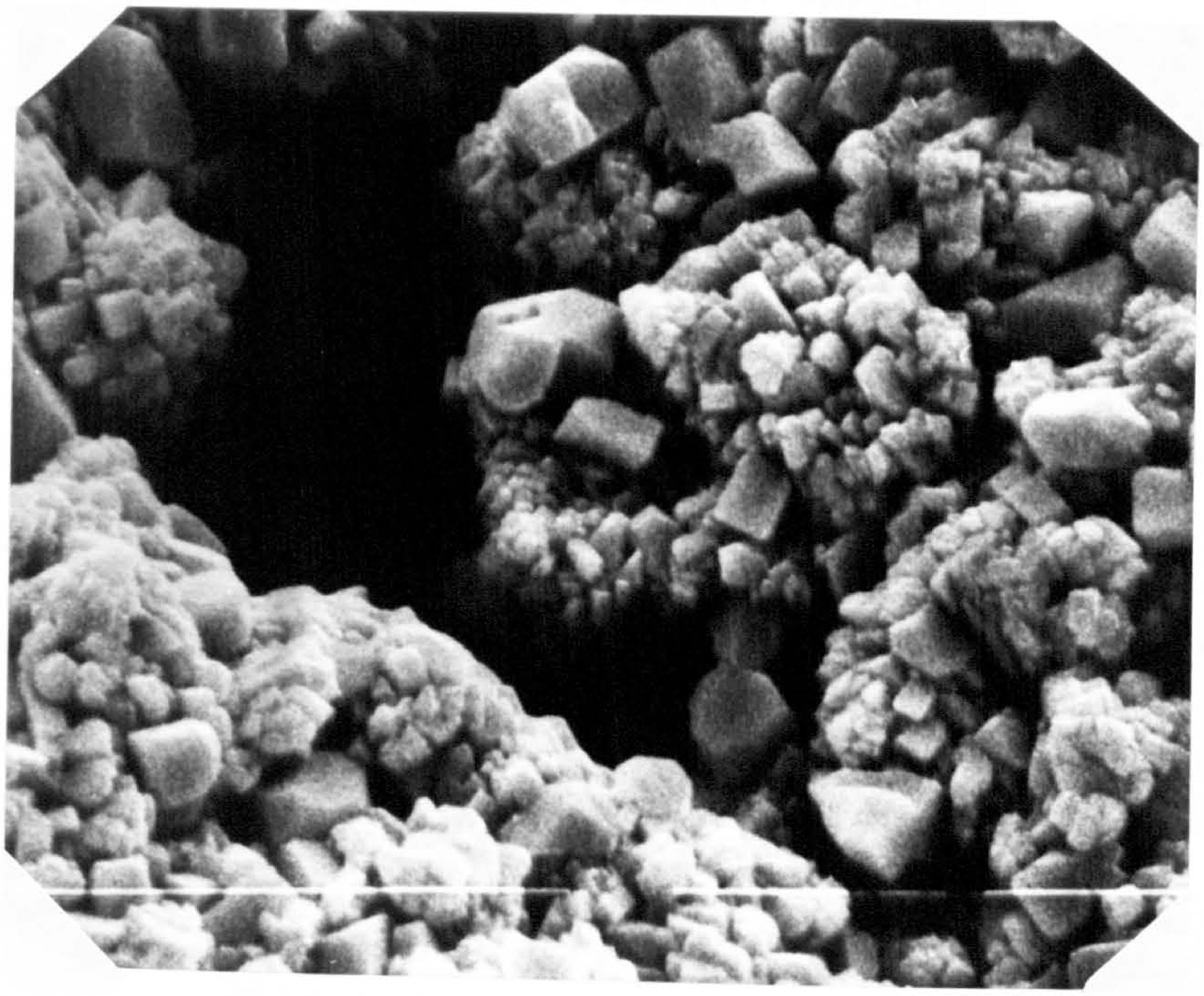

the form of stubs which screwed into the end of the rotating disc electrode. After the various potential step experiments had been performed on the two sets of electrodes, the electrodes were washed with triply distilled water, rinsed with acetone and stored in a vacuum desiccator. For microscopic study the electrodes were coated with a thin layer of gold by diode sputtering and examination was carried out using an ISI Alpha-9 scanning electron microscope.

11.3 Results and Discussion

11.3.1 Pasted Pb-Sb(1.88%) electrode

Fig. 11.1 shows the surface morphology of the front of the porous PbO_2 on the Pb-Sb support after the "leady" oxide paste had been galvanostatically oxidised in 0.3 M H_2SO_4. As can be seen the porous matrix is made up of "spongy" PbO_2 crystals which are of fairly even size and exist in clumps [107]. Fig. 11.2 displays the porous PbO_2 after it has just undergone a potentiostatic reduction pulse (from 1240 mV to 700 mV). (All potentials were referred to a Hg/Hg_2SO_4 electrode in 5 M H_2SO_4). It seems that the PbO_2 crystals have cracked and peeled back but there does not appear to be any $PbSO_4$ crystal formation.

Fig. 11.3 typifies the surface of the porous Pb-Sb electrode after it had been maintained in the $PbSO_4$ region for 3 min. The surface is covered with prismatic $PbSO_4$ crystals of varying sizes together with some residual PbO_2. Hence the surface coverage of $PbSO_4$ causes the front of the electrode to become highly resistive and the current has to come from increasingly much deeper within the porous matrix.

After the electrode has been completely discharged as judged by a zero-current output, the surface of the porous matrix is completely covered with $PbSO_4$ as shown in Fig. 11.4. Fig. 11.5 corresponds to the porous electrode subjected to a complete discharge and then stepped back

Fig. 11.5

Pb-Sb electrode subjected to a complete discharge in 5M H_2SO_4 and then stepped back into the PbO_2 region (1240 mV).

Magnification x 8500

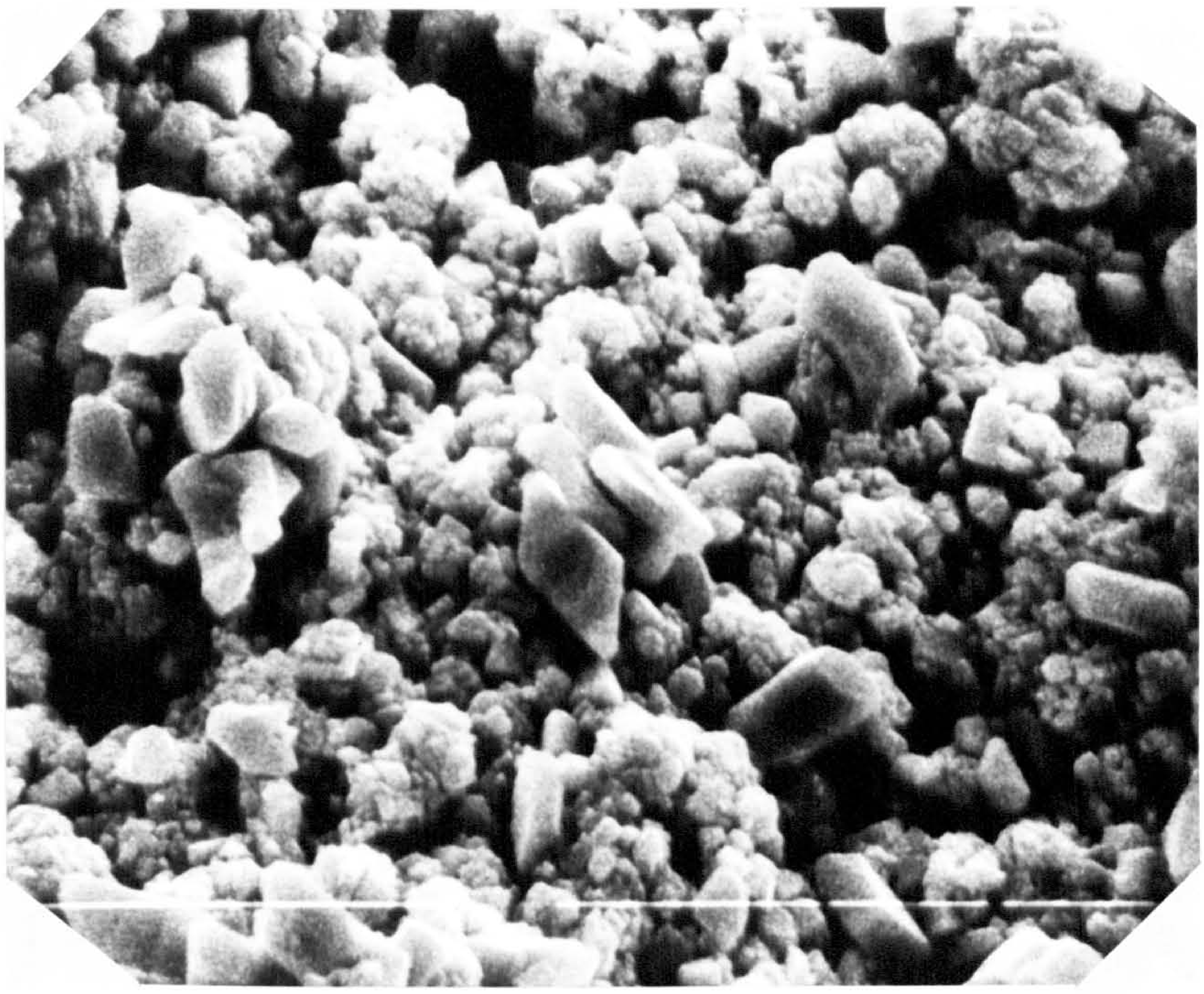

Fig. 11.6

Electrode as in Fig. 11.5, but staying in the PbO_2 region in 5M H_2SO_4 for 4h.

Magnification x 4250

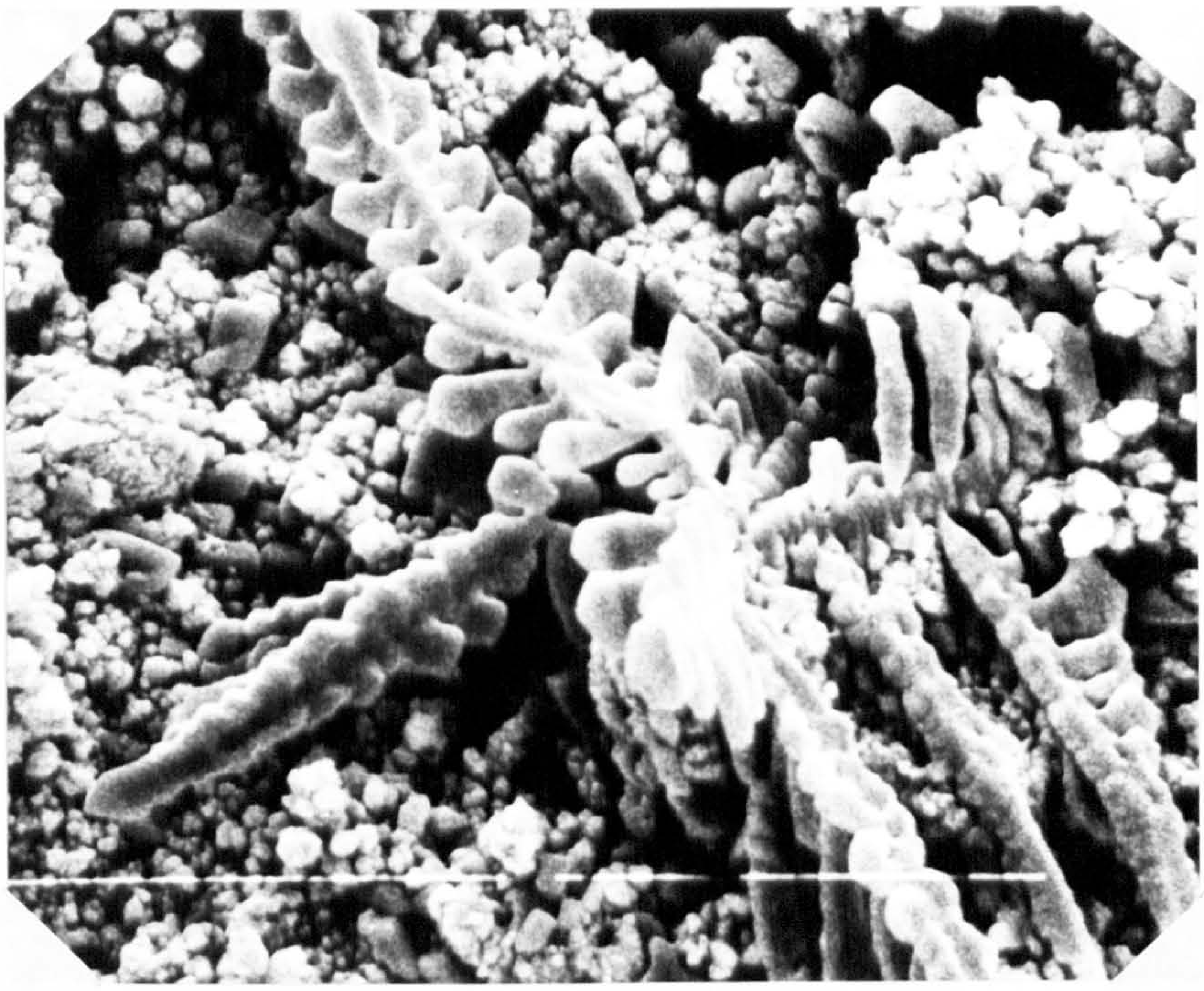

Magnification x 8500

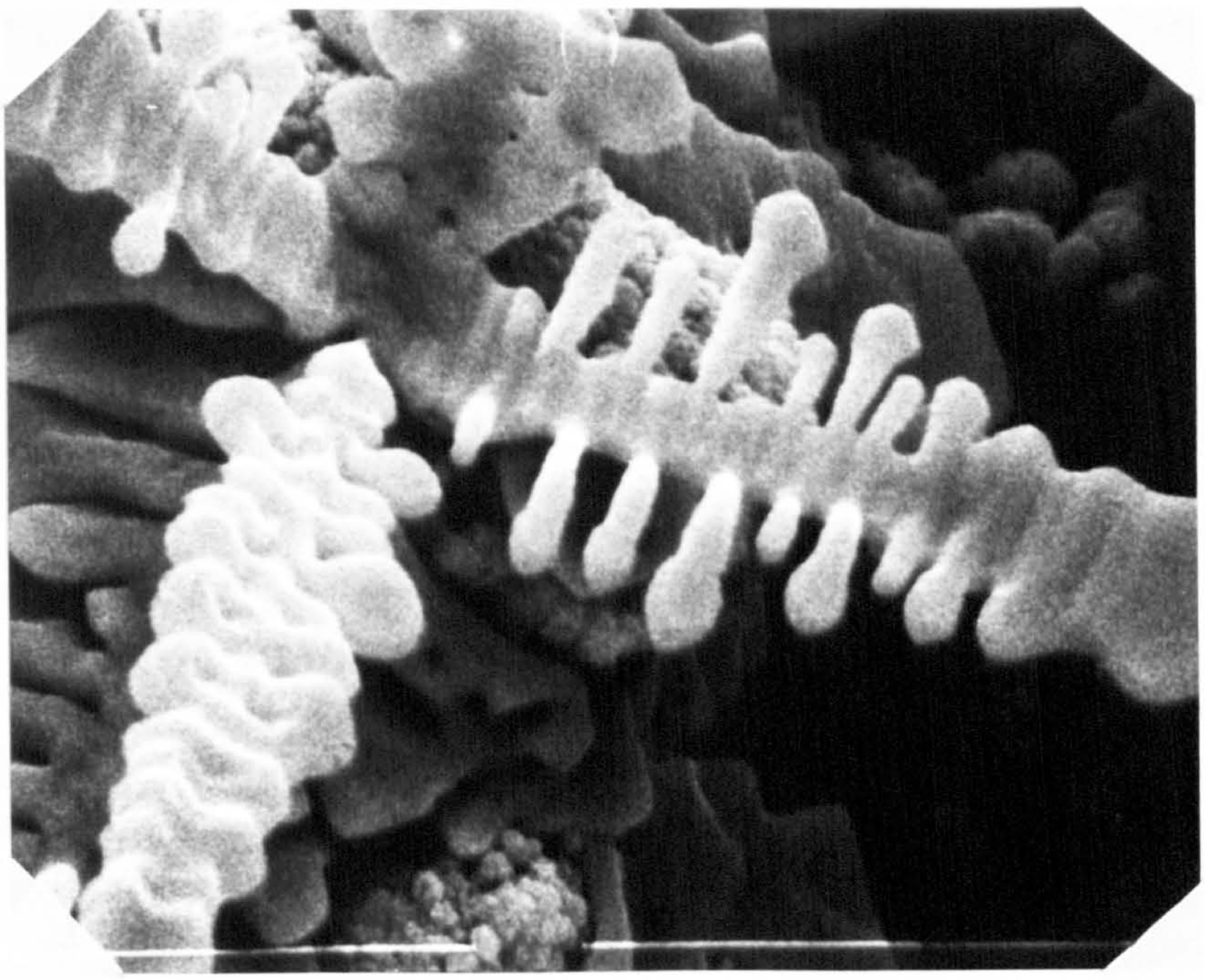

Fig. 11.7

Electrode as in Fig. 11.6, but a different area on the electrode surface.

Magnification x 4250

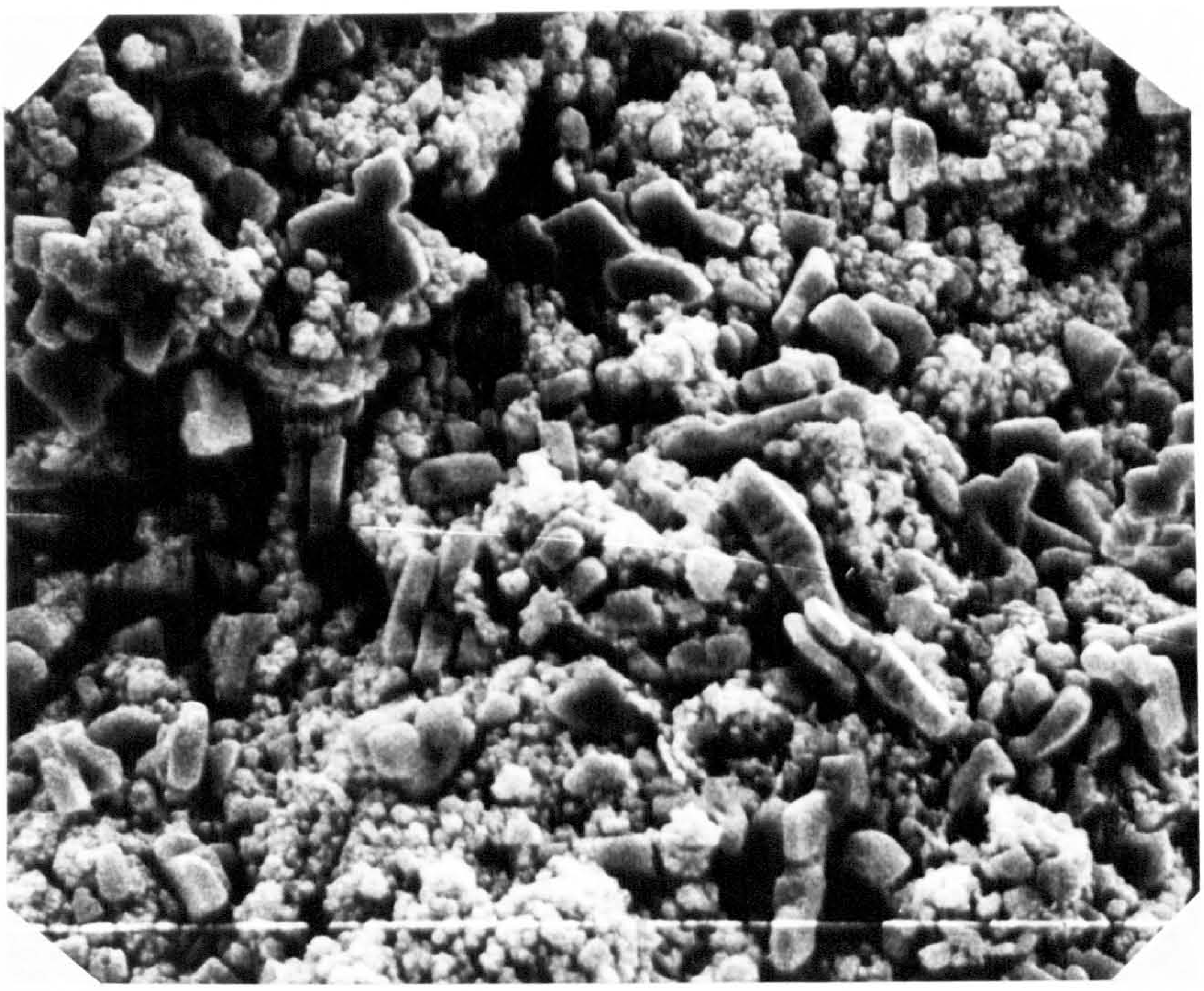

Magnification x 8500

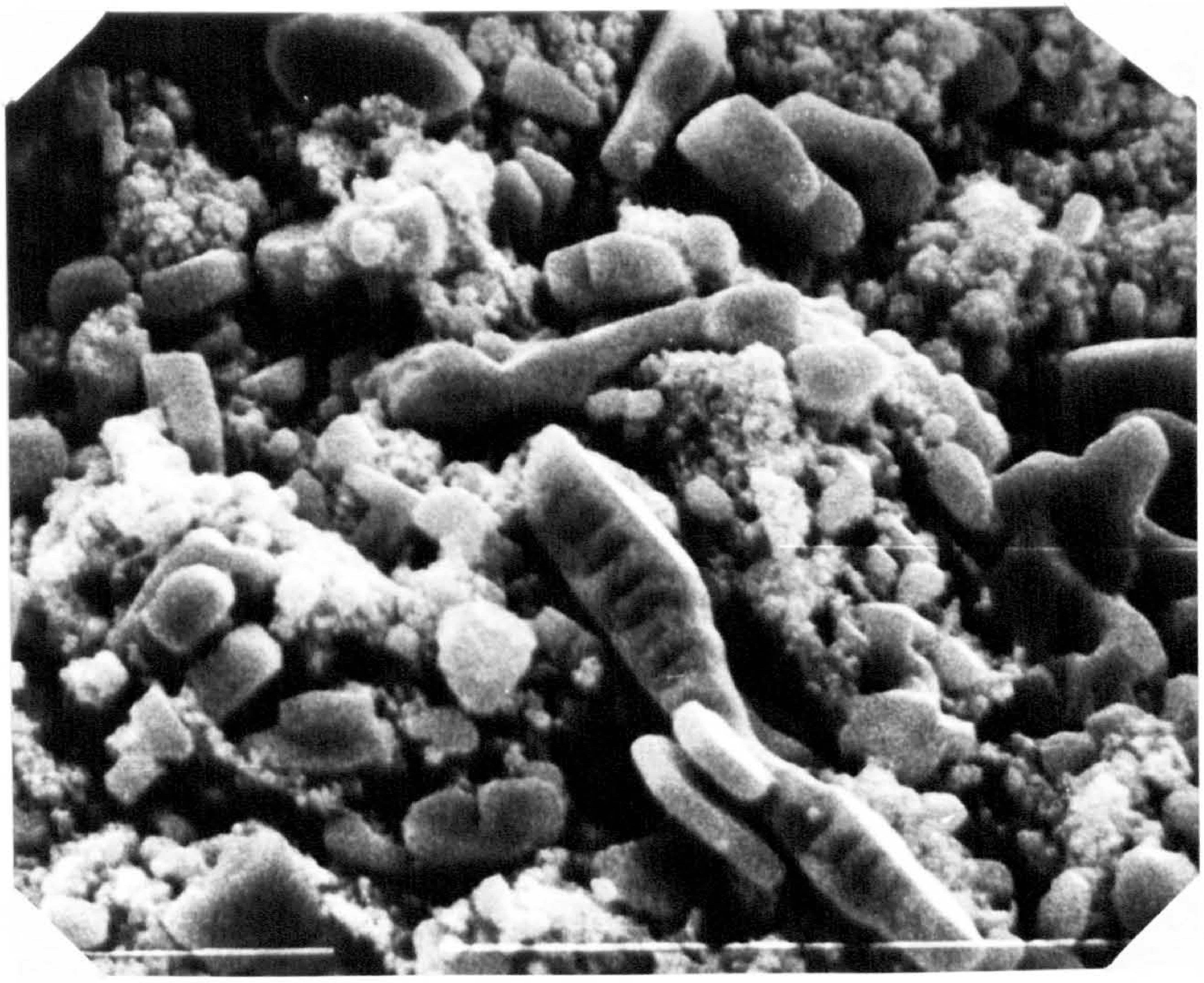

into the PbO_2 region (1240 mV). Although there is a fair amount of $PbSO_4$ present, clearly the formation of PbO_2 between the $PbSO_4$ crystals can be seen. However, after 4h in the PbO_2 region (complete discharge and oxidative pulse followed by 4h at 1240 mV), unusual dendritic growths are observed as typified in Figs. 11.6 and 11.7. In Fig. 11.6, apart from some $PbSO_4$ still remaining and some PbO_2 being reformed as small spongy crystallites, a high degree of PbO_2 grows away from the surface as well-defined dendritic crystals with numerous branches in areas where there is room for growth, i.e. cracks and voids are present in the porous surface. Fig. 11.7 shows an area on the electrode surface where the porous matrix is much more closely packed, hence restricting the growths seen in Fig. 11.6. However, some of the crystals in Fig. 11.7 have the shape which, given the space, would produce the dendritic growth. Similar PbO_2 growths to those shown in Fig. 11.6 have been observed by Acton [108] when he electrodeposited α-PbO_2 onto a pasted plate in NaOH solution.

11.3.2 Pasted Pb-Sn (0.34%)-Ca(0.086%) electrode

Fig. 11.8 corresponds to the fully oxidised surface morphology of the porous PbO_2 on the Pb-Sn-Ca support. The picture is very much the same as in Fig. 11.1 for the porous PbO_2 on a Pb-Sb support. The porous matrix consists of small crystals that congregate into clumps. In Fig. 11.9 immediately after a reductive pulse there does not seem to be any sign that $PbSO_4$ is being formed; however, there appears to be an absence of cracking of the PbO_2 crystallites as is shown in Fig. 11.2 for the Pb-Sb case.

Fig. 11.10 corresponds to the Pb-Sn-Ca electrode after it has remained in the $PbSO_4$ region for 2 min. The $PbSO_4$ crystals are small and few in number which is very surprising considering that the current

Fig. 11.8

Front of pasted Pb-Sn-Ca electrode following galvanostatic oxidation to PbO_2 in 0.3M H_2SO_4 (25 $mAcm^{-2}$).

Magnification x 8500

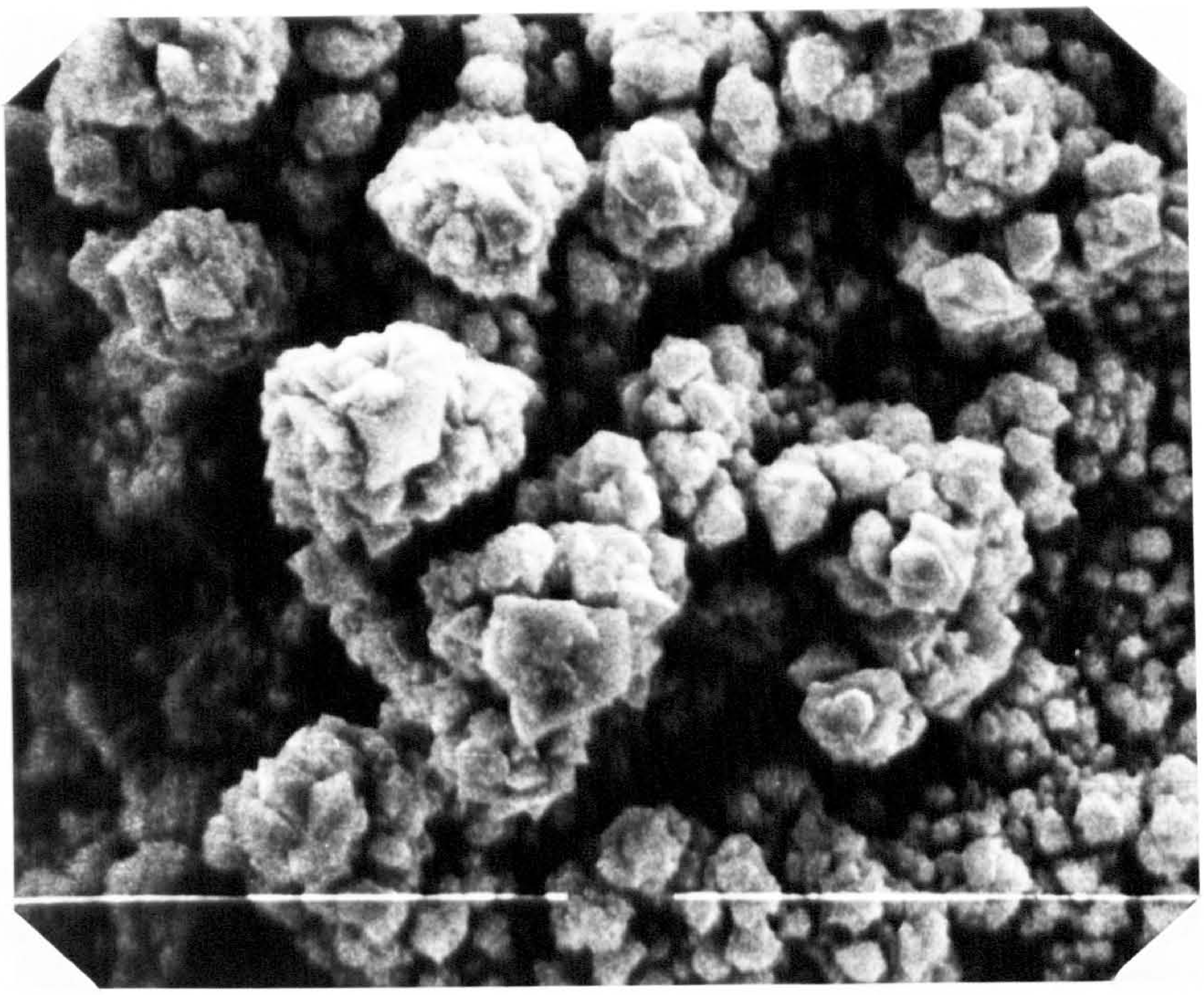

Fig. 11.9

Electrode as in Fig. 11.8, followed by a reductive pulse (from 1240 to 700 mV) in 5M H_2SO_4.

Magnification x 8500

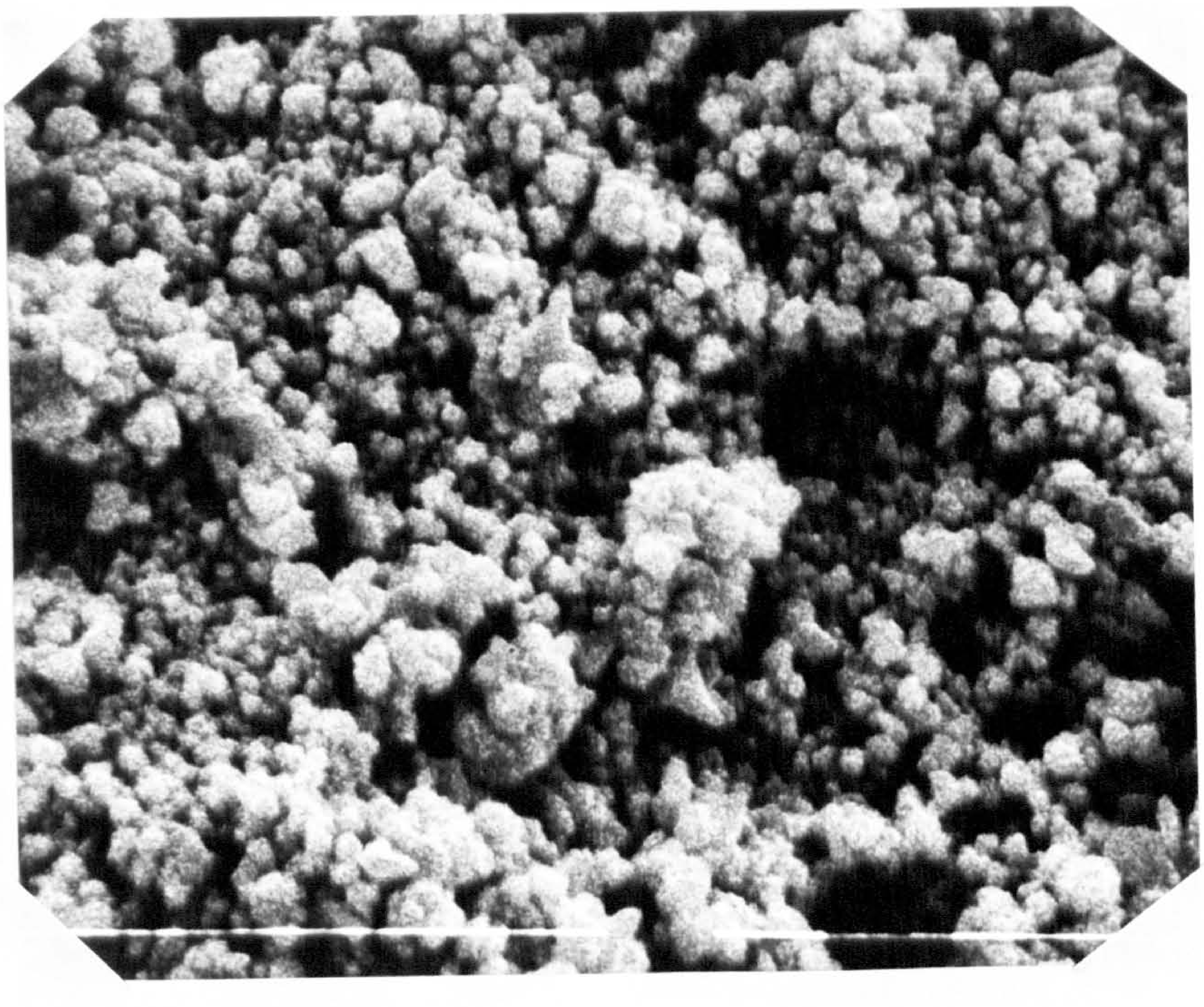

Fig. 11.10

Electrode as in Fig. 11.8, but remaining in the $PbSO_4$ region in 5M H_2SO_4 for 2 min.

Magnification x 8500

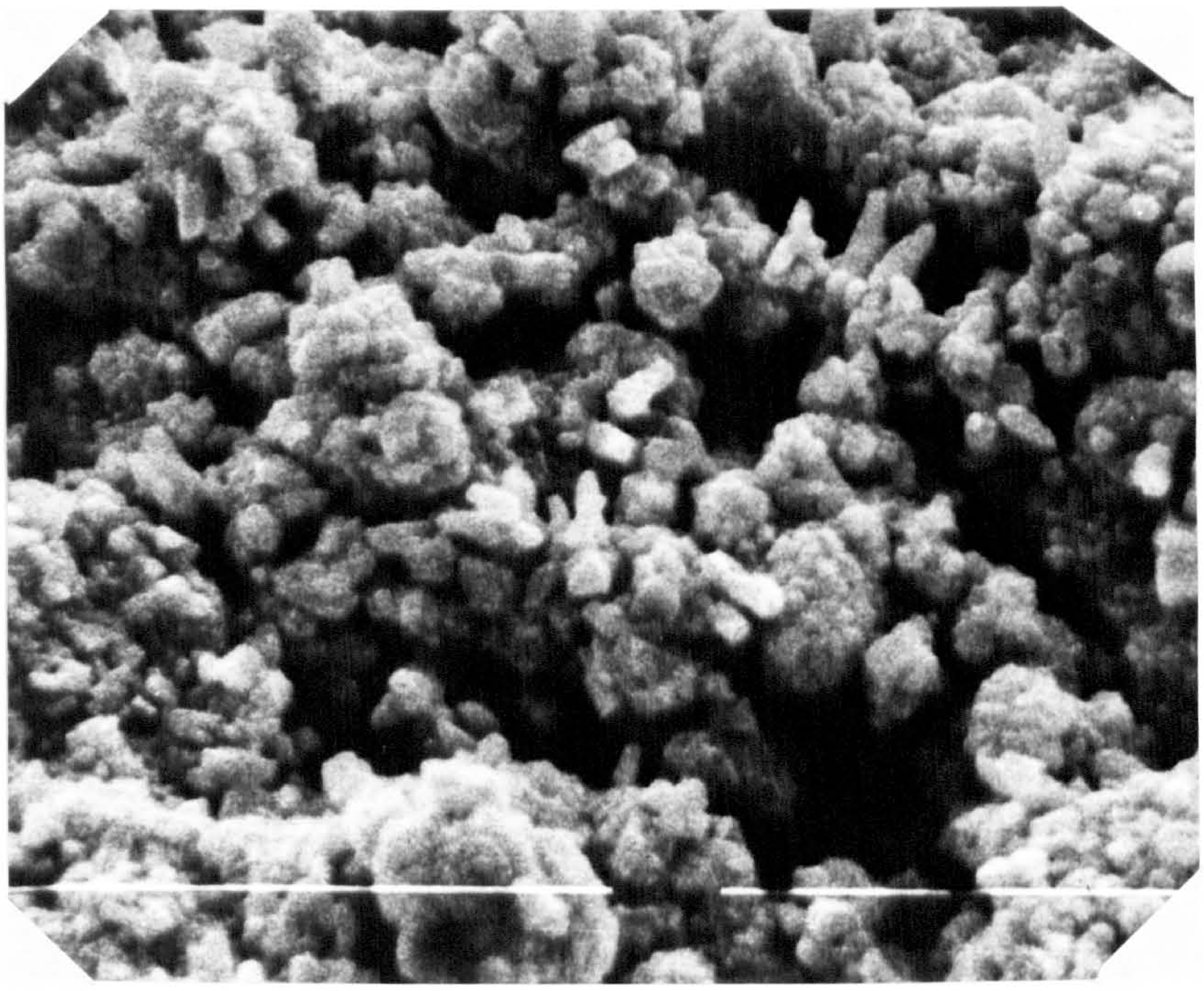

Fig. 11.11

Electrode as in Fig. 11.8, but after it has been fully discharged in 5M H_2SO_4.

Magnification x 8500

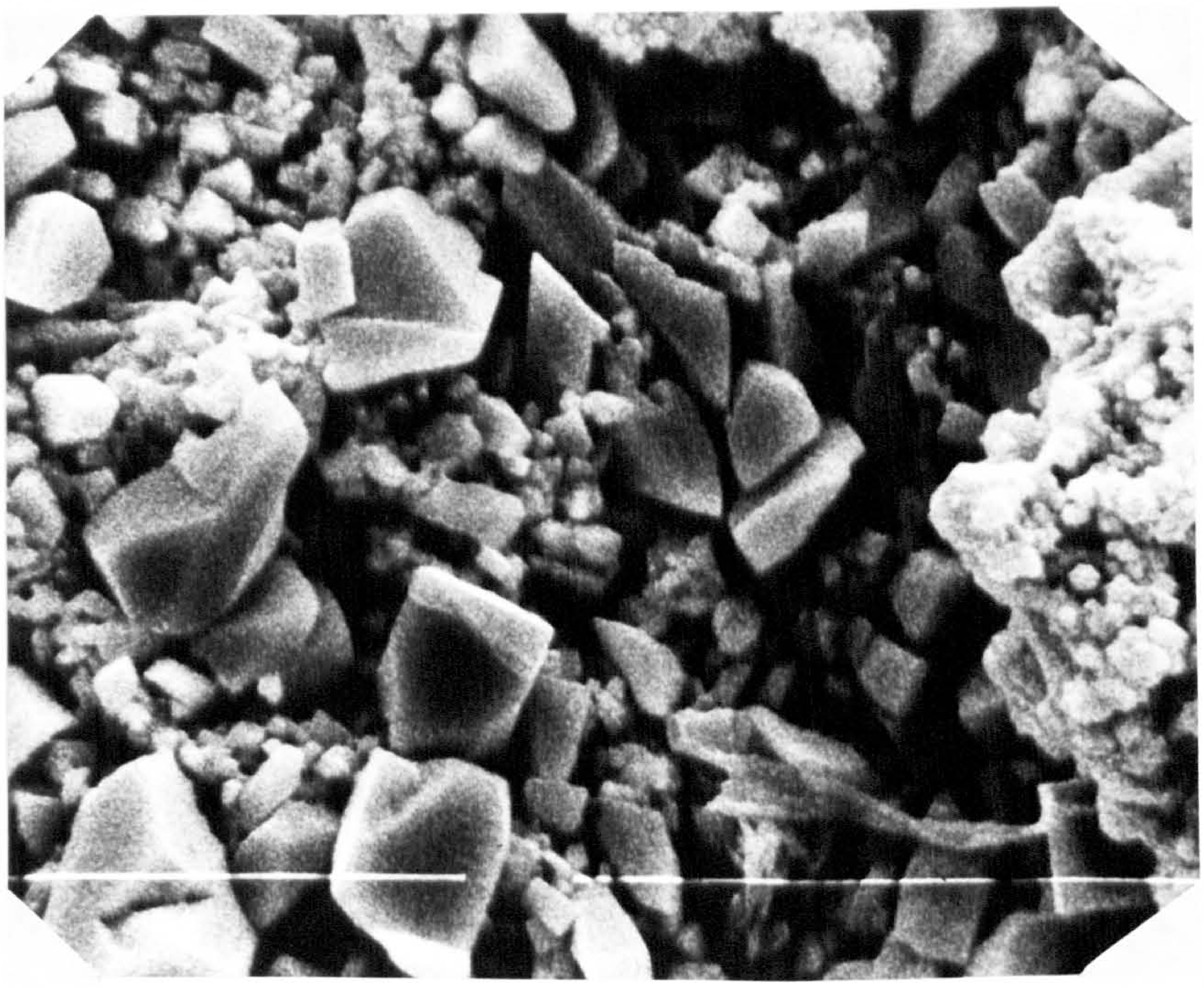

output, after a potentiostatic reduction, from the Pb-Sn-Ca electrode was greater than with the Pb-Sb electrode. After a complete discharge, Fig. 11.11 shows the surface of the electrode to be fully covered with $PbSO_4$ crystals which is similar to Fig. 11.4 although the crystals in this case are slightly larger.

After a complete discharge followed by an oxidative pulse back into the PbO_2 region the $PbSO_4$ crystals are dominant although PbO_2 is beginning to be reformed, as shown in Fig. 11.12. However, after 4h in the PbO_2 region Fig. 11.13 shows that much of the $PbSO_4$ crystals had been reformed into spongy PbO_2 with no unusual dendritic growth.

With the porous PbO_2 on the Pb-Sn-Ca support, stepping from the $PbSO_4$ region to the PbO_2 region after fully discharging the crystal structure of the porous matrix, as highlighted by Fig. 11.13, is quite similar to Fig. 11.8. This indicates that the pasted Pb-Sn-Ca electrode can be cycled, via a potentiostatic step method, with no detrimental effect on the porous matrix although some $PbSO_4$ still remains when in the PbO_2 region. However, with the pasted PbO_2 deposit disposed on a Pb-Sb electrode, a different crystalline form of PbO_2 is produced. This might explain why the charge acceptance of electrodes on these supports is poorer compared with the pasted Pb-Sn-Ca electrode as reported in Chapter 10.

X-ray diffraction was carried out on the electrodes used to explore the identity of the Pb-Sb and Pb-Sn-Ca electrodes corresponding to Figs. 11.6 and 11.13 respectively. With the Pb-Sb positive the X-ray diffraction pattern indicated a high content of α-PbO_2 together with some β-PbO_2. Hence the rather unusual dendritic growths are α-PbO_2, β-PbO_2 being probably the spongy crystallites. The Pb-Sn-Ca positive showed the presence of a large amount of β-PbO_2 together with some α-PbO_2 and a possible trace of calcium.

Fig. 11.12

Pb-Sn-Ca electrode subjected to a complete discharge in 5M H_2SO_4 and then stepped back into the PbO_2 region (1240 mV).

Magnification x 8500

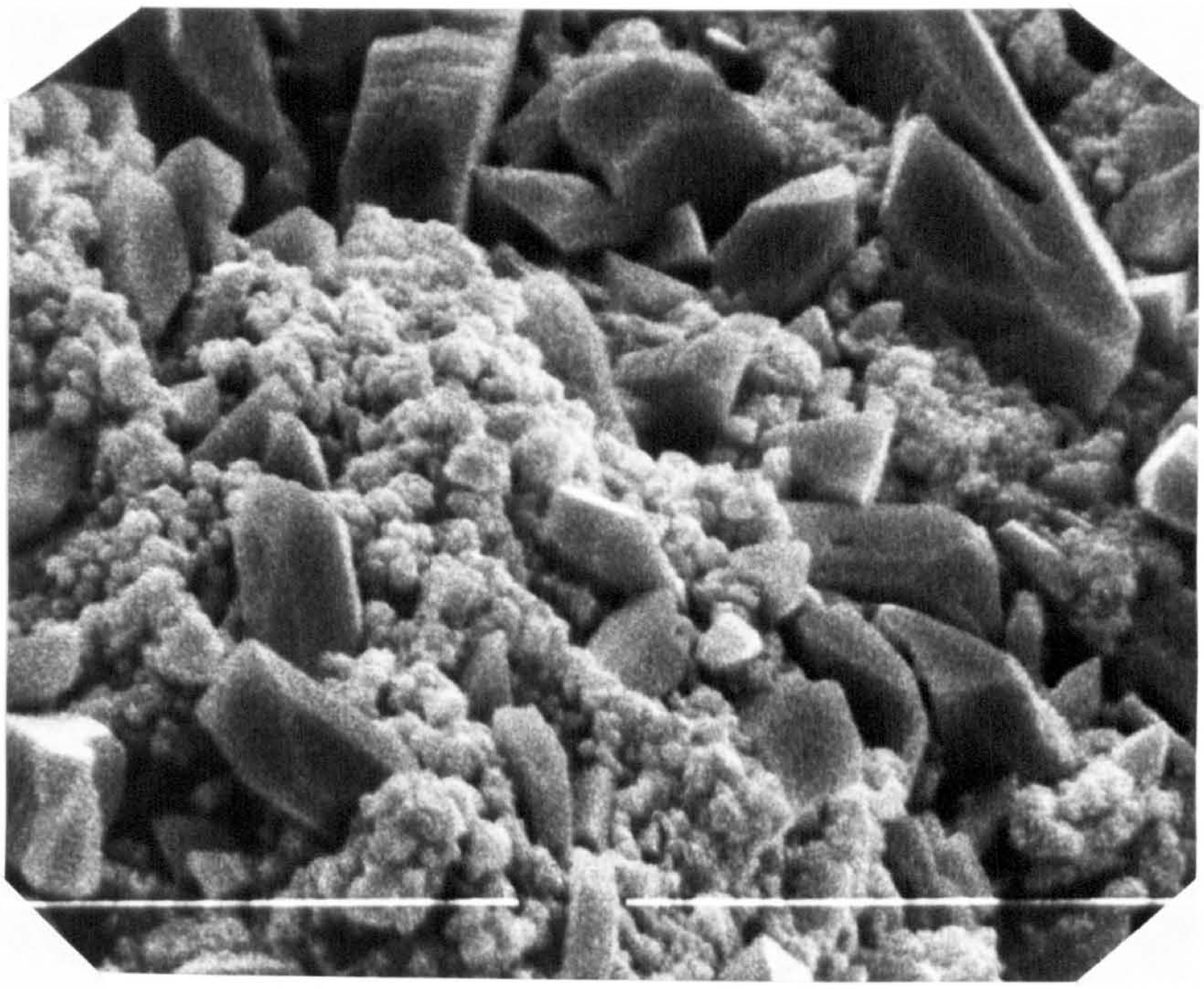

Fig. 11.13

Electrode as in Fig. 11.12 but staying in the PbO_2 region in 5M H_2SO_4 for 4h.

Magnification x 8500

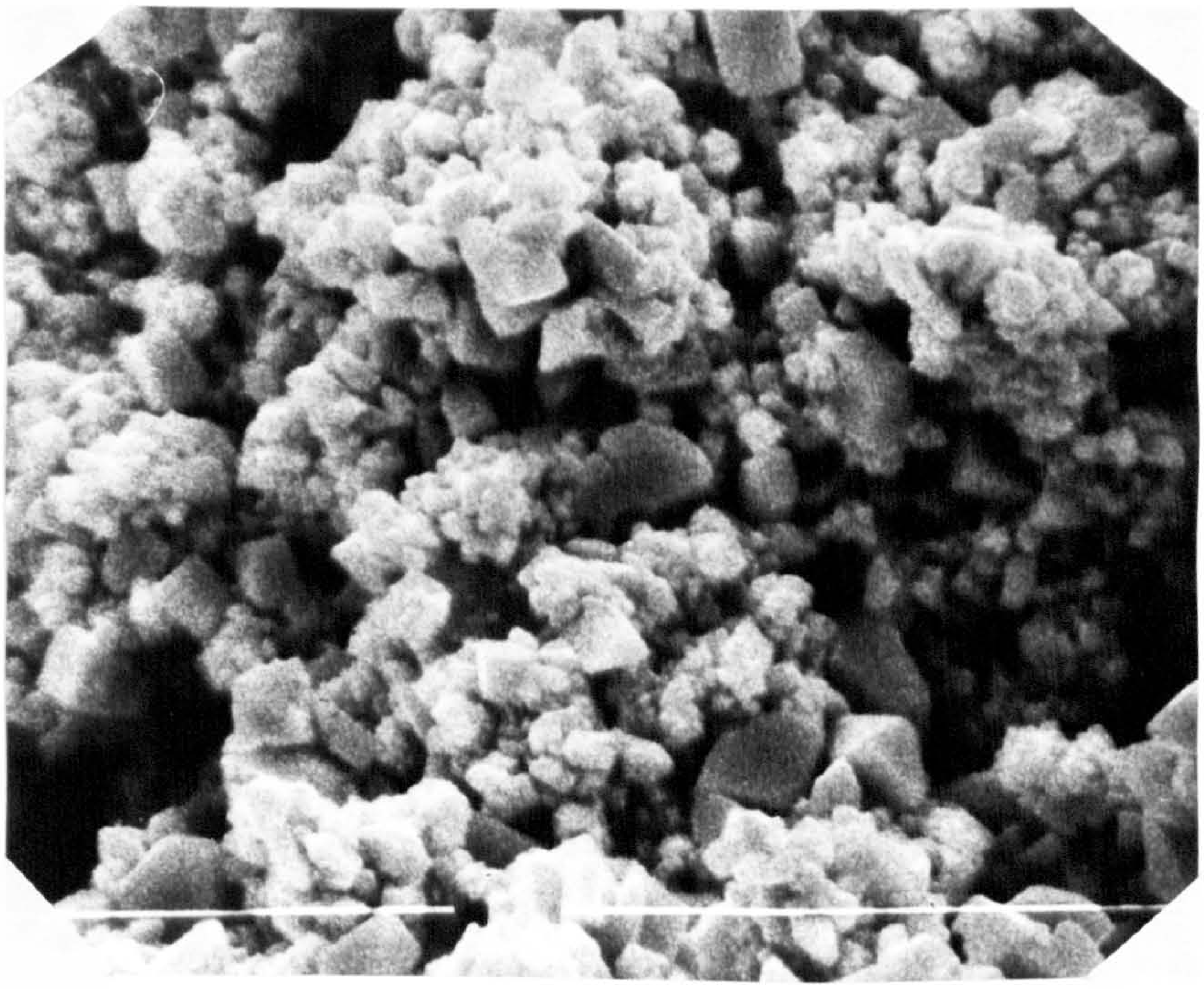

Electron microprobe analysis on the abovementioned electrodes showed that with the Pb-Sb positive no antimony could be detected on the surface of the porous matrix. Hence the α-PbO_2 may have been formed because of acid depletion within the pores of the PbO_2 matrix [97] as the oxidation (at 1240 mV) continues for 4h, resulting in the production of an alkaline medium. With the Pb-Sn-Ca positive some calcium could be found on the surface showing that, when the electrode was discharged, calcium leached from the support and diffused onto the surface of the electrode via the cracks and voids in the porous matrix.

As already noted, the current output of the Pb-Sn-Ca electrode, after a reductive pulse (from 1240 to 700 mV), was higher than with the Pb-Sb electrode. This may be attributed to the fact, as mentioned by Burbank <u>et al</u> [5], that in a mixture of the two polymorphs α-PbO_2 and β-PbO_2 the β-PbO_2 gives rise to more electrochemical capacity from the positive side of the battery. Since the Pb-Sb electrode has a high degree of the α-PbO_2 and thus less β-PbO_2 compared with the Pb-Sn-Ca positive, it seems reasonable that the Pb-Sb positive should accept less charge than the Pb-Sn-Ca electrode.

CHAPTER 12

A COMPARISON OF DIFFERENT PASTED LEAD ALLOY ELECTRODES IN SULPHURIC ACID

12.1 Introduction

In the literature addition of bismuth (0.05%) [109] to lead-tin-calcium alloys has some beneficial effect on the electrochemical properties of the calcium alloys. Although it has little effect on the metallurgical properties of a binary lead alloy, in terms of maintenance-free usage bismuth has minimal influence on the gassing rates and self-discharge processes compared with antimony. Further work has indicated that addition of bismuth seemed to improve the retention of capacity especially in the initial cycles.

Recent work has been directed towards the use of different density 'leady' oxide pastes so as to improve the cycling performance and constant current recharge characteristics of the positive plate. This chapter shows what effects potentiostatic step and cyclic voltammetry techniques have on the porous electrodes. They were made of different Pb alloy supports with a porous PbO_2 matrix overlaying the base alloy. The PbO_2 phase was derived from various pastes (different densities) which were galvanostatically oxidised.

12.2 Experimental procedure

The electrode preparation and the linear sweep/potentiostatic step experiments (all carried out in 5 M H_2SO_4) controlled by a micro-computer have already been described in Chapter 10. A Hg/Hg_2SO_4 reference electrode was used throughout and all potentials are quoted on this scale (23 ± 1^oC).

The four Pb-alloy supports used were:

A - Pure Pb

B - Pb - Sb (1.88%)

C - Pb - Sn (0.34%) - Ca (0.086%)

D - Pb - Sn (0.34%) - Bi (0.15%) - Ca (0.086%).

The three pastes used contained 100% grey oxide (41% Pb and 59% PbO) and their densities were:

(i) 4.25 gcm^{-3}

(ii) 4.55 gcm^{-3}

and (iii) 4.85 gcm^{-3}

Hence there were three electrodes containing the pure Pb support (A), each one having a different paste mounted on the base lead. The same procedure was carried out with alloys B, C and D. The twelve electrodes were then galvanostatically oxidised to PbO_2 as described by Kelly et al [103] before the electrochemical experiments were carried out. The electrodes are designated hereafter A.i to signify paste No. i on alloy A etc.

12.3 Results and Discussion

12.3.1 Uncycled Electrodes

Fig. 12.1 shows the current-time transients of the different paste density Pb electrodes as the potential is instantaneously stepped from the lead dioxide region (1240 mV) to the lead sulphate region (700 mV). Of these electrode combinations A.i was found to be the most reactive in the electrical sense giving the highest peak current output as the result of the step. Table 12.1 shows that the positives which were derived from the 4.25 gcm^{-3} paste, that is, on Pb, Pb-Sb, Pb-Sn-Ca and Pb-Sn-Bi-Ca bases, have higher discharge capacities. Fig. 12.2 corresponds to Fig. 12.1 except here the Pb-Sb electrodes are used. As can be seen the peak current outputs are generally lower than those shown in Fig. 12.1.

FIG. 12.1. Potentiostatic pulse experiments (1240 → 700 mV) on pasted Pb electrodes.

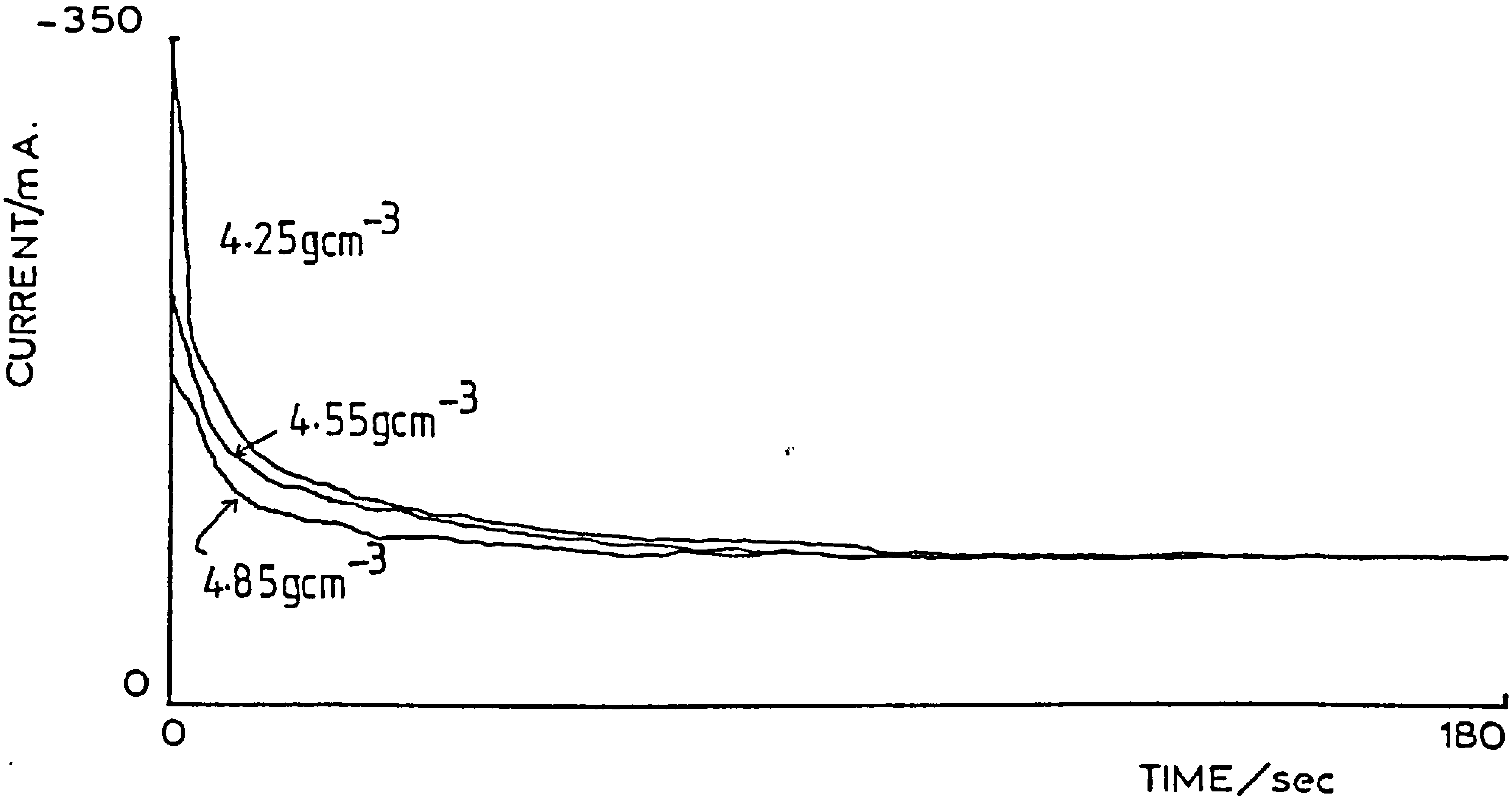

FIG. 12.2 As in Fig 12.1 but on pasted Pb-Sb electrodes.

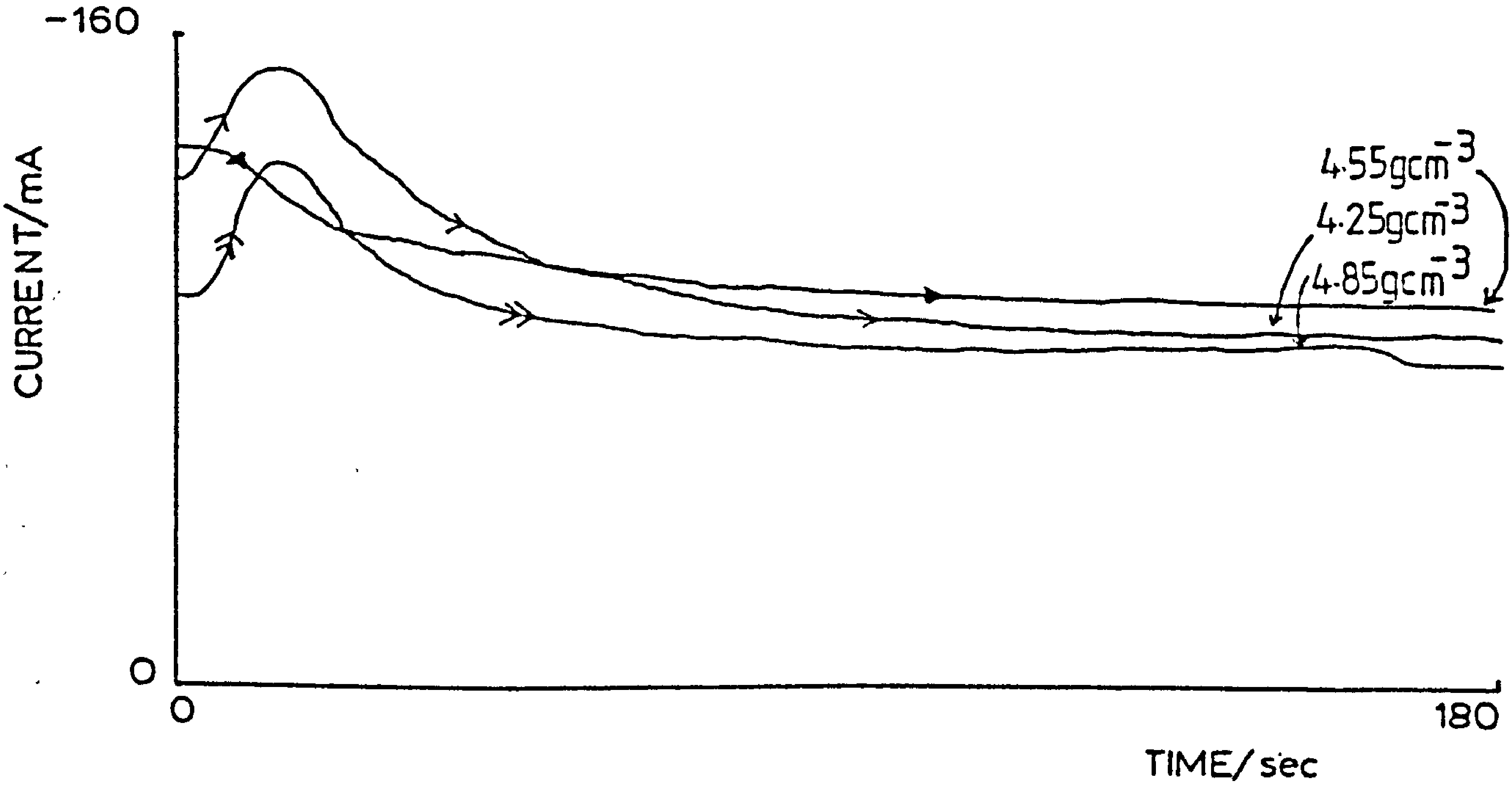

FIG. 12.3 As in Fig. 12.1 but on pasted Pb-Sn-Ca electrodes.

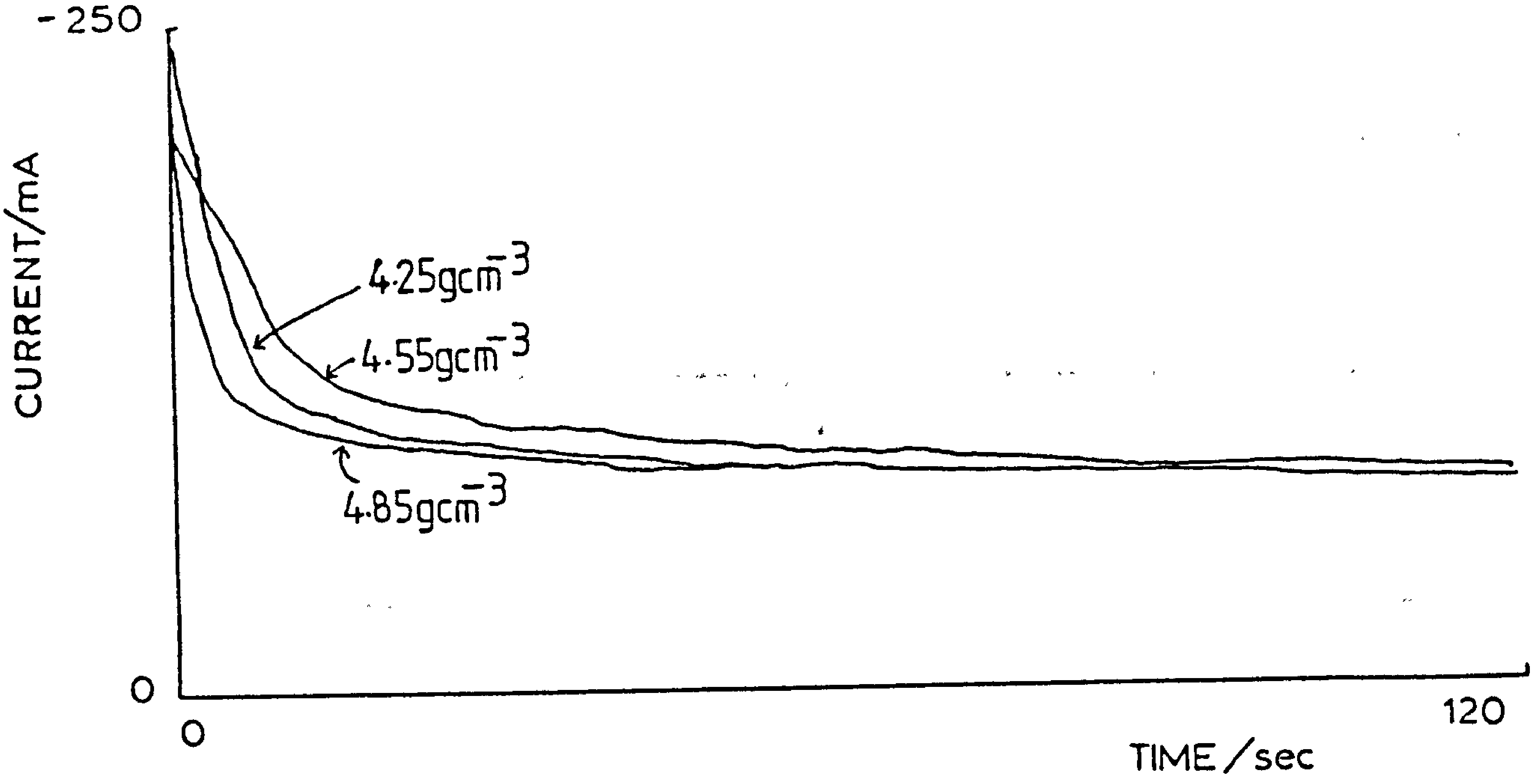

FIG. 12.4 As in Fig. 12.1 but on pasted Pb-Sn-Bi-Ca electrodes.

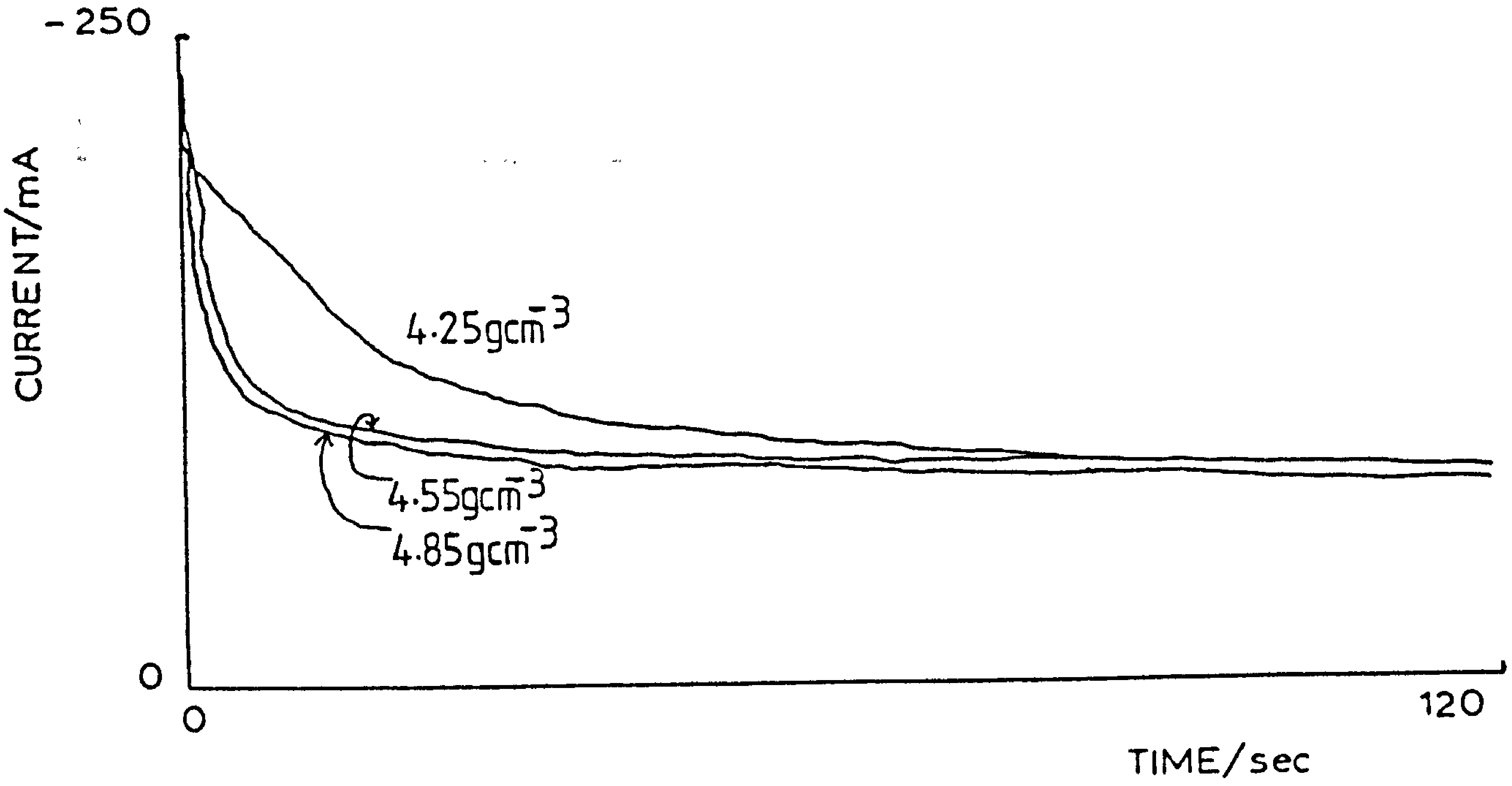

TABLE 12.1

Current output and capacity values for the uncycled porous electrodes subjected to potentiostatic reduction followed by oxidation.

Electrodes (paste density/gcm^{-3})	Discharge capacity/C	Time to reach full discharge capacity/min	Recharge capacity after 4 hours/C	% charge regained
Pb				
4.25	8.51	105	2.19	25.7
4.55	7.61	55	2.62	34.4
4.85	7.36	80	2.46	33.4
Pb-Sb				
4.25	12.60	162	1.51	12.0
4.55	8.01	150	1.46	18.2
4.85	6.79	110	2.26	33.3
Pb-Sn-Ca				
4.25	8.65	115	1.46	16.8
4.55	7.59	60	1.33	17.5
4.85	6.04	115	2.35	38.9
Pb-Sn-Bi-Ca				
4.25	12.82	91	2.94	22.9
4.55	6.60	55	2.37	35.9
4.85	6.51	105	3.36	51.6

Figs. 12.3 and 12.4 correspond to Fig. 12.1 but pasted Pb-Sn-Ca and Pb-Sn-Bi-Ca electrodes are respectively employed instead. The peak current output values shown in Figs. 12.3 and 12.4 are of the same order showing that on discharge there is no significant difference between the Pb-Sn-Ca and Pb-Sn-Bi-Ca electrodes.

As mentioned above the 4.25 gcm^{-3} pasted electrodes discharge more than the other electrodes. Although the difference among the pastes is the water content and SO_4^{2-}, when the pastes are packed into the recess of the electrodes so as to cover the Pb alloy support, there is less grey oxide per volume present in the case of the 4.25 gcm^{-3} electrode. Thus, on galvanostatic oxidation the PbO_2 phase produced is very porous, that is, there is a larger surface area available for the acid to attack creating conditions of low pH within the pores. This results in a greater formation of β-PbO_2 and hence high peak current outputs as described in Chapter 10.

Fig. 12.5 shows the current-time responses for reoxidising (at 1240 mV) the electrodes used in Fig. 12.1. The curve corresponding to the electrode A.ii contain several current peaks which indicates that there is more than one reaction occurring and may mean that several layers of PbO_2 have been formed. Fig. 12.6 shows similar data for the reoxidation of the porous electrodes formed on antimonial lead (B). Figs. 12.7 and 12.8 illustrate the reoxidation of porous PbO_2 on Pb-Sn-Ca and Pb-Sn-Bi-Ca alloy bases respectively. Fig. 12.8 displays the fact that the 4.85 gcm^{-3} pasted Pb-Sn-Bi-Ca electrode has the highest peak current output and charge acceptance and thus it implies that Bi has a significant effect on the Pb-Sn-Ca alloy.

The data in Table 12.1were statistically analysed (i.e. comparing variance values) to see if there were any trends concerning the paste densities. A trend was found showing that with increasing paste density

FIG. 12.5 Potentiostatic pulse experiments (700 → 1240 mV) on pasted Pb electrodes following full discharge.

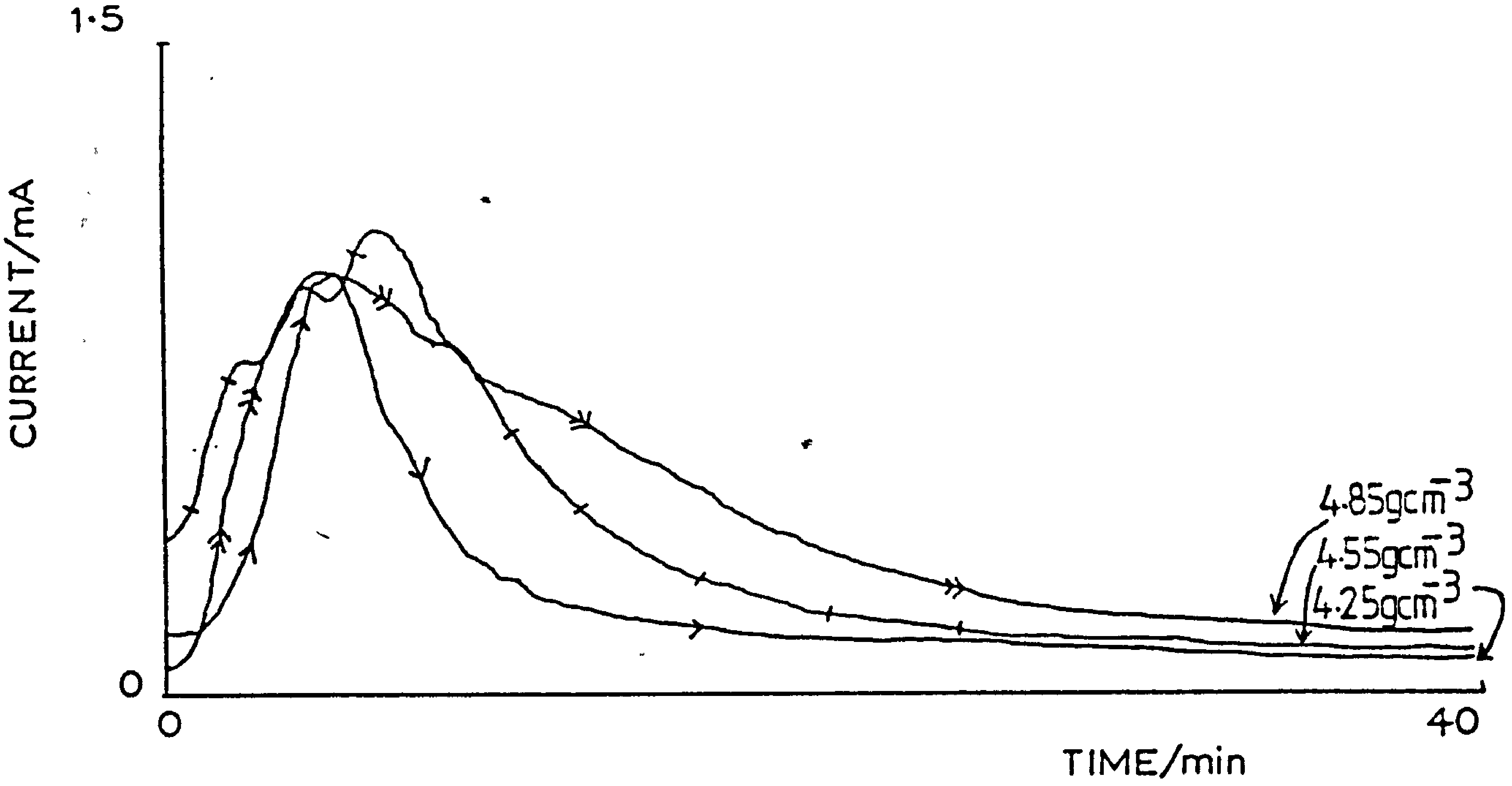

FIG. 12.6 As in Fig. 12.5 but on pasted Pb-Sb electrodes.

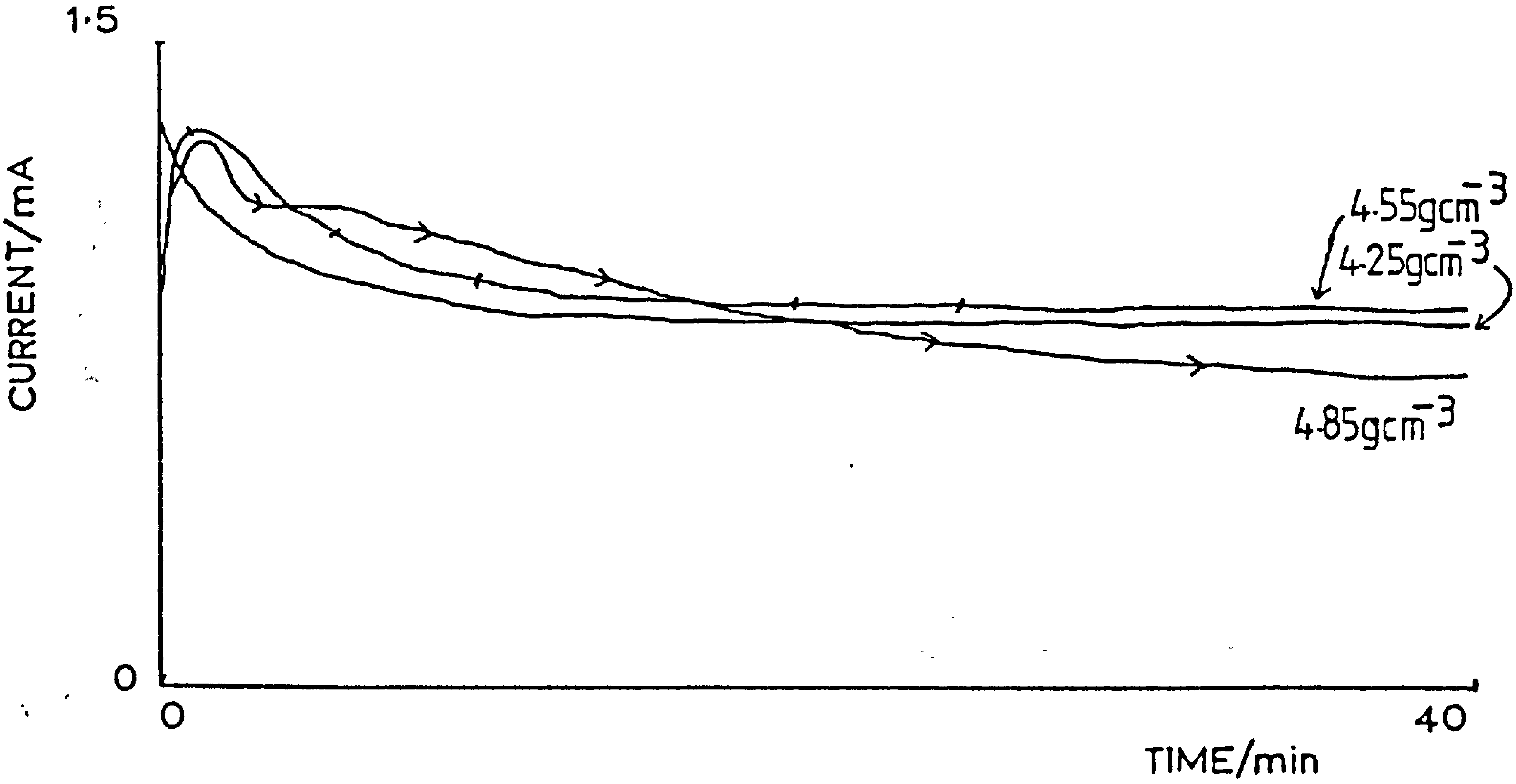

FIG. 12.7 As in Fig. 12.5 but on pasted Pb-Sn-Ca electrodes.

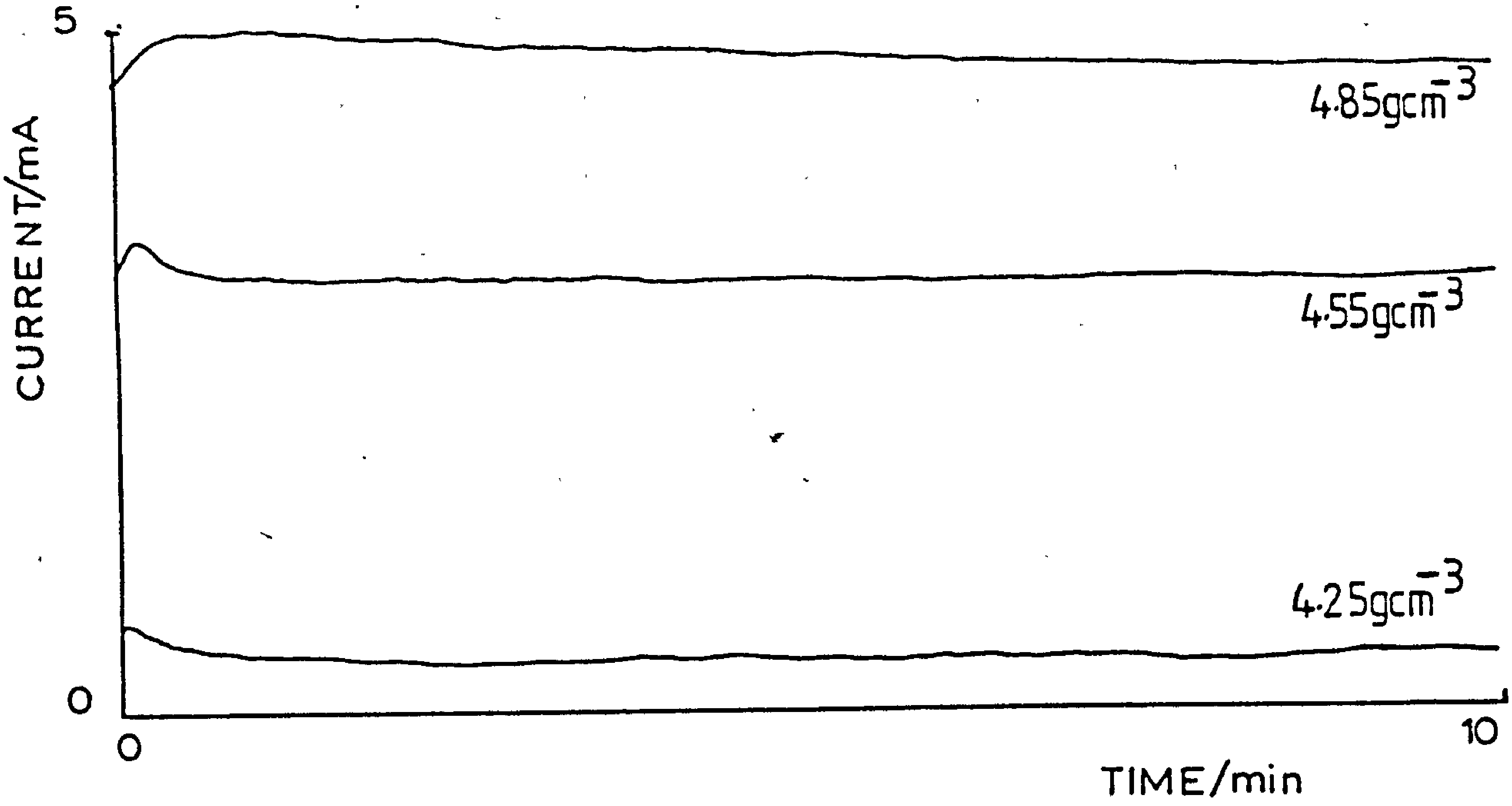

FIG. 12.8 As in Fig. 12.5 but on pasted Pb-Sn-Bi-Ca electrodes.

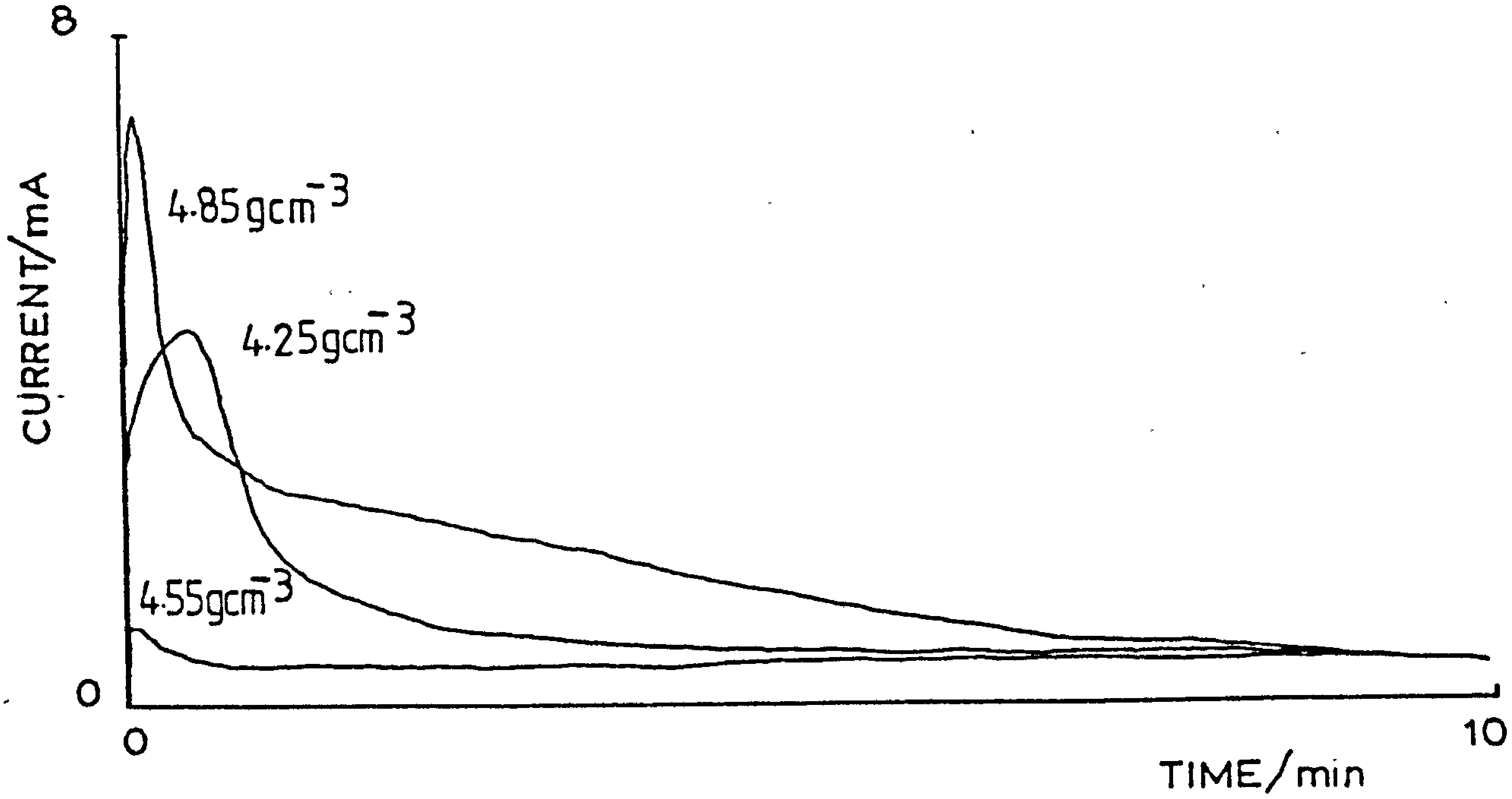

the less the Pb alloy support had an effect on the discharge capacity and recharge capacity (after 4h). This seems feasible whereby the PbO_2 matrix, formed from the 4.85 gcm^{-3} paste, is not very open and restricts the movement of sulphuric acid towards the Pb alloy support to a greater extent compared with the other paste densities used.

There is an imbalance between the discharge capacity and the charge acceptance values because the potentiostatic oxidative step (700 → 1240 mV) is ineffective in charging the electrode efficiently (as discussed in Chapter 10) and thus a higher potential is needed to fully reform the PbO_2 matrix.

Using the transients in Figs. 12.1-12.8, the nature of the electrocrystallisation process appropriate for each system was identified. Employing the Least Squares Fit method described earlier only two curves were found to follow well-defined (established) current-time relationships [105, 110, 111]. The initial rise in the curve corresponding to the 4.25 gcm^{-3} pasted Pb-Sb electrode, when undergoing potentiostatic reduction (see Fig. 12.2), followed an i vs. t^2 relationship. This indicates that the process followed initially is either one that is a two dimensional growth and progressive nucleation or three dimensional (hemispherical) growth and instantaneous nucleation. Scanning electron microscopy [110] can be used to determine which nucleation law is employed. The falling part of the same curve follows a ln i vs. $t^{-\frac{1}{2}}$ relationship. In Fig. 12.8, corresponding to the Pb-Sn-Bi-Ca electrodes subjected to a potentiostatic oxidation, the falling part of the curve relating to the 4.55 gcm^{-3} pasted electrode follows a linear relation connecting ln (i/t) and t^2. This suggests that there is a two dimensional growth and instantaneous nucleation process occurring.

12.3.2 Cycled Electrodes

Before each potentiostatic pulse experiment the porous electrode was cycled for 20 cycles of discharge and charge (1240 → 700 mV) at 10 mVs^{-1} and back again, using cyclic voltammetry. After the preparatory cycling, when the current output was low and constant, the reductive pulse (1240 → 700 mV) was carried out. Figs. 12.9-12.12 correspond to the current-time transients for the different pasted electrodes after they have undergone a potentiostatic reduction. Fig. 12.9 shows the current-time response for the various paste density Pb electrodes. Compared with the uncycled cases, the peak current output is lower, as with all the cycled electrodes. Also, the discharge capacity values have decreased (Table 12.2) as is the case with all the other positives.

Fig. 12.10 relates to the Pb-Sb positive where the current output values have not decreased significantly compared with the uncycled Pb-Sb positives although there has been a decrease in capacity as shown by Table 12.2. Figs. 12.11 and 12.12 correspond to the ternary and quaternary electrodes and as mentioned earlier on, they discharge less than their uncycled cases. The decrease in the discharge capacity is due to 'passivated' $PbSO_4$ being formed during the preparatory cycling as mentioned in Chapter 10.

The current-time transients corresponding to the reoxidation of reduced electrodes (potentiostatic step to 700 mV, Figs. 12.9-12.12)are shown in Figs. 12.13-12.16. In Fig. 12.13 the transient corresponding to the 4.25 gcm^{-3} Pb electrode dips very sharply whereas with the other two electrodes, there is no significant curvature in their transients due to overlap of growing PbO_2 centres indicating that the current flows are mostly due to oxygen evolution. Fig. 12.14 corresponds to the Pb-Sb electrodes and, as can be seen, the shoulder appearing on the falling part of all the three transients indicates that another process may occur at long times. The peak

FIG. 12.9 Current-time transients for potentiostatic pulse experiments (1240 → 700 mV) on cycled (20 cycles) pasted Pb electrodes.

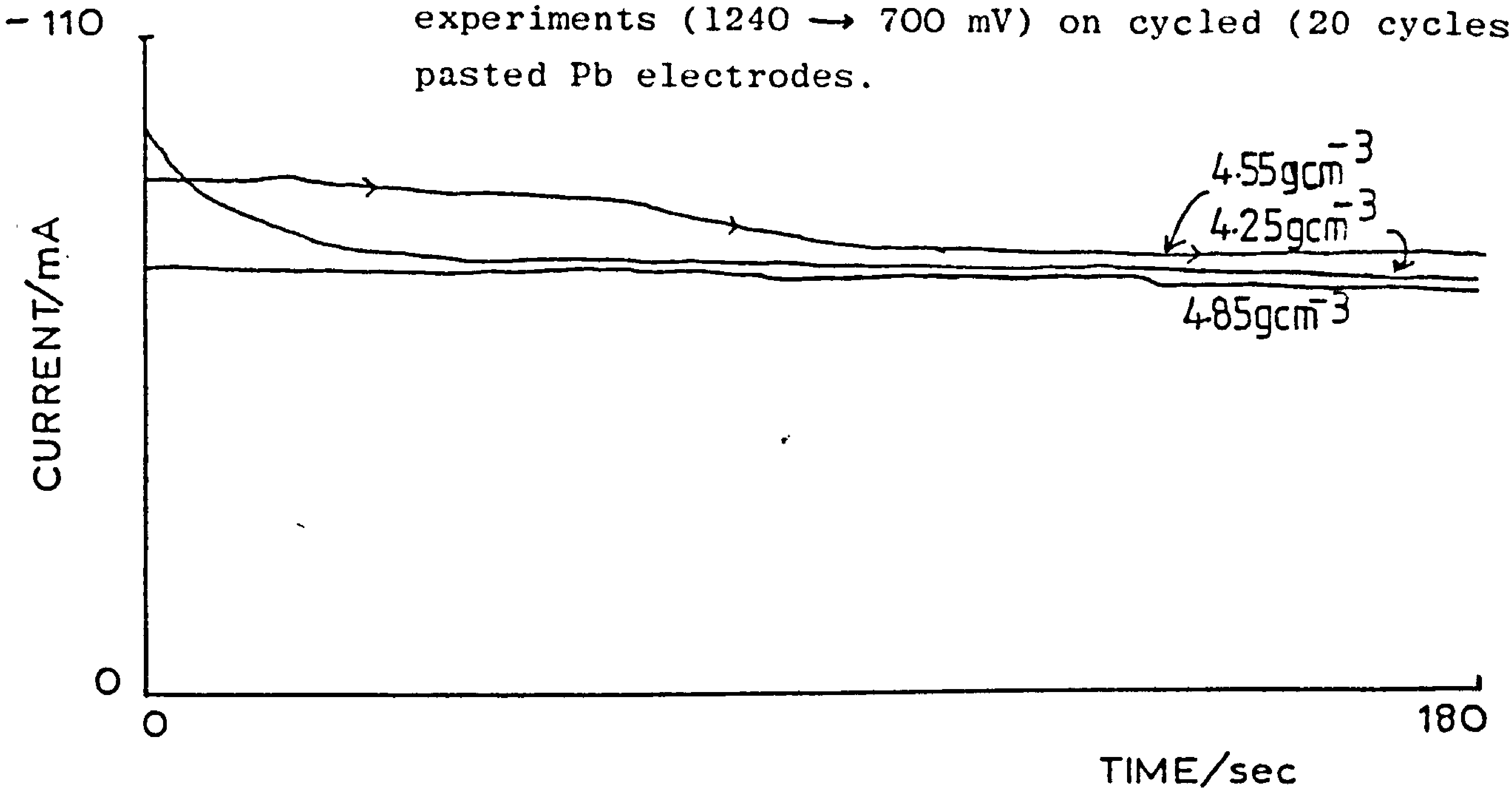

FIG. 12.10 As in Fig. 12.9 but on pasted Pb-Sb electrodes.

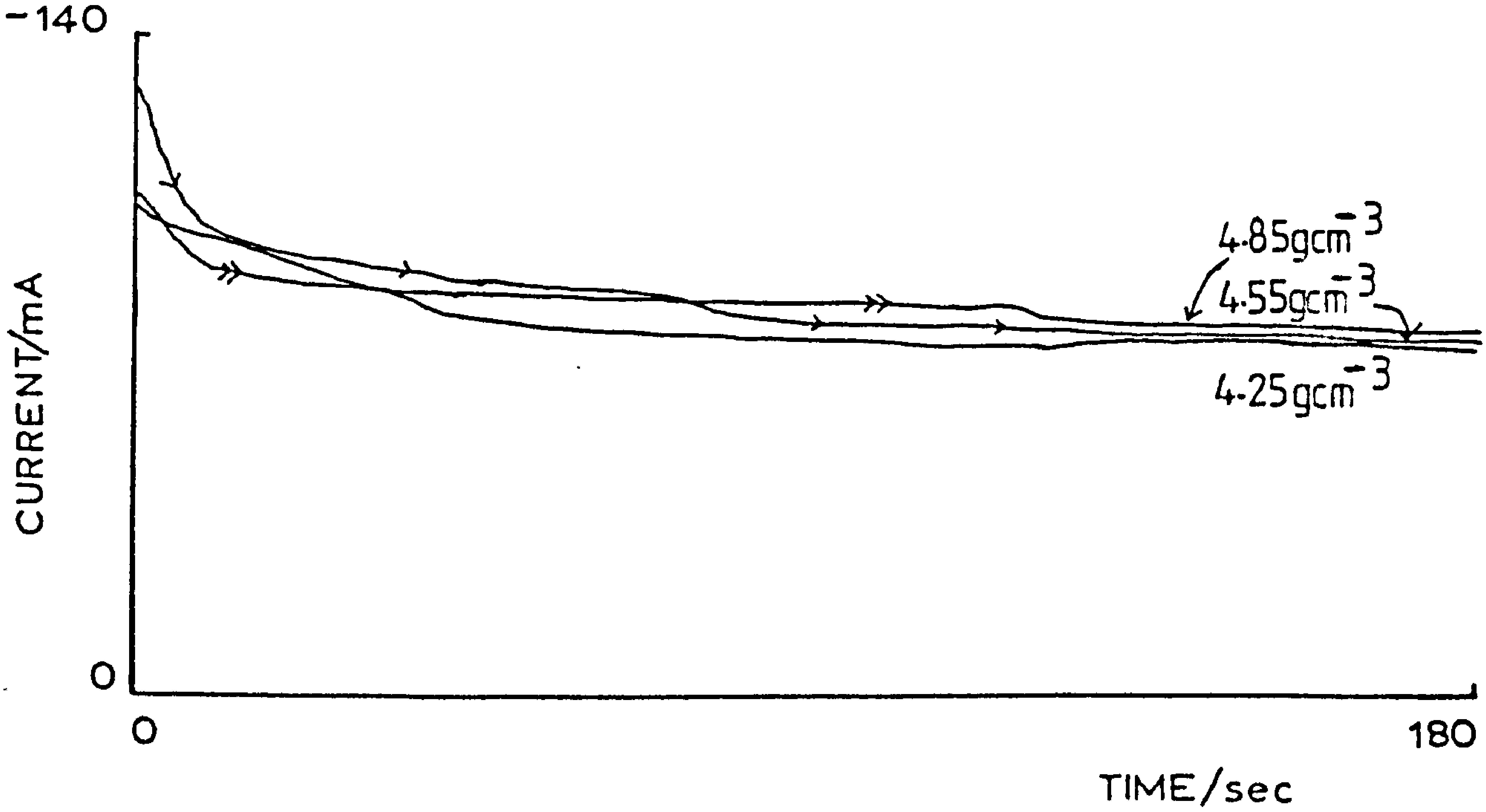

FIG. 12.11 As in Fig. 12.9 but on pasted Pb-Sn-Ca electrodes.

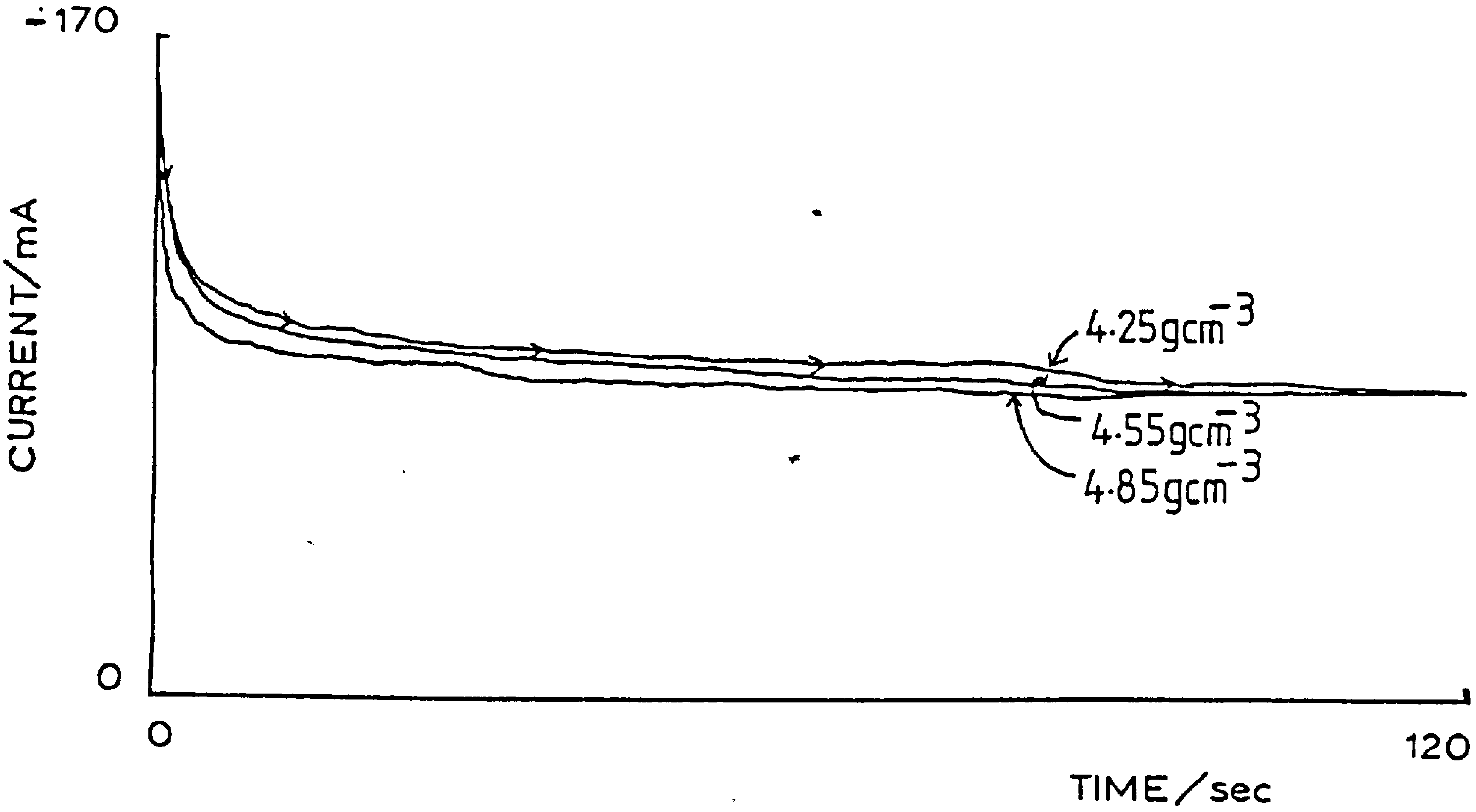

FIG. 12.12 As in Fig. 12.9 but on pasted Pb-Sn-Bi-Ca electrode

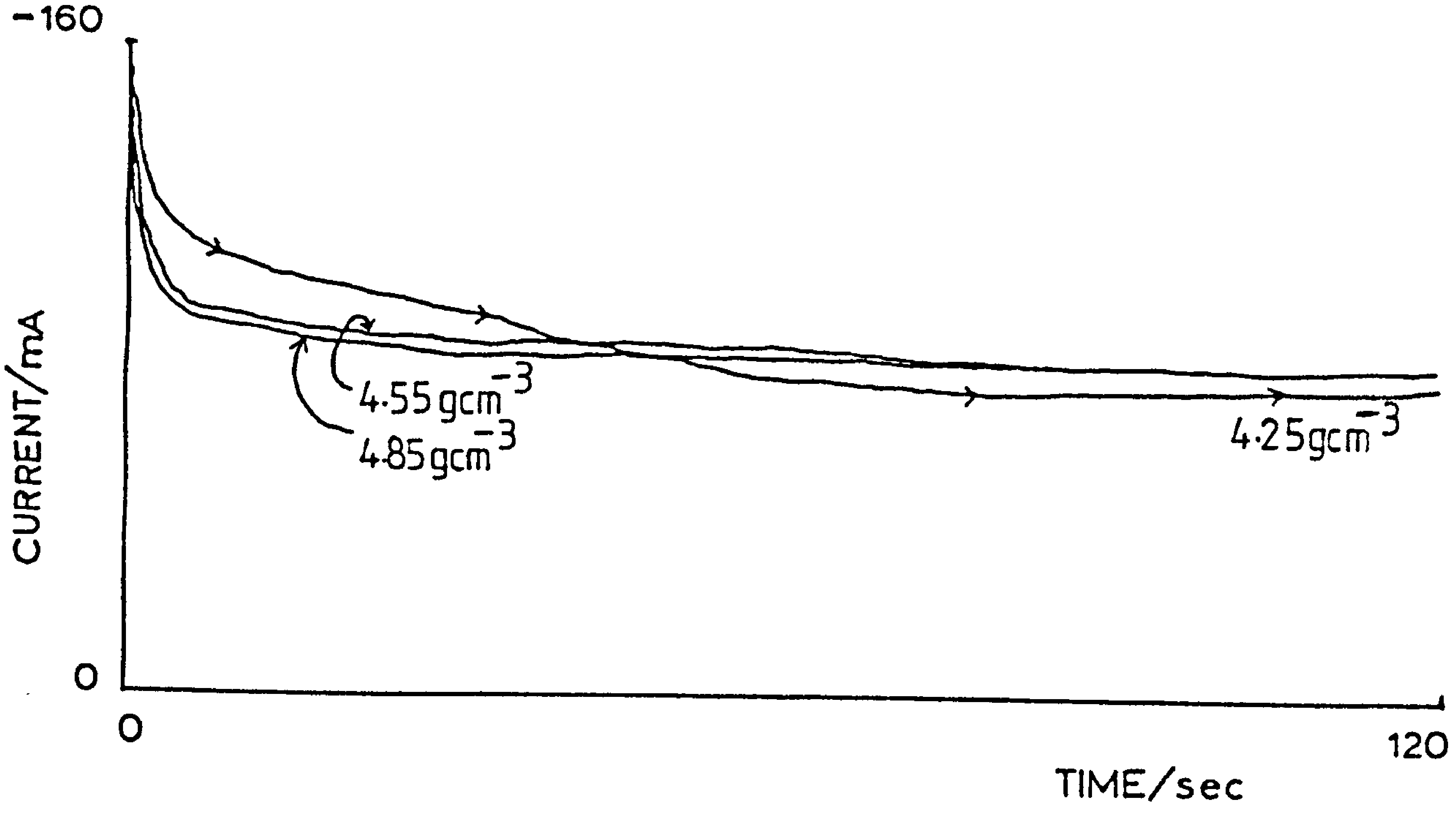

FIG. 12.13 Current-time transients for potentiostatic pulse experiments (700 → 1240 mV) on cycled (20 cycles) pasted Pb electrodes, following a full discharge.

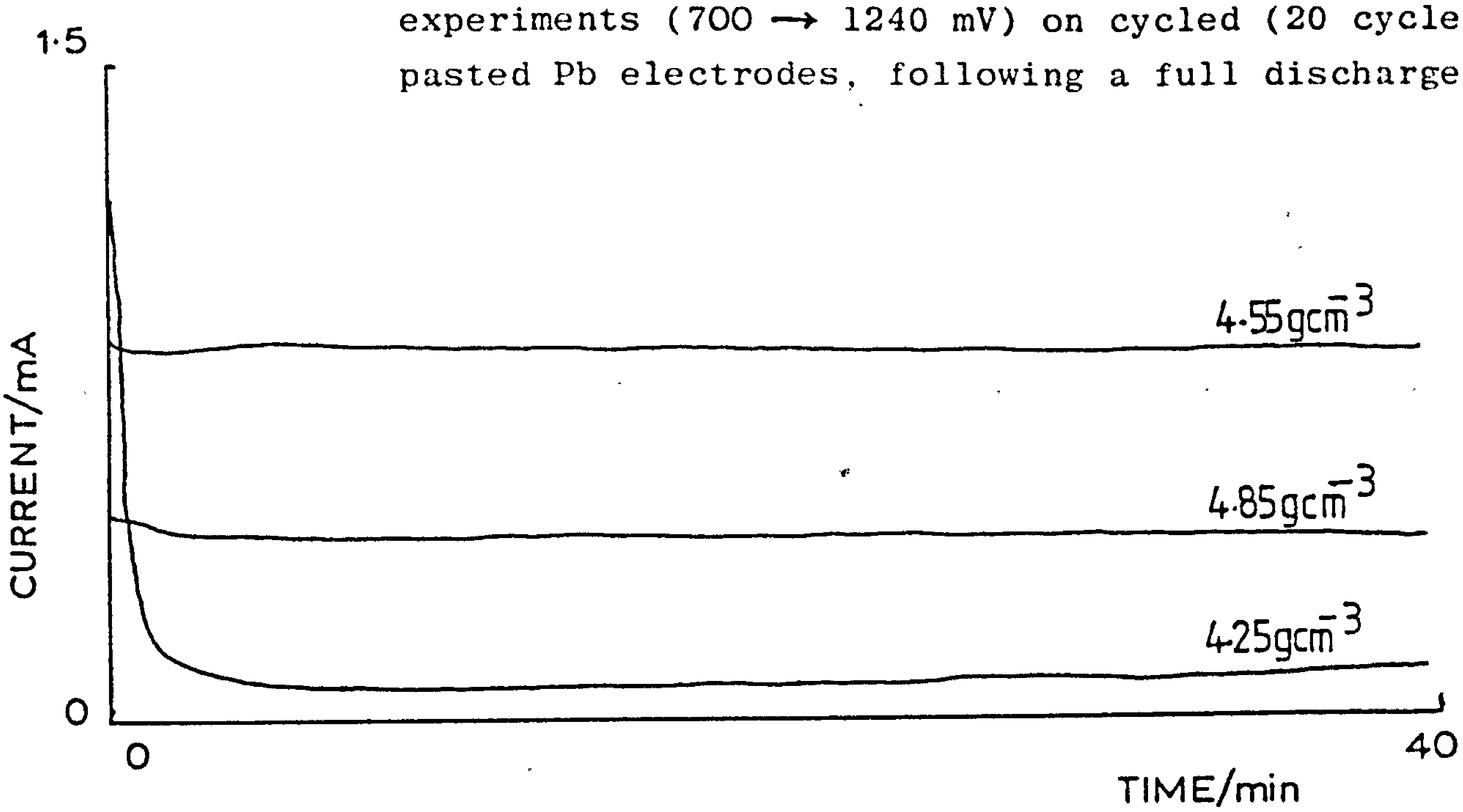

FIG. 12.14 As in Fig. 12.13 but for pasted Pb-Sb electrodes.

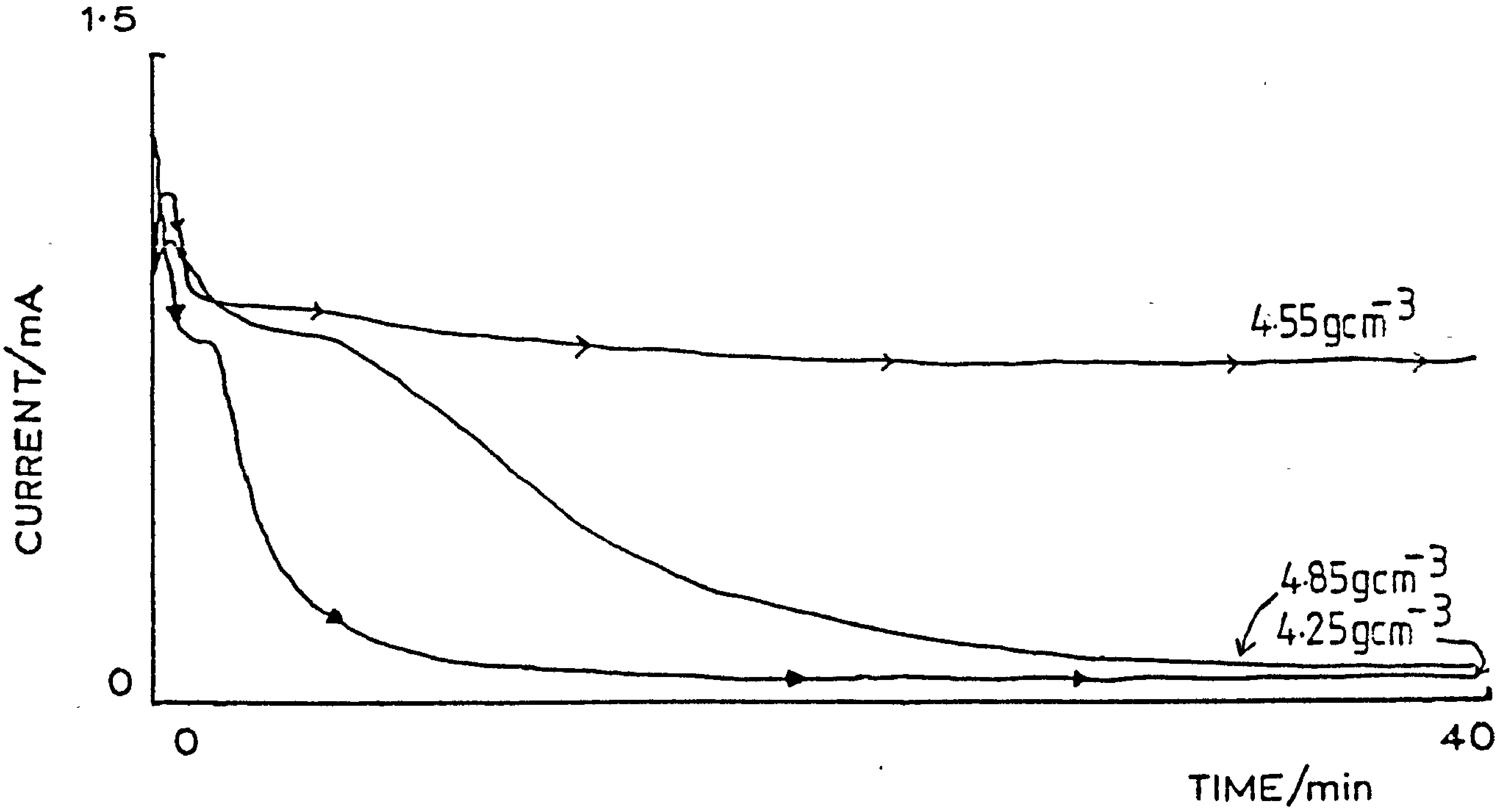

FIG. 12.15. As in Fig. 12.13 but for pasted Pb-Sn-Ca electrodes.

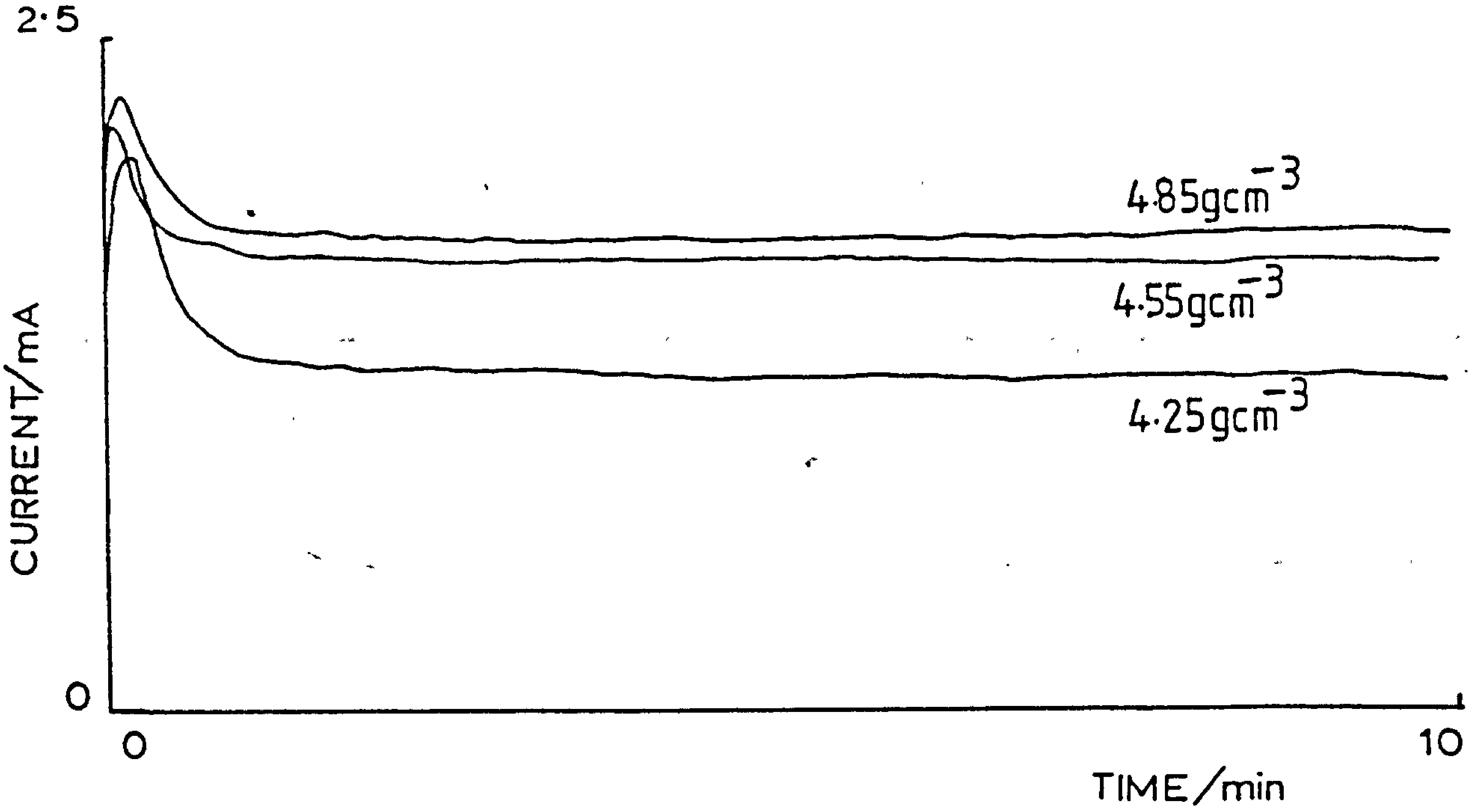

FIG. 12.16 As in Fig. 12.13 but for pasted Pb-Sn-Bi-Ca electrodes

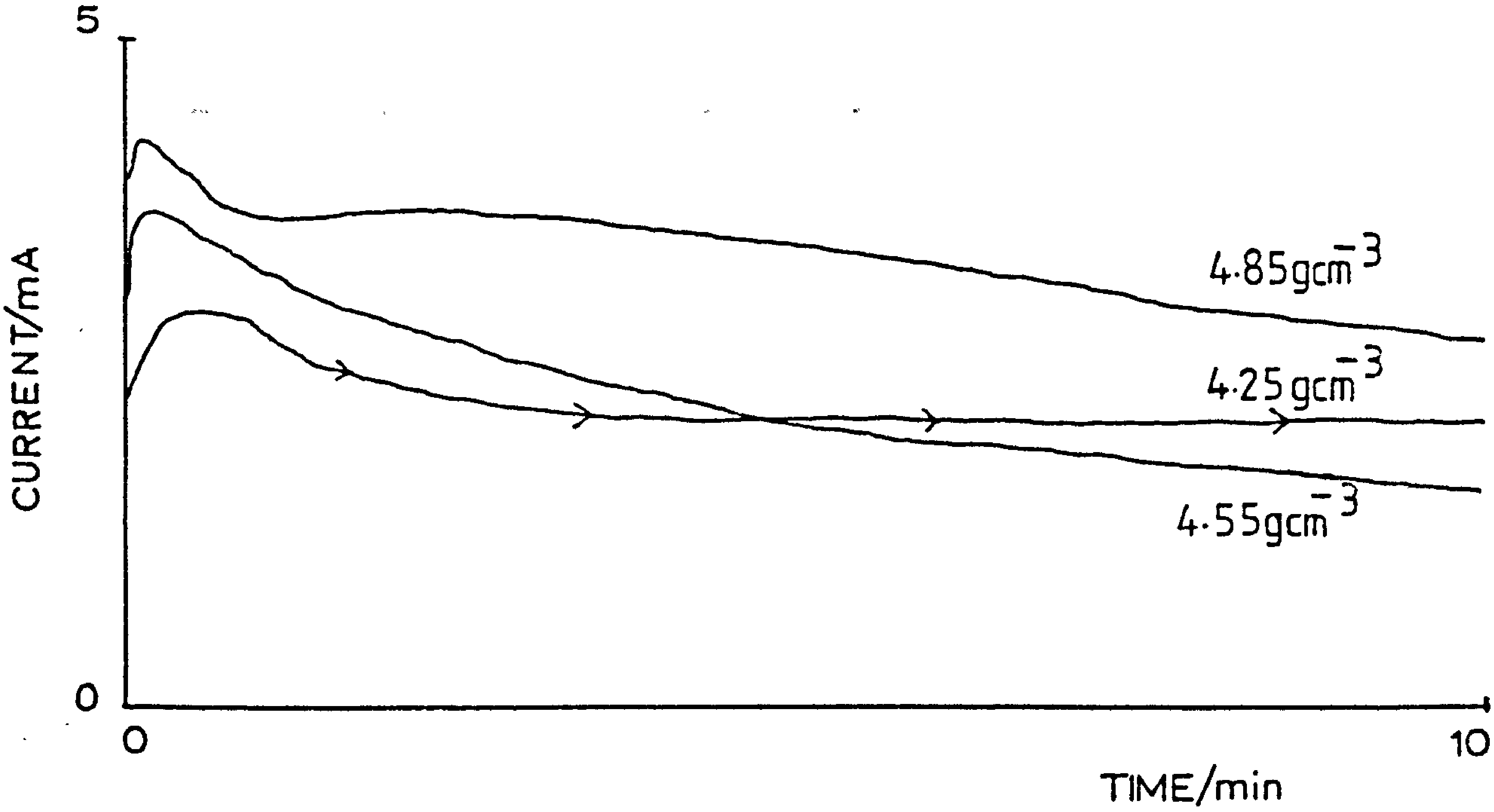

TABLE 12.2

As Table 12.1 but for cycled (20 cycles) porous electrodes.

Electrodes (paste density/gcm^{-3})	Discharge capacity/C	Time to reach full discharge capacity/min	Recharge capacity after 4 hours/C	% charge regained
Pb				
4.25	2.20	32	0.99	45.0
4.55	3.64	70	2.89	79.4
4.85	2.93	75	1.18	40.3
Pb-Sb				
4.25	2.83	70	1.84	65.0
4.55	4.49	72	1.72	38.3
4.85	3.76	105	1.96	52.1
Pb-Sn-Ca				
4.25	4.36	50	1.35	31.0
4.55	4.12	75	0.98	23.8
4.85	3.00	75	1.95	65.0
Pb-Sn-Bi-Ca				
4.25	3.68	47	0.75	20.4
4.55	2.18	40	1.42	65.1
4.85	2.65	88	1.88	70.9

current output values obtained with the cycled Pb and Pb-Sb positives are fairly similar to their corresponding ones obtained before the 20 cycles. With the cycled Pb-Sn-Ca and Pb-Sn-Bi-Ca positives, however, the peak current output values are less than the uncycled cases but are still higher than those obtained with the corresponding Pb and Pb-Sb electrodes.

After statistically analysing the,data in Table 12.2 with respect to paste density it was found that with the 4.85 gcm^{-3} pasted electrodes the alloy support had less effect on the discharge and recharge capacities, even less compared with the corresponding uncycled electrodes. Hence with cycling prior to the pulse experiments it seems that the porous PbO_2 matrix (formed from 4.85 gcm^{-3} paste) on each Pb alloy support has been transformed to such an extent that they are quite similar.

As in the previous section a series of standard current-time relationships for electrocrystallisation processes were matched to the transients in Figs. 12.9-12.16. With the falling parts of the transients corresponding to electrodes A.ii and D.ii, as well as C.iii and D.iii, after they have been potentiostatically reduced (1240 → 700 mV), they all followed a i vs. $t^{-\frac{1}{2}}$ relationship. This is indicative of β-PbO_2 being reduced to $PbSO_4$ as reported by Dawson <u>et al</u> [106]. The discharge proceeds via two mechanisms, the first being a dissolution-precipitation process, and the second an electrocrystallisation process within the pores of the growing $PbSO_4$ layer together with some diffusion. However, diffusion in the bulk solution could not be detected by rotating disc experiments since the current output was independent of rotation speed. Of all the twelve electrodes used only two were found to follow a well-defined electrocrystallisation process, that is, ln (i/t) vs. t^2 which is indicative of a two dimensional growth and instantaneous nucleation process. The electrodes concerned were A.iii (see Fig. 12.9) and A.ii (see Fig. 12.13). Figs. 12.17 and 12.18 are examples of straight line plots obtained with

FIG. 12.17 i vs. $t^{-0.5}$ for falling part in Fig. 12.12 for cycled (20 cycles) pasted 4.85 gcm^{-3} Pb-Sn-Bi-Ca electrode.

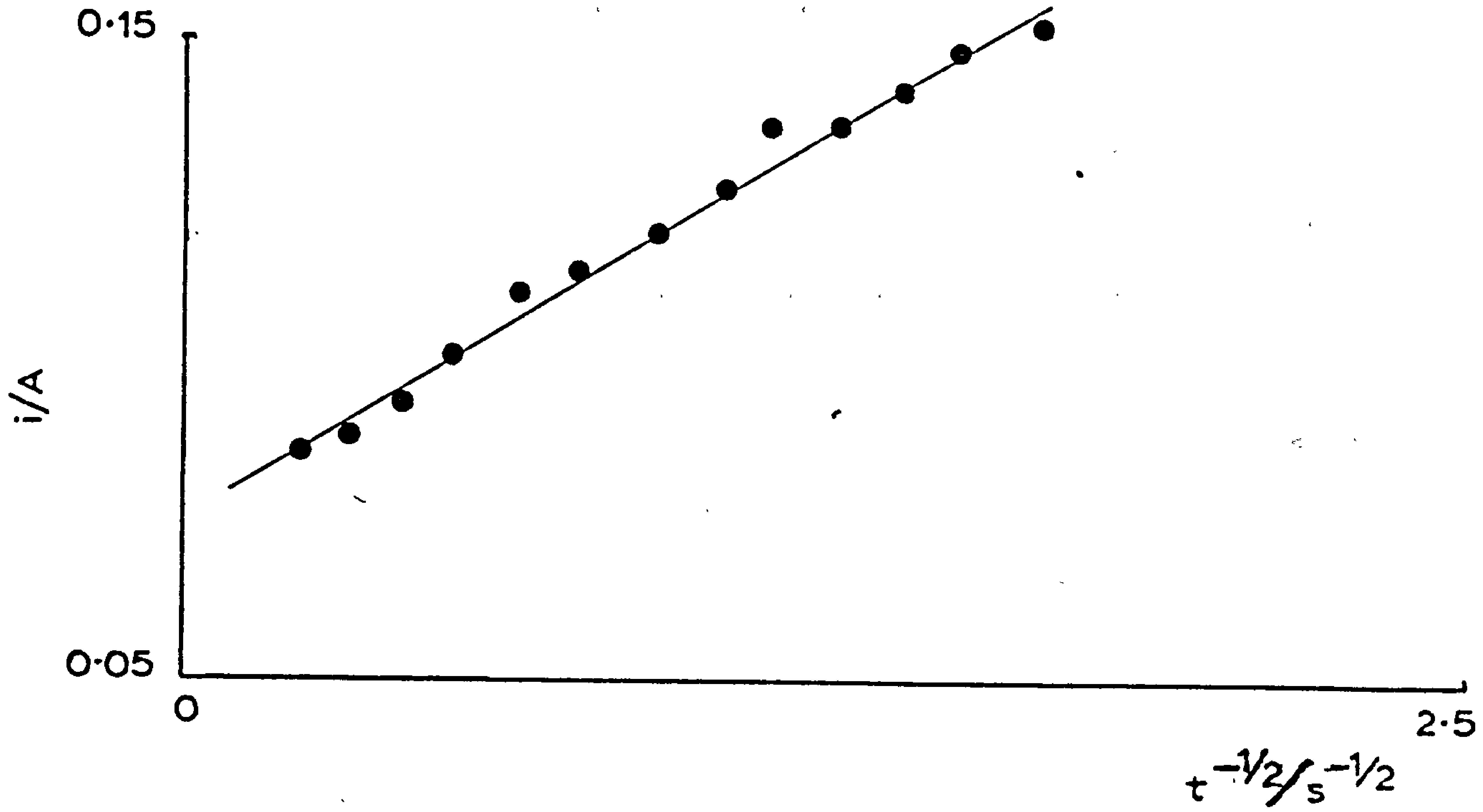

FIG. 12.18 ln ($^{i}/t$) vs. t^2 for falling part in Fig. 12.9 for cycled (20 cycles) pasted 4.85 gcm^{-3} Pb electrode.

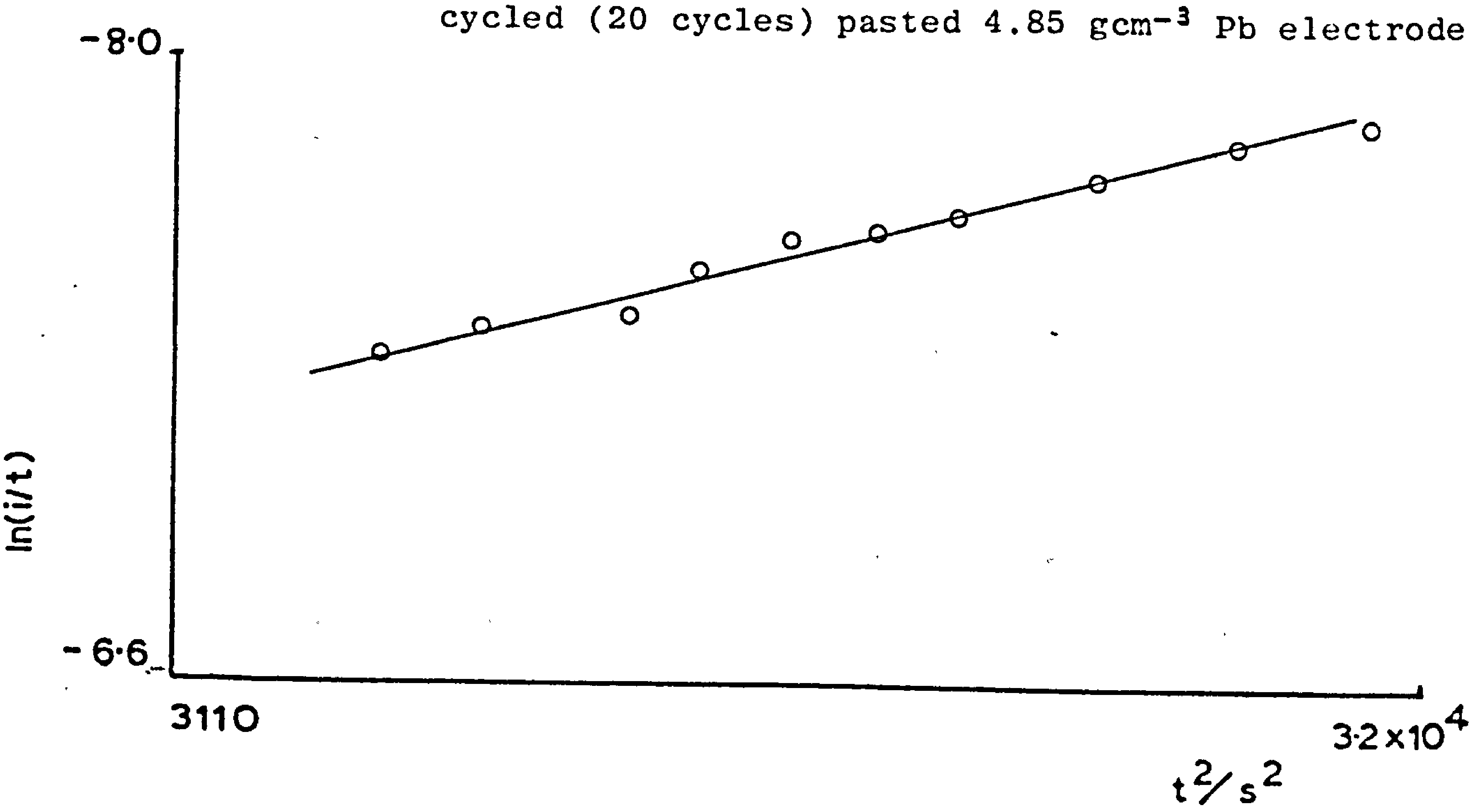

the electrodes. Fig. 12.17 corresponds to electrode D.ii following a i vs. $t^{-\frac{1}{2}}$ relationship (the data in Fig. 12.12 is used). Fig. 12.18 shows the linear plot of ln (i/t) vs. t^2 for electrode A.iii.

Some of the electrodes were subjected to 100 linear sweep cycles before undergoing potentiostatic reduction (1240 → 700 mV). It was found that after this cycling which is in a sense simulated battery service, the high density paste electrodes had the higher peak current outputs and deliverable charge on discharge. Statistical analysis on the data in Table 12.3 shows that the Pb alloy tends to have little effect on either the 4.25 gcm^{-3} paste or the 4.85 gcm^{-3} paste employed to form the porous PbO_2 matrices. Hence, it seems that after 100 cycles, the porous matrices of both the 4.25 gcm^{-3} and the 4.85 gcm^{-3} pasted electrodes have been transformed to such a point where they must be all very similar in nature. The 4.85 gcm^{-3} pasted Pb-Sn-Ca positive has the highest discharge capacity (1240 → 700 mV) probably because it contains a higher proportion of β-PbO_2 which as mentioned before contributes more to the electrochemical capacity of the positive battery plate.

12.4 Conclusions

1. Electrodes with the oxidised 4.25 gcm^{-3} paste gave the highest peak current output and discharge values as the result of a potentiostatic reduction.
2. The cycled positives have lower peak current output and discharge values.
3. Using statistical analysis it was found that with the uncycled and cycled (20 cycles) 4.85 gcm^{-3} pasted electrodes the Pb alloy support had little effect on the discharge and recharge capacities.

TABLE 12.3

As Table 12.2 but for cycled (100 cycles) porous electrodes.

Electrodes (paste density/gcm^{-3})	Discharge capacity/C	Time to reach full discharge capacity/min.
Pb		
4.25	0.51	16
4.85	1.11	50
Pb-Sb		
4.25	0.64	30
4.85	1.42	42
Pb-Sn-Ca		
4.25	1.71	38
4.85	2.40	44
Pb-Sn-Bi-Ca		
4.25	1.23	29
4.85	1.81	33

CHAPTER 13

THE a.c. IMPEDANCE OF POROUS PbO_2 ON A Pb SUPPORT IN SULPHURIC ACID

NOMENCLATURE

C_{ads}	adsorption capacitance
C_{dL}	double-layer capacitance
C_{ext}	external film capacitance
E	potential
R_{ads}	adsorption resistance
R_{ext}	external film resistance
R_{Ω}	electrolyte resistance
Z_D	impedance as defined by Equation 13.1
Z_F	impedance as defined by Equation 13.2
Z_A	impedance as defined by Equation 13.3
Z_B	impedance as defined by Equation 13.4
Z_C	impedance as defined by Equation 13.5
Z'	impedance as defined by Equation 13.6
θ	charge transfer resistance
σ	Warburg coefficient
ω	angular frequency

13.1 Introduction

Recent work in the Electrochemistry laboratory at Loughborough University has been reported which describes the impedance of PbO_2 in sulphuric acid. This is an important system and has been much investigated for it remains the major electrical storage cell positive electrode (cathode). The first measurements were made using PbO_2 deposited onto Pt [112]. It was clear from this investigation that the system was complex and that it was necessary to investigate the system over a wide frequency range and further that it was desirable to have some knowledge of the porosity and roughness. A study of the faradaic impedance of lead in 5 M H_2SO_4 in the anodic region enabled well-defined electrodes to be investigated [113]. Here the potential of an initially smooth lead surface in 5 M H_2SO_4 was held at potentials where the electrode interphase conformed to an established well-defined composition. The results of this study were again complex and it was concluded that in addition to charge transfer and Warburg impedances due to phase formation, crystallisation, nucleation and adsorption were also present. The use of frequency response analysers in order to study the PbO_2/H_2SO_4 system considerably simplified the experimental technique [114] and it was found that exchange current density measurements obtained from electrodeposited β-PbO_2 were in good agreement with the earlier reported data of others.

The ultimate system for investigation is the porous electrode where a layer of PbO_2 overlays a lead base. This conforms to the positive electrode of the lead acid cell. Two methods are available for the production of this complex system. In the first and original Planté process lead is oxidised to lead dioxide using a forming agent. In this process PbO_2 is produced from the actual support. Lazarides <u>et al</u> [115, 116] have investigated Planté formed microelectrodes. The behaviours of electrodes under a wide variety of conditions have been reported including potentiostatically controlled systems under known polarisations and equilibrium situations obtained by reducing (discharging) the systems in 3.58M H_2SO_4 (this concentration conforms to the industrial convention for Planté cells). The impedance curves were interpreted in terms of charge transfer "semicircle" followed by a Warburg line which is distorted from the expected $\pi/4$ dihedral of the planar electrode by porosity and phase $PbSO_4$ formation. The presence of an inductive component at more positive potentials was interpreted tentatively as due to the oxygen evolution reaction although other explanations could not be ruled out. Forcing the electrode potential to more negative potentials enabled charge transfer parameters to be estimated from changes in the charge transfer resistance when an allowance was made via the experimental double layer capacitance for the effective electrode area. The charge transfer coefficients obtained agreed with established data.

For the case of a mixed $PbO_2/PbSO_4$ electrode formed on pure lead by oxidation of the electrode in 5 M H_2SO_4 followed by partial reduction Kelly et al [117] found that although it was possible to match the electrode behaviour to a complicated model including adsorption of electrode species there was no possibility of abstracting the kinetic parameters as had been done with the other systems. The formation of $PbSO_4$ blocked the electrode at the potentials involved to such an extent that potential-dependent kinetic relationships were obscured by the passivating effect of the films. A rather crude extrapolation [117] allowed the estimation of the exchange current to be made and this turned out to be rather higher than that for the massive (electrodeposited) PbO_2 as expected [114]. The work on the impedance of electroformed PbO_2 in the absence of a forming agent on lead in 5 M H_2SO_4 has been extended to lead alloys [118, 119]. Alloying ingredients Sb and Bi were chosen since these were of commercial interest. Considerable differences in the impedance spectrum were engendered by the addition of these ingredients and it was argued that the effect of the alloying elements to the base lead contributed some semiconductor properties to the electrode interphase.

The most important case for experimental study is the porous PbO_2 electrode produced by the electrooxidation of a "paste" of basic lead sulphates overlaying base lead alloy. Here the electrode really consists of a PbO_2 covered lead or lead-alloy basis on which is generated (by oxidation of the leady paste) a thick porous layer of PbO_2. There are consequently two layers of PbO_2 produced one from the massive basis the other produced from the paste. With the possibility of the introduction of other elements into the lead base which can (and do) modify the behaviour of the base overlay PbO_2 the situation can quite clearly be given rise to a complex behaviour. This situation corresponds to the positive electrodes of the lead acid cell which are manufactured by pasting a mixture of leady oxide and aqueous sulphuric acid into a grid structure cast from an alloy of lead and antimony or lead, tin and calcium. The depth of the porous structure which overlays the alloy basis is 0.75 - 1mm in the case of automotive batteries which are the most frequently encountered lead cells. The system is therefore one of some complexity since it embraces elements of all the primarily considered systems. In this chapter the results of an impedance study of the simplest of these systems in which a porous structure of PbO_2 formed from a "paste" overlays a pure lead basis is presented.

13.2 Experimental procedure

The porous PbO_2 electrode was prepared in the manner reported by Kelly et al [103]. The pure lead support was arranged so that the surface was beneath the level of a Teflon shrouding. By forcing the positive paste into the cavity, a porous layer was produced (3 mm diameter; 0.76 mm deep) which terminated the electrode. A conventional lead acid battery positive paste was used as the paste; this paste consisted originally of grey oxide [41% Pb and 59% PbO (tetragonal)], sulphuric acid and water;

Fig. 13.1 The complex-plane plot (Sluyters plot) for porous PbO_2 on a pure Pb support (nominal surface area = 0.07 cm^2) in 5M H_2SO_4 at 23°C; 1190 mV; frequencies in hertz are given on the plot. The crosses (+) show experimental data and the line shows the computer match.

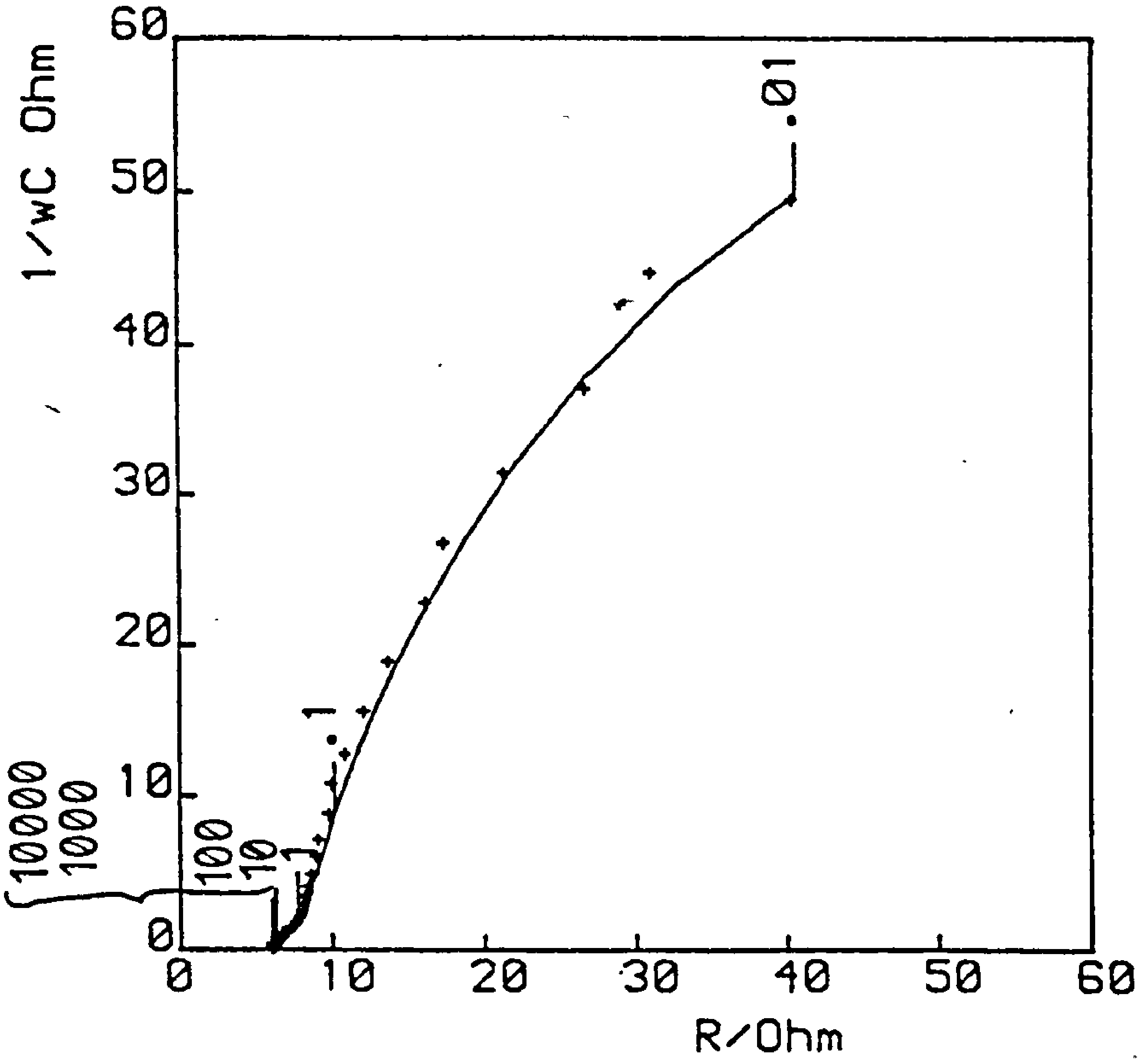

Fig. 13.2 The Randles plot corresponding to the system of Fig. 13.1 at 1190 mV. + and x correspond to experimental data (R and 1/ωC respectively) and the lines show the computer matches.

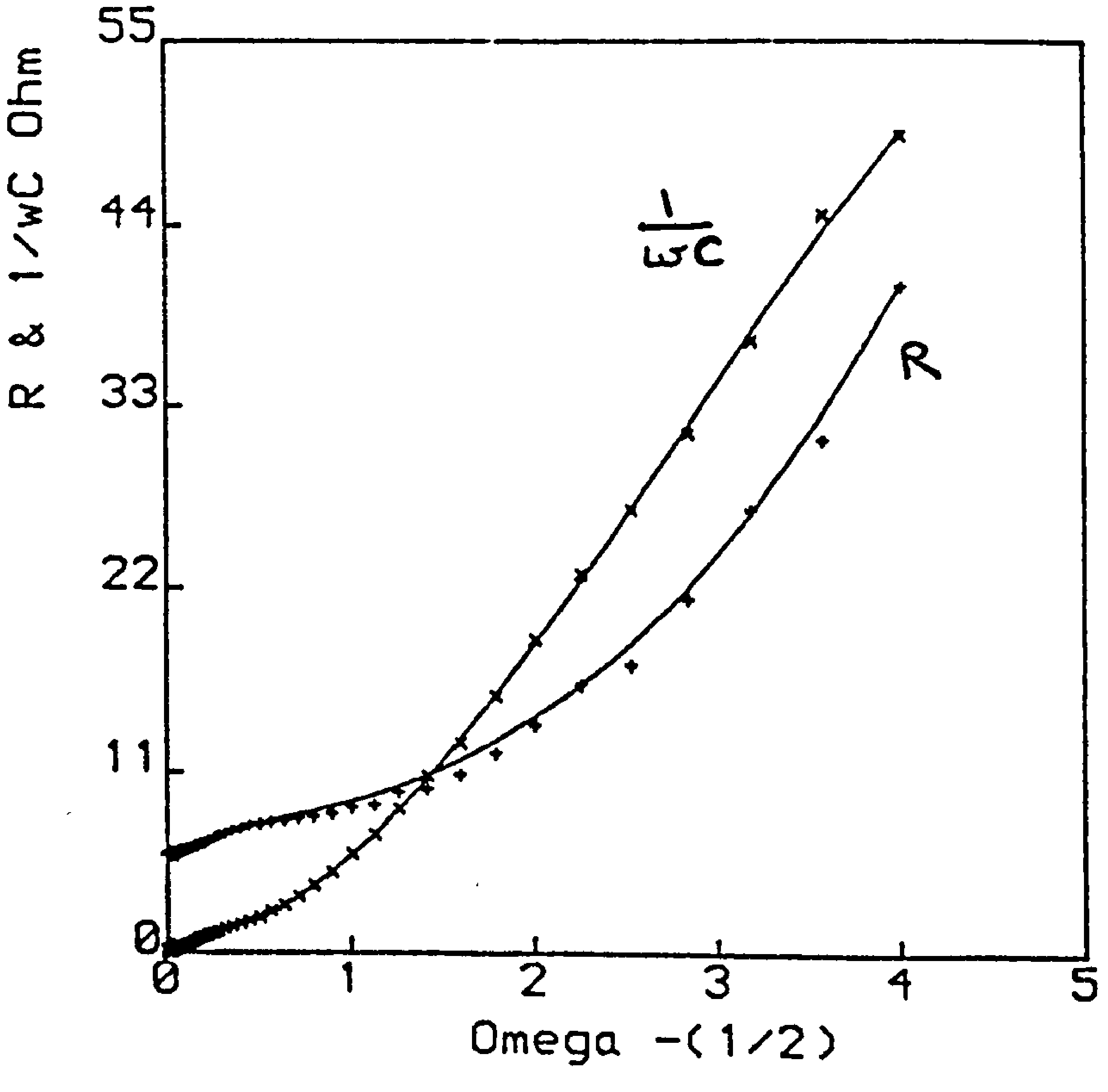

this is transformed by aerial oxidation as it loses some of the water to harden and set forming a complex structure, nominally of PbO, $PbSO_4$ and mixed basic sulphates. The final density of the paste is 4.25 gcm^{-3}. The transformation of the set paste to PbO_2 was carried out in 0.3 M H_2SO_4 [103] by oxidation for 24 hours with a total charge input of 300% based on the total oxidisable capacity of the paste. The PbO_2 content was 96%.

The electrode after formation was transferred from the dilute H_2SO_4 to 5 M H_2SO_4 and allowed to equilibrate with the electrolyte solution; the open circuit potential was 1.190V*. The impedance measurements were performed with a frequency response analyser (Solartron 1170) in conjunction with the 1186 electrochemical interface (Solartron 1186). Impedance measurements were made in the range 10 kHz - 0.01 Hz at a series of sequential potentials negative with respect to the initial open circuit potential. These were achieved by stepping from 1.190V and allowing the electrode to remain at the new potential for 0.5h prior to the impedance measurements. In this way, the impedance data corresponded to constant electrode states for after this time the measurable current had fallen to a constant low value.

13.3 Results and Discussion

Fig. 13.1 shows a complex plane (Sluyters) plot corresponding to the porous PbO_2 on a pure Pb support in 5 M H_2SO_4 at 1190mV. The shape of the plot is a rising curve exhibiting neither a well-defined high-frequency semicircle nor a Warburg line indicating the occurrence of mixed solid-state and solution processes. However, the plot curves towards the real axis at low frequency. The Randles plot (Fig. 13.2) (R and $^1/\omega C$) for the

---

*All potentials are referred to the Hg/Hg_2SO_4 electrode in the same solution.

Fig. 13.3 Details as in Fig. 13.1 but at 1180 mV.

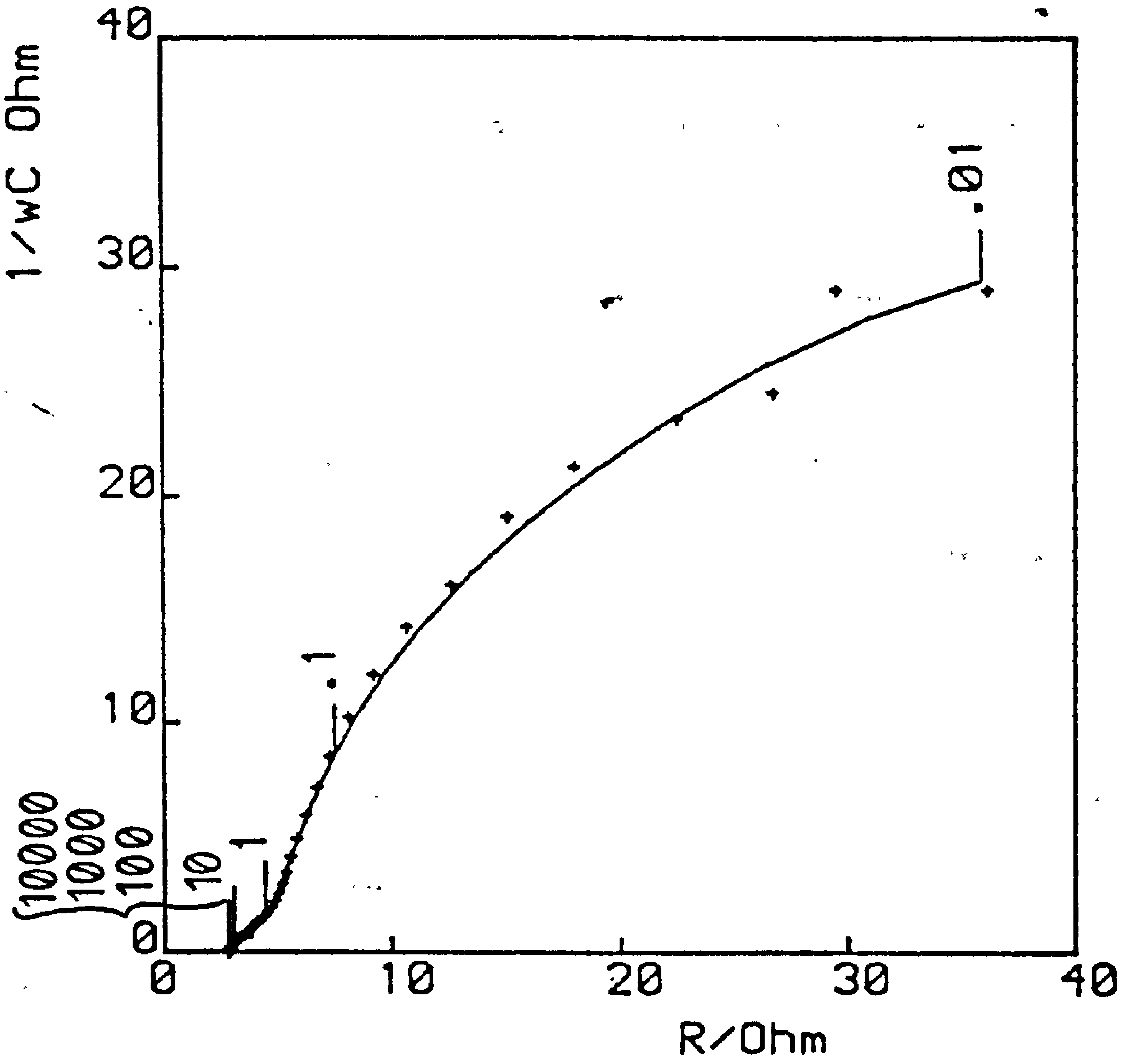

Fig. 13.4 Details as in Fig. 13.2 but at 1180 mV.

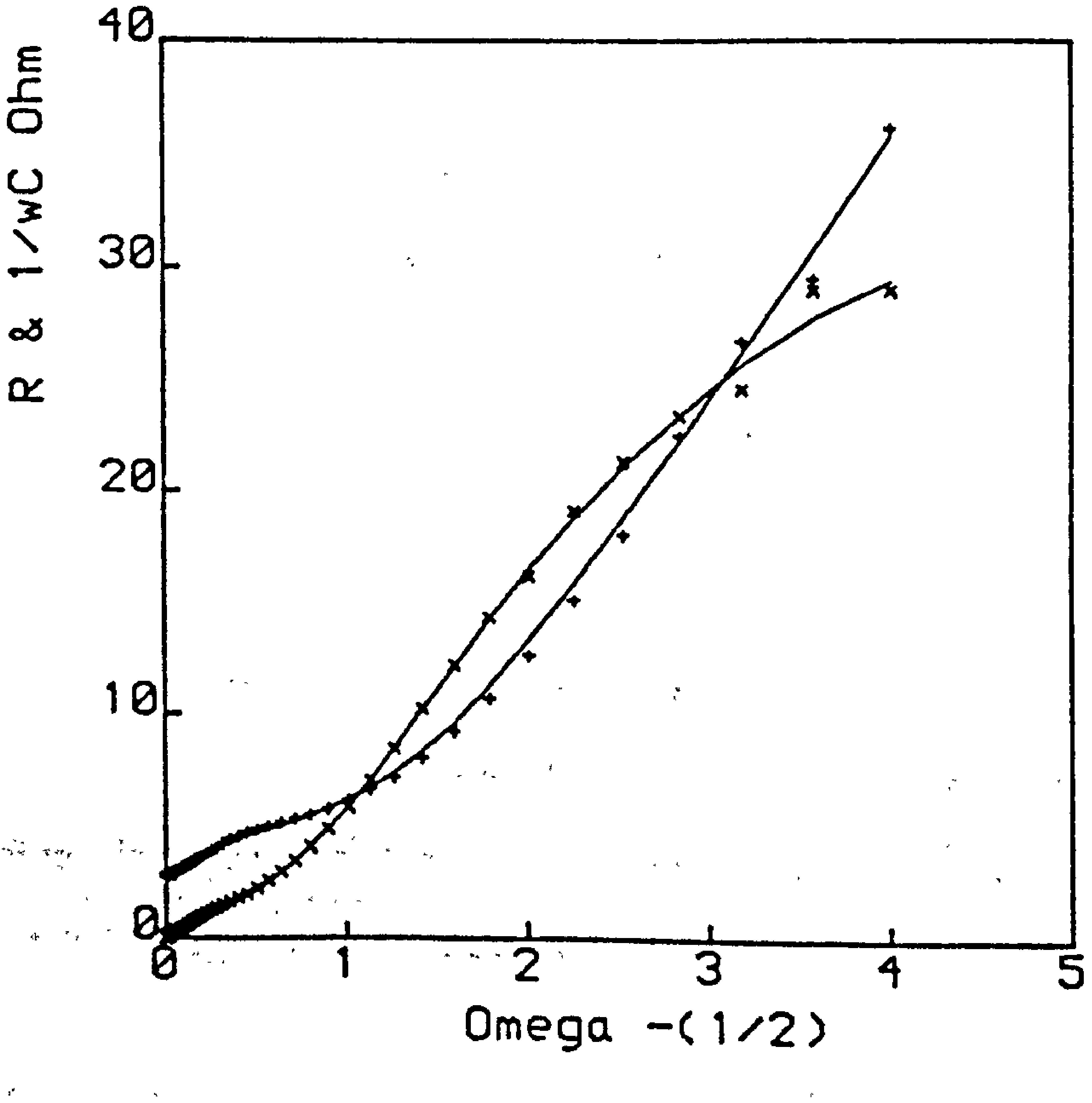

in-phase and out-of-phase components of the electrode impedance show behaviour indicative of charge-transfer and diffusion at high frequency and a cross-over at intermediate frequencies. Figs. 13.3 and 13.4 correspond to the electrode kept at the potential $E = 1.180V$ and the Sluyters plot (Fig. 13.3) shows that the line is curving more towards the real axis. The two lines in Fig. 13.4 still cross over which indicates adsorption of reactants which is confirmed by the presence of a positive intercept as a result of plotting $^1/C$ against $\omega^{-\frac{1}{2}}$ [113]. The identity of the adsorbed species cannot be stated with certainty. There is evidence [120] that the reduction takes place by a process analogus to the following:

$$PbO_{2(s)} + 2H^+ \rightleftharpoons PbO_2(H^+)_{2(ads)} \qquad (a)$$

$$PbO_2(H^+)_{2(ads)} + 2e^- \rightleftharpoons Pb(OH)_2 \qquad (b)$$

$$Pb(OH)_2 + H_2SO_4 \rightleftharpoons PbSO_{4(s)} + 2H_2O \qquad (c)$$

This scheme is open to the objection that the electrode potential may be too positive for the adsorption of H^+. However, the reaction scheme:

$$PbO_2 + 2H_2SO_4 \rightleftharpoons PbO_2.2H_2SO_{4(ads)} \qquad (d)$$

$$PbO_2.2H_2SO_{4(ads)} + 2e^- \longrightarrow PbSO_4 + 2H_2O + SO_4^{2-} \qquad (e)$$

would appear to be less objectionable. The simple adsorption of the bisulphite ion at the high positive potential will also contribute to the pseudo-capacitance. Attempts to describe the impedance spectrum in terms of a simple Randles circuit modified for an adsorption process indicated that although such a model fitted the data in a very limited high frequency range, in order to explain a dihedral at low frequency greater than $\pi/4$ a capacitive component external to the interphase is required.

Kelly et al [117] established that for a PbO_2 surface formed on pure lead and partially converted to $PbSO_4$ for frequencies up to 70.5 Hz a series capacitance was sufficient for the representation of the film of $PbSO_4$. At the lower frequencies employed in most of the present work this was found to be inadequate and a parallel resistance-capacitance circuit combination was required in order to express the ability of the reduced layer (mainly $PbSO_4$) to conduct electricity. Adsorption had been introduced in the electrode analogue developed by Kelly et al [117] for the partially discharged PbO_2 film and a pure lead basic electrode by a resistance-capacitance series conversion shunting the double layer in parallel with the faradaic path in the manner of Laitinen and Randles [87] representing a reaction in the adsorbed state and for which reactants and products do not leave the reaction site. (It is of interest in this connection to note that Lazarides et al [115] experimenting with Planté-formed electrodes (perchlorate formation) did not need to take into account adsorption at all at the electrode in the frequency range down to ∿ 1 Hz.). This model was found to be inadequate for the representation of the present duplex complex electrode and the presence of charge transfer reaction involving a preceding reaction of the types inherent in the equations (a)-(e) was recognised as represented in Fig. 13.2. It must be concluded at this stage that the behaviour reported here is indicative of the porous front of the electrode, that observed by Lazarides et al [115] representing the behaviour of the layer underlying the gross porous matrix.

Figs. 13.5 and 13.6 correspond to the electrode at E = 1.170V. The Sluyters plot still curves downwards and the lines in the Randles plot touch each other for a period and then separate into diverging curves. Figs. 13.7-13.16 relate to the electrode behaviour for a series of potentials in the range 1150 - 700 mV. A feature of the Sluyters plots

Fig. 13.5 Details as in Fig. 13.1 but at 1170 mV.

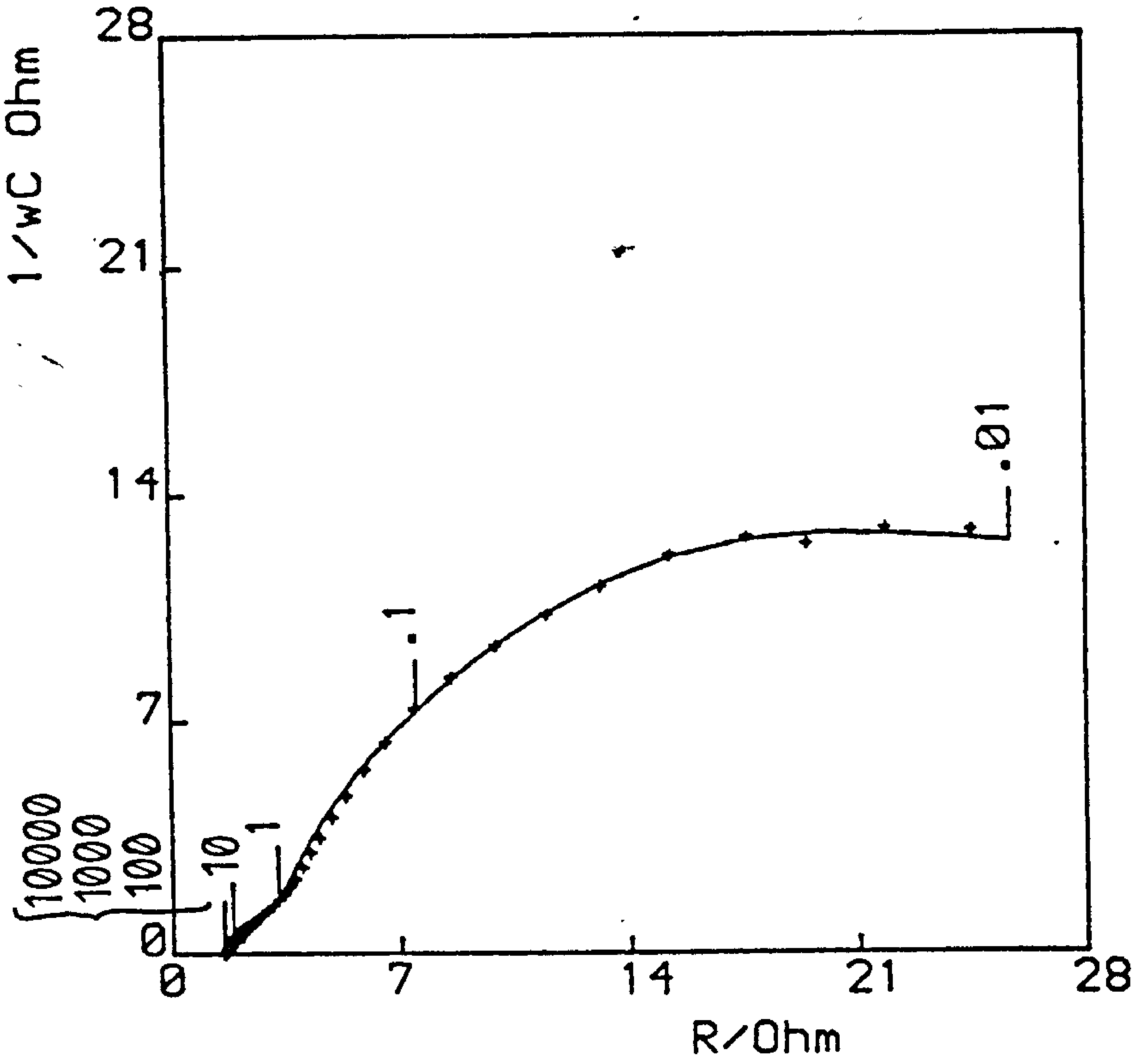

Fig. 13.6 Details as in Fig. 13.2 but at 1170 mV.

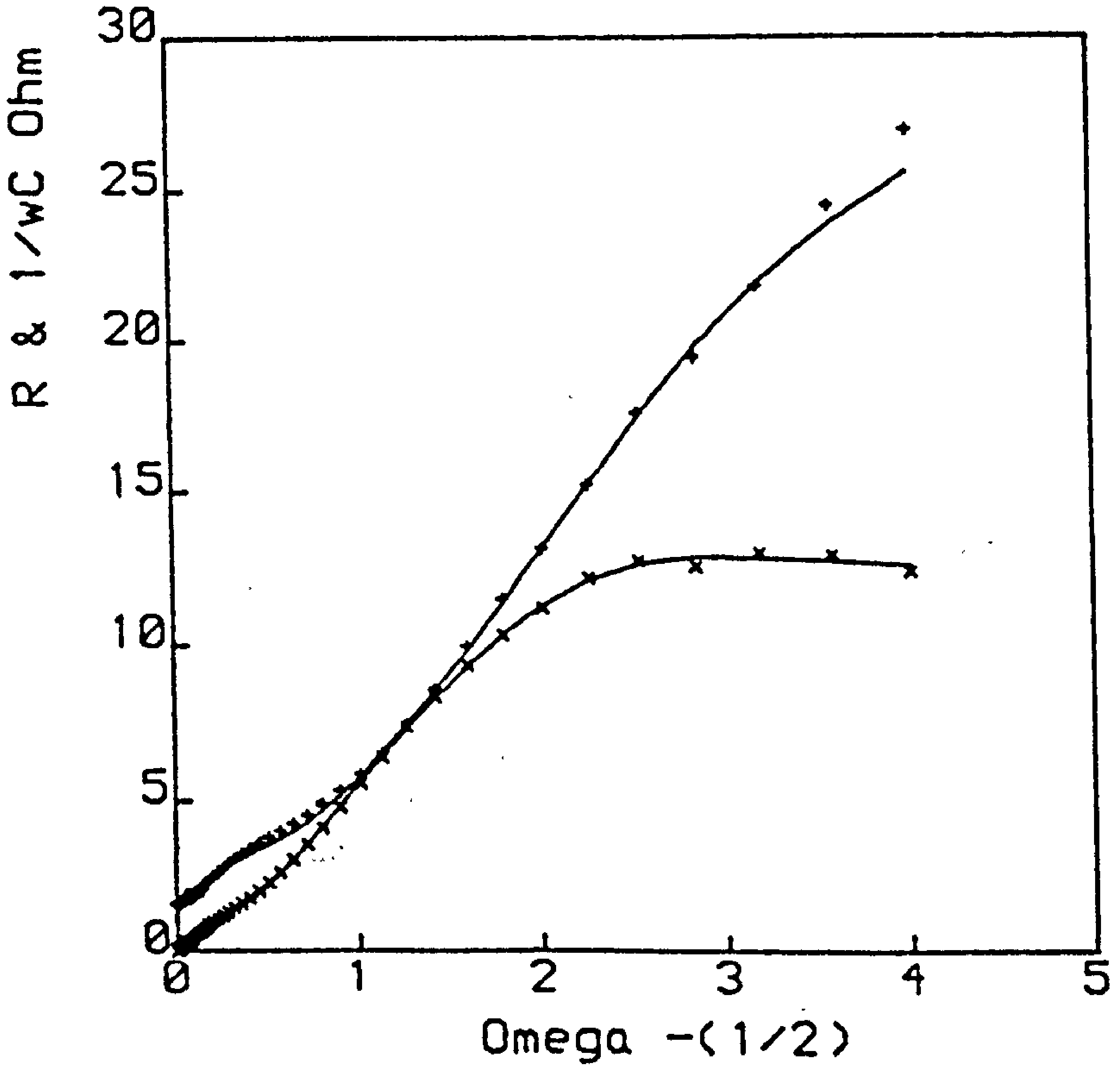

Fig. 13.7 Details as in Fig. 13.1 but at 1150 mV.

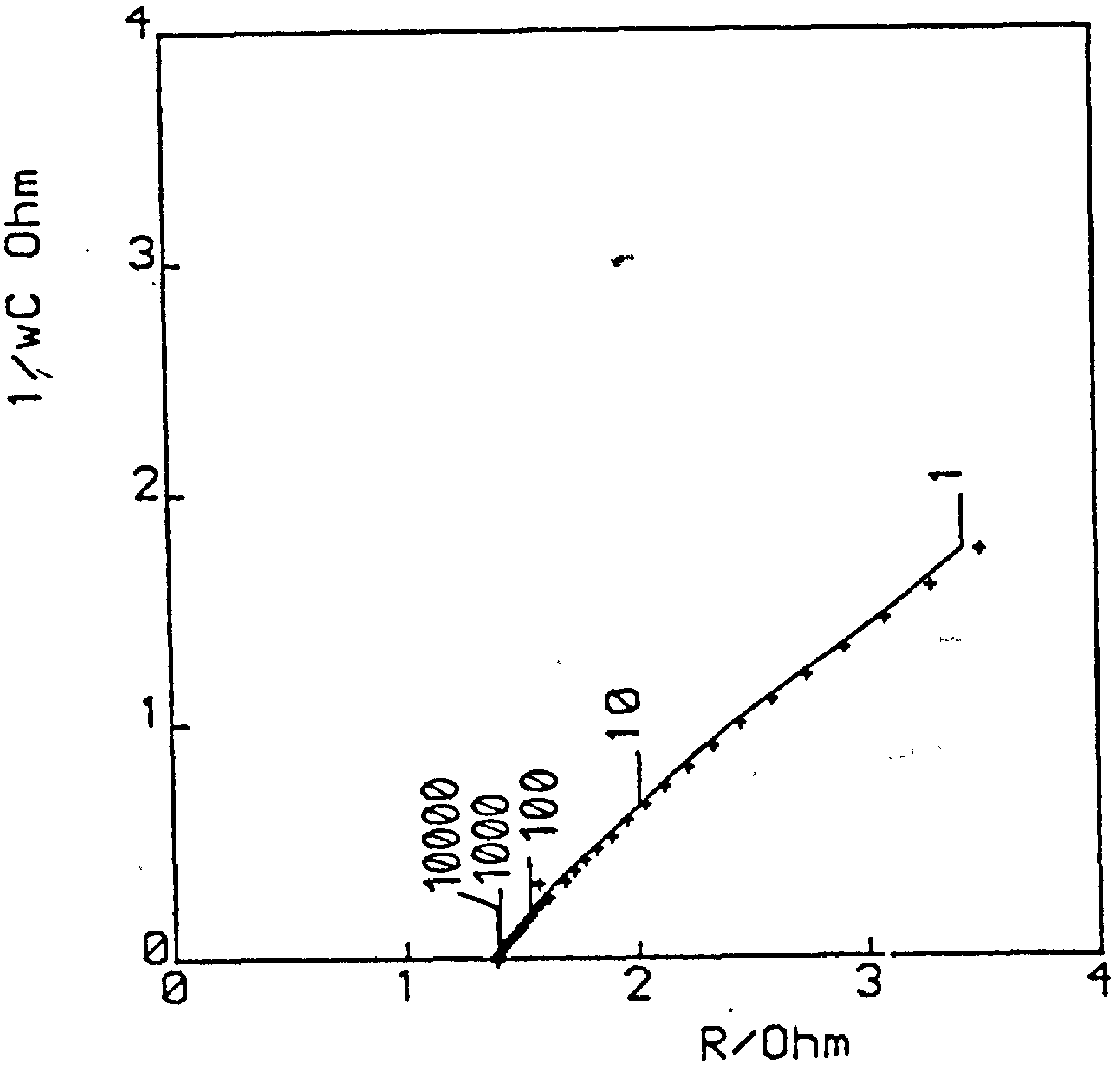

Fig. 13.8 Details as in Fig. 13.2 but at 1150 mV.

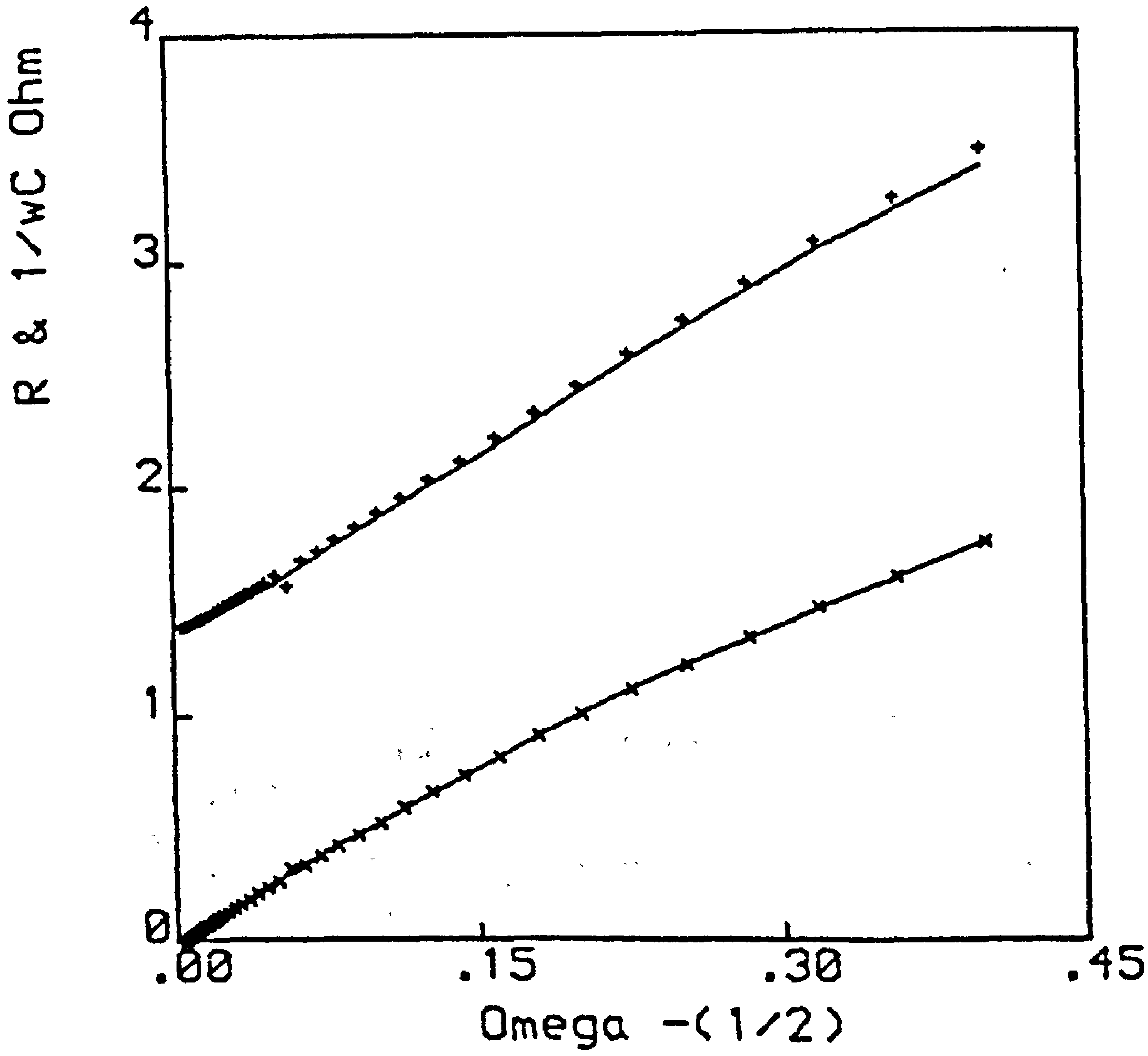

Fig. 13.9 Details as in Fig. 13.1 but at 1100 mV.

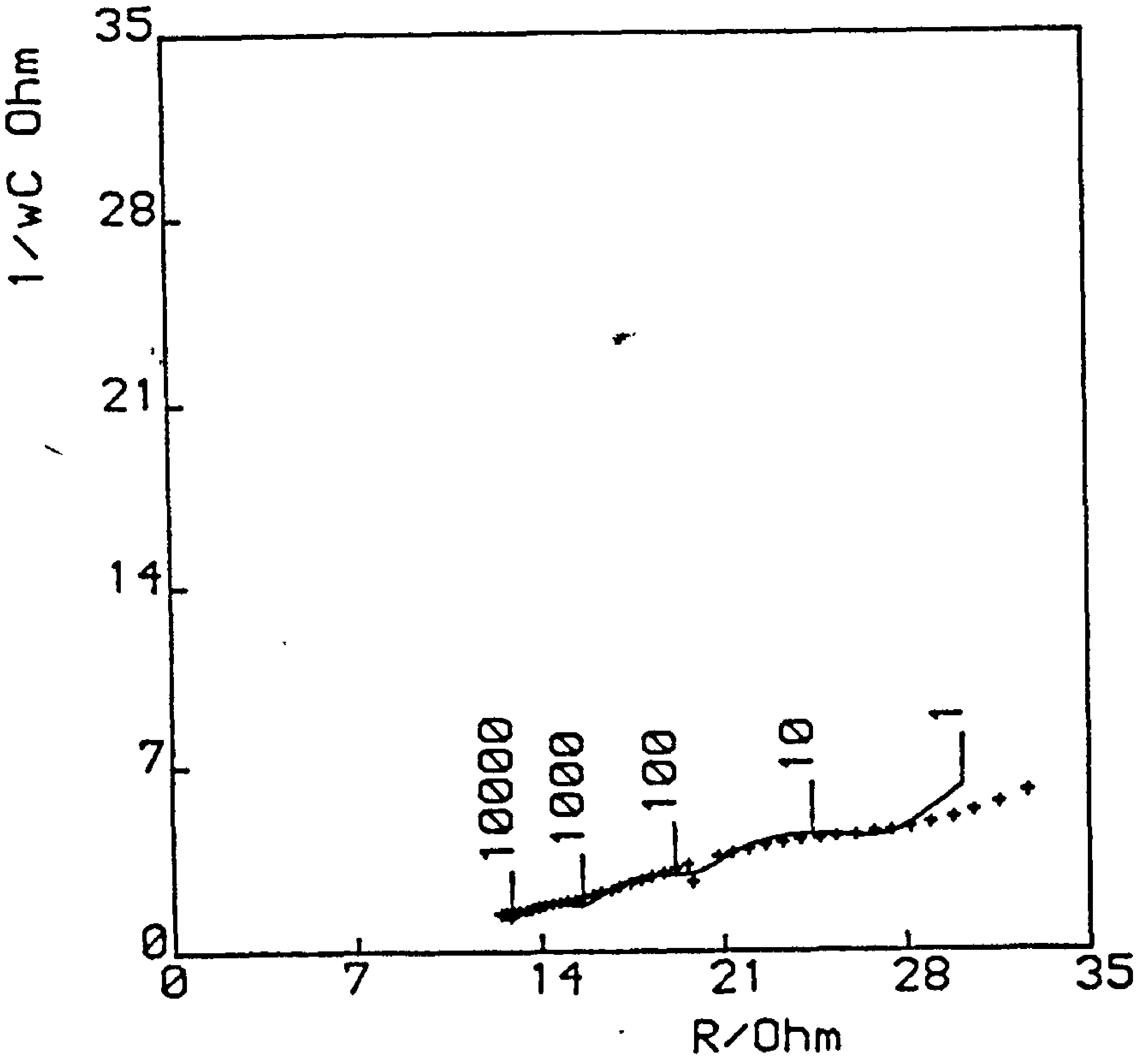

Fig. 13.10 Details as in Fig. 13.2 but at 1100 mV.

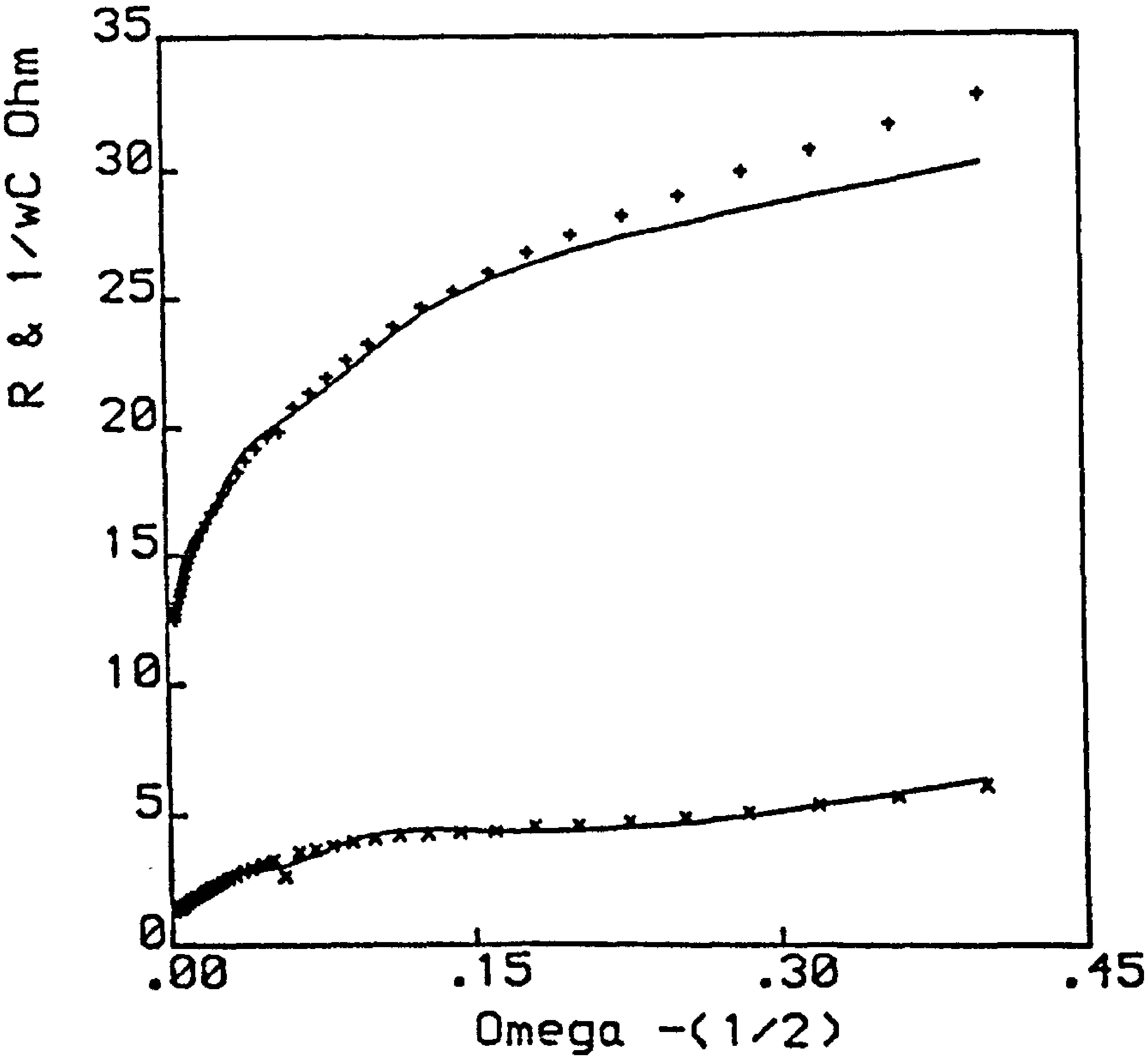

Fig. 13.11 Details as in Fig. 13.1 but at 1000 mV.

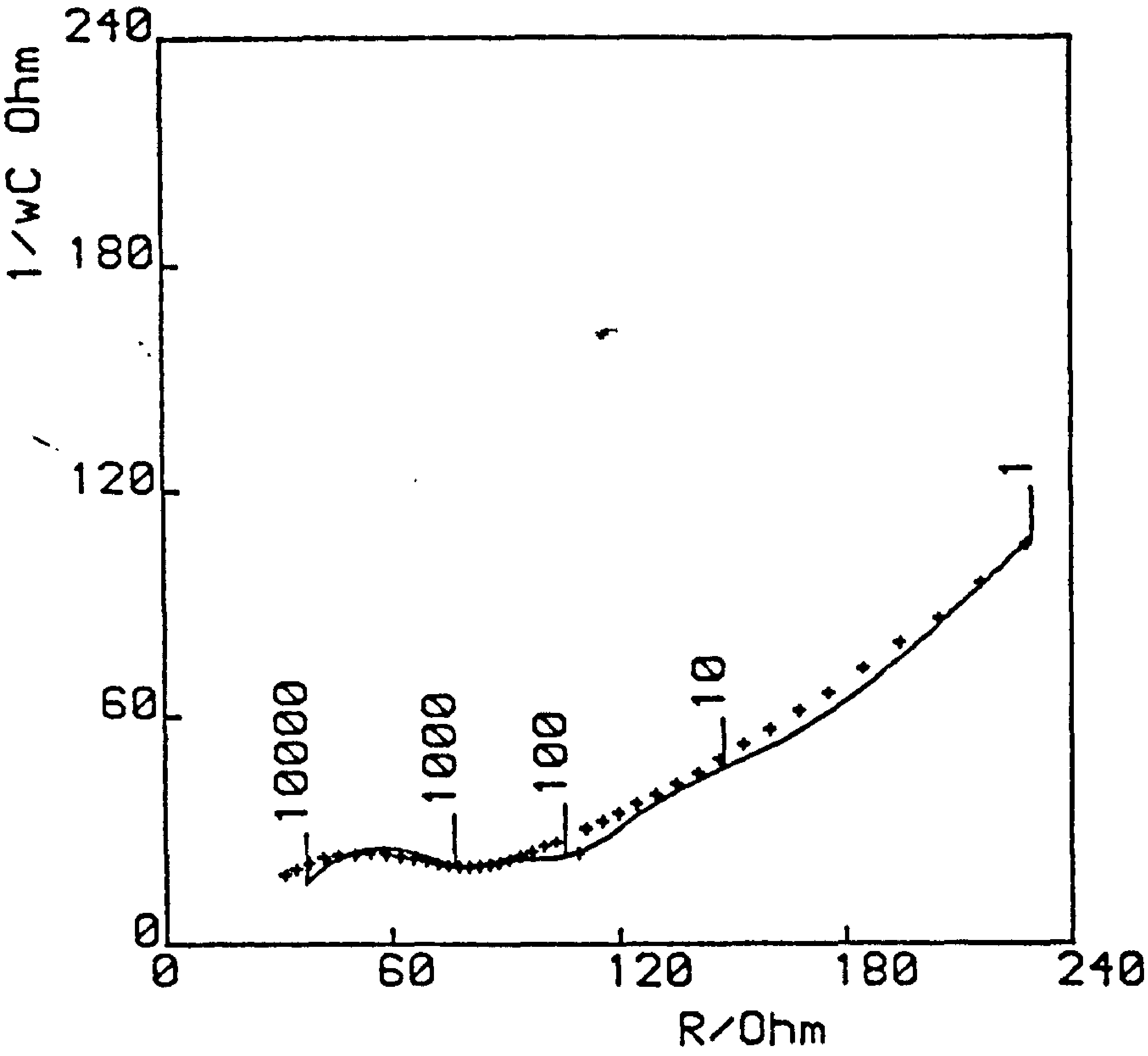

Fig. 13.12 Details as in Fig. 13.2 but at 1000 mV.

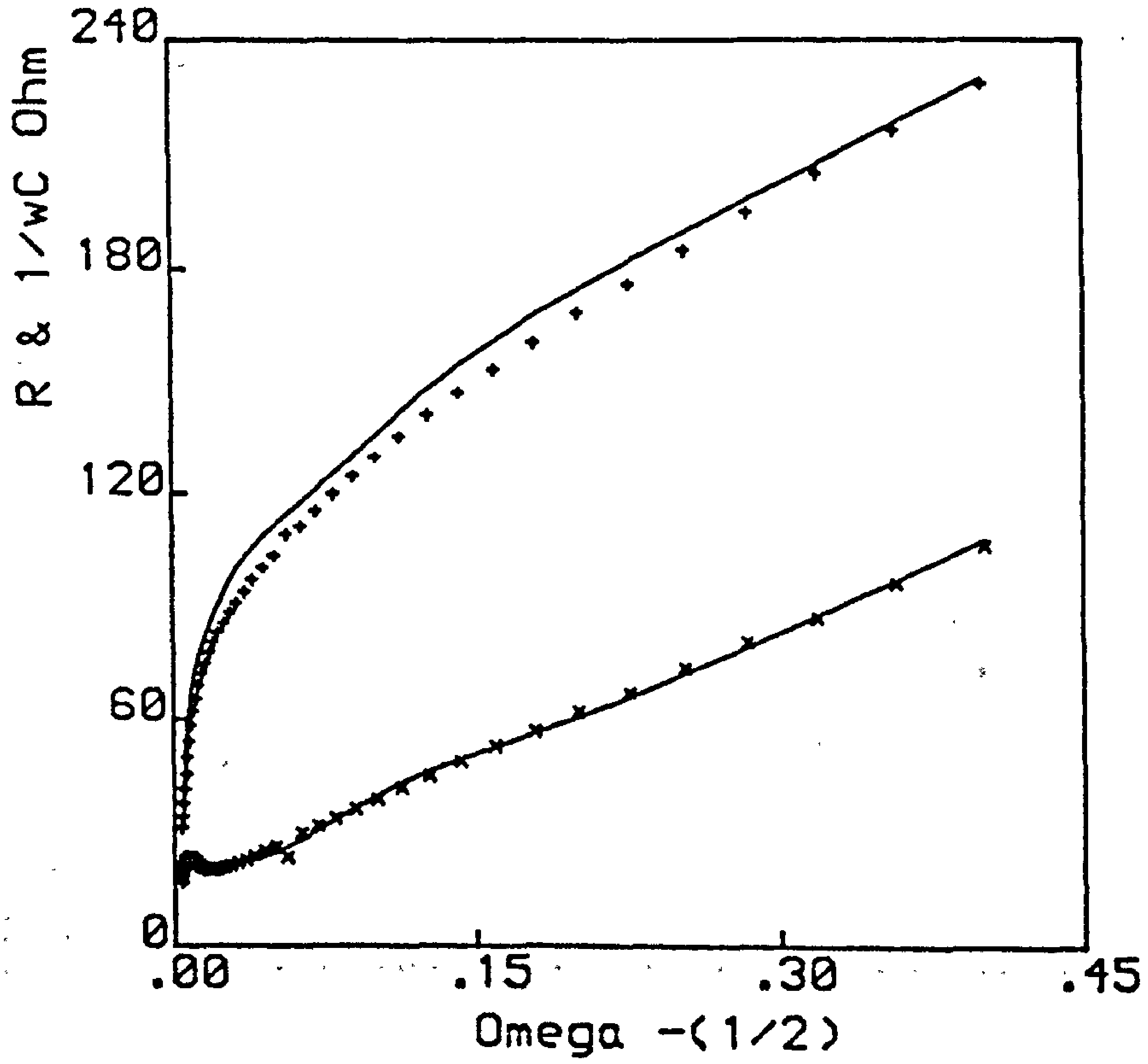

Fig. 13.13 Details as in Fig. 13.1 but at 900 mV.

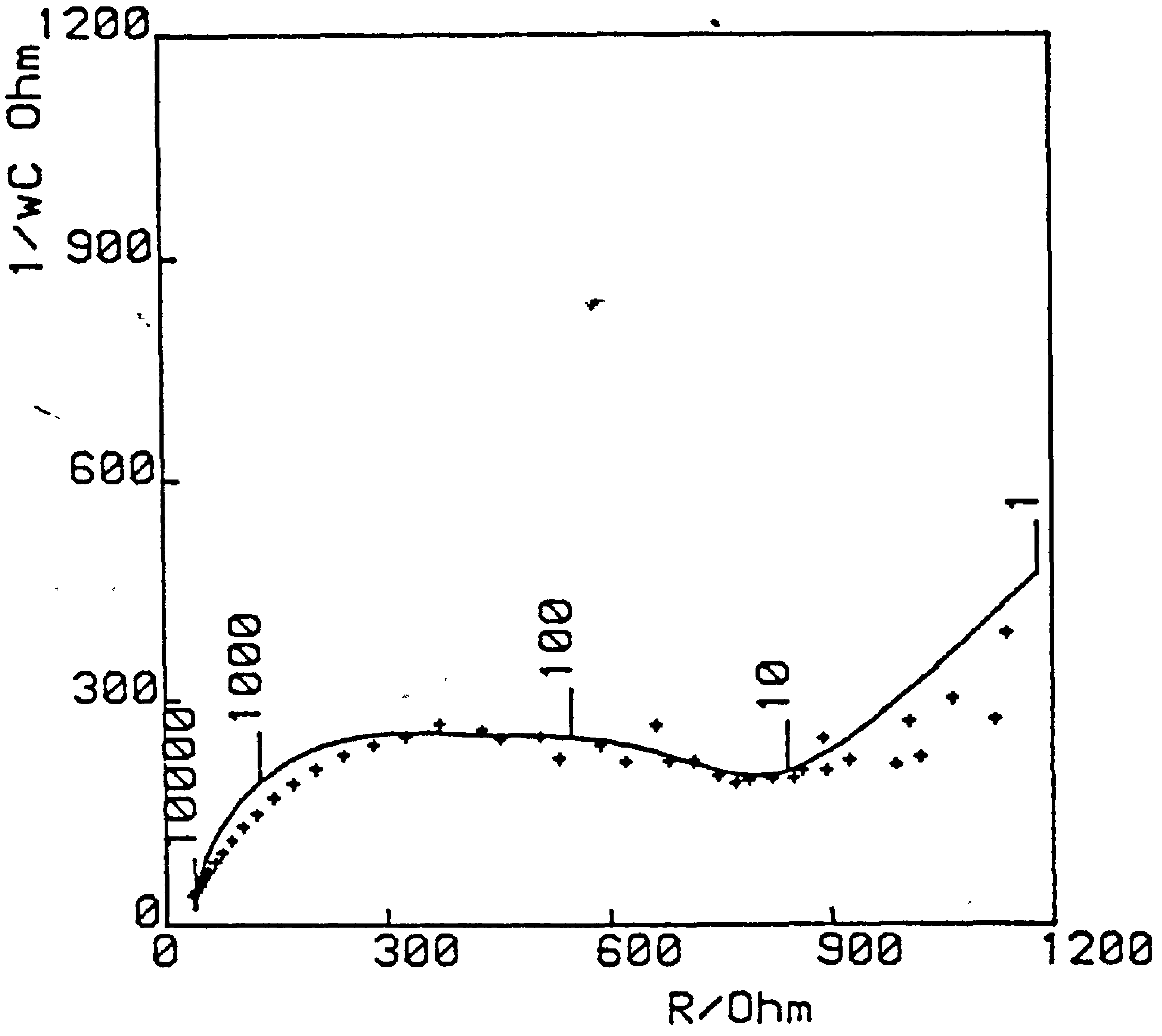

Fig. 13.14 Details as in Fig. 13.2 but at 900 mV.

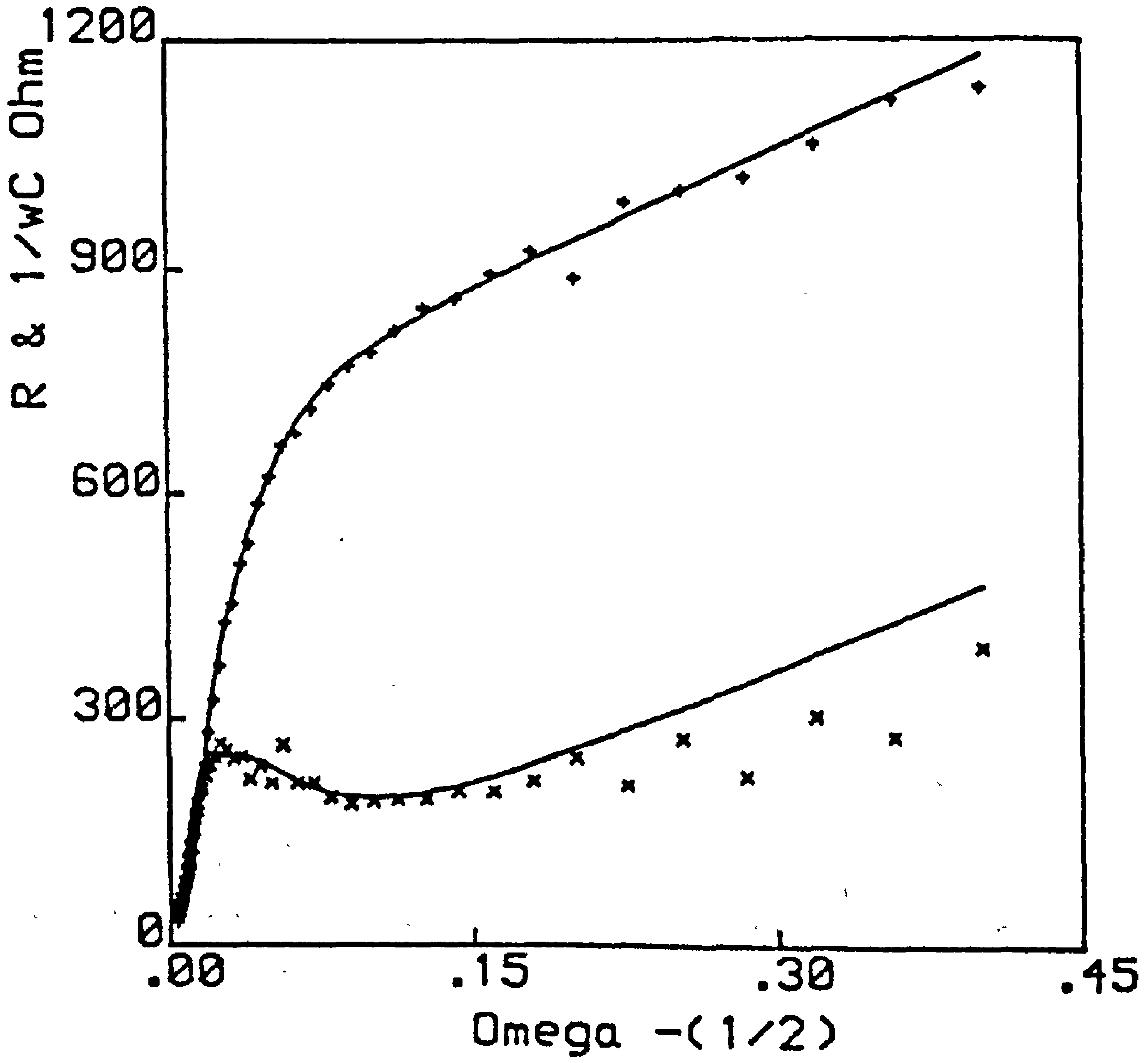

Fig. 13.15   Details as in Fig. 13.1 but at 700 mV.

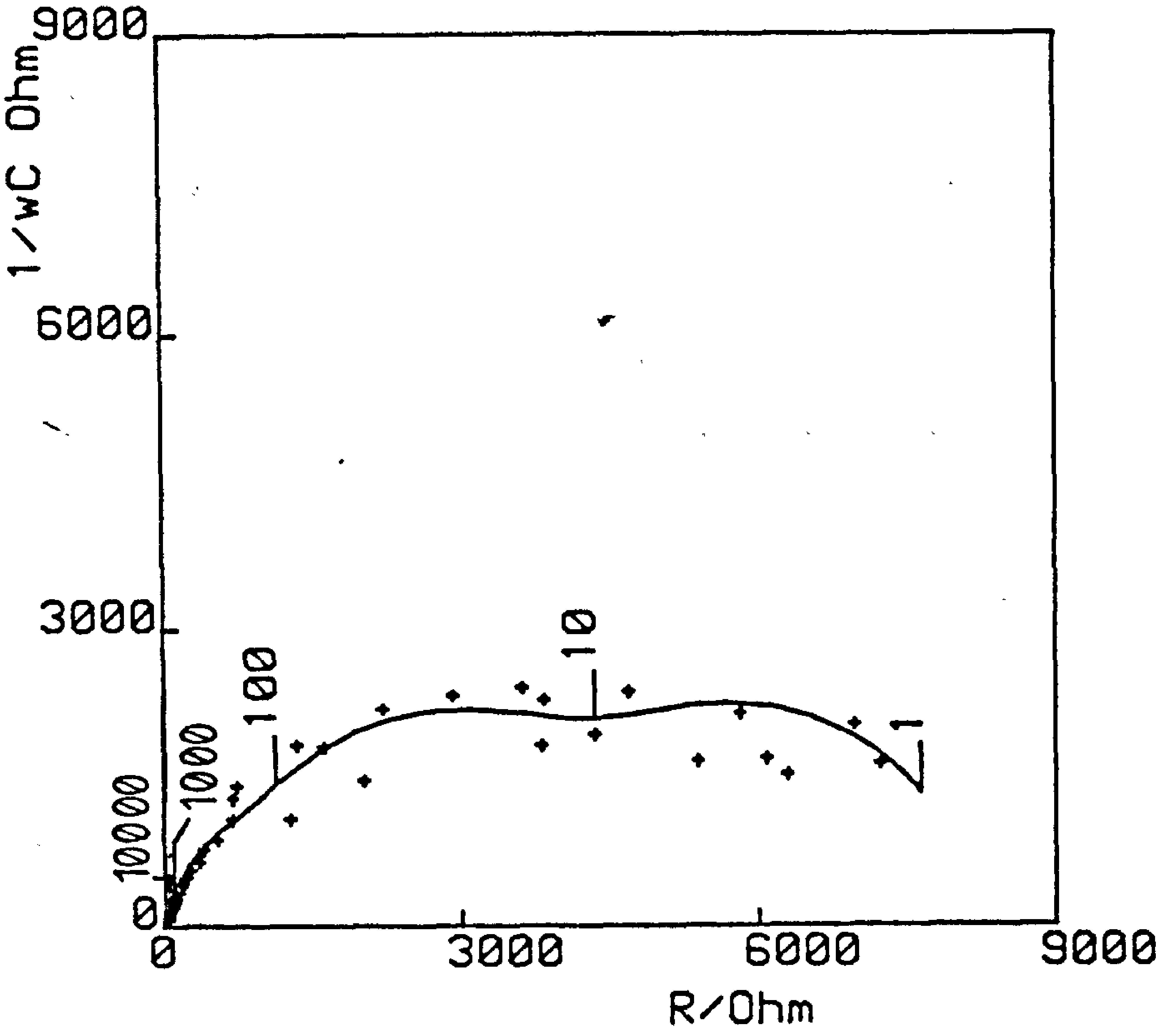

Fig. 13.16   Details as in Fig. 13.2 but at 700 mV.

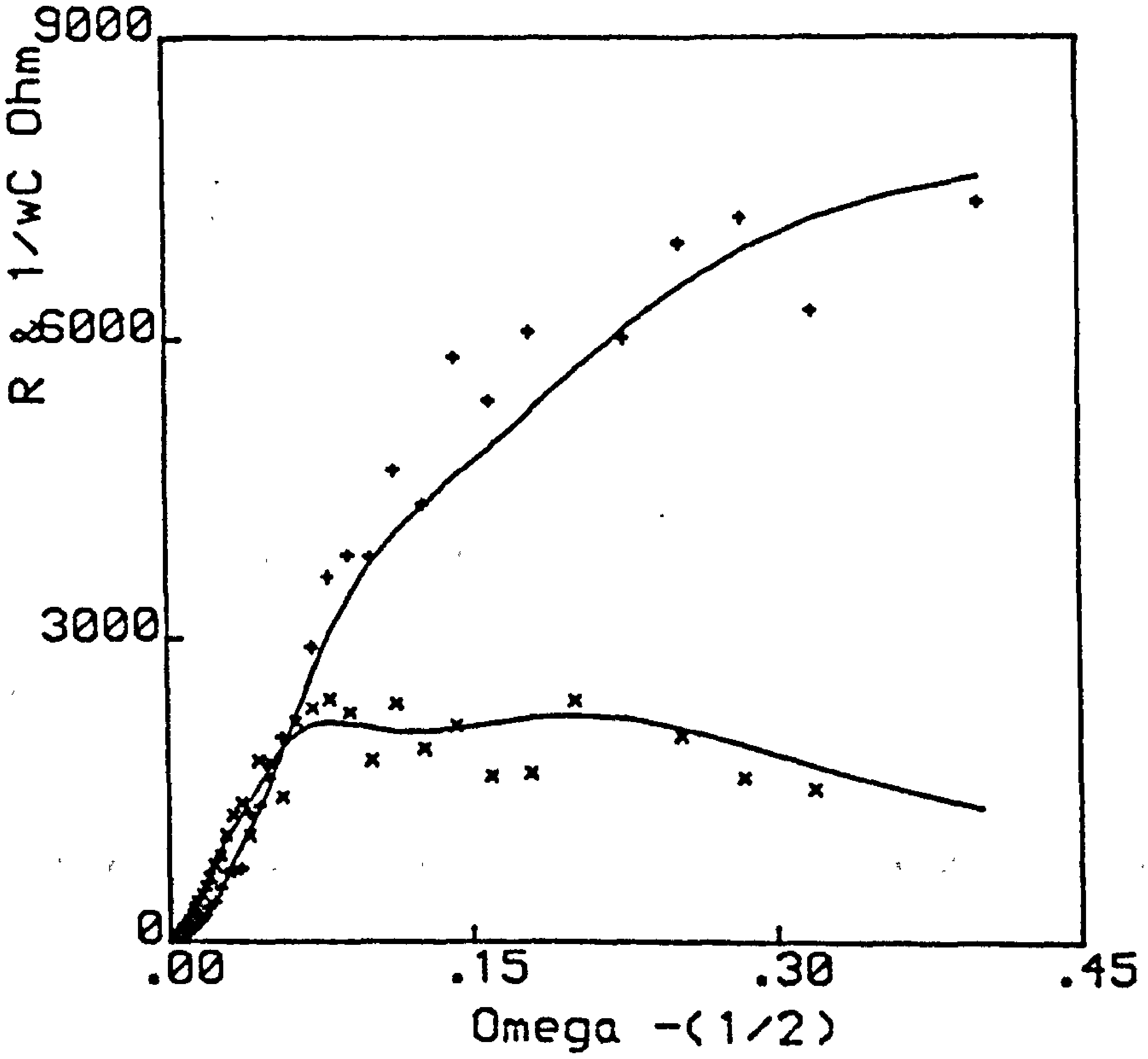

is that a semicircle appears in the high frequency region, together with a Warburg line, as the electrode approaches 700 mV. From 1000 - 700 mV the high-frequency semicircle increases in size which emphasises the thickening of the lead sulphate film on the PbO_2 surface. At 700 mV the sulphate layer does not totally passivate the electrode because there is still current flowing through the electrode surface, rather the rate of reaction (as shown by the increased value of θ) has slowed down.

The analogue shown in Fig. 13.17 expresses a reaction occurring at the electrode which is controlled by charge transfer, diffusion in solution and adsorption in series, coupled to a potential-dependent surface film. Adsorption refers to lead dioxide adsorbing various species and is represented by resistive and capacitive circuit elements in parallel and the surface film, again resistive and capacitive components, represents the lead sulphate layer. Hence the analogue in Fig. 13.17 was used to match the experimental data in Figs. 13.1-13.16 and as can be seen, the computer matches fit the results very well. This matching was performed by writing the complex equations for the cell analogue:

$$Z_D = -i/\omega C_{dL} \tag{13.1}$$

$$Z_F = \theta + (\sigma\omega^{-\frac{1}{2}} - i\sigma\omega^{-\frac{1}{2}}) \tag{13.2}$$

$$Z_A = \left(\frac{1}{R_{ads}} + \frac{1}{-i/\omega C_{ads}} \right)^{-1} \tag{13.3}$$

$$Z_B = Z_F + Z_A \tag{13.4}$$

$$Z_C = \left(\frac{1}{R_{ext}} + \frac{1}{-i/\omega C_{ext}} \right)^{-1} \tag{13.5}$$

for which the impedance is given by:

$$Z' = R_\Omega + \left(\frac{1}{Z_D} + \frac{1}{Z_B} \right)^{-1} + Z_C \tag{13.6}$$

Using the complex number handling capabilities of the Honeywell

Fig. 13.17 Proposed model for cell analogue.

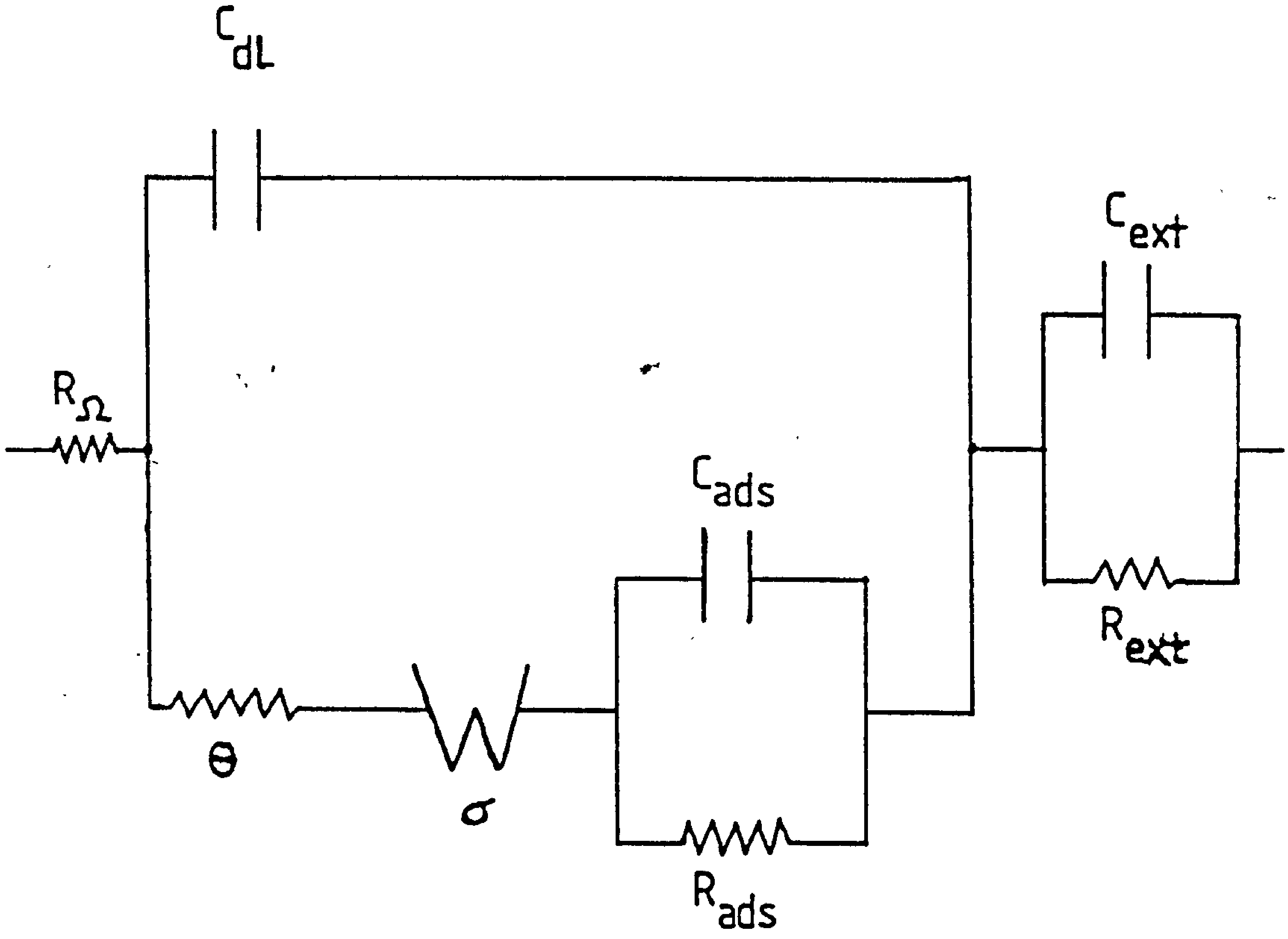

Fig. 13.18 Plot of $\log_{10}$ θ vs. potential for porous PbO_2 on a pure Pb support in the potential region 700 - 1150 mV.

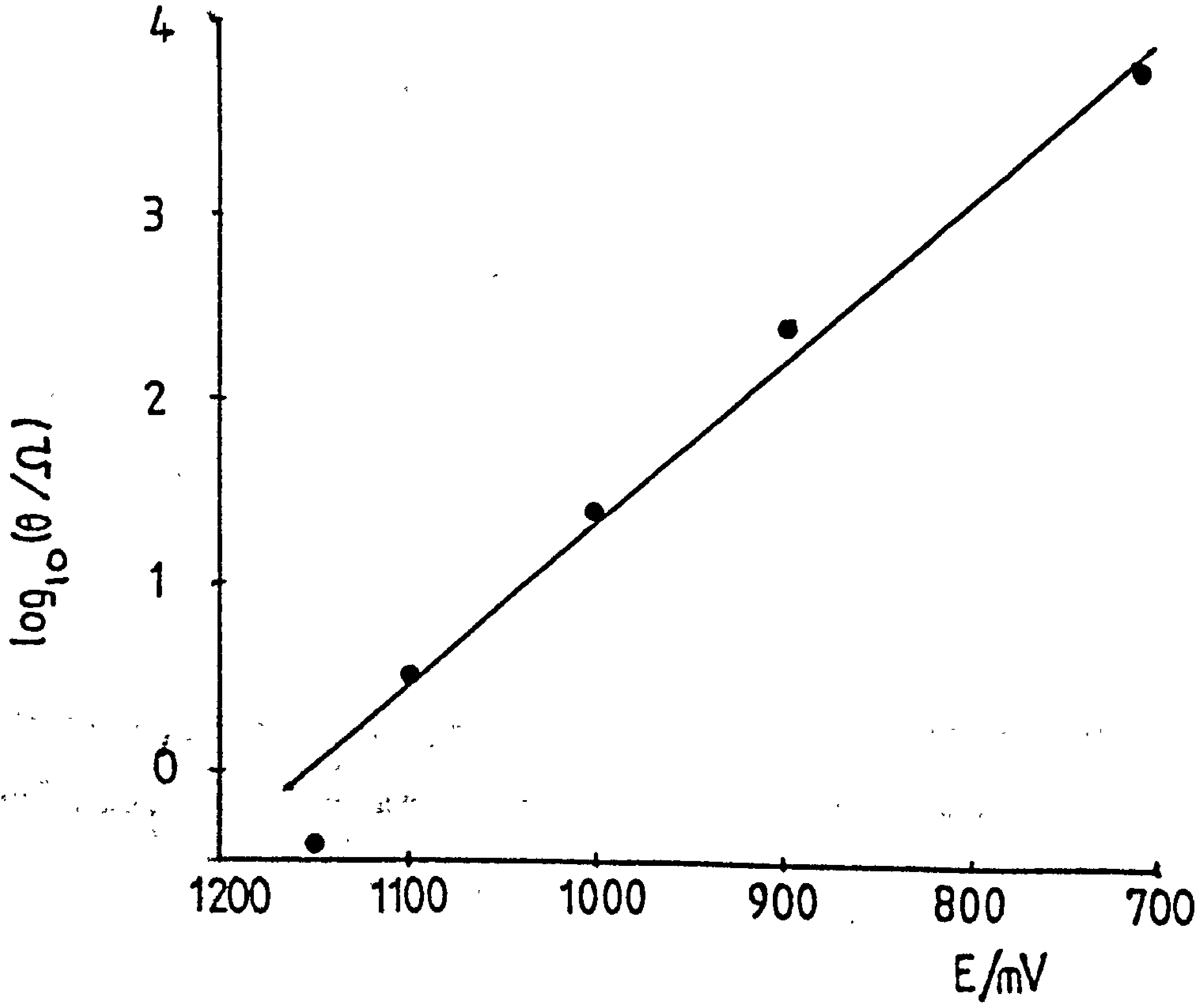

Multics DPS8/M computer equation (13.6) was decomposed into real and imaginary parts (R and C equations). The impedance data were matched on the basis of either of these equations. The procedure involves giving estimated values (x') for the circuit elements (x) and each approximate value (x') is expanded using Taylor's theorem but the second-order and higher order terms are neglected.

$$x = x' + \Delta x \tag{13.7}$$

The values of the impedance components are then calculated using the approximate values for the circuit elements for each of the data points available. A least-squares process is used to reduce these equations to the number required to solve for all the circuit elements. The process is repeated until a sufficiently accurate value of each impedance component has been obtained [116, 118, 121].

As the Figs. 13.1-13.16 show the behaviour of the electrode is well described by the model. The magnitudes of the kinetic parameters of Table 13.1 indicate that the electrode is becoming rapidly blocked by a passivating layer of $PbSO_4$ as the potential is stepped sequentially to more negative potentials. The magnitudes of C_{ext} and R_{ext} indicate an abrupt thickening of the $PbSO_4$ layer as the potential moves from 1.170 to 1.150V.

An important difference in the electrode behaviour was that at the more negative of the potentials investigated the electrode could only be matched to the analogue in Fig. 13.17 down to $\sim$ 1 Hz. This behaviour has been discussed [88] and it was stressed that at such low frequencies the impedances due to crystallisation and nucleation reactions ought to be important. Another possibility is that as the electrode is forced progressively negative the electrode becomes coated with $PbSO_4$ giving rise to pore blocking and complete obscuring of the electrode. At

TABLE 13.1

Electrode characteristics obtained from computer match for a porous PbO_2 electrode at various potentials (nominal surface area = 0.07 cm^2).

Potential/V — Kinetic Parameters	1.190	1.180	1.170	1.150	1.100	1.000	0.900	0.700
	10kHz - 0.01Hz			10kHz - 1Hz				
R_Ω/Ω	6.08	2.81	1.57	1.39	12.49	31.68	37.38	45.00
Charge transfer θ/Ω	1.455	1.470	1.499	0.3833	3.499	30.81	327.5	4040
C_{dL}/F	2.0944E-2	2.0E-2	2.0328E-2	6.8262E-3	1.2823E-5	1.493E-5	4.9755E-6	1.3622E-6
$\sigma/\Omega s^{-\frac{1}{2}}$	1.854	2.094	1.803	4.065	14.77	261.6	1139	536.7
R_{ads}/Ω	3.238	11.31	2.782	0.2614	3.355	20.5	565	2770
C_{ads}/F	1.320	0.4418	0.4542	0.1526	2.4245E-4	5.619E-4	2.2079E-2	1.6485E-5
C_{ext}/F	0.2982	0.5788	0.4279	4.9076E-3	2.3682E-3	9.3677E-7	7.7234E-7	7.3874E-7
R_{ext}/Ω	98.04	36.24	14.77	8.3144E-2	4.950	44.75	380.4	909.1

low frequency ∿ 1mHz the impedance plots approach the real axis suggesting that the electrochemistry is controlled mainly by the transport of charge through a thick film of lead sulphate.

Qualitatively the behaviour can be understood if at sufficiently low frequency the signal penetrates to the primary underlayer of PbO_2 which overlays the lead base, once this has been reduced the electrode is effectively blocked.

Referring back to the data corresponding to the last five potentials (1150-700mV) R_Ω increases as more $PbSO_4$ is produced on the electrode. The adsorption resistance, R_{ads}, and the external film resistance, R_{ext}, increase with decreasing potential as the PbO_2 surface is covered more effectively with $PbSO_4$. However, the capacitance of the electrode sulphate layer (C_{ext}) decreases at more negative potential. This is to be expected since at more negative potentials the lead sulphate layer thickens and the capacitance decreases according to the prediction of the flat capacitor theory.

It was considered unadvisable to reduce the potential further since the preferred working limit of the PbO_2 electrode is only ∿ 300mV less negative than the fully charged open circuit potential ∿ 1.160 V; forcing the electrode more negative than this usually results in undesirable effects. However, it is clear that as the electrode is reduced (discharged) the general impedance behaviour remains constant. Kelly et al [118] showed that the change in θ with potential was approximately 84 mV per decade for a flat lead electrode covered with PbO_2 in a limited potential region (930-970 mV). The data plotted out in Fig. 13.18, over the range 1150-700 mV, show that θ for the porous electrode changes by 90 mV per decade. It is difficult to interpret the meaning of this figure, however, it does show quite clearly that the "passivity factor" due to sulphate blocking the electrode swamps out the change in reaction rate due to kinetic effects.

13.4 Conclusions

1. The proposed model for the porous PbO_2 electrode in this chapter has been found to fit the experimental data quite well. However, the analogue does have limitations since it does not take into account crystallisation and nucleation reactions.
2. The model in Fig. 13.17 has been tested successfully on another porous PbO_2 matrix on a pure lead support.
3. Various other models have been tried, some were simpler than the model shown in Fig. 13.17 and others more complicated, but each could not match the experimental data very well over the potential range employed.

CHAPTER 14

THE a.c. STUDIES ON POROUS PbO_2 ON VARIOUS LEAD ALLOY SUPPORTS IN SULPHURIC ACID

NOMENCLATURE

C_{ads}	adsorption capacitance
C_{dL}	double-layer capacitance
C_{ext}	external film capacitance
E	potential
R_{ads}	adsorption resistance
R_{ext}	external film resistance
R_{Ω}	electrolyte resistance
θ	charge transfer resistance
σ	Warburg coefficient

14.1 Introduction

In the previous chapter the impedance behaviour of a porous PbO_2 matrix formed electrochemically from a conventional paste of leady oxides and sulphuric acid which overlayed a PbO_2-covered lead basis was discussed. It has been emphasised that such a complicated duplex electrode represents the positive electrode in the lead-acid cell. The impedance-frequency relationships have been explained in terms of charge-transfer at an electrode at which strongly adsorbed intermediates and reactants are present.

Pure lead supports are never used for the supporting grids in the lead cell. Alloying with Sb or Ca/Sn produces a much more mechanically satisfactory support. The former is rather an objectionable additive since the overvoltage at the Sb electrode is very low which combined with the "solubility" of Sb at the operating potentials serves to increase the hydrogen evolution rate on the negative electrode with attendant loss of charging efficiency and shelf life. The use of both Sb and Ca/Sn introduce changes in operational behaviour of the lead cell which are both fundamental and well-known. It is important to know if the impedance method is able to detect such differences and if possible provide explanations for any differences observed. This chapter records the results of experiments on three alloys of interest.

14.2 Experimental procedure

The experimental details are exactly the same as in Chapter 13. The three lead-alloy supports used were:

Pb-Sb (1.88%),
Pb-Sn (0.34%) - Ca (0.086%),
Pb-Sn (0.34%) - Bi (0.15%) - Ca (0.086%).

The density of the positive paste was 4.25 gcm^{-3}. Measurements were taken at constant pre-electrode states at the following decreasing potentials:

1190, 1180, 1170, 1150, 1100, 1000, 900 and 700 mV.

The influence of the density of the paste from which the PbO_2 matrix is produced by electrooxidation is also reported for two paste densities in excess of 4.25 gcm^{-3}, they are 4.55 gcm^{-3} and 4.85 gcm^{-3}.

14.3 Results and Discussion

a). Pasted Pb-Sb (1.88%) electrode

Fig. 14.1 shows the Sluyters plot for porous PbO_2 on a Pb-Sb

Fig. 14.1 The complex-plane plot (Sluyters plot) for porous PbO_2 on a Pb-Sb (1.88%) support (nominal surface area = 0.07 cm^2) in 5M H_2SO_4 at 23°C; 1190 mV; frequencies in hertz are given on the plot. The crosses (+) show experimental data and the line shows the computer match.

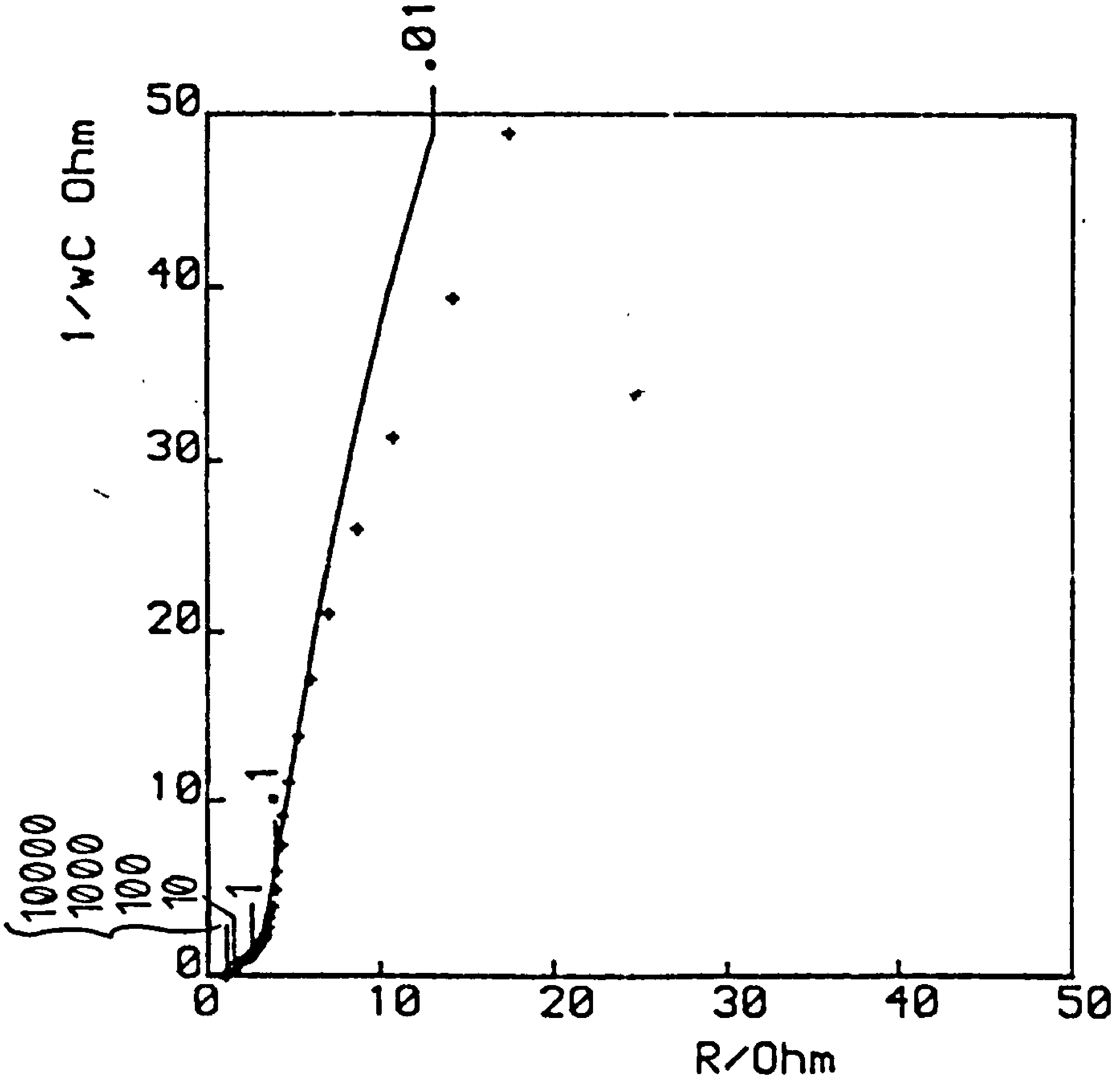

Fig. 14.2 The Randles plot corresponding to the system of Fig. 14.1 at 1190 mV. + and x correspond to experimental data (R and 1/ωC respectively) and the lines show the computer matches.

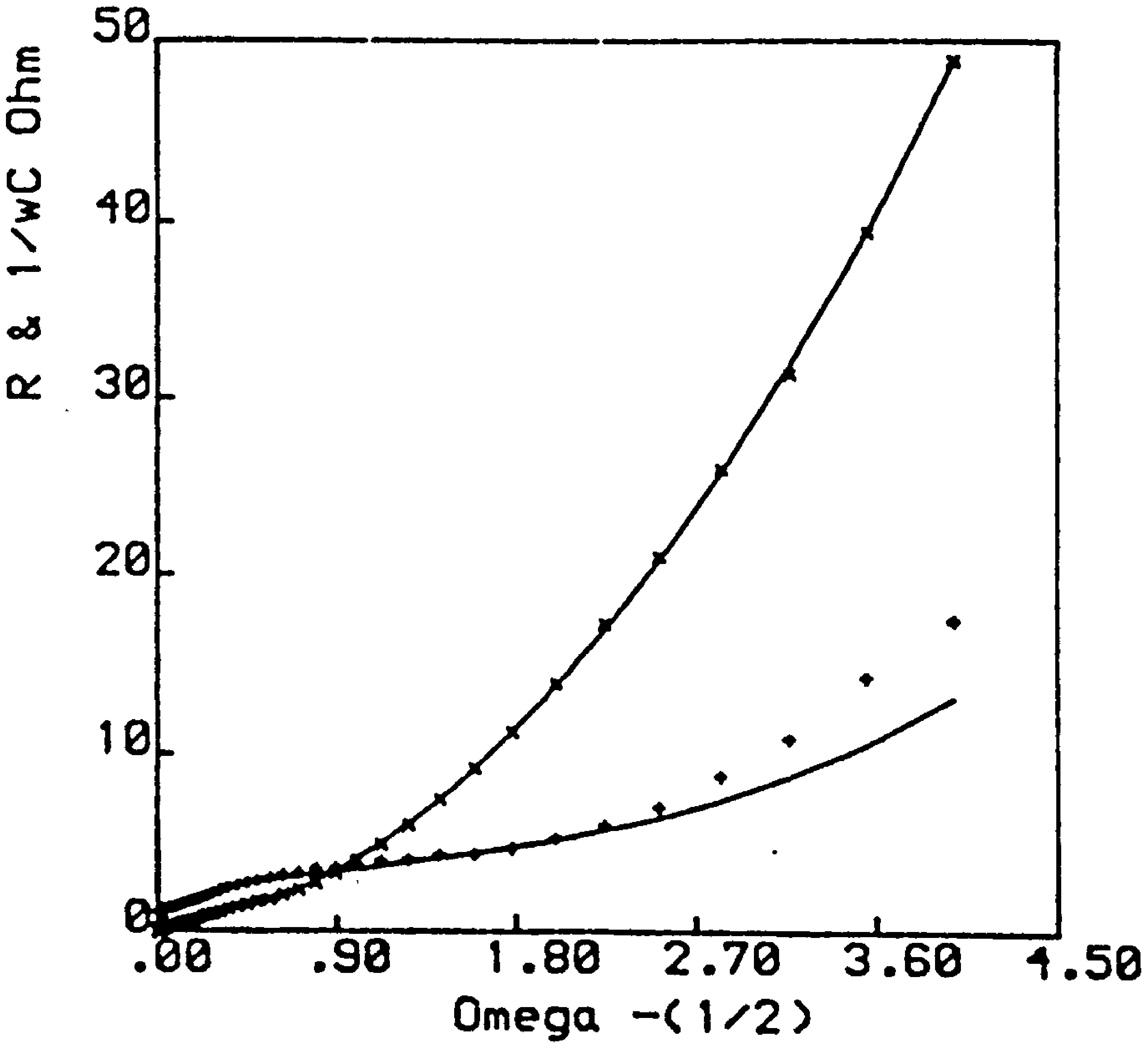

Fig. 14.3 Details as in Fig. 14.1 but at 1180 mV.

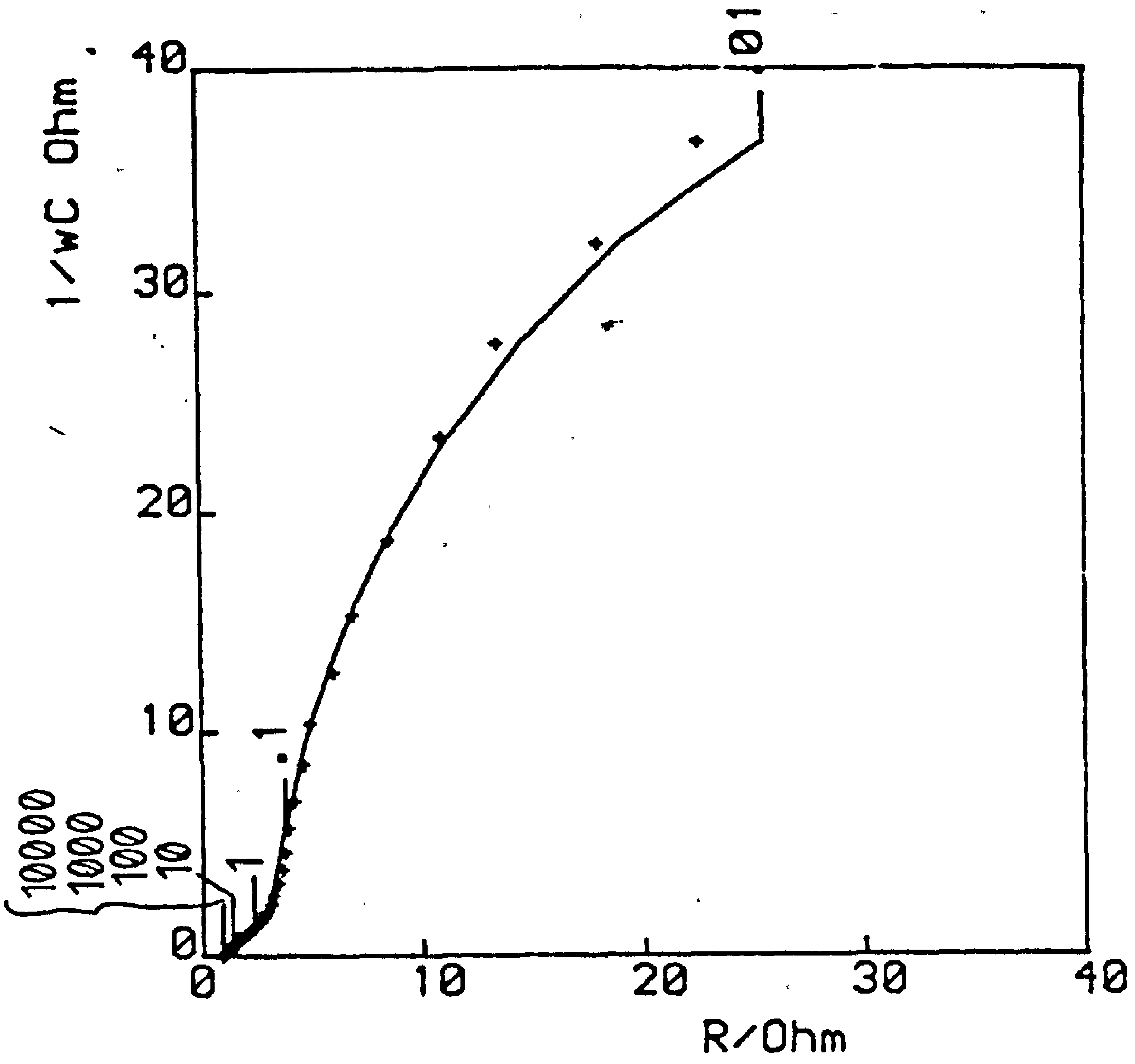

Fig. 14.4 Details as in Fig. 14.2 but at 1180 mV.

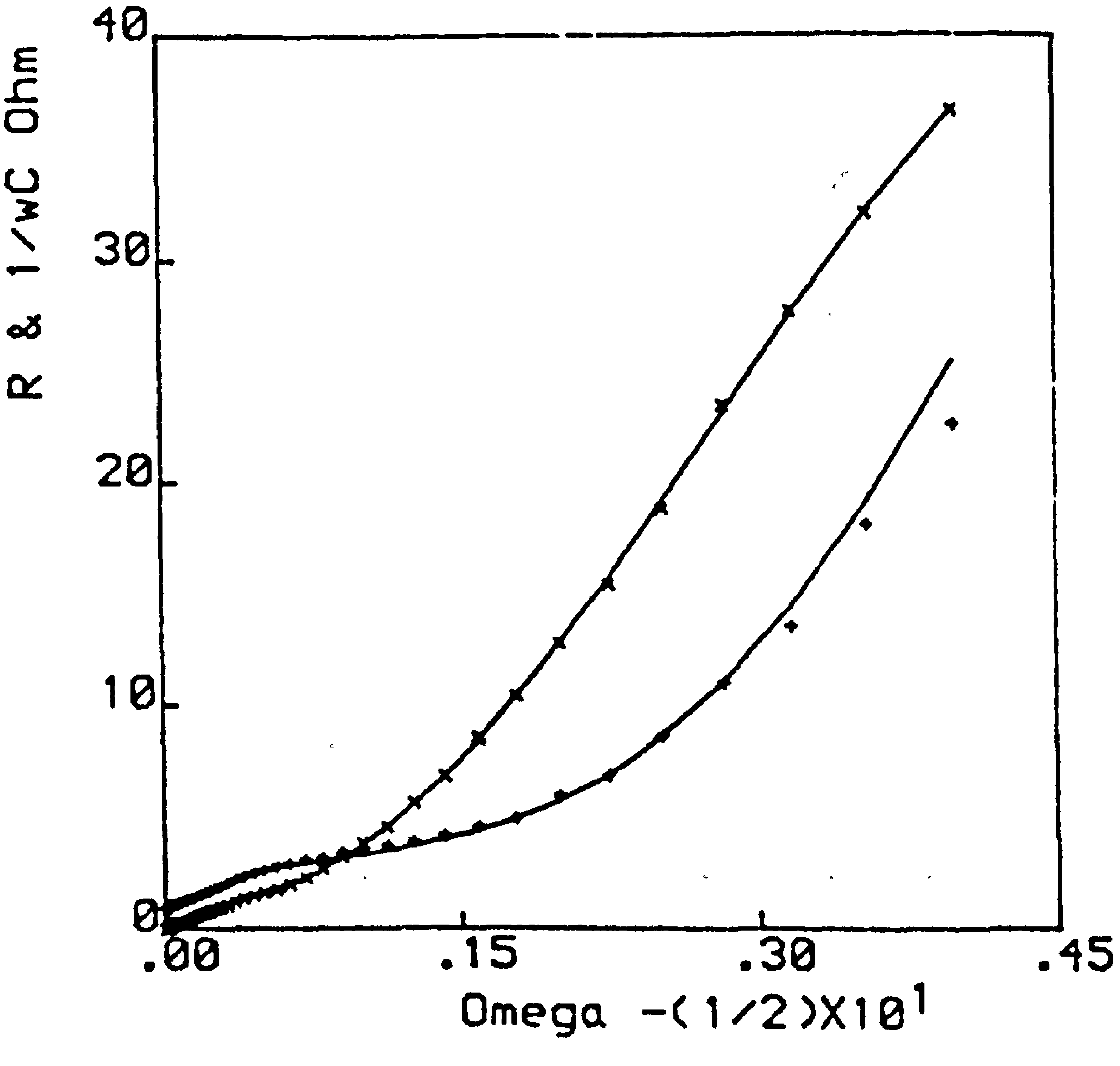

Fig. 14.5 Details as in Fig. 14.1 but at 1170 mV.

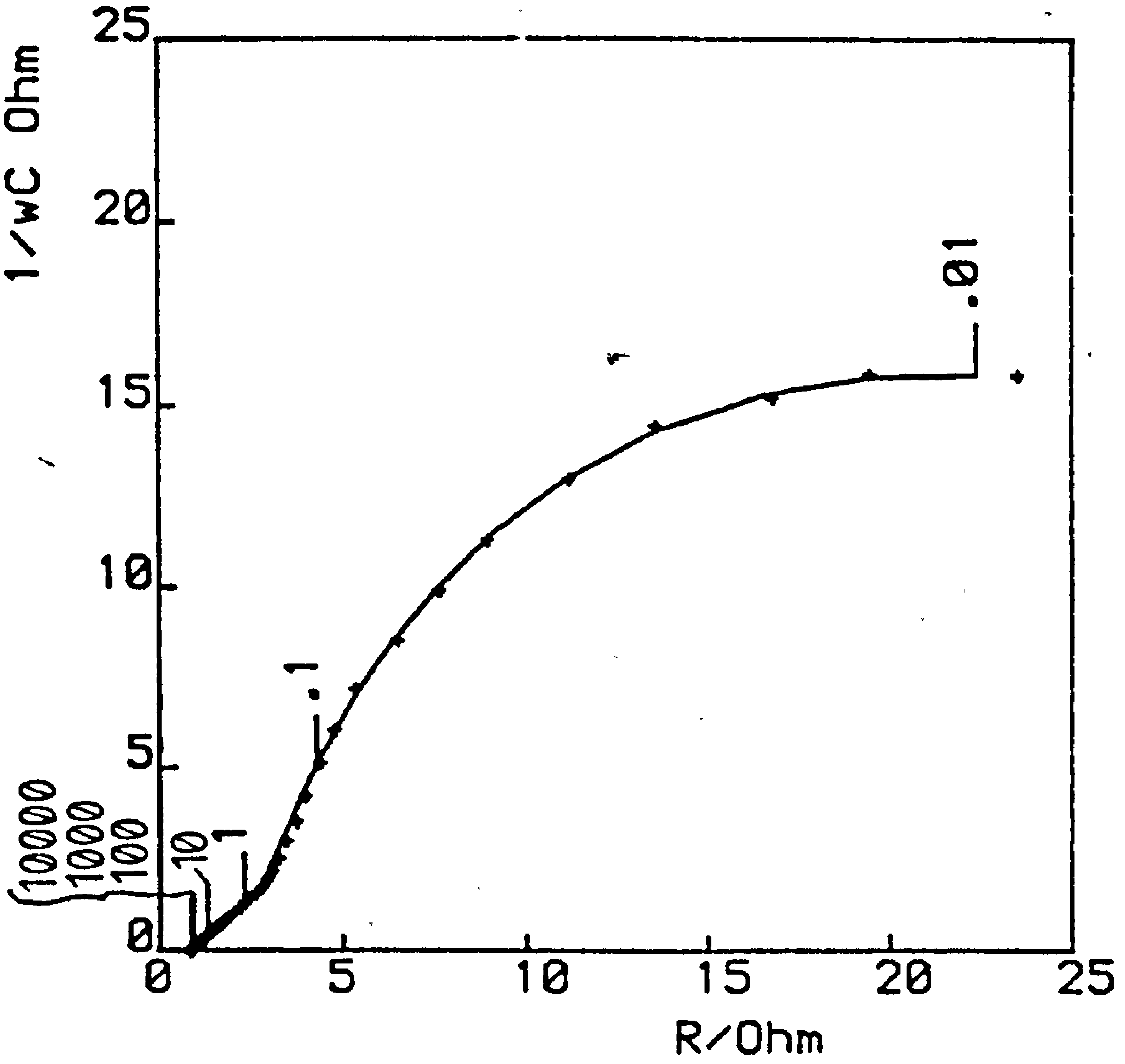

Fig. 14.6 Details as in Fig. 14.2 but at 1170 mV.

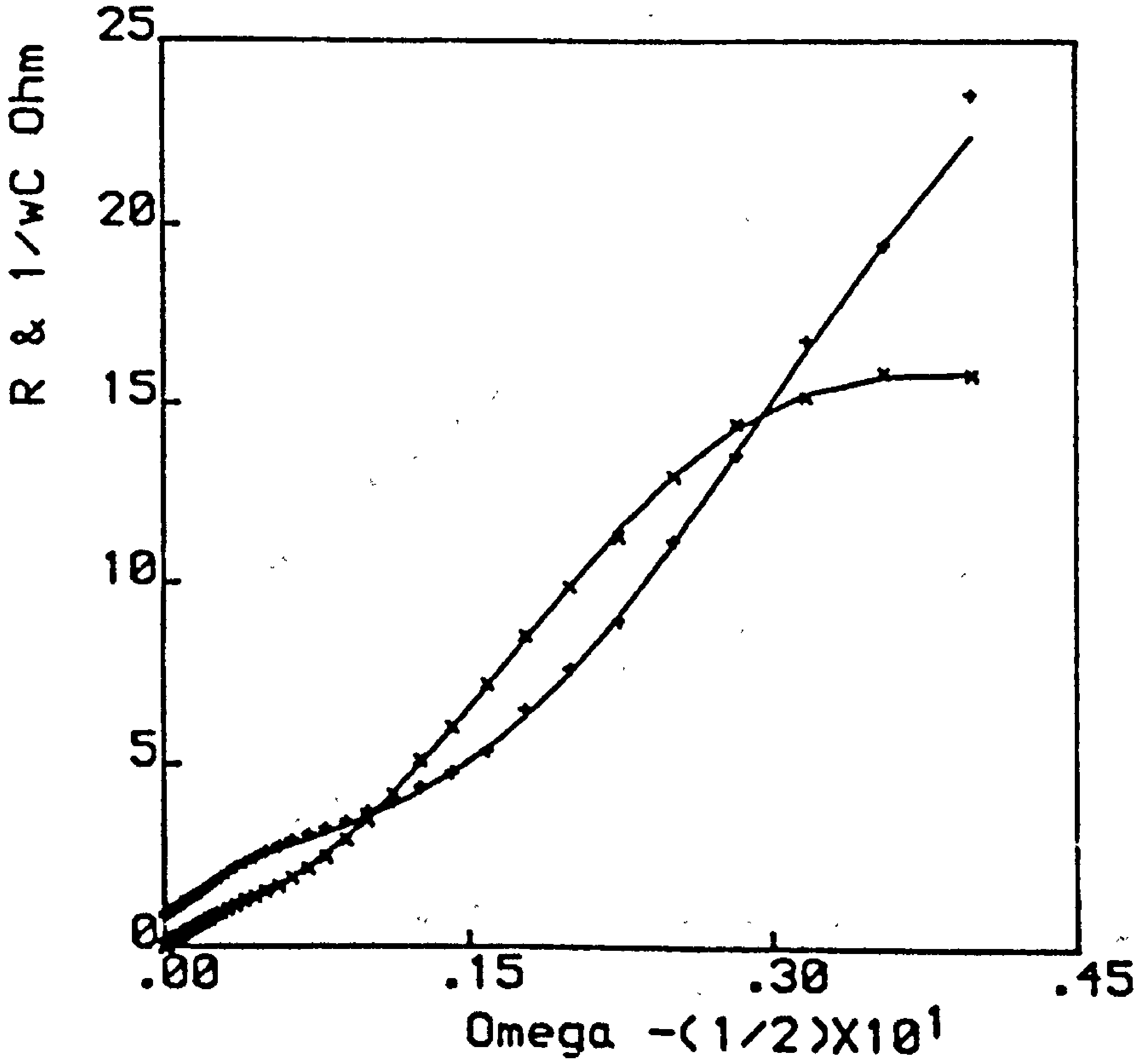

Fig. 14.7 Details as in Fig. 14.1 but at 1150 mV.

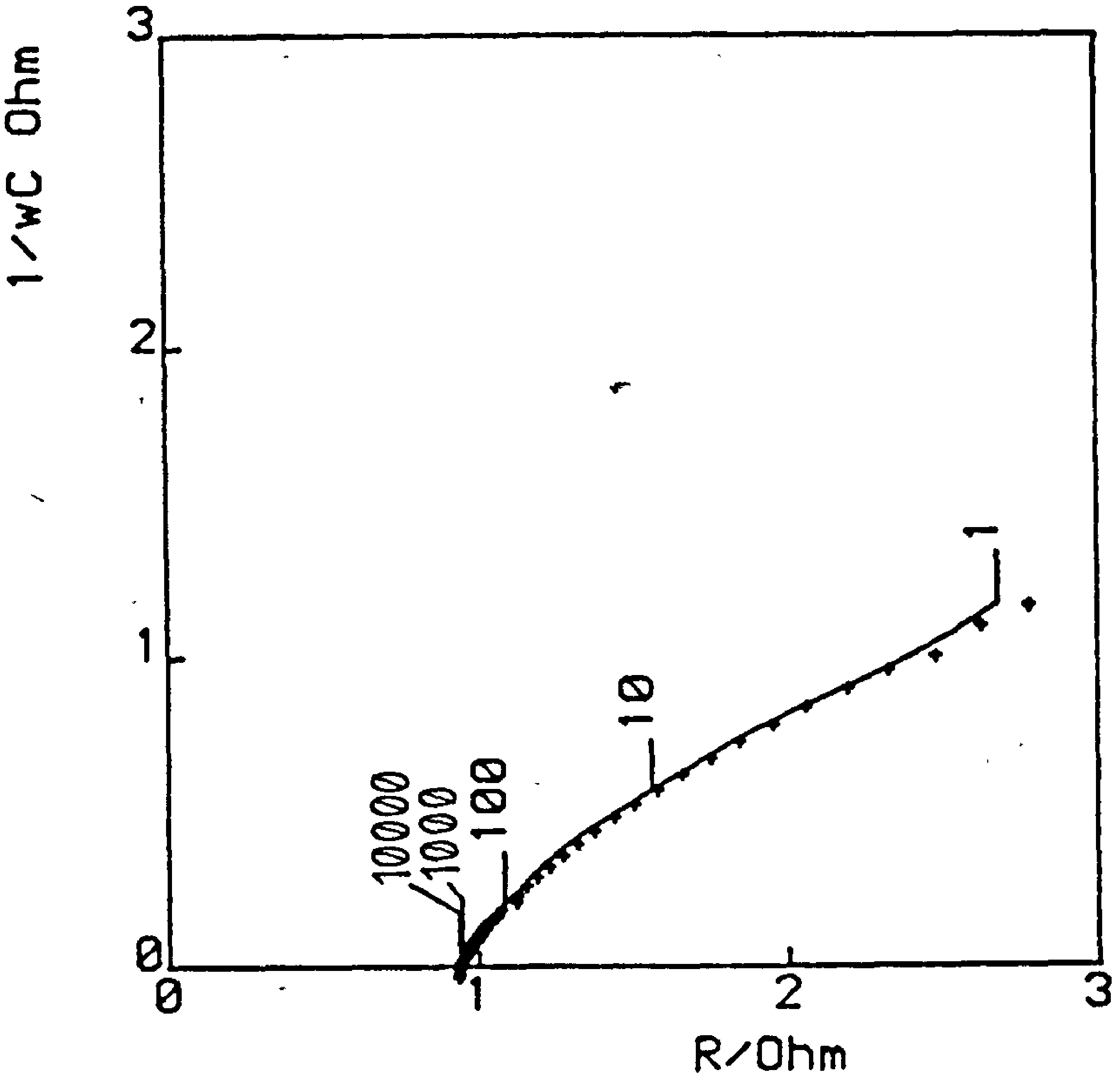

Fig. 14.8 Details as in Fig. 14.2 but at 1150 mV.

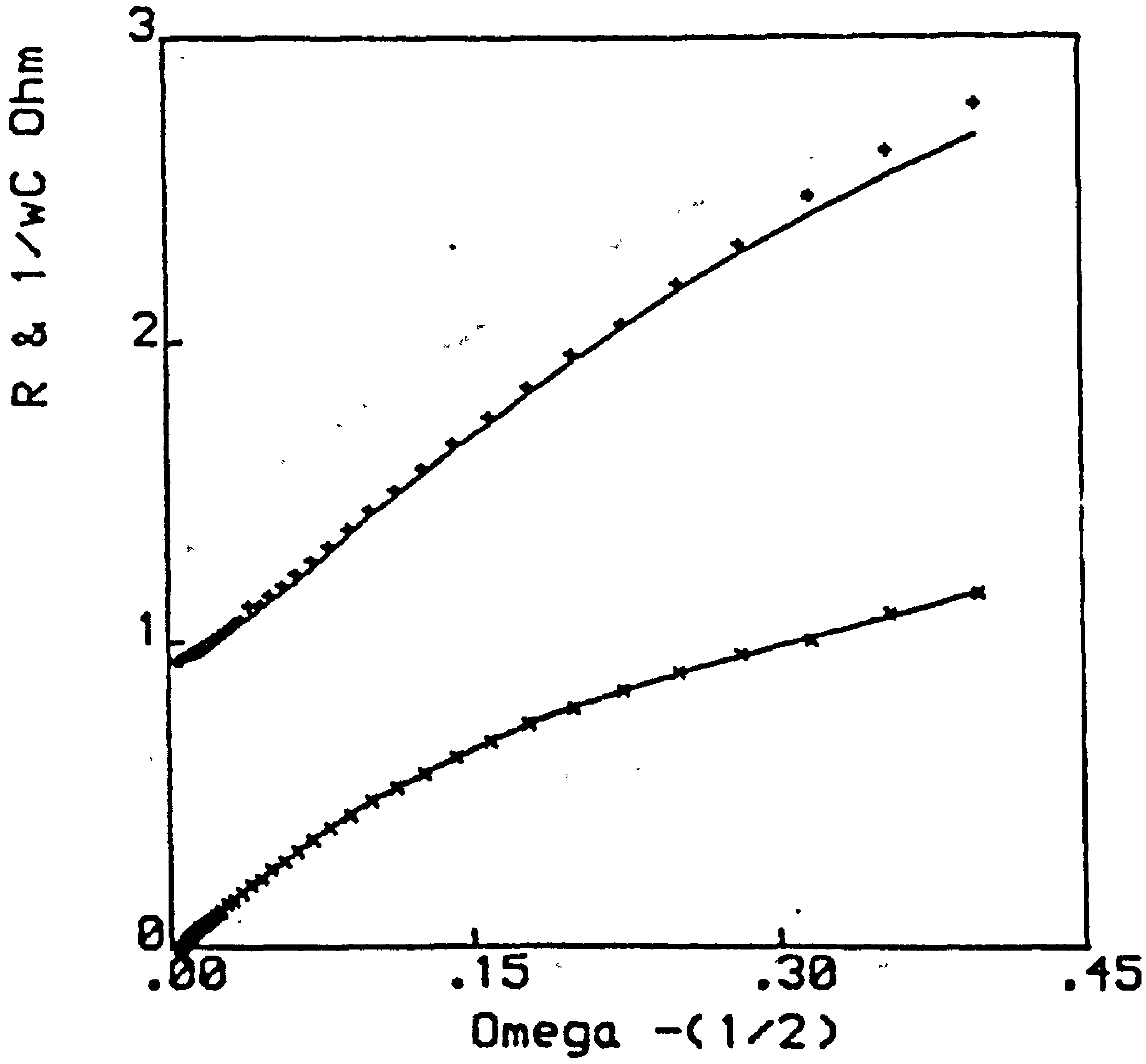

Fig. 14.9 Details as in Fig. 14.1 but at 1100 mV.

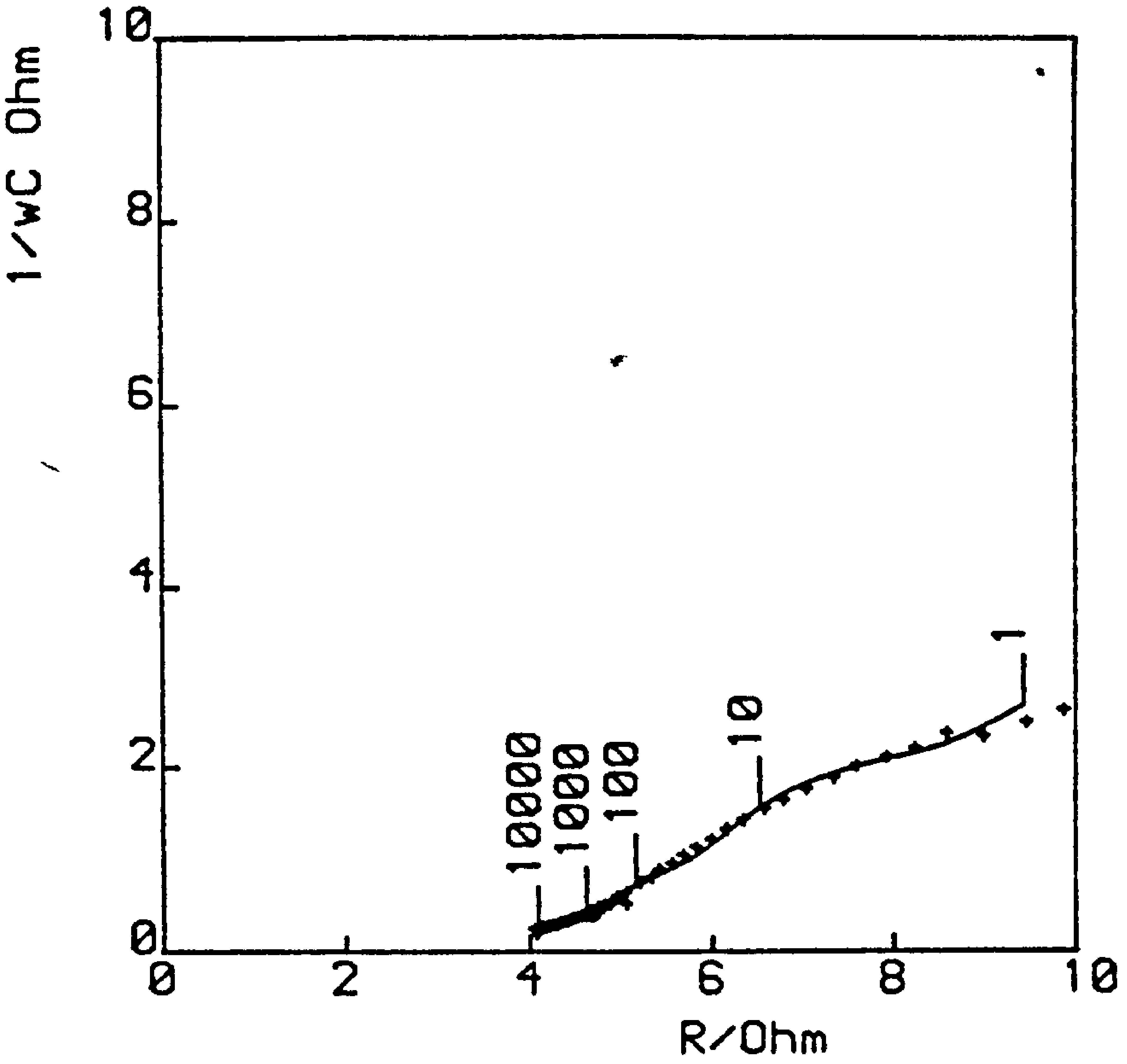

Fig. 14.10 Details as in Fig. 14.2 but at 1100 mV.

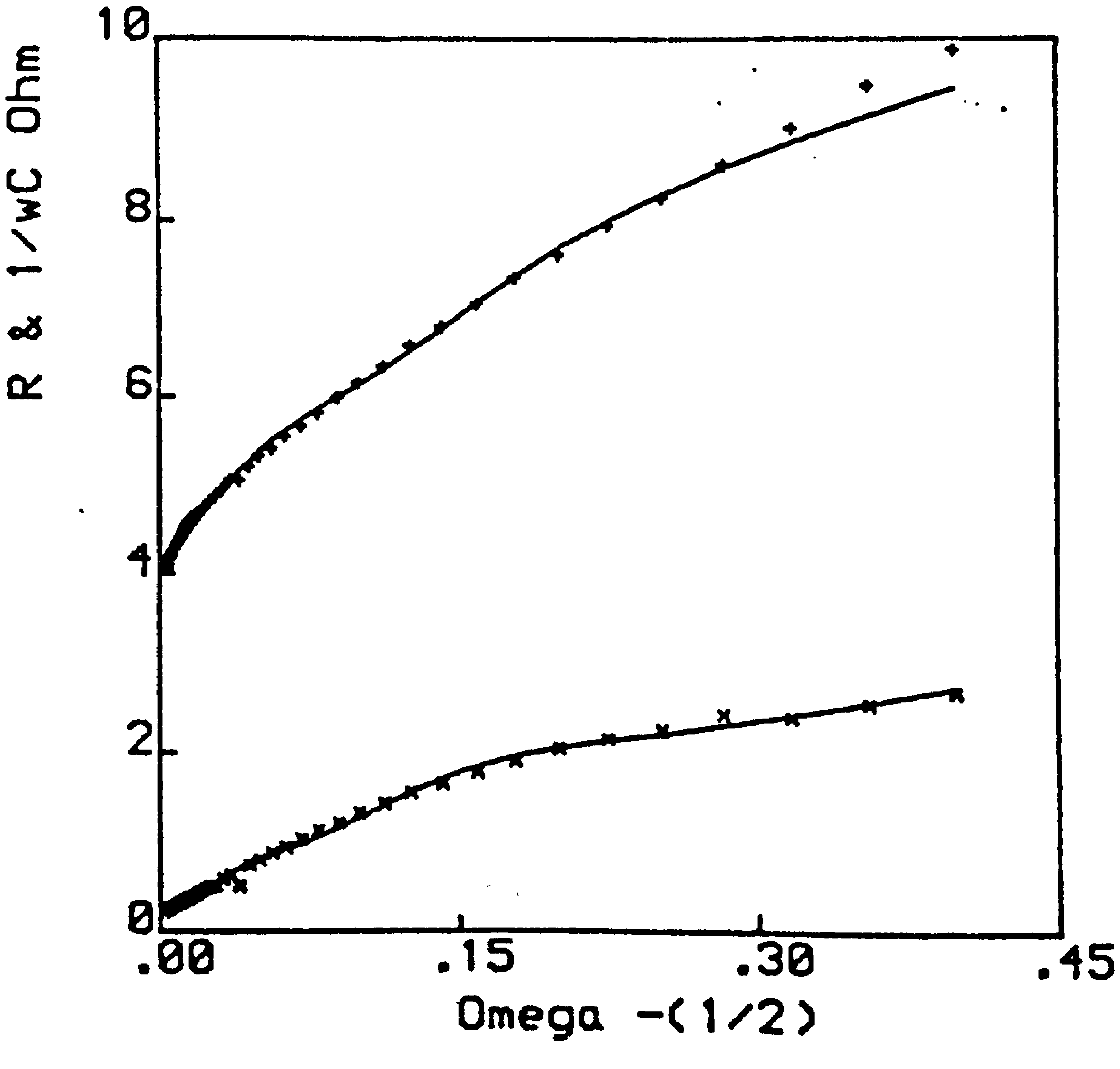

Fig. 14.11 Details as in Fig. 14.1 but at 1000 mV.

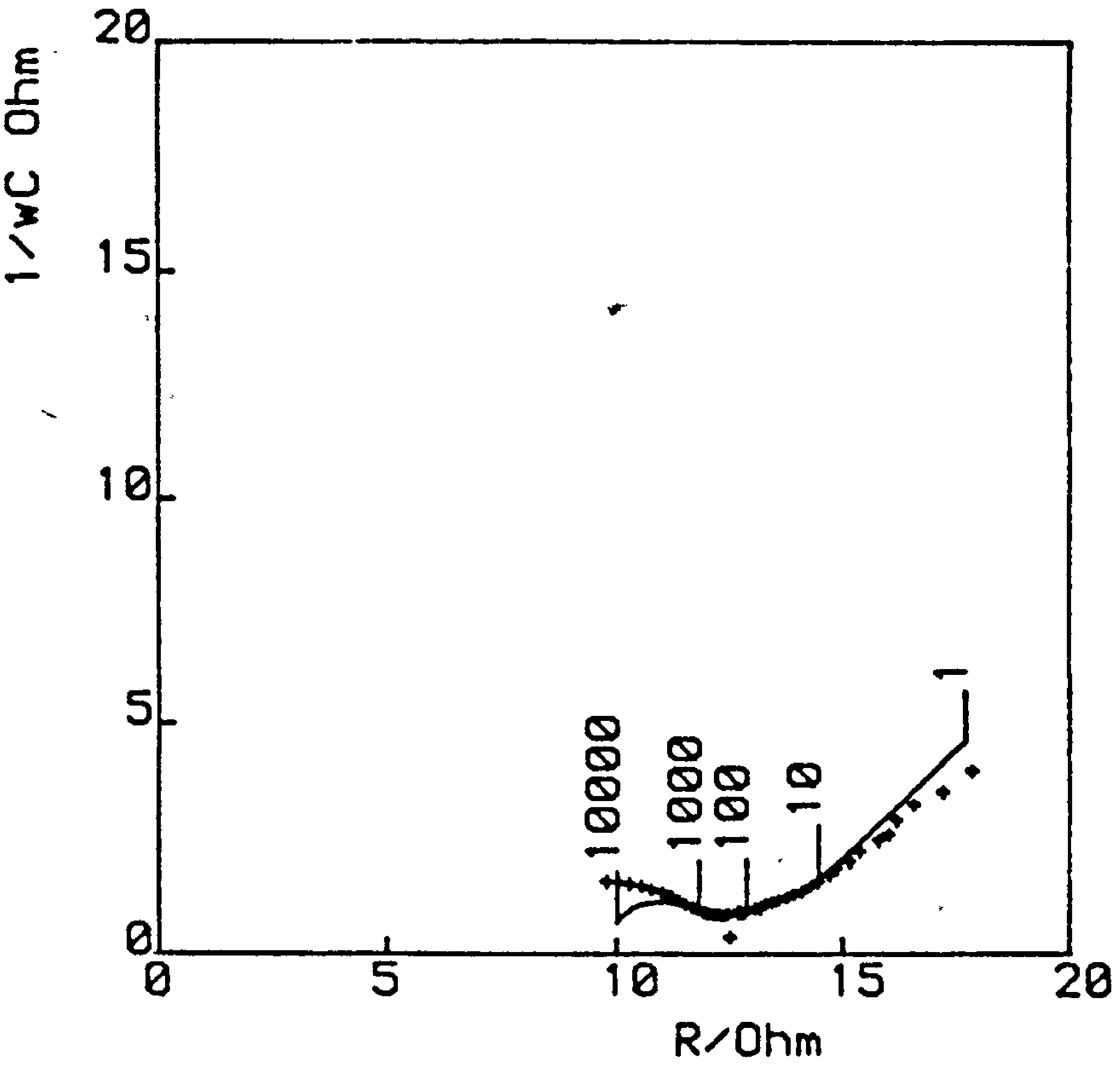

Fig. 14.12 Details as in Fig. 14.2 but at 1000 mV.

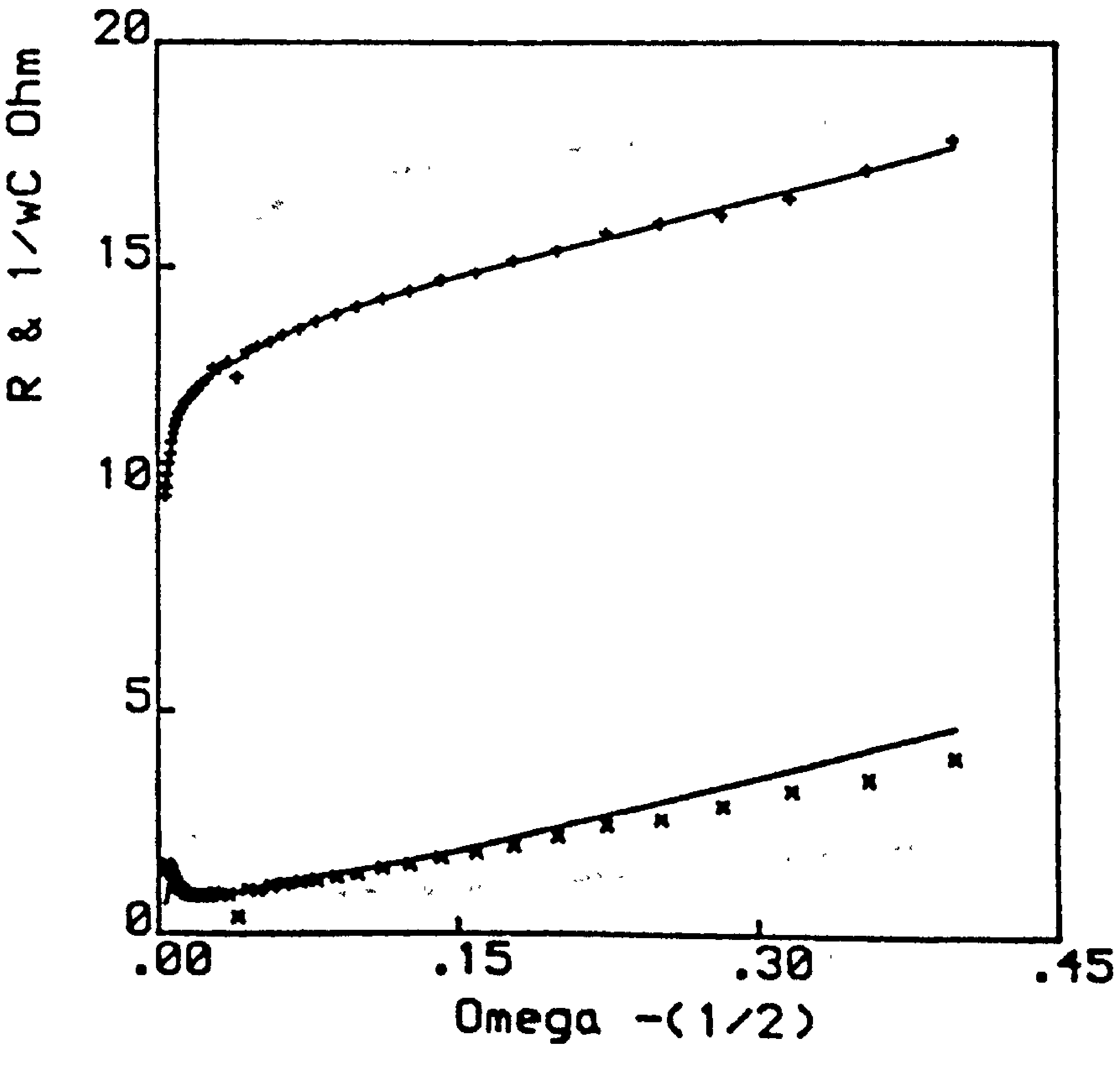

Fig. 14.13 Details as in Fig. 14.1 but at 900 mV.

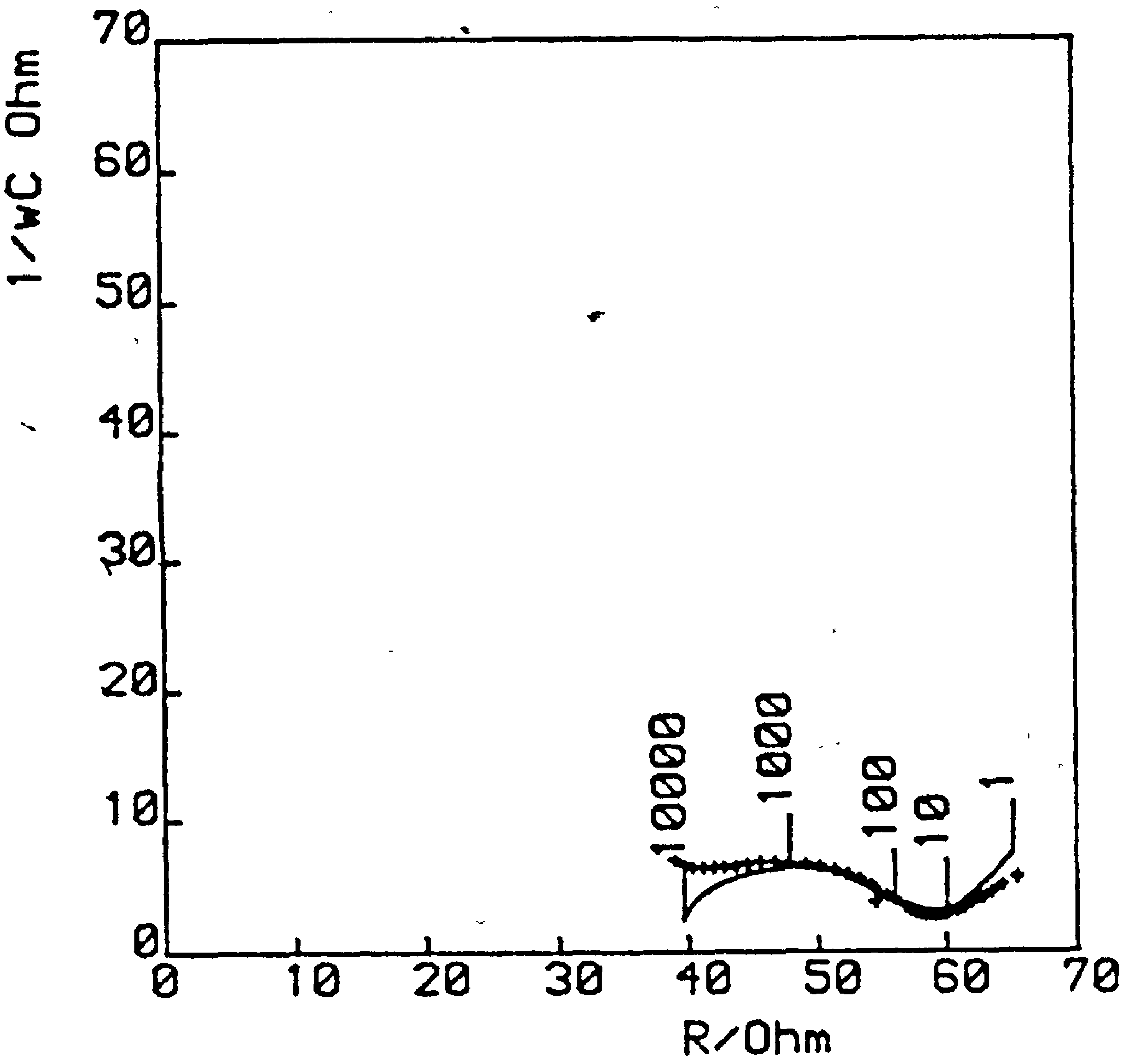

Fig. 14.14 Details as in Fig. 14.2 but at 900 mV.

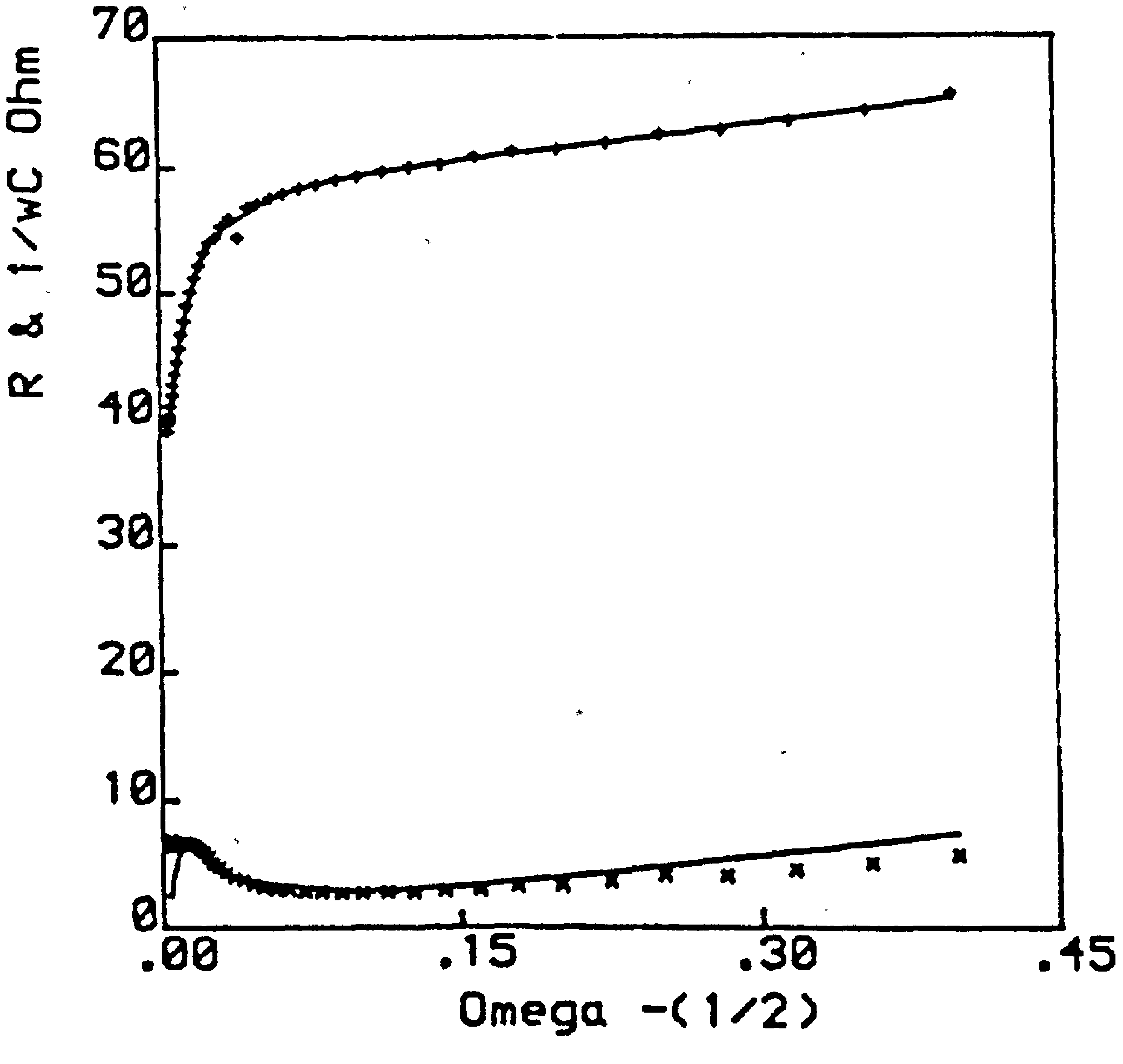

Fig. 14.15 Details as in Fig. 14.1 but at 700 mV.

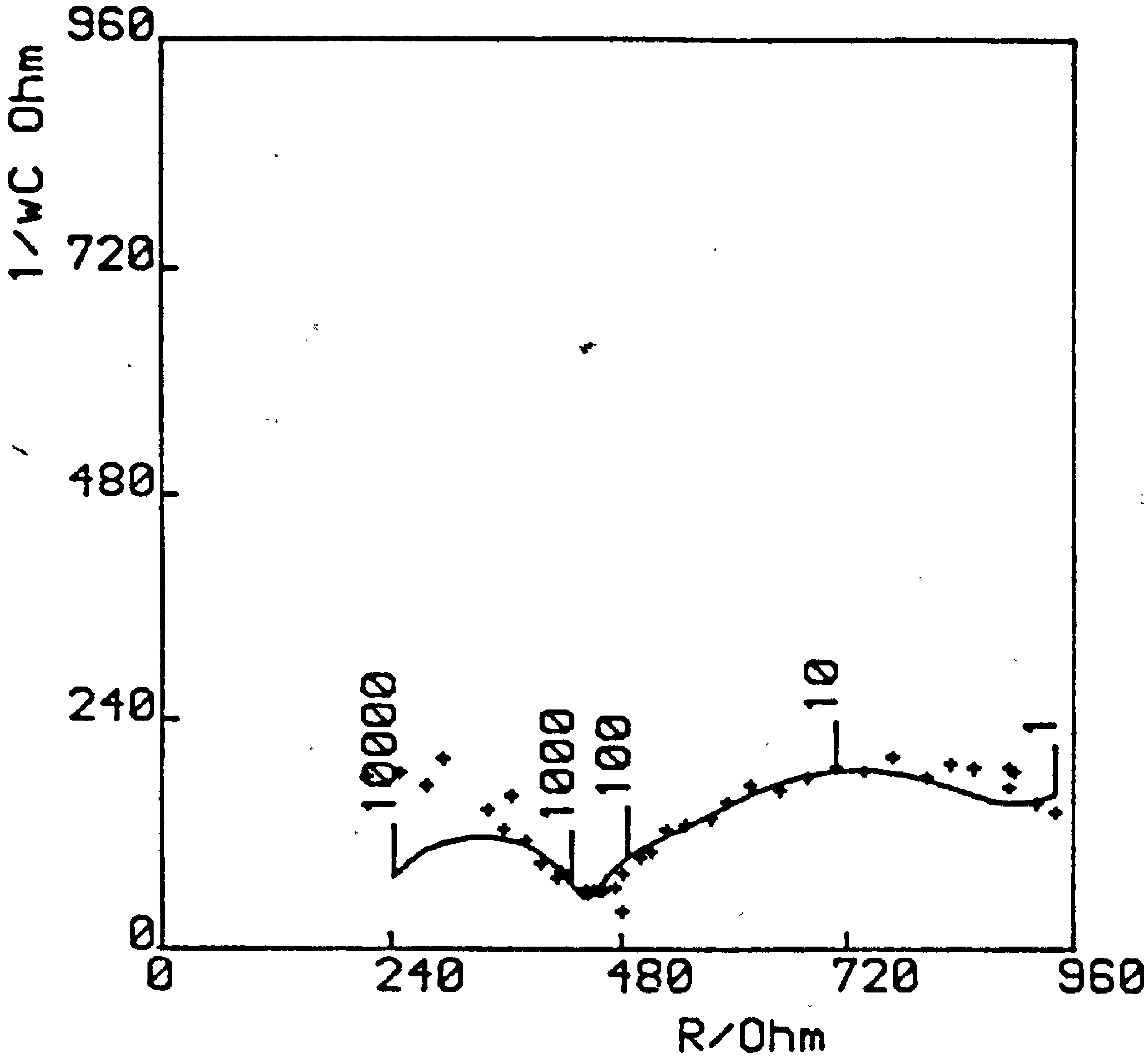

Fig. 14.16 Details as in Fig. 14.2 but at 700 mV.

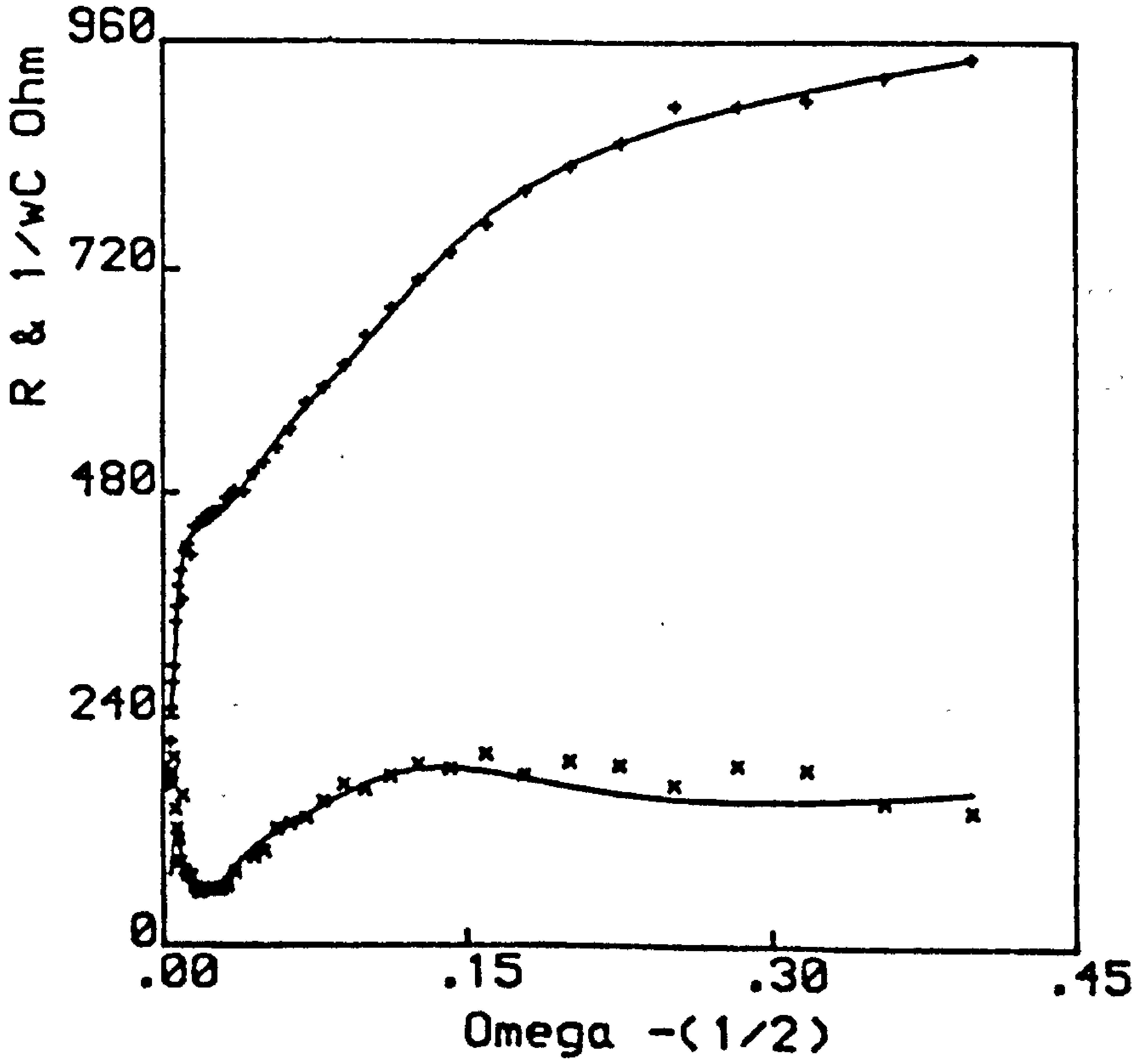

(1.88%) support at the open circuit potential, 1190 mV. The rising curve does not show a well-defined high-frequency semicircle or a Warburg line (as in the previous chapter). The Randles plot corresponding to this behaviour is shown in Fig. 14.2. The plot exhibits two lines which cross over each other and they correspond to resistive and capacitive components of the electrode system.

Figs. 14.3-14.16 represent the Sluyters and corresponding Randles plots for the electrode at different potentials as it is stepped sequentially in a decreasing manner towards the $PbSO_4$ region. The first three Randles plots (Figs. 14.2, 14.4 and 14.6) are indicative of the reaction occurring at the electrode surface as being completely in the adsorbed state [85, 118] with nothing leaving the electrode. From 1000-700 mV two joining semicircles are formed which increase in size. This emphasises the thickening of the lead sulphate film on the PbO_2 surface. The model shown in Fig. 13.17 was matched successfully to the experimental data in Figs. 14.1-14.16 with the aid of a computer (as in Chapter 13).

Table 14.1 shows that at potentials more negative than 1170 mV the electrode behaviour could only be matched to the analogue in Fig. 13.17 down to ∿ 1 Hz. The reason for this has been discussed in the previous chapter. In the potential range 1150-700 mV the electrolyte resistance, R_Ω, the Warburg coefficient, σ, and the external film resistance, R_{ext}, increase with decreasing potential. This shows that the PbO_2 surface is progressively being covered with $PbSO_4$. The double-layer capacitance, C_{dL}, the adsorption capacitance, C_{ads}, and the external film capacitance, C_{ext}, decrease with decreasing potential. This is to be expected because at more negative potentials the lead sulphate layer thickens and hence the capacitance decreases due to the theory for a flat capacitor.

TABLE 14.1

Electrode characteristics obtained from computer match for porous PbO_2 on a Pb-Sb (1.88%) support at various potentials (nominal surface area = 0.07 cm^2).

Potential/V	1.190	1.180	1.170	1.150	1.100	1.000	0.900	0.700
Kinetic Parameters	10 kHz - 0.01 Hz			10 kHz - 1 Hz				
R_Ω/Ω	1.055	0.9069	0.8706	0.9382	4.053	9.794	38.95	215.9
θ/Ω	0.4375	0.6242	0.4078	0.1616	1.218	0.9024	9.532	201.4
C_{dL}/F	6.7904E-3	1.2928E-2	8.4681E-3	3.5225E-3	1.3734E-3	3.0905E-4	2.6241E-5	1.3278E-5
$\sigma/\Omega s^{-\frac{1}{2}}$	1.264	0.8155	1.543	2.59	5.888	11.57	18.32	318.5
C_{ads}/F	8.5321E-2	0.1126	0.1109	0.1046	1.8175E-2	5.9414E-3	1.0319E-3	7.3837E-5
R_{ads}/Ω	0.8272	1.010	0.6679	0.4139	1.422	0.5145	2.410	183.0
C_{ext}/F	0.3578	0.3532	0.5159	3.6136E-2	1.0728E-4	2.1861E-5	7.6253E-6	1.8867E-7
R_{ext}/Ω	341.2	76.34	20.87	0.2386	0.6479	1.995	6.98	227.6

b). Pasted Pb-Sn (0.34%) - Ca (0.086%) electrode

Figs. 14.17 and 14.18 correspond to the Sluyters and Randles plots respectively for porous PbO_2 on a Pb-Sn (0.34%) - Ca (0.086%) support at the open circuit potential, 1190 mV. At the potential 1180 mV the Randles plot in Fig. 14.20 shows the adsorptive nature of the electrode but in Fig. 14.22 resistive and capacitive components do not touch each other indicating that the adsorption process has ceased fairly quickly during the discharge.

As in the previous section Figs. 14.17-14.32 correspond to the Sluyters and Randles plots for the electrode at the same potentials as it is discharged. Also, as highlighted by Figs. 14.17 and 14.19 there is no well-defined Warburg line appearing at low frequencies with a constant dihedral ($\pi/8$ for a porous electrode) which indicates that the diffusion of the electroactive species is far away from the electrode and is not important. Hence what diffusion control there is, when the $PbSO_4$ layer is produced, occurs very close to the electrode. This suggests that the reactions at the electrodes do not involve free diffusion of species. The model in Fig. 13.17 was again able to adequately fit the experimental data in Figs. 14.17-14.32.

Using the potential range 1150-700 mV in Table 14.2 the charge transfer resistance, θ, Warburg coefficient, σ, the adsorption resistance, R_{ads}, and the external film resistance, R_{ext}, increase with decreasing potential; the converse happens with C_{dL}, C_{ads} and C_{ext}. At 700 mV the values for θ, σ and R_{ads} are much higher than those obtained for the Pb-Sb positive at the same potential. This implies that the $PbSO_4$ film produced is much thicker than the one formed on the porous PbO_2 on the Pb-Sb support. Another interesting feature in Table 14.2 is that the value obtained for R_{ext} for the electrode at the open circuit potential is very high, that is, $R_{ext} = 1\times10^{12}\Omega$. This suggests that the PbO_2 matrix

Fig. 14.17 The complex-plane plot (Sluyters plot) for porous PbO_2 on a Pb-Sn (0.34%) - Ca (0.086%) support (nominal surface area = 0.07 cm^2) in 5M H_2SO_4 at 23°C ; 1190 mV; frequencies in hertz are given on the plot. The crosses (+) show experimental data and the line shows the computer match.

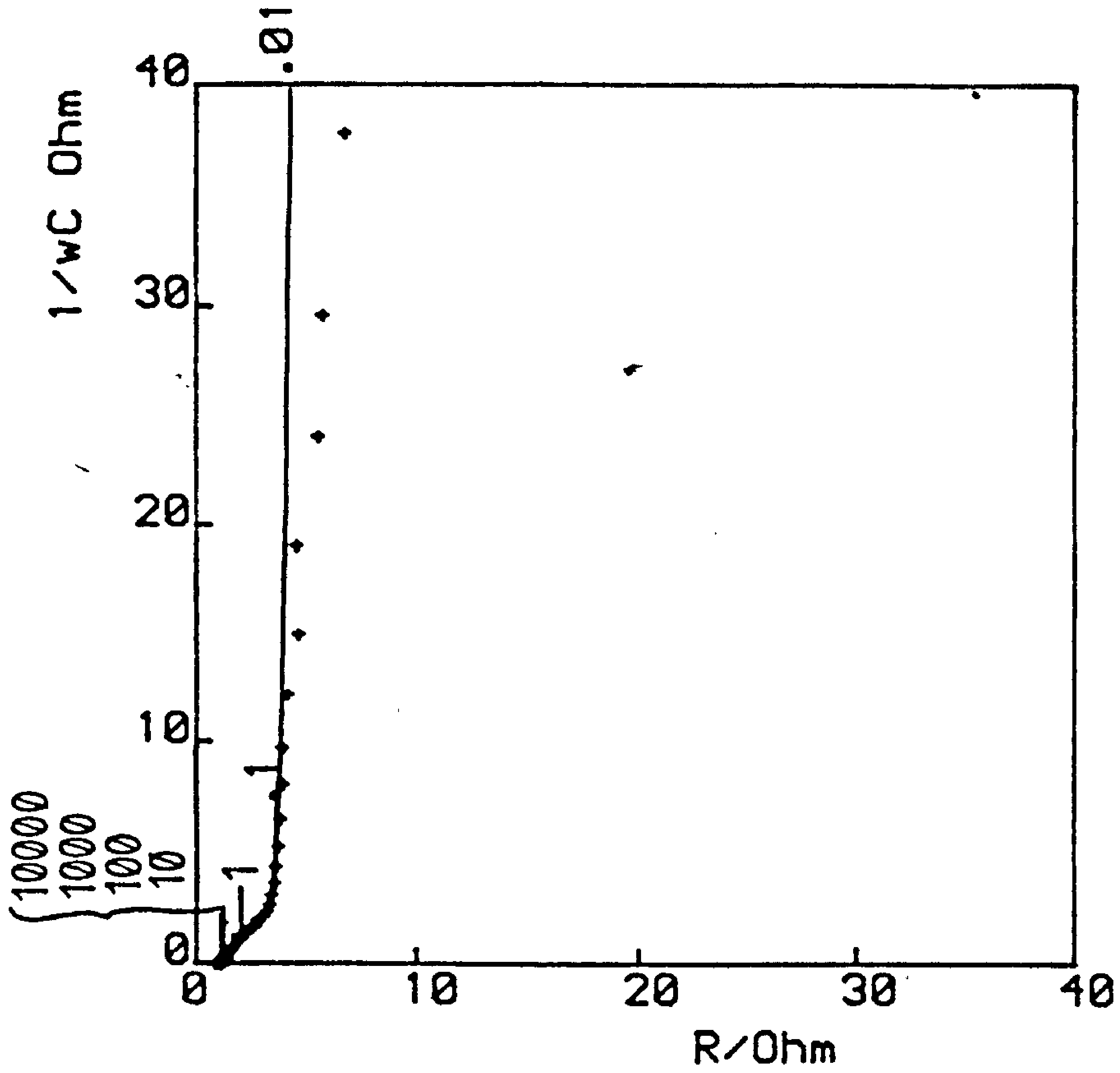

Fig. 14.18 The Randles plot corresponding to the system of Fig. 14.17 at 1190mV, + and x correspond to experimental data (R and 1/ωC respectively) and the lines show the computer matches.

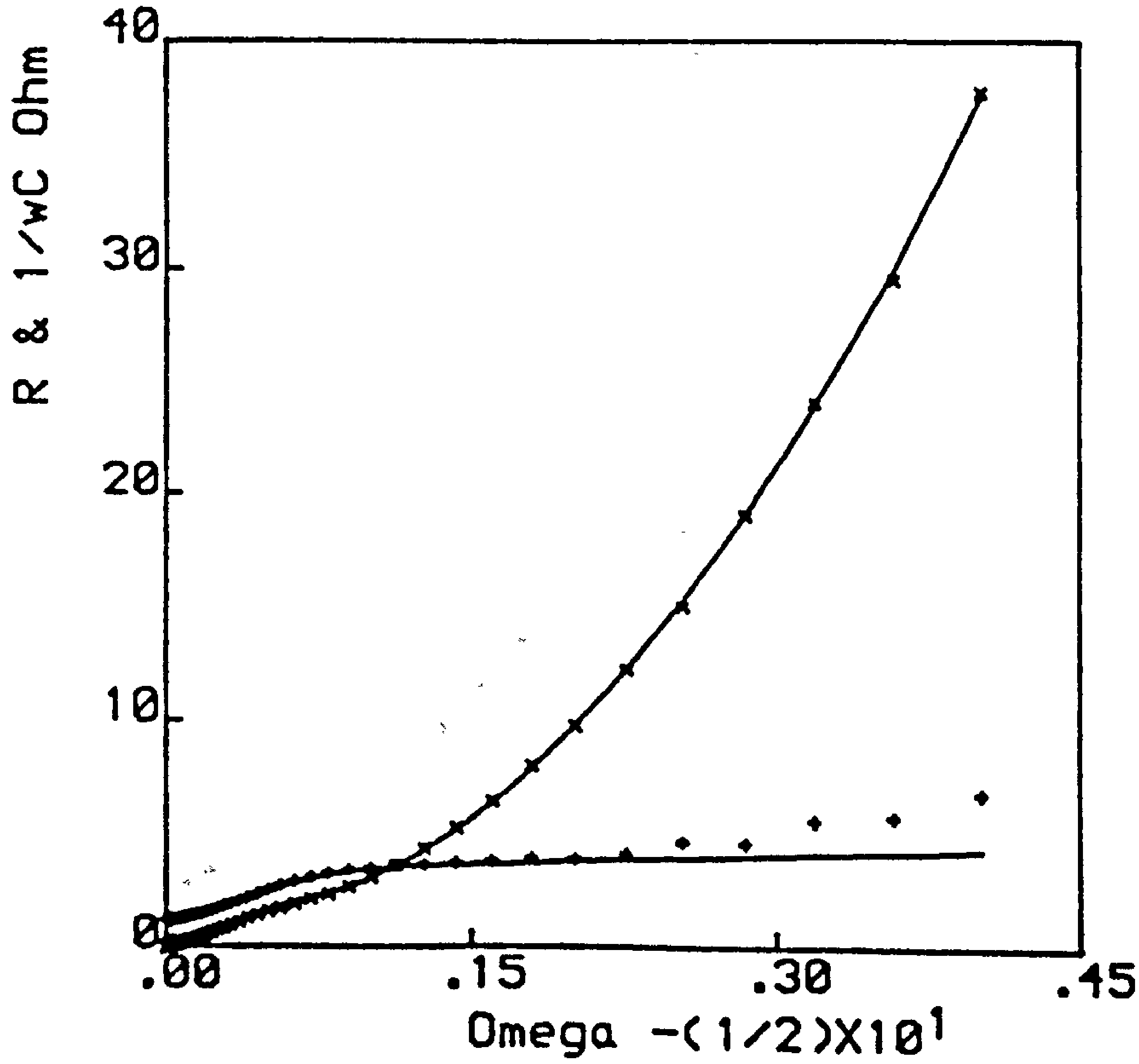

Fig. 14.19 Details as in Fig. 14.17 but at 1180 mV.

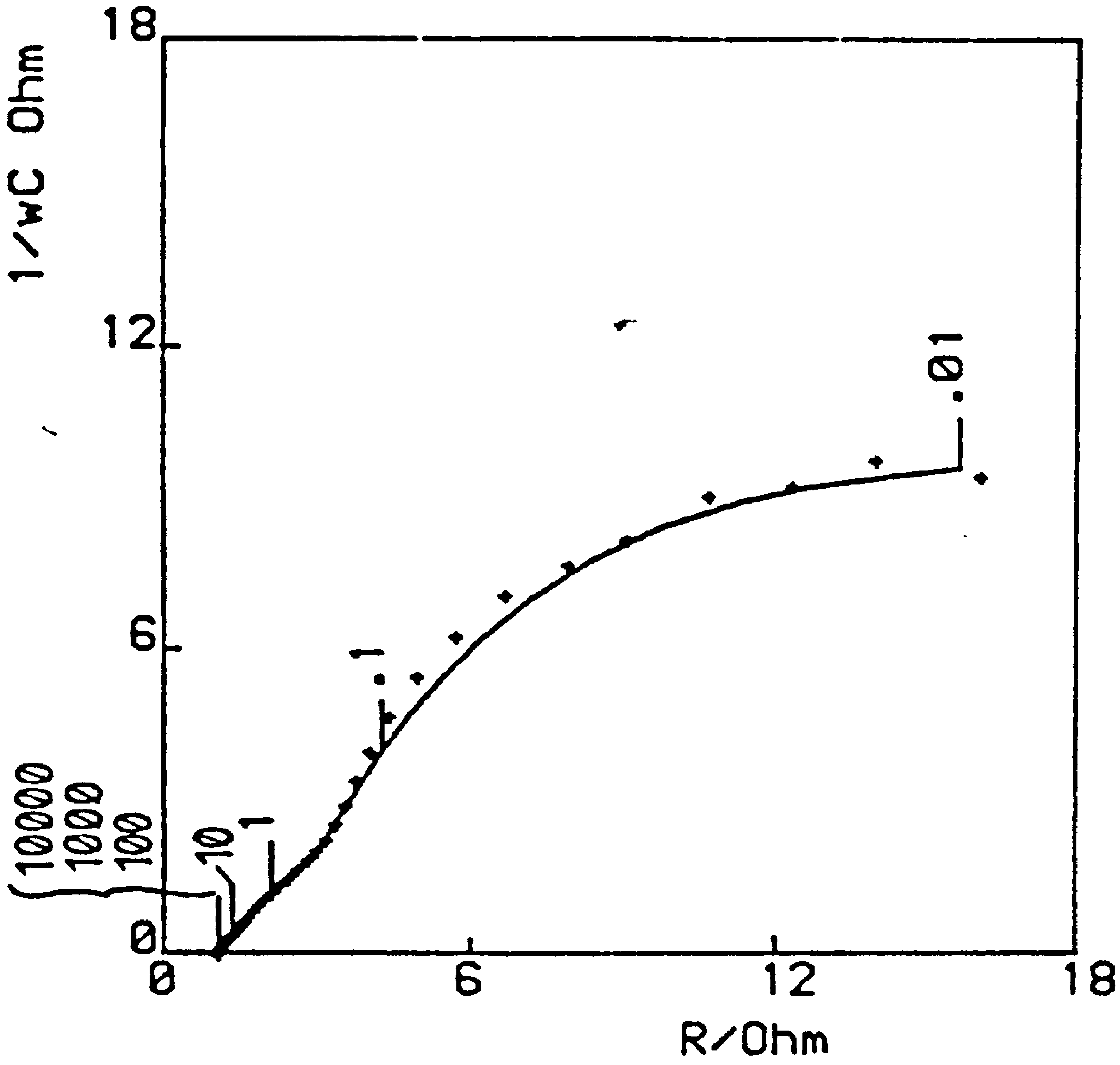

Fig. 14.20 Details as in Fig. 14.18 but at 1180 mV.

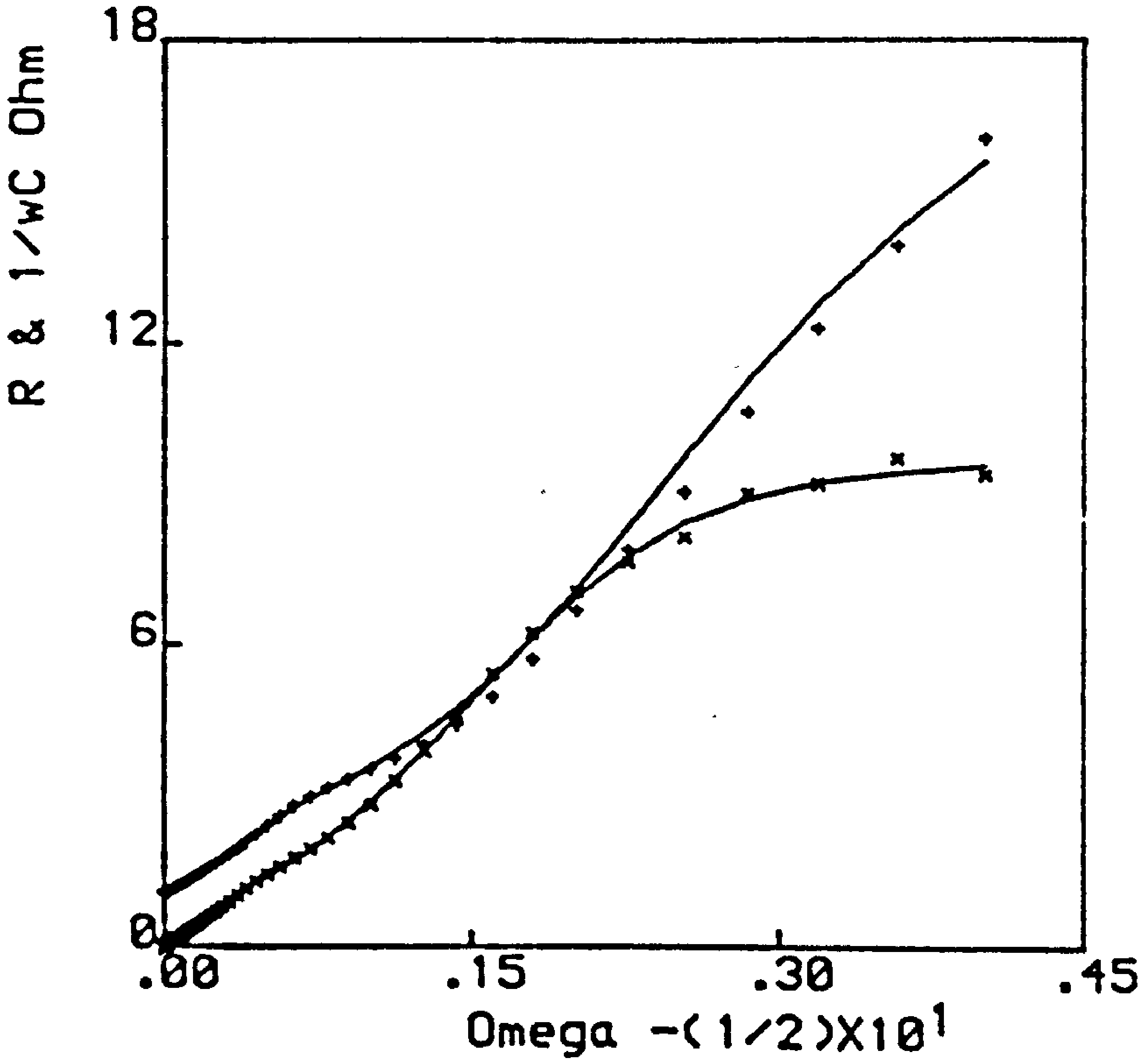

Fig. 14.21 Details as in Fig. 14.17 but at 1170 mV.

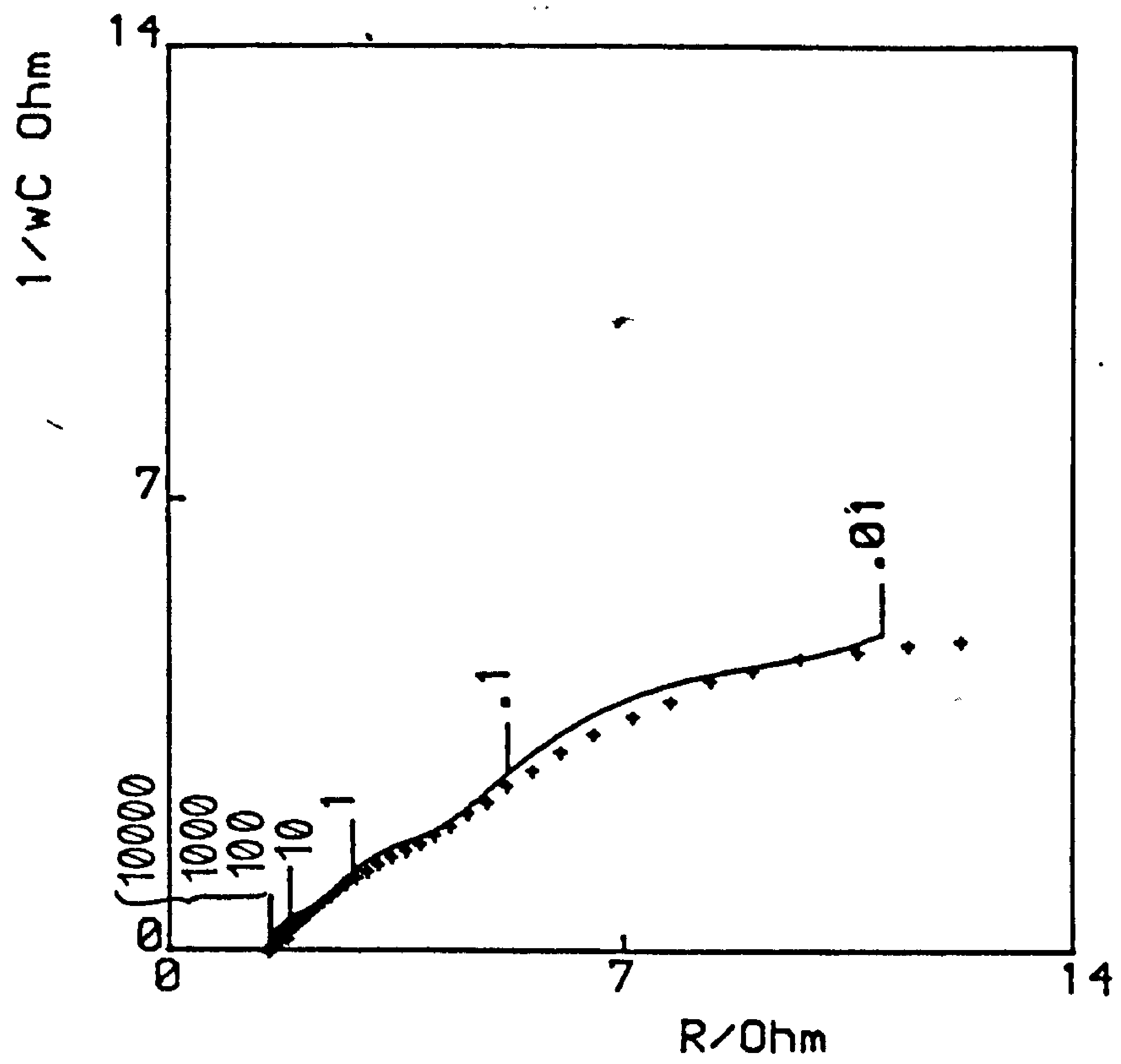

Fig. 14.22 Details as in Fig. 14.18 but at 1170 mV.

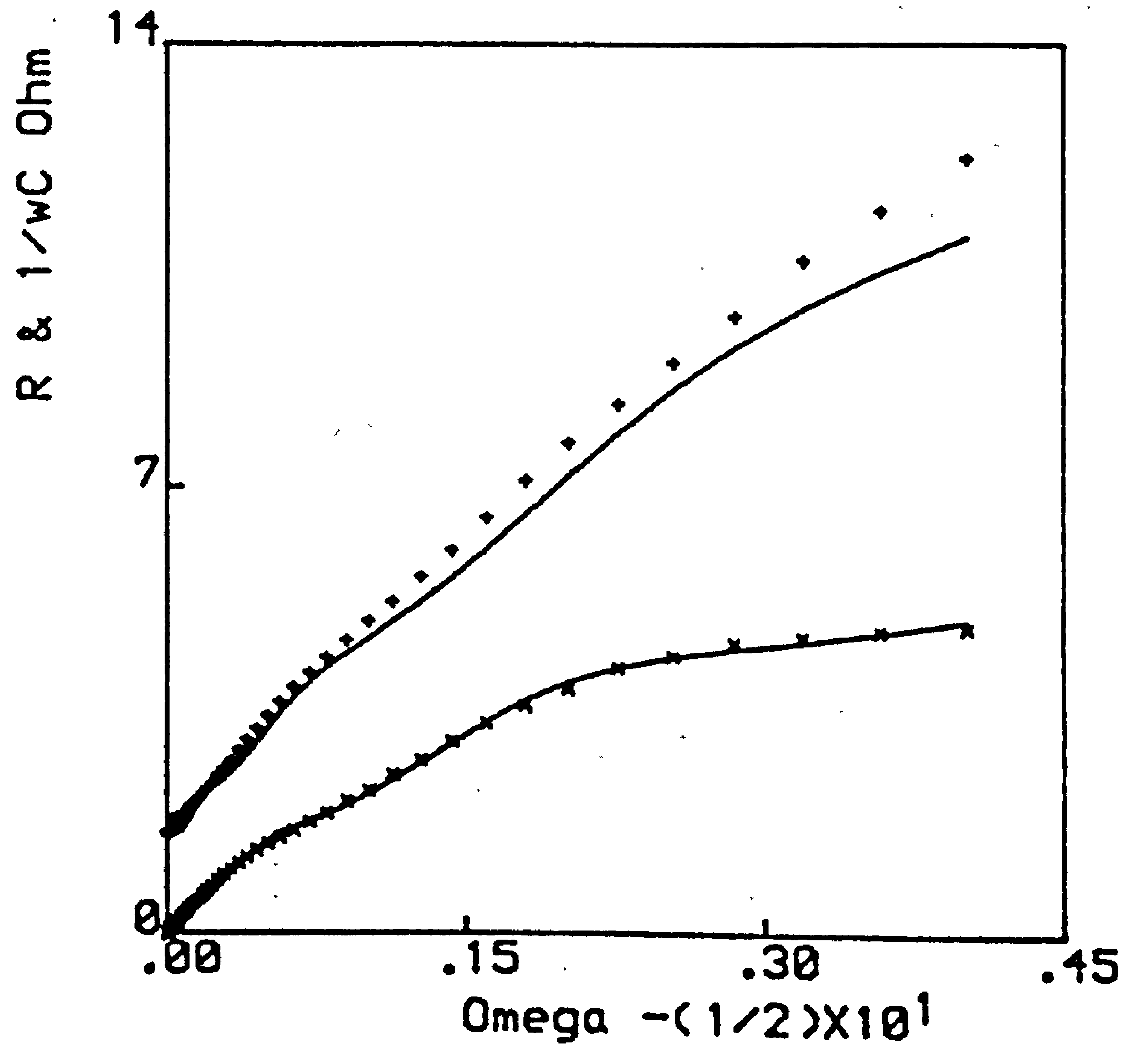

Fig. 14.23 Details as in Fig. 14.17 but at 1150 mV.

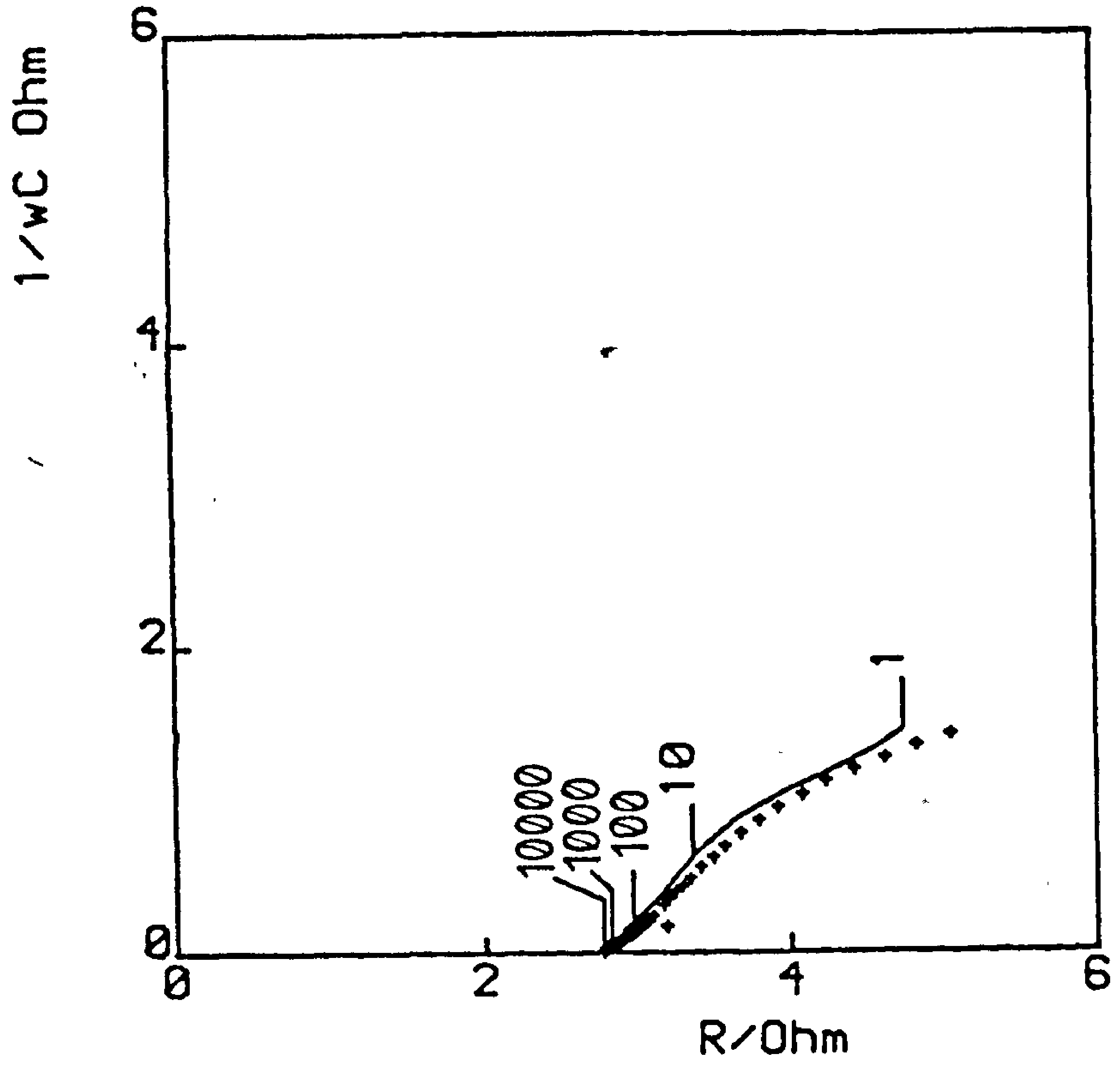

Fig. 14.24 Details as in Fig. 14.18 but at 1150 mV.

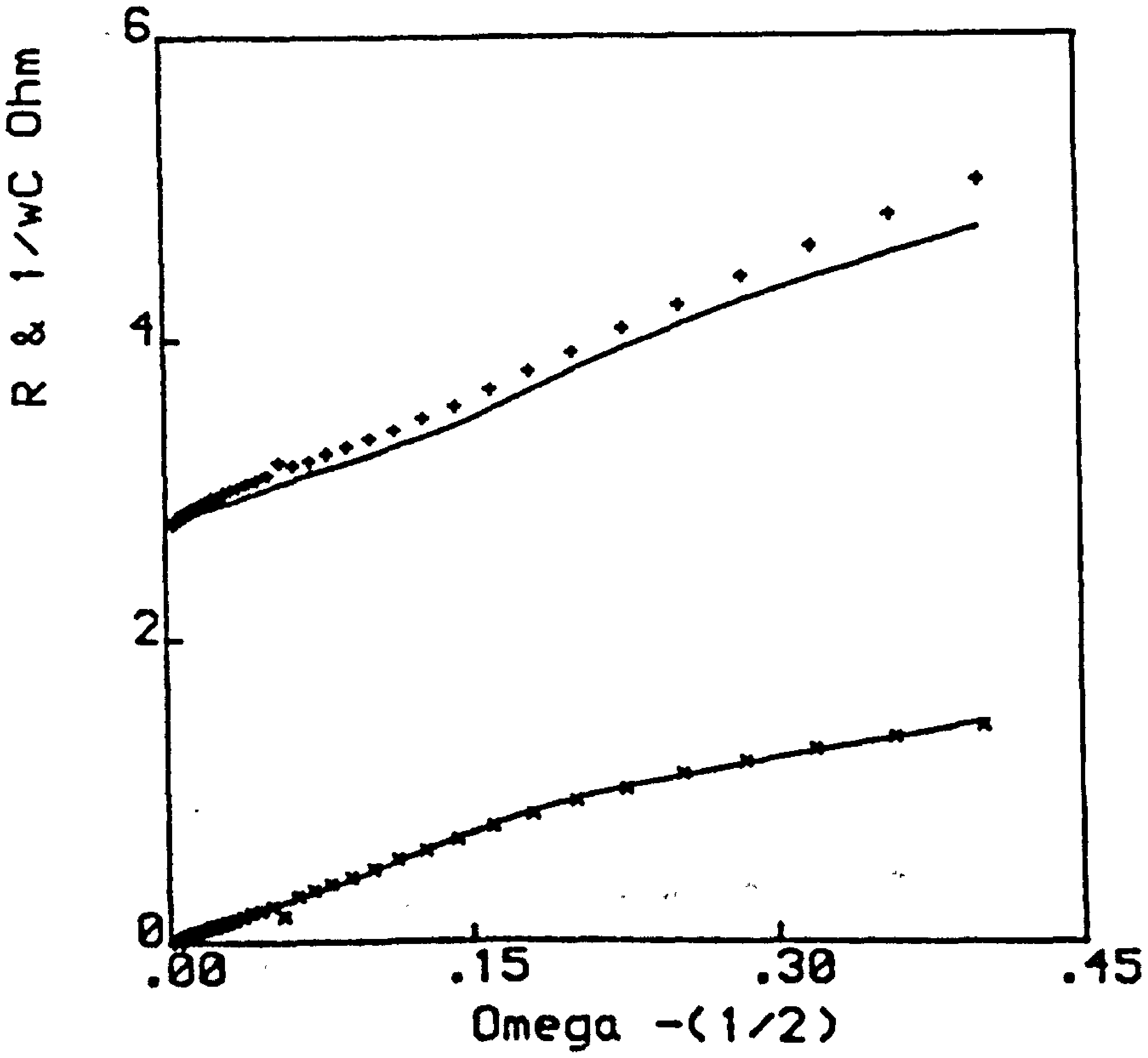

Fig. 14.25 Details as in Fig. 14.17 but at 1100 mV.

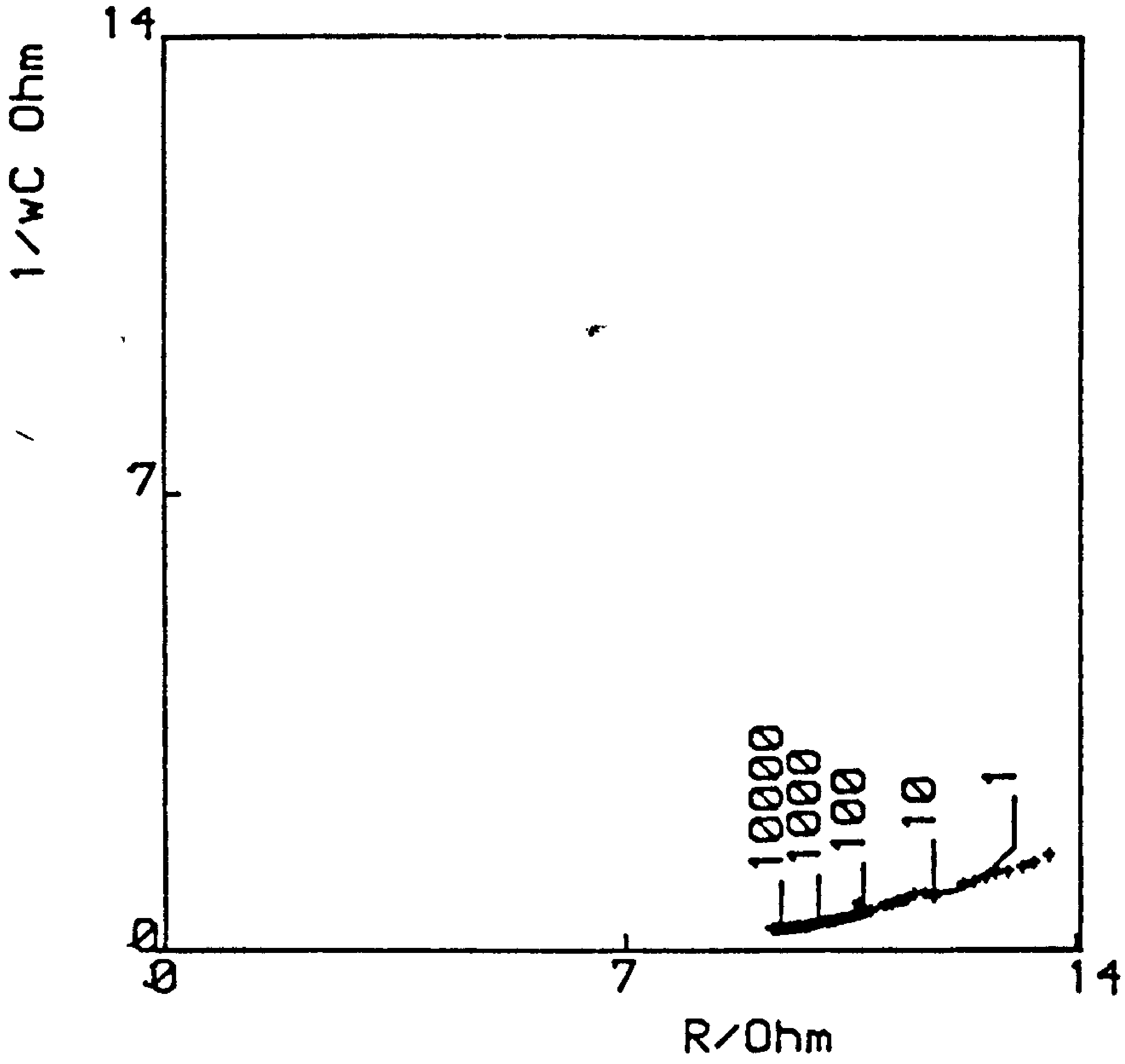

Fig. 14.26 Details as in Fig. 14.18 but at 1100 mV.

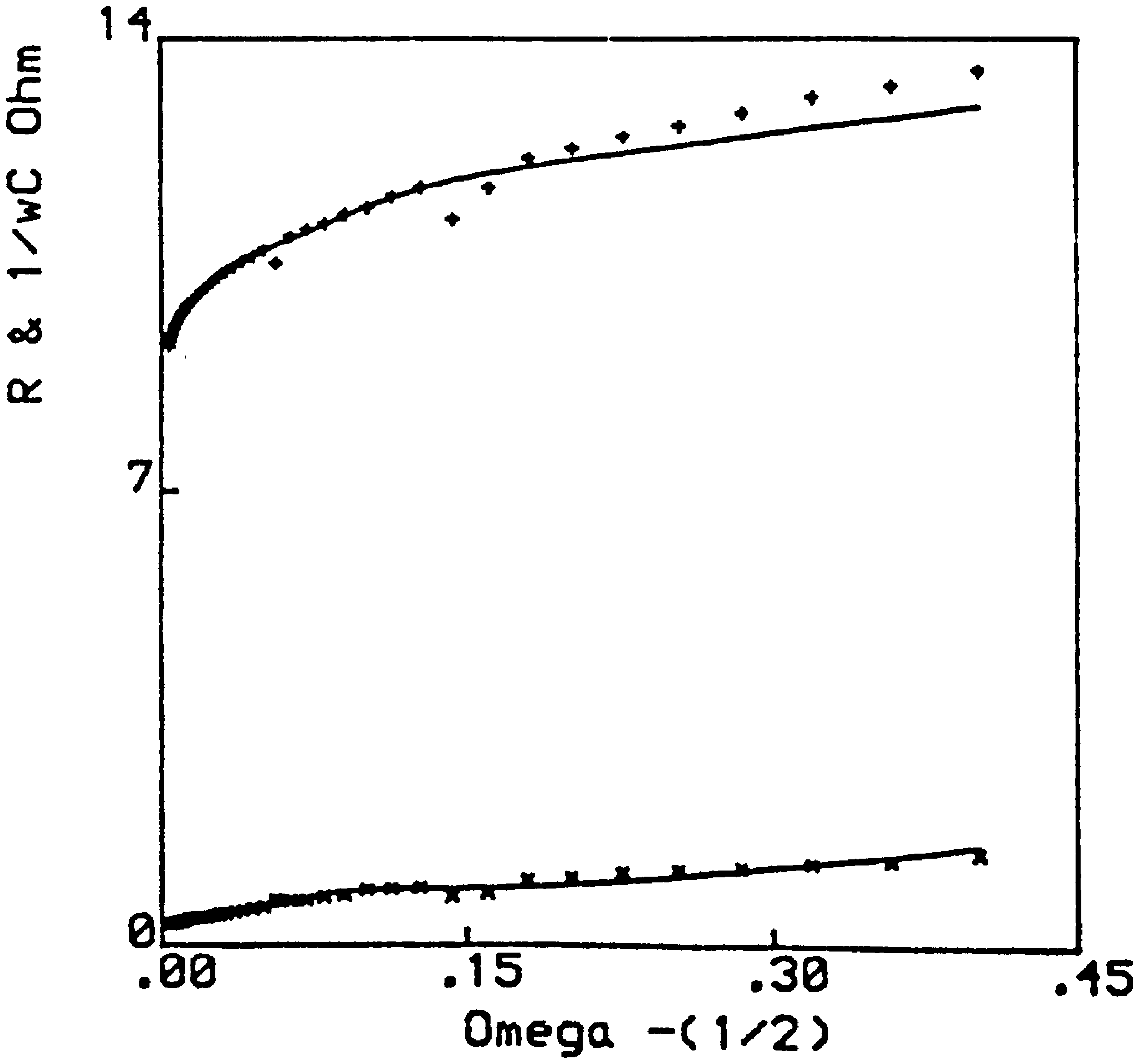

Fig. 14.27 Details as in Fig. 14.17 but at 1000 mV.

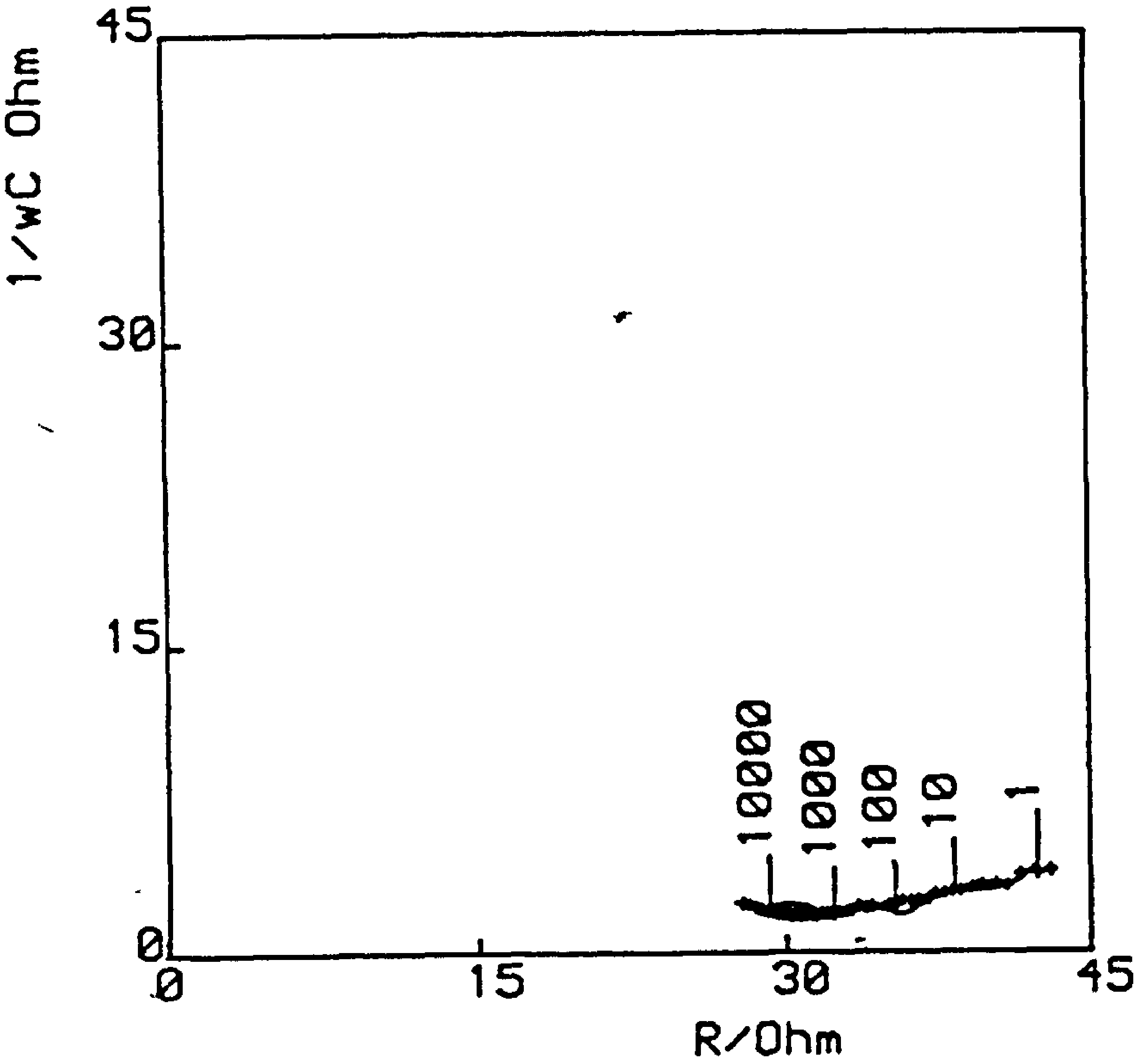

Fig. 14.28 Details as in Fig. 14.18 but at 1000 mV.

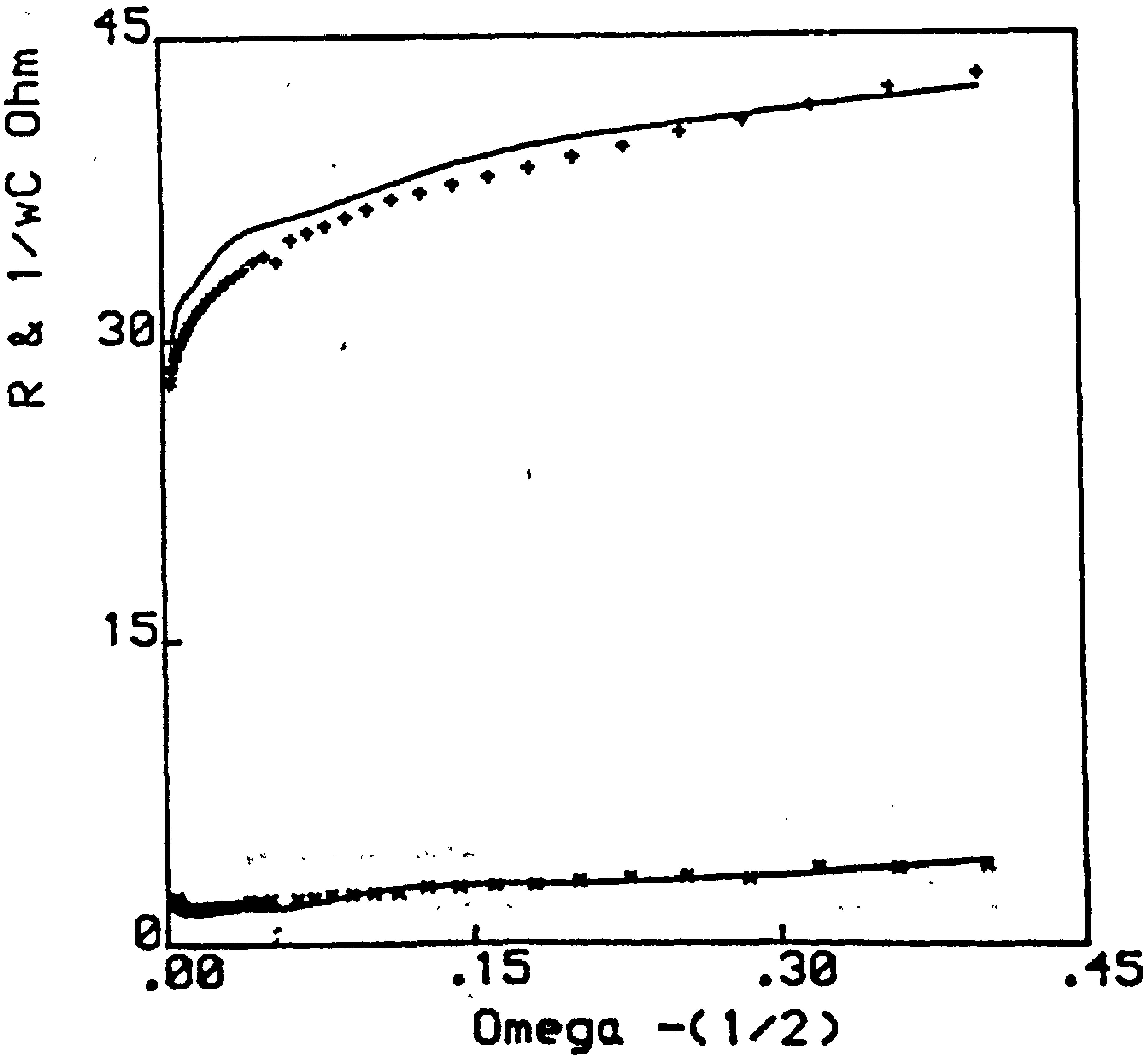

Fig. 14.29 Details as in Fig. 14.17 but at 900 mV.

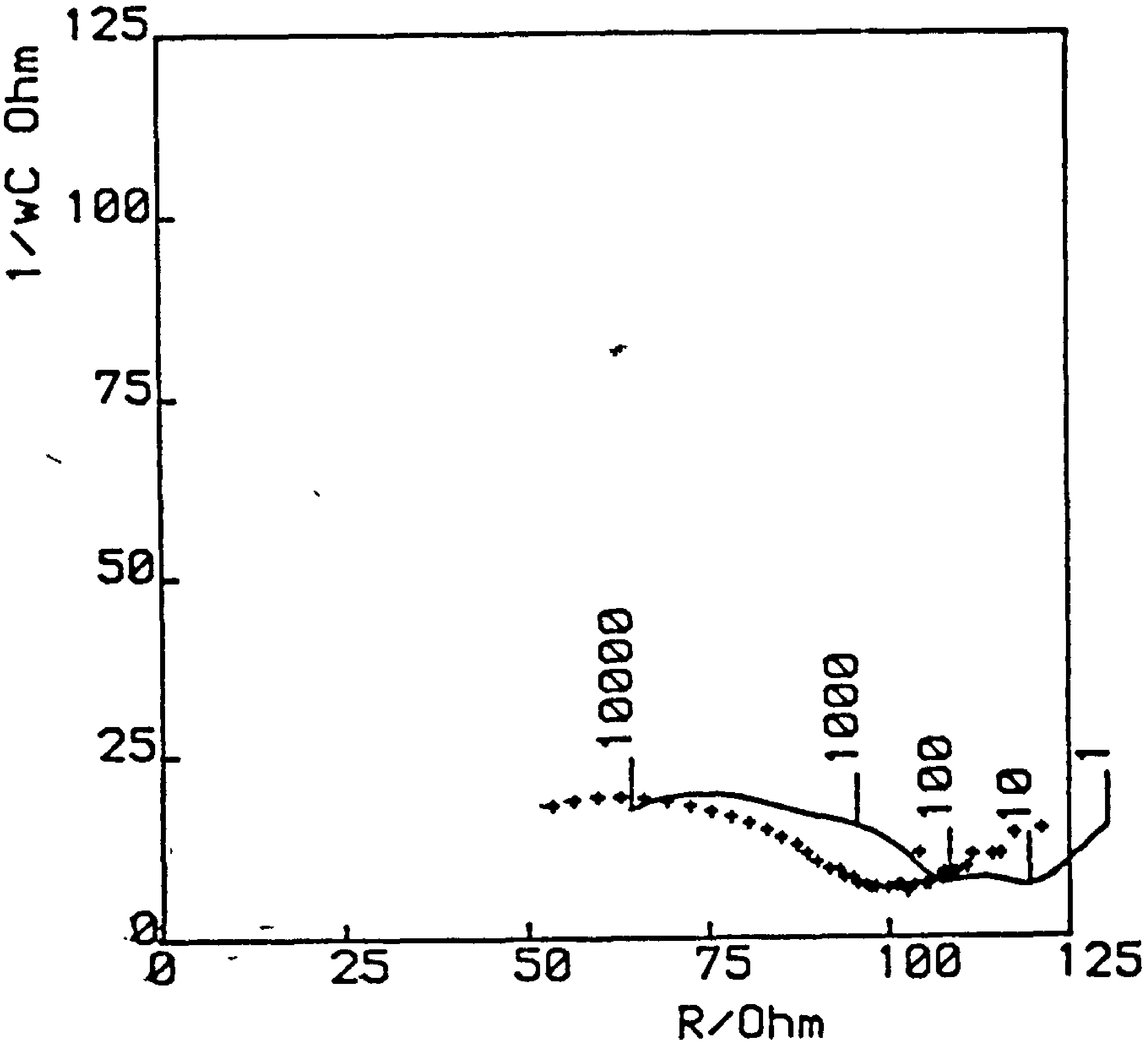

Fig. 14.30 Details as in Fig. 14.18 but at 900 mV.

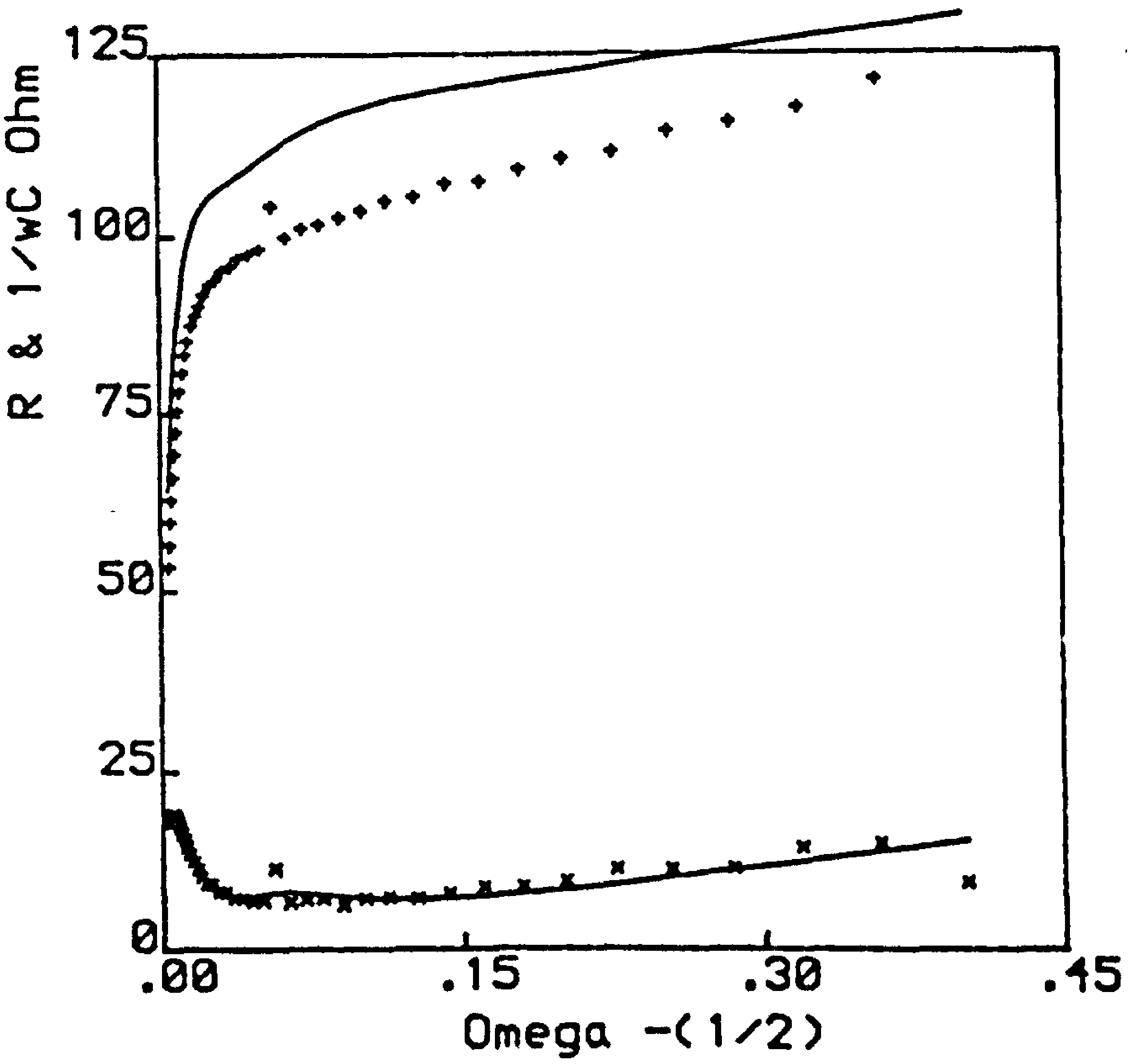

Fig. 14.31 Details as in Fig. 14.17 but at 700 mV.

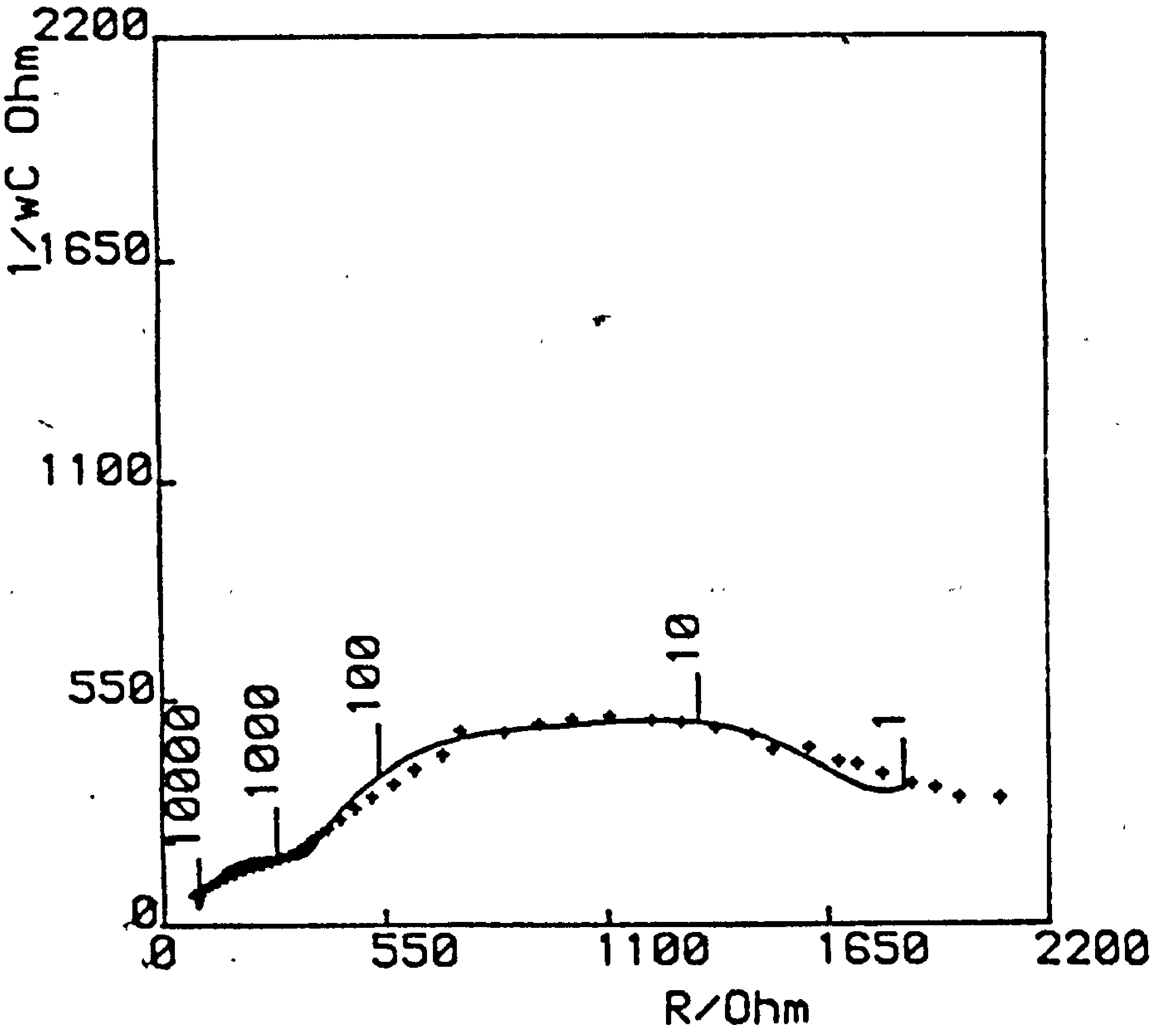

Fig. 14.32 Details as in Fig. 14.18 but at 700 mV.

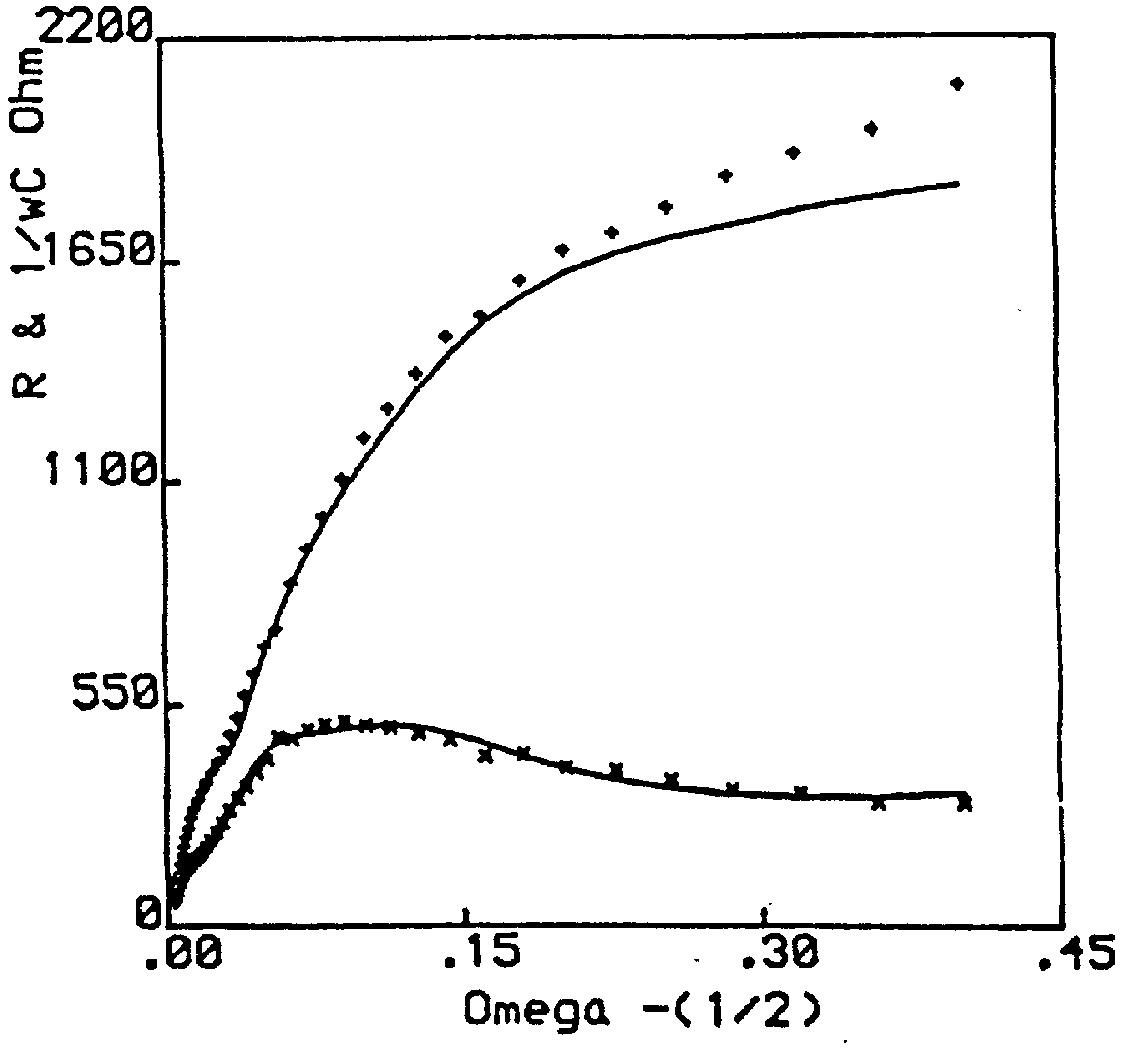

TABLE 14.2

Electrode characteristics obtained from computer match for porous PbO_2 on a Pb-Sn (0.34%) - Ca (0.086%) support at various potentials (nominal surface area = 0.07 cm^2).

Potential/V	1.190	1.180	1.170	1.150	1.100	1.000	0.900	0.700
Kinetic Parameters	10 kHz - 0.01 Hz			10 kHz - 1 Hz				
R_Ω/Ω	1.157	1.081	1.559	2.764	0.253	27.79	53.48	82.4
θ/Ω	0.956	0.2952	0.9071	0.2508	0.8396	3.655	20.24	844.6
C_{dL}/F	4.5163E-2	1.5561E-2	2.0523E-2	5.2374E-3	6.1003E-4	1.5125E-4	8.0321E-6	3.5073E-6
$\sigma/\Omega s^{-\frac{1}{2}}$	0.2064	1.513	0.9646	3.133	3.708	9.647	37.16	609.1
C_{ads}/F	0.1911	0.2272	0.2051	6.2465E-2	1.0152E-2	5.0974E-3	4.2903E-4	3.5414E-5
R_{ads}/Ω	1.364	0.6903	1.268	0.5829	0.7763	2.775	8.529	412.7
C_{ext}/F	0.4393	0.8058	1.224	1.4836E-3	4.9964E-5	5.417E-6	7.0791E-7	3.6695E-7
R_{ext}/Ω	(1E12)	9.220	3.773	9.2939E-2	0.6539	4.404	33.14	278.4

is acting as a pure capacitor.

c) Pasted Pb-Sn (0.34%) - Bi (0.15%) - Ca (0.086%) electrode

Figs. 14.33 and 14.34 represent the Sluyters and Randles plots respectively for porous PbO_2 on a Pb-Sn (0.34%) - Bi (0.15%) - Ca (0.086%) support at the open circuit potential , 1190 mV. With the first three potentials the corresponding Randles plots (Figs. 14.34, 14.36 and 14.38) highlight the adsorptive nature of the discharge process on the electrode surface. As with the earlier two sections Figs. 14.33-14.48 represent the Sluyters and Randles plots for the positive in the potential range 1190-700 mV. Again, Figs. 14.33 and 14.35 show no well-defined Warburg lines at low frequencies. Another interesting feature is that the shapes of the curves observed in the figures (Figs. 14.33-14.48) are similar to the corresponding ones in the previous sections (that is, Figs. 14.1-14.16 and Figs. 14.17-14.32). Using the computer, the data in Figs. 14.33-14.48 were tested successfully with the analogue in Fig. 13.17.

Table 14.3 shows the calculated kinetic parameters which make up the analogue for the Pb-Sn-Bi-Ca positive. Using the potential range 1150-700 mV, again the charge transfer resistance, Warburg coefficient, adsorption resistance and external film resistance increase with decreasing potential. At 700 mV the values obtained for θ and σ are similar to those gained with the Pb-Sn-Ca positive, however, the values for R_{ads} and R_{ext} are very high indicating the formation of a thick $PbSO_4$ layer.

Looking at Tables 14.1, 14.2 and 14.3 there is no significant relationship between the electrolyte resistance and the nature of the alloy bases. It is important to note that the R_Ω values which contain any purely ohmic contribution from the interaction of the alloy and the transformed paste are not influenced by alloy structure, this has often been a point of debate in the lead battery manufacturing industry.

Fig. 14.33 The complex-plane plot (Sluyters plot) for porous PbO_2 on a Pb-Sn (0.34%) - Bi(0.15%) - Ca (0.086%) support (nominal surface area = 0.07 cm^2) in 5M H_2SO_4 at 23°C; 1190 mV; frequencies in hertz are given on the plot. The crosses (+) show experimental data and the line shows the computer match.

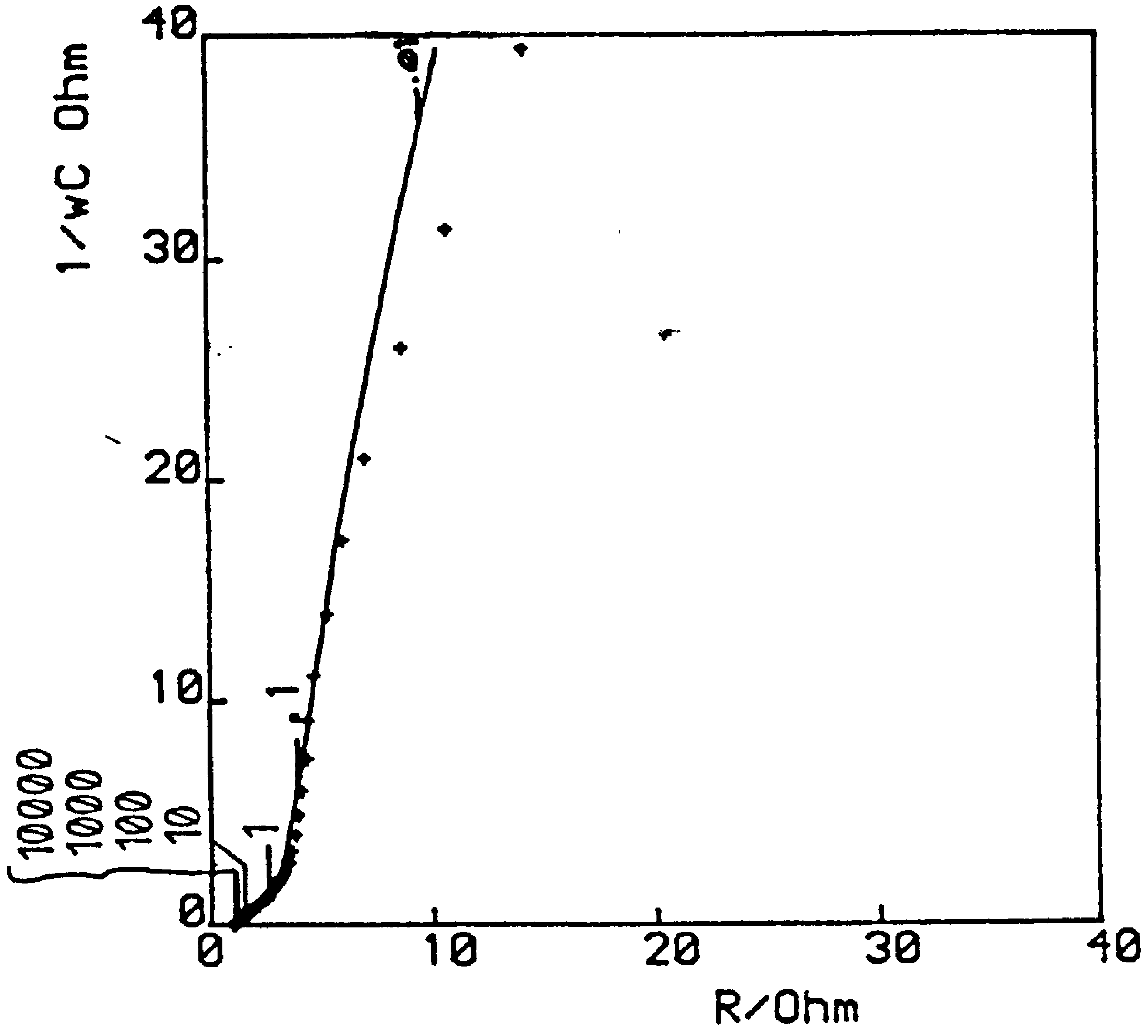

Fig. 14.34 The Randles plot corresponding to the system of Fig. 14.33 at 1190 mV. + and x correspond to experimental data (R and 1/ωC respectively) and the lines show the computer matches.

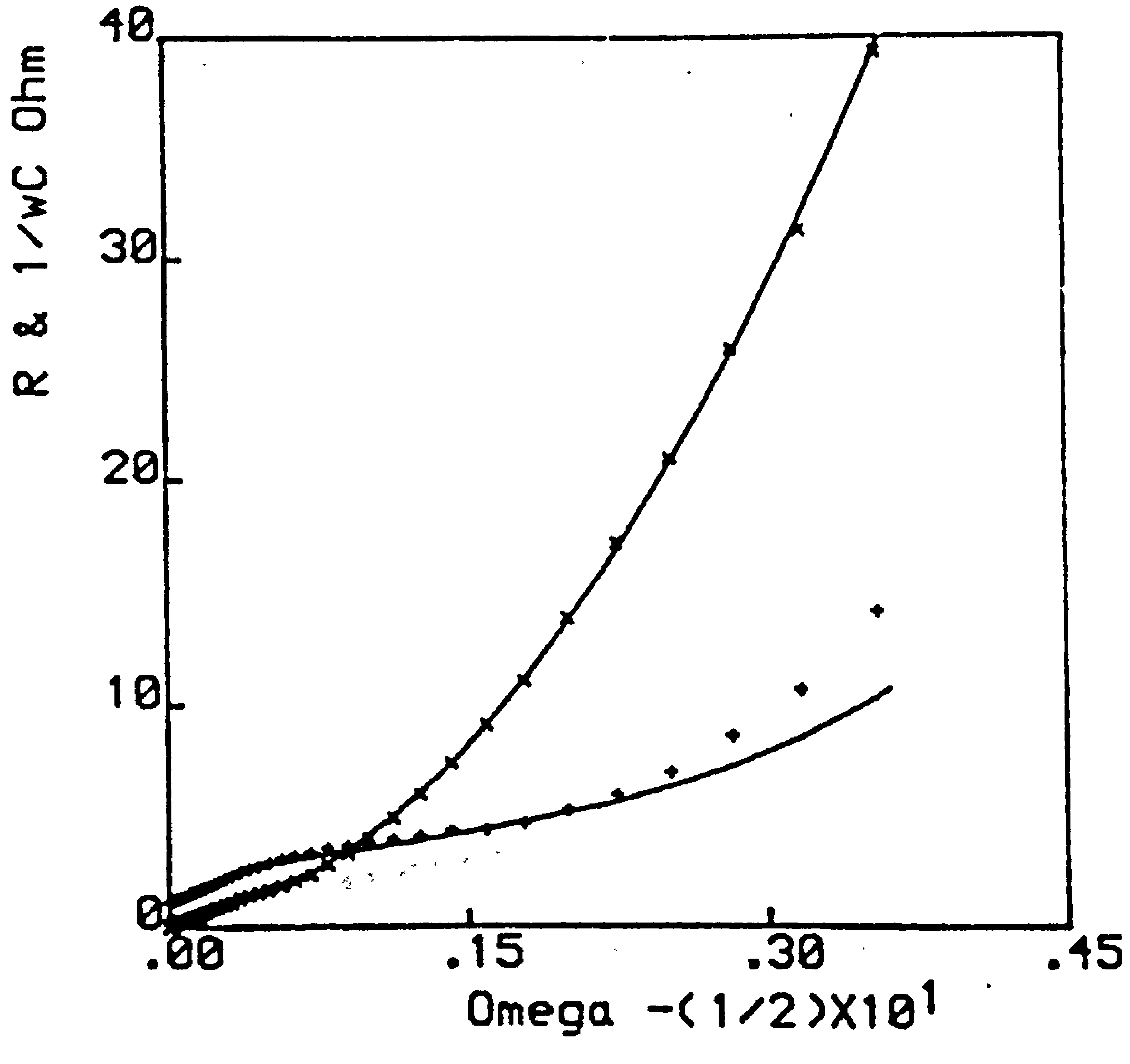

Fig. 14.35 Details as in Fig. 14.33 but at 1180 mV.

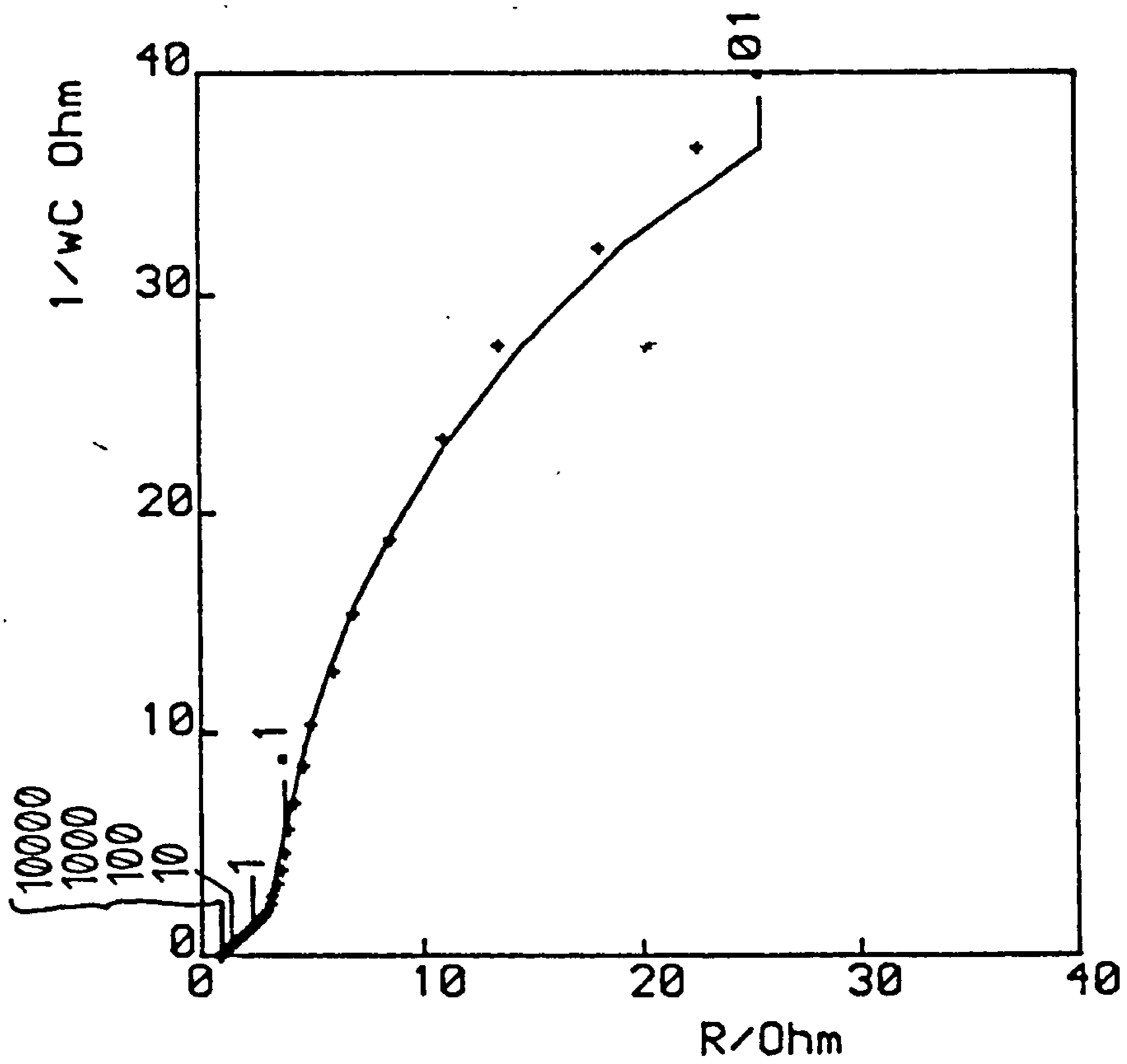

Fig. 14.36 Details as in Fig. 14.34 but at 1180 mV.

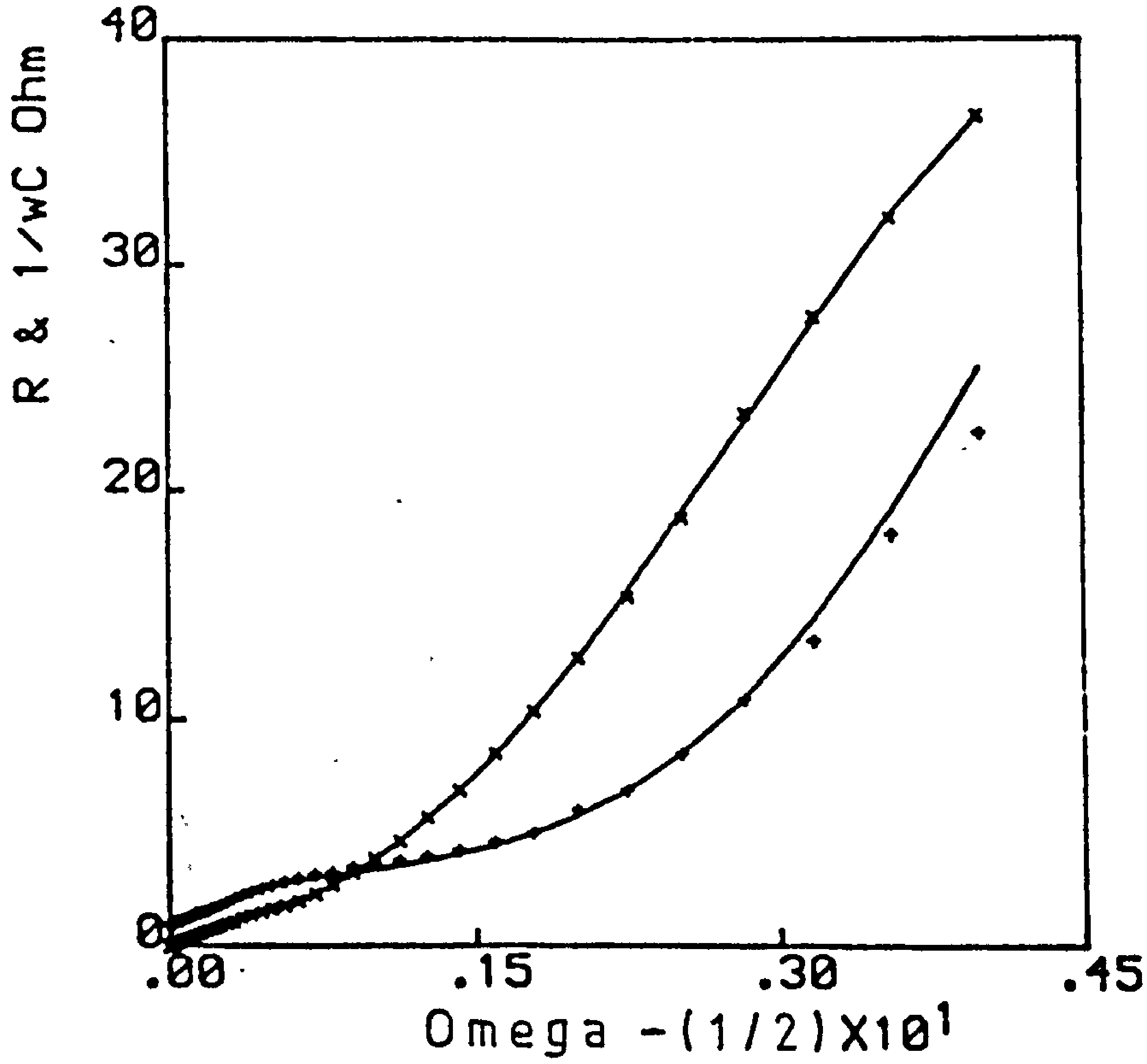

Fig. 14.37 Details as in Fig. 14.33 but at 1170 mV.

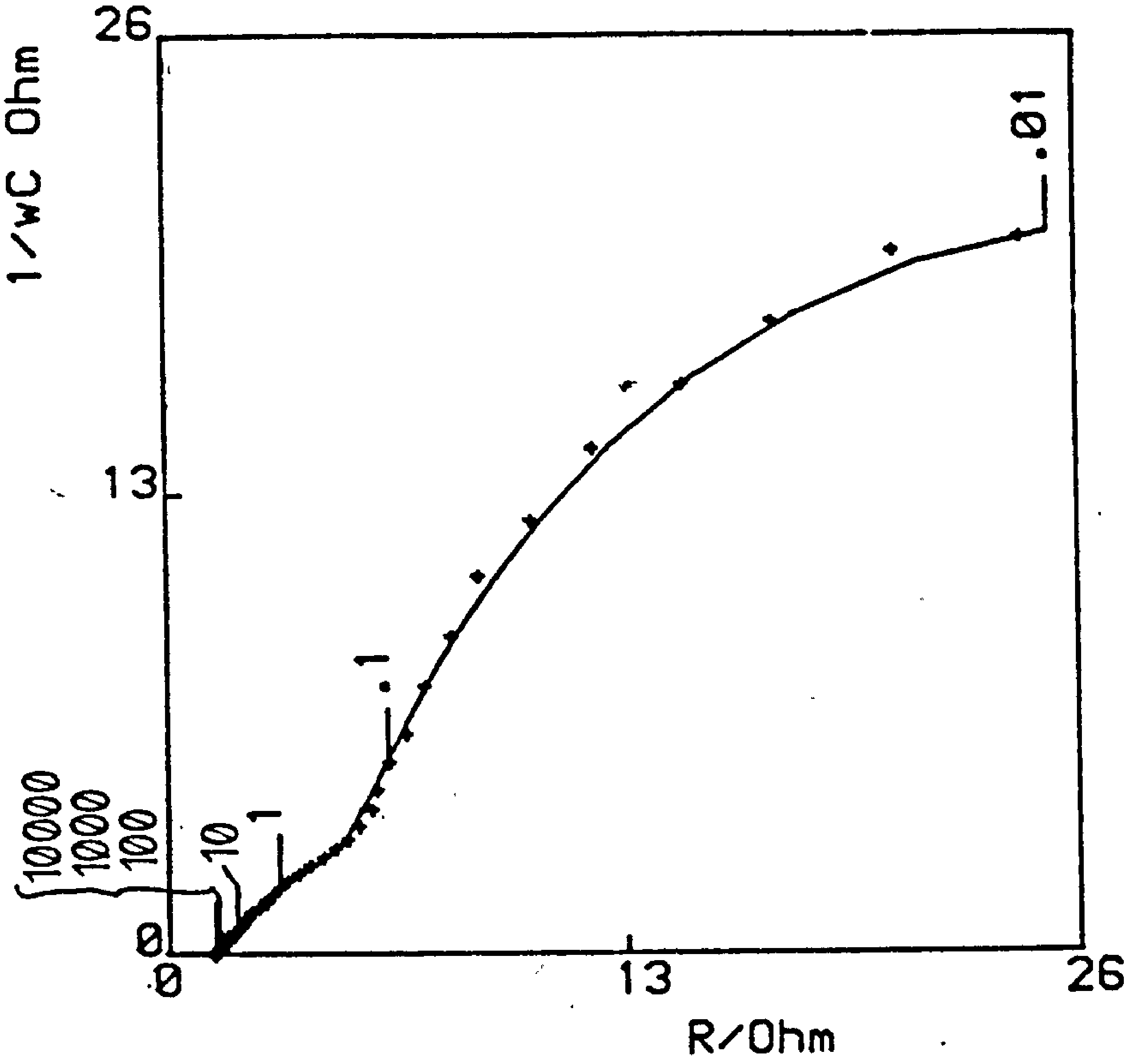

Fig. 14.38 Details as in Fig. 14.34 but at 1170 mV.

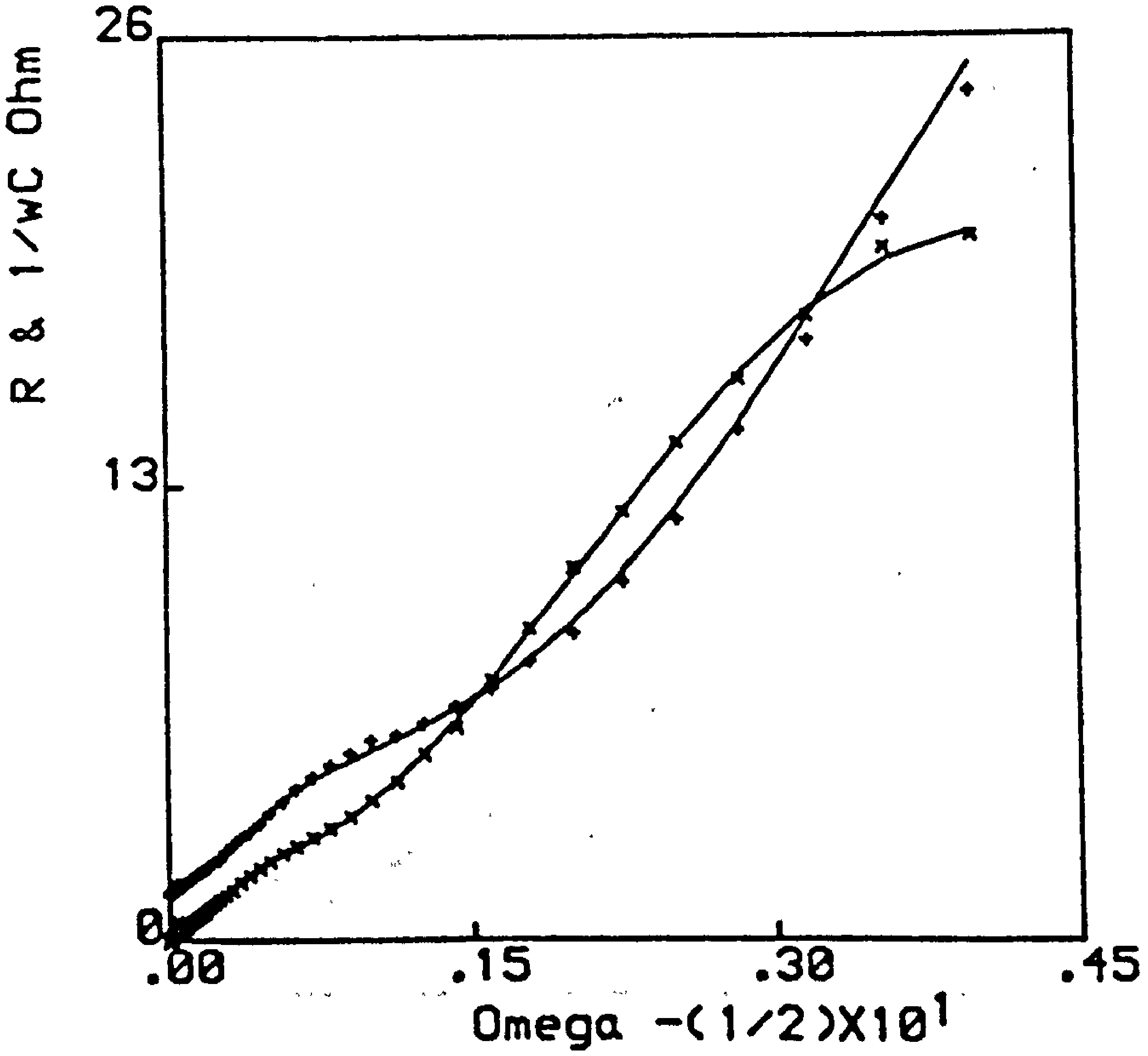

Fig. 14.39 Details as in Fig. 14.33 but at 1150 mV.

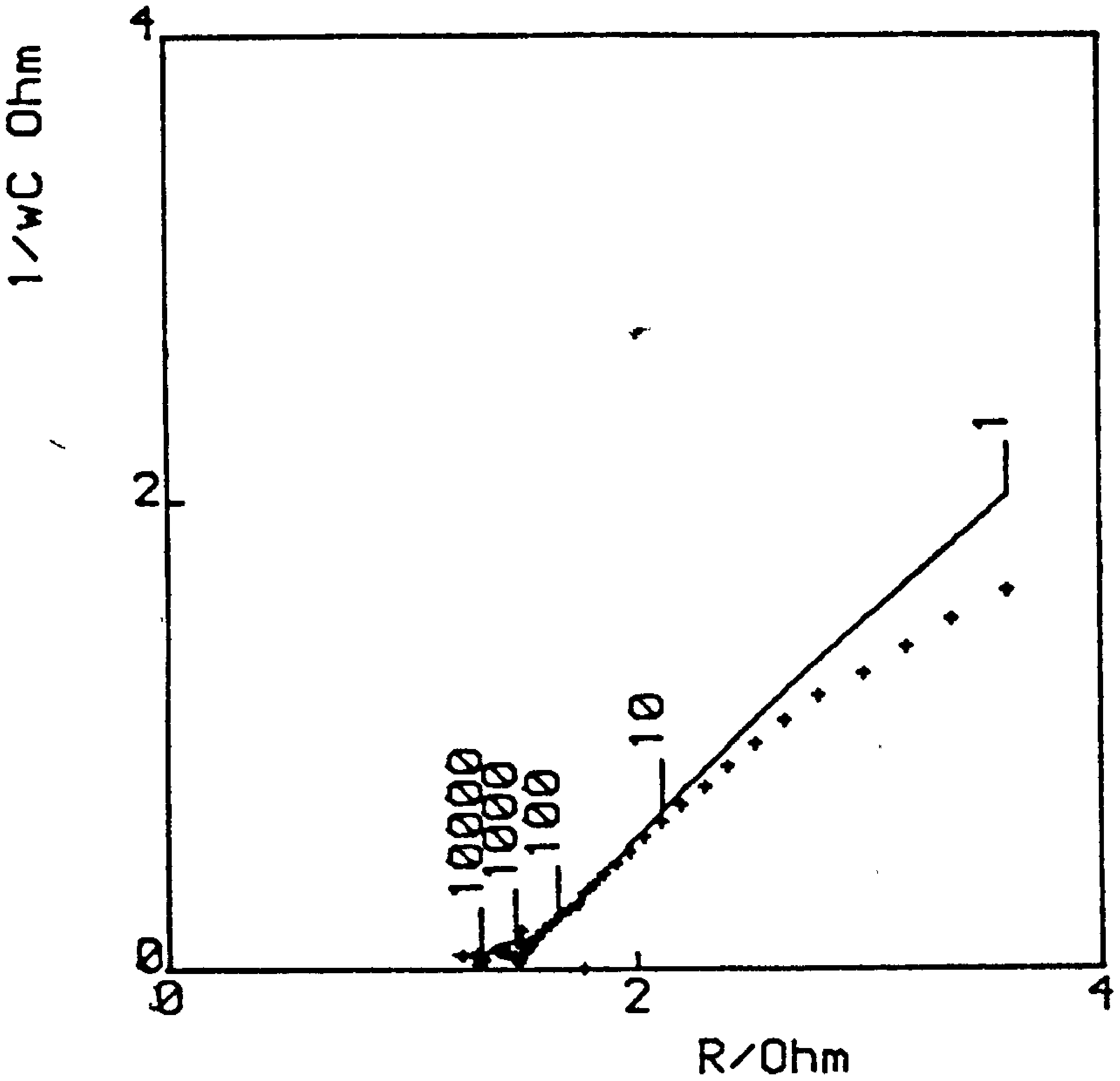

Fig. 14.40 Details as in Fig. 14.34 but at 1150 mV.

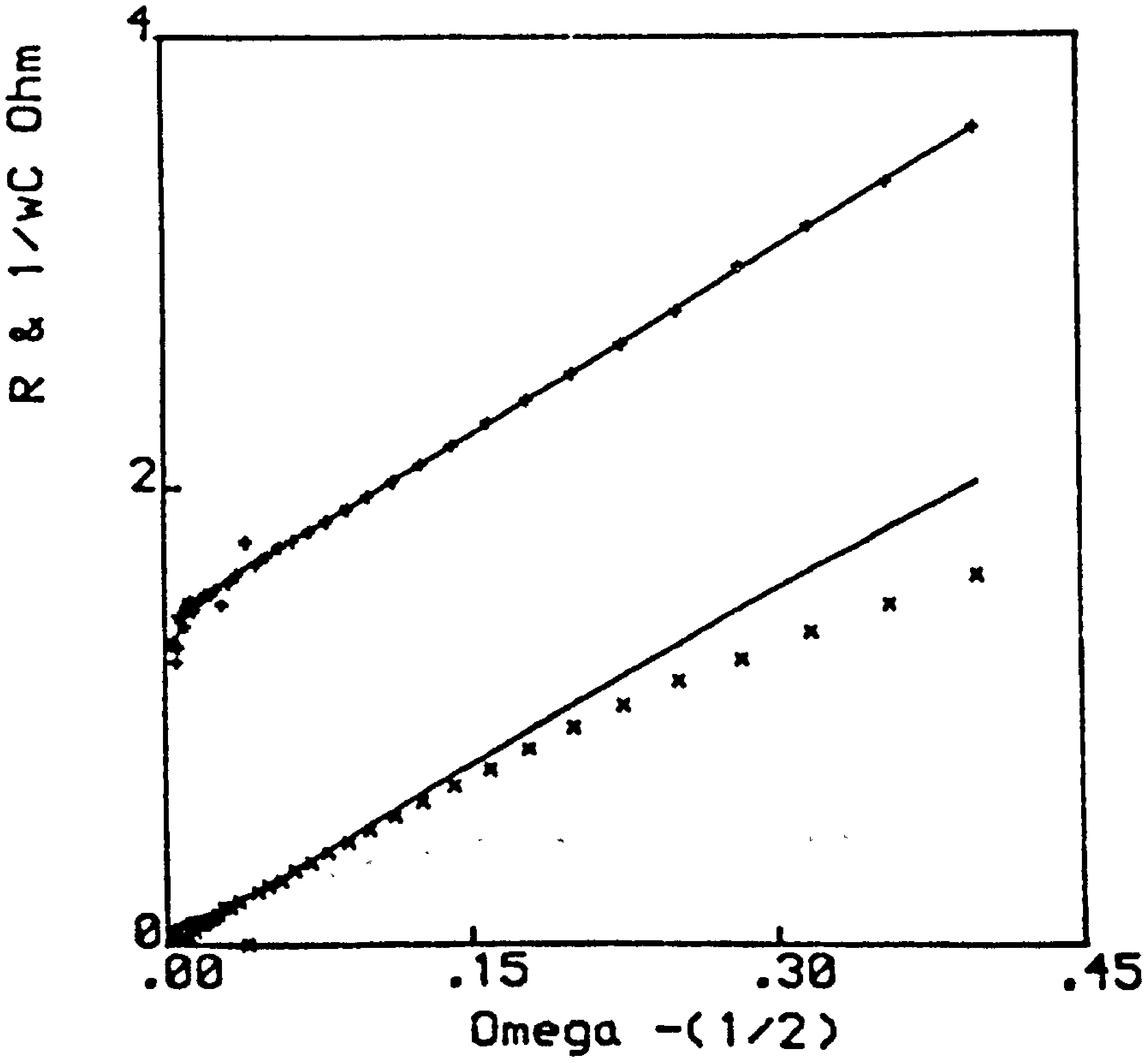

Fig. 14.41 Details as in Fig. 14.33 but at 1100 mV.

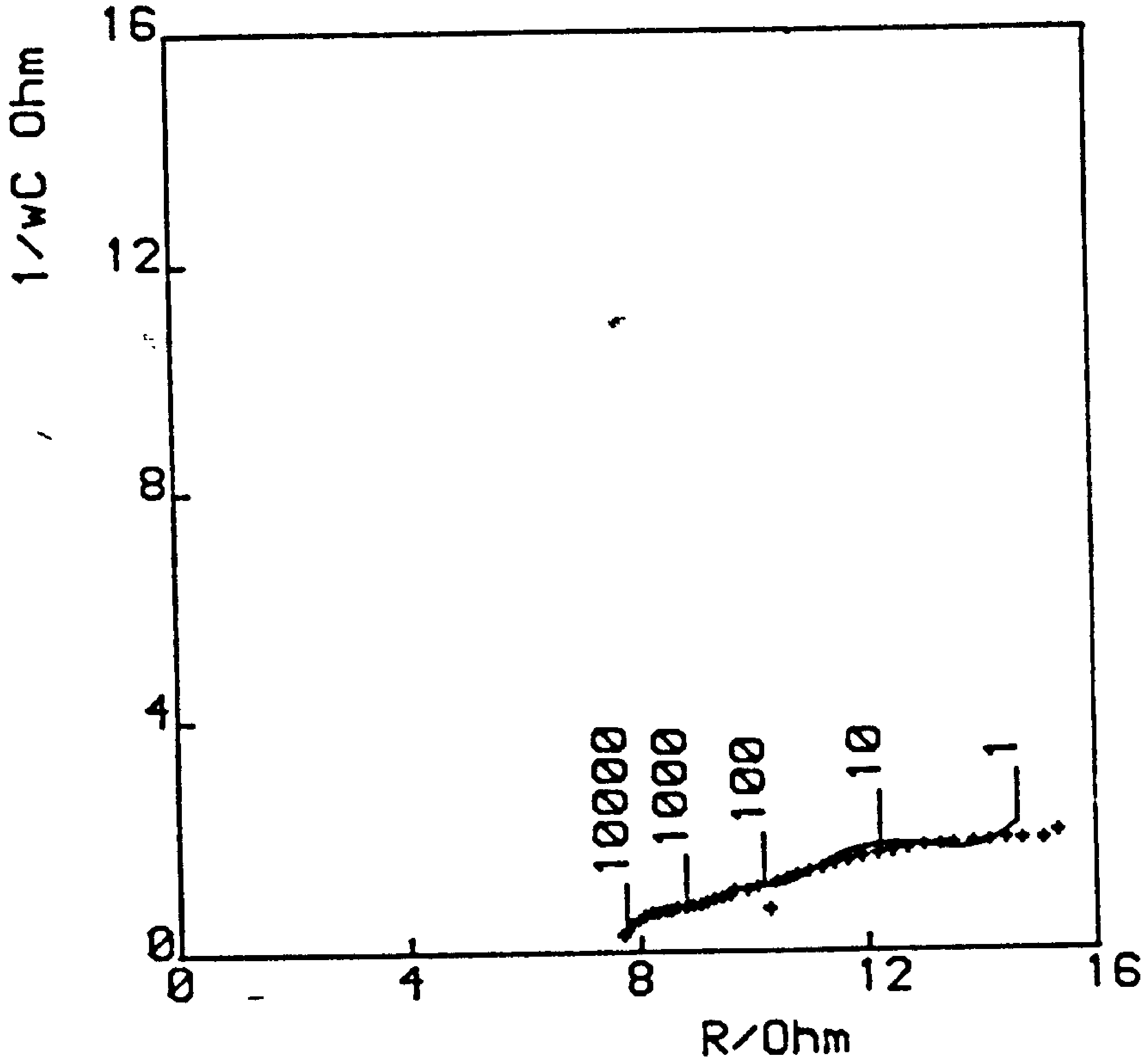

Fig. 14.42 Details as in Fig. 14.34 but at 1100 mV.

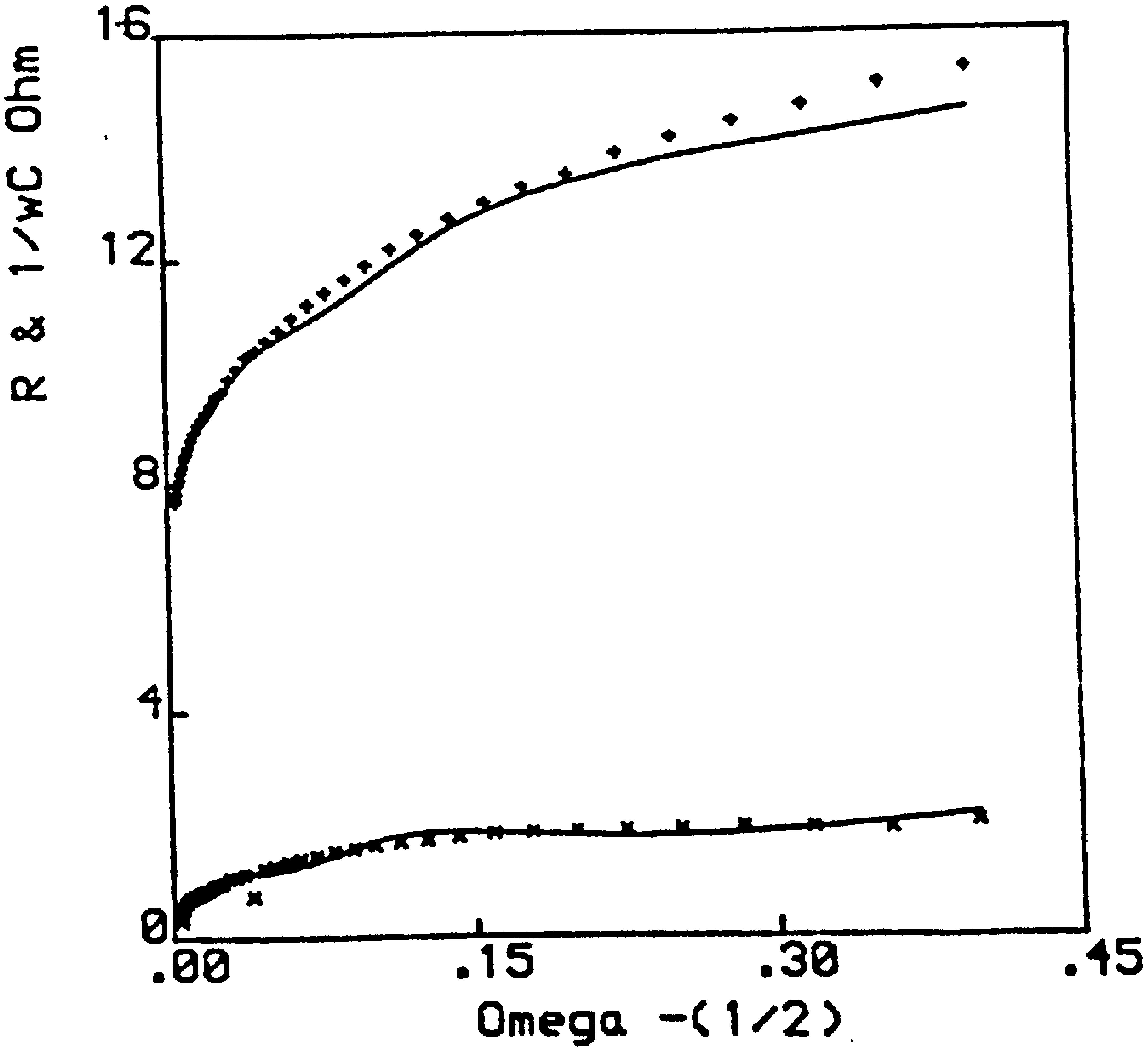

Fig. 14.43 Details as in Fig. 14.33 but at 1000 mV.

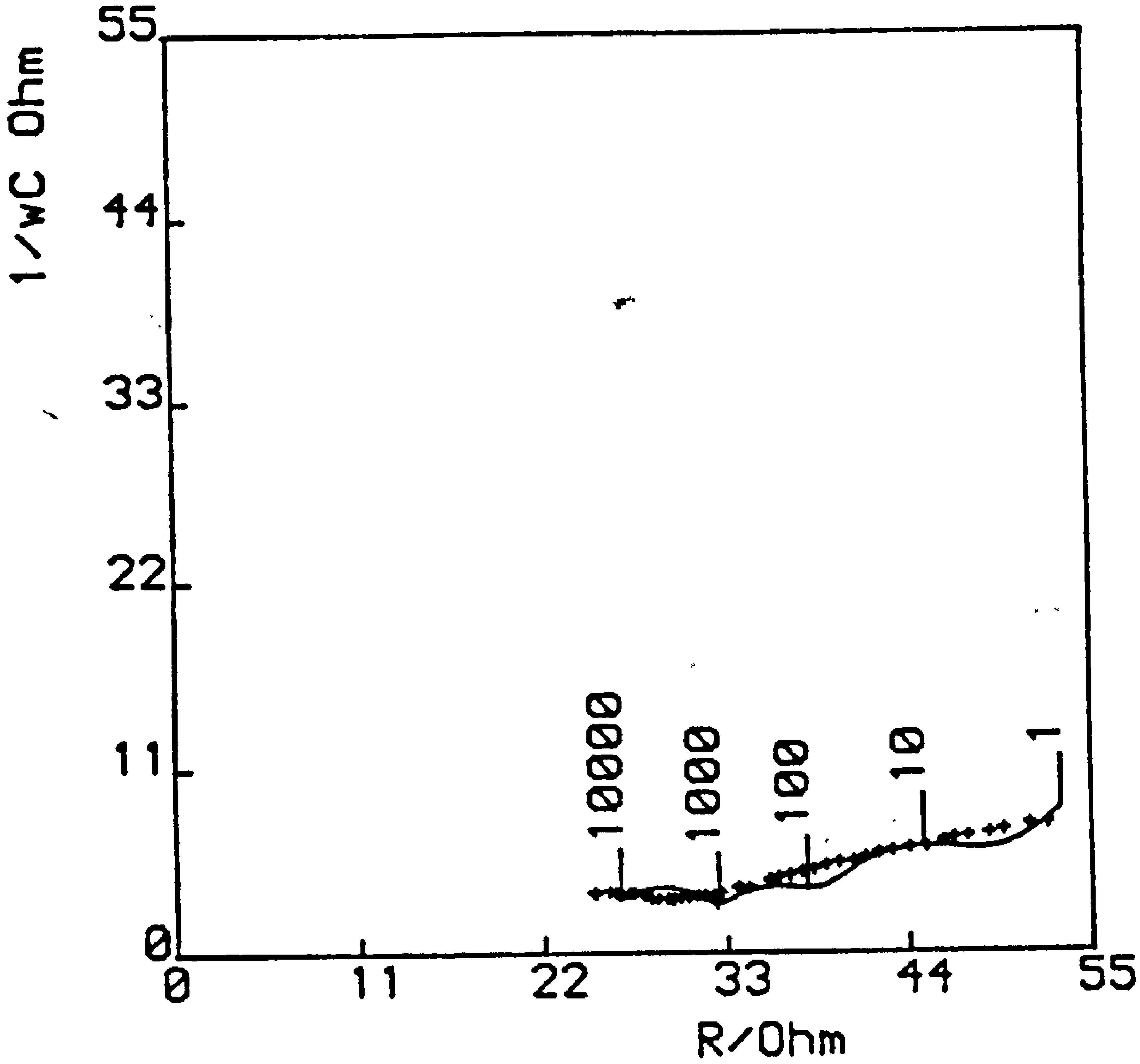

Fig. 14.44 Details as in Fig. 14.34 but at 1000 mV.

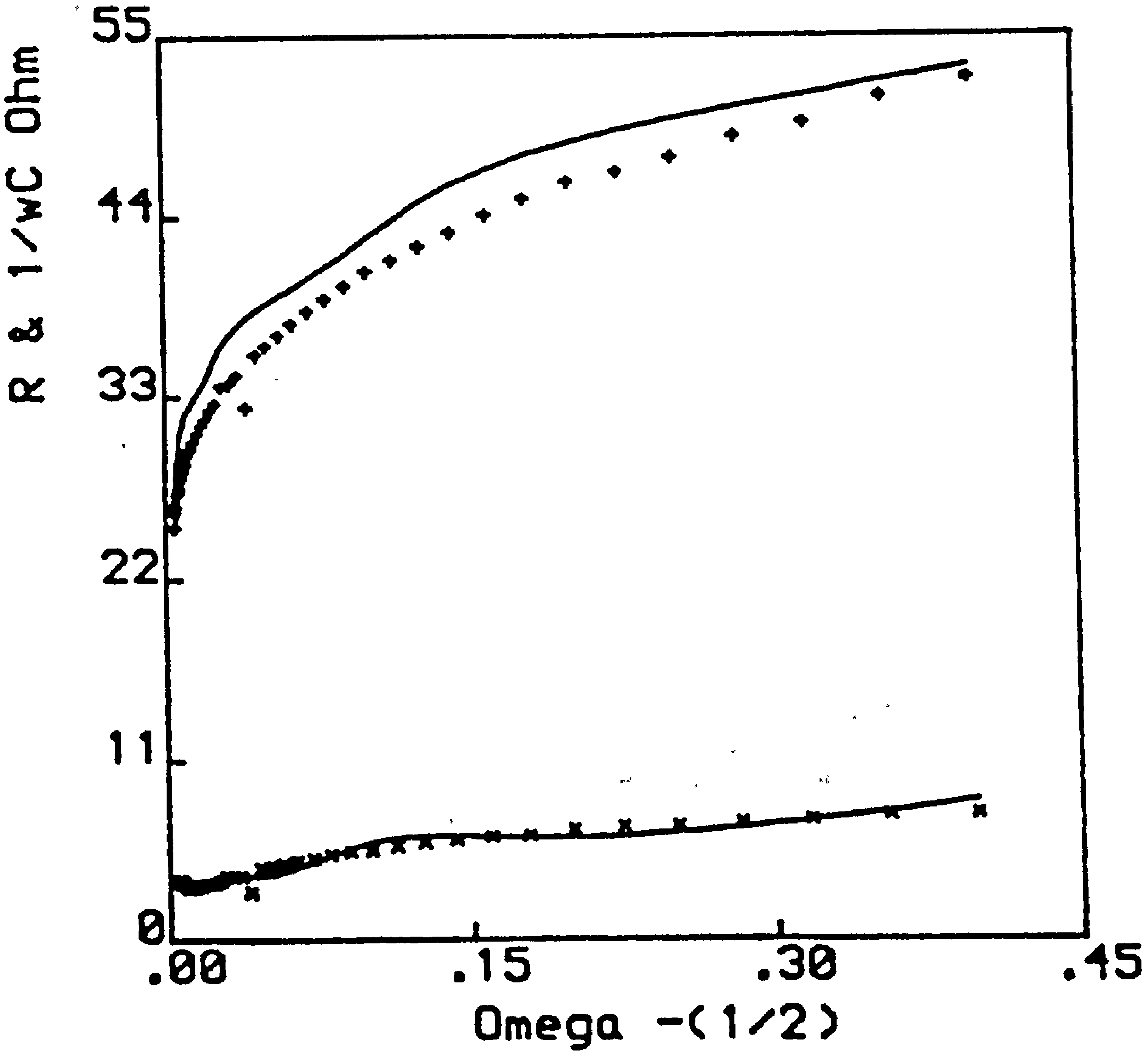

Fig. 14.45 Details as in Fig. 14.33 but at 900 mV.

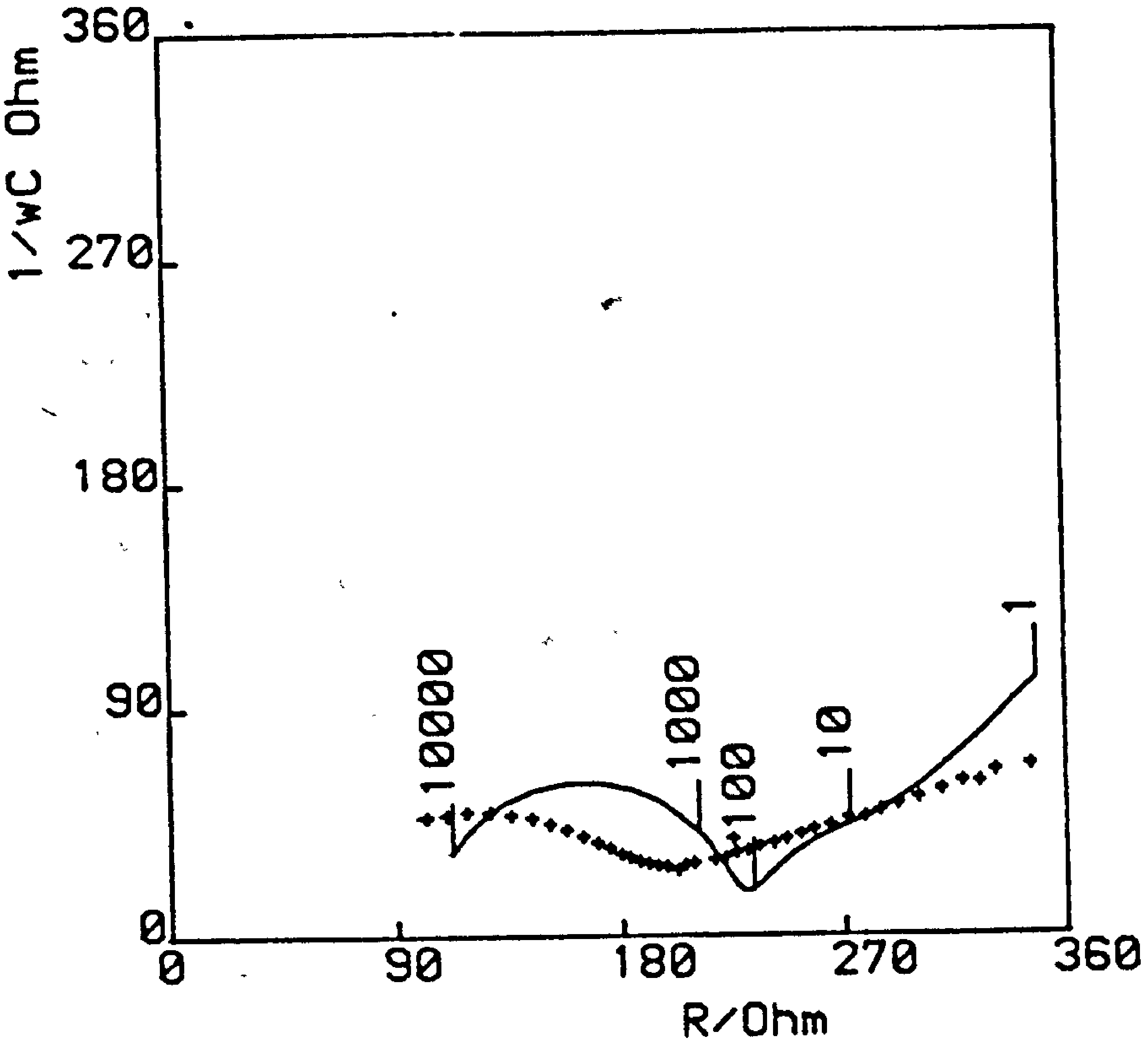

Fig. 14.46 Details as in Fig. 14.34 but at 900 mV.

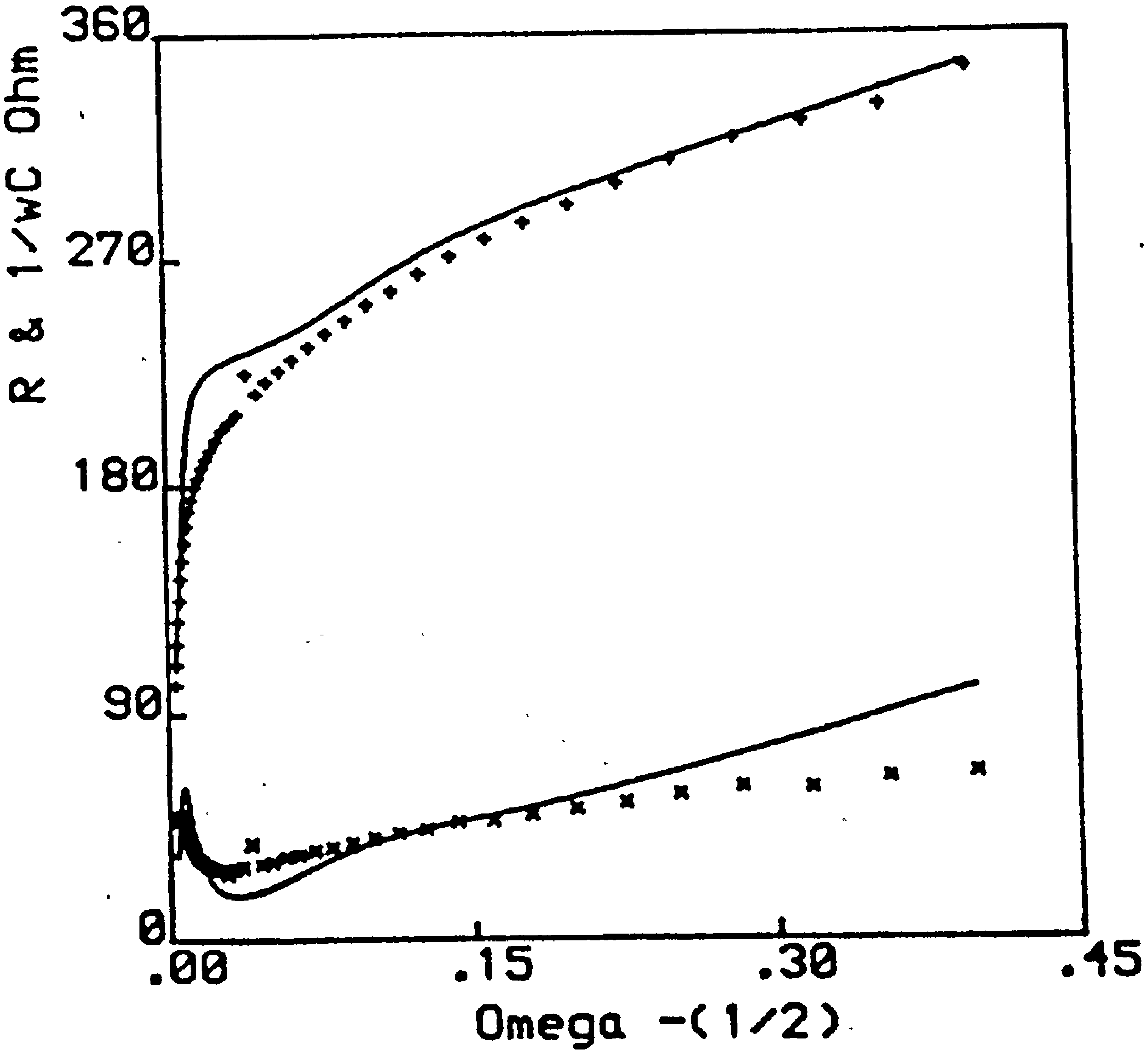

Fig. 14.47 Details as in Fig. 14.33 but at 700 mV.

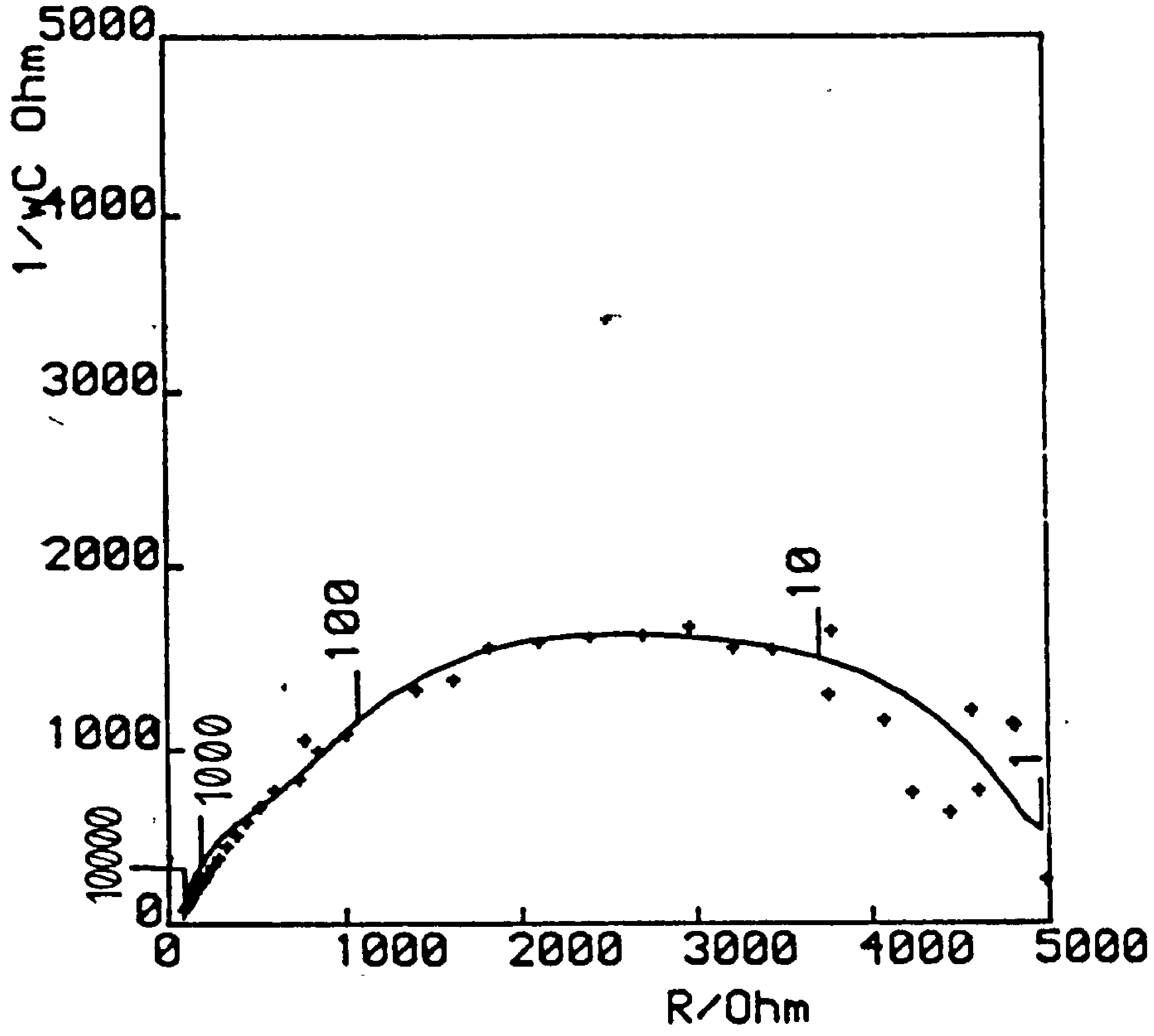

Fig. 14.48 Details as in Fig. 14.34 but at 700 mV.

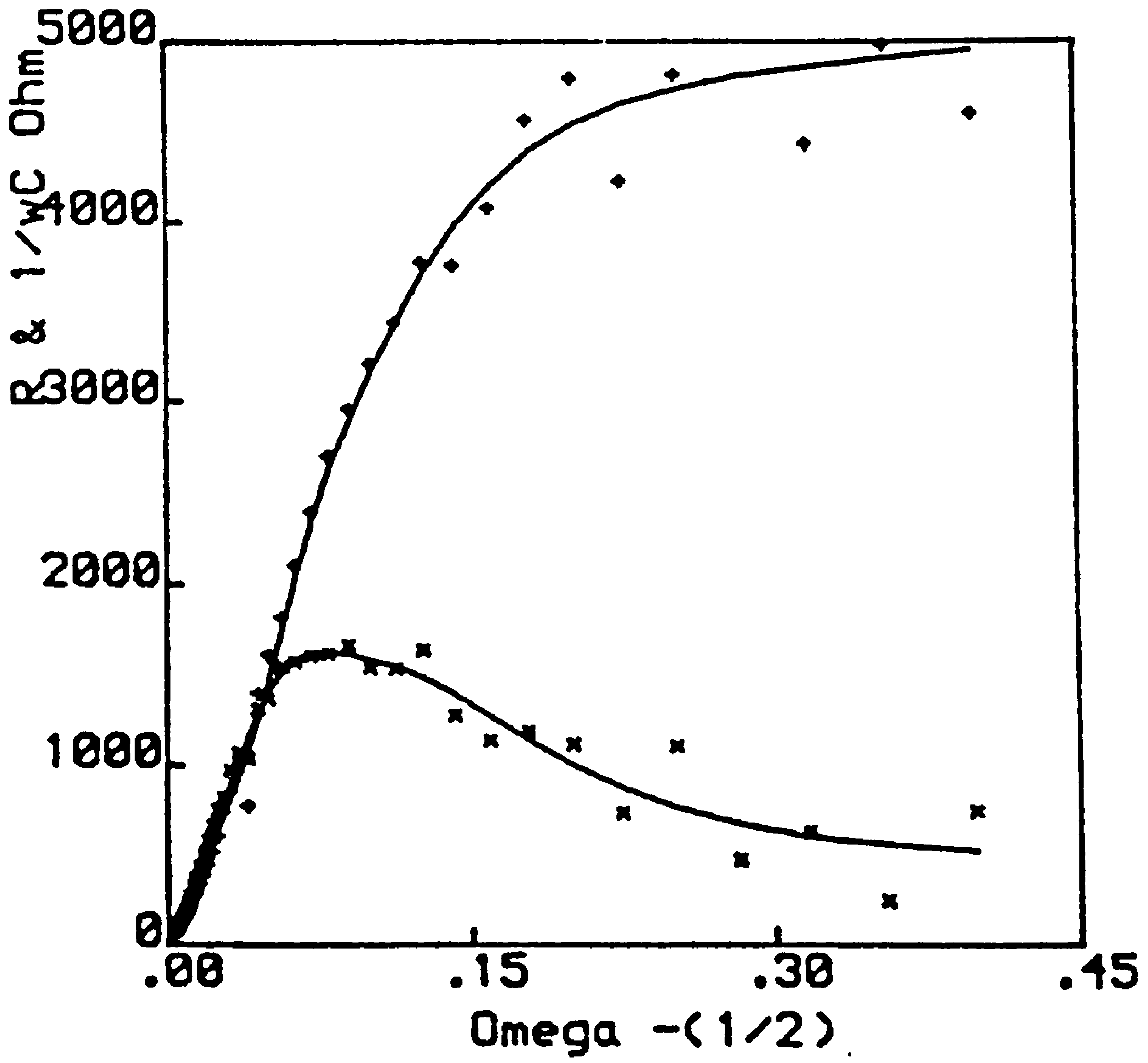

TABLE 14.3

Electrode characteristics obtained from computer match for porous PbO_2 on a Pb-Sn (0.34%) - Bi (0.15%) - Ca (0.086%) support at various potentials (nominal surface area = 0.07 cm^2).

Potential/V Kinetic Parameters	1.190	1.180	1.170	1.150	1.100	1.000	0.900	0.700
	10 kHz - 0.01 Hz			10 kHz - 1Hz				
R_Ω/Ω	1.055	0.9069	1.330	1.319	7.700	25.04	102.0	88.34
θ/Ω	0.4388	0.6261	0.5629	0.1721	1.896	6.779	43.80	732.6
C_{dL}/F	6.8256E-3	1.2986E-2	5.5864E-3	3.2126E-4	5.2799E-4	9.3579E-5	1.4554E-6	5.7074E-7
$\sigma/\Omega s^{-\frac{1}{2}}$	1.264	0.8149	1.869	4.865	4.827	19.70	248.1	688.1
C_{ads}/F	8.5499E-2	0.1130	0.107	0.5077	7.024E-3	1.8256E-3	4.3095E-4	9.0655E-6
R_{ads}/Ω	0.8262	1.009	1.770	0.1865	1.918	6.427	25.92	1748
C_{ext}/F	0.3578	0.3532	0.5597	0.4282	5.6589E-5	4.2061E-6	6.3253E-7	1.6954E-6
R_{ext}/Ω	340.9	76.35	26.04	4.7515E-2	1.281	7.323	78.22	2137

From the previous chapter the θ values for porous PbO_2 on a pure Pb support have been used in Fig. 14.49. This figure shows linear relationships between $\log_{10} \theta$ and E for the various PbO_2 electrodes in the potential region 1150-700 mV. As can be seen they all tend to have the same slope, that is, 146 mV per decade. Hence the difference among the positives is the magnitudes of the charge transfer resistances for each electrode. Fig. 14.49 shows that the antimonial positive discharges more efficiently than the other electrodes due to the lower values obtained for θ. Addition of Bi to the Pb-Sn-Ca alloy does not seem to enhance the electrode behaviour.

There is no well-defined relationship between C_{dL} and E; the data relating σ and E are scattered, however, in the main diffusing area of each of the electrodes is independent of the alloy backings as required by theory. The capacitances of the adsorption film are shown in Tables 14.1, 14.2 and 14.3, even though they decrease with potential as required by flat capacitor theory for a progressively thickening layer, there appears to be no pronounced influence of the alloy although the capacitances are rather larger in the case of the Sb alloy. The C_{ext} values do not show any clear correlation with alloy type although in general they decrease with potential as expected for the ultimate development of a thick passivating layer of lead sulphate.

Figs. 14.50 and 14.51 correspond to plots of $\log_{10} R_{ads}$ vs. E and $\log_{10} R_{ext}$ vs. E respectively. As can be seen the R_{ads} and R_{ext} values show the same change with potential for the alloys. This is to be expected since the characteristics of the films ought to be independent of the electrochemical activities.

d) Various porous PbO_2 electrodes

Figs. 14.52 and 14.53 correspond to the Sluyters and Randles plots respectively for the 4.55 gcm^{-3} pasted (porous) PbO_2 on a Pb-Sb (1.88%) support at the open circuit potential, 1190 mV. Figs. 14.54 and 14.55

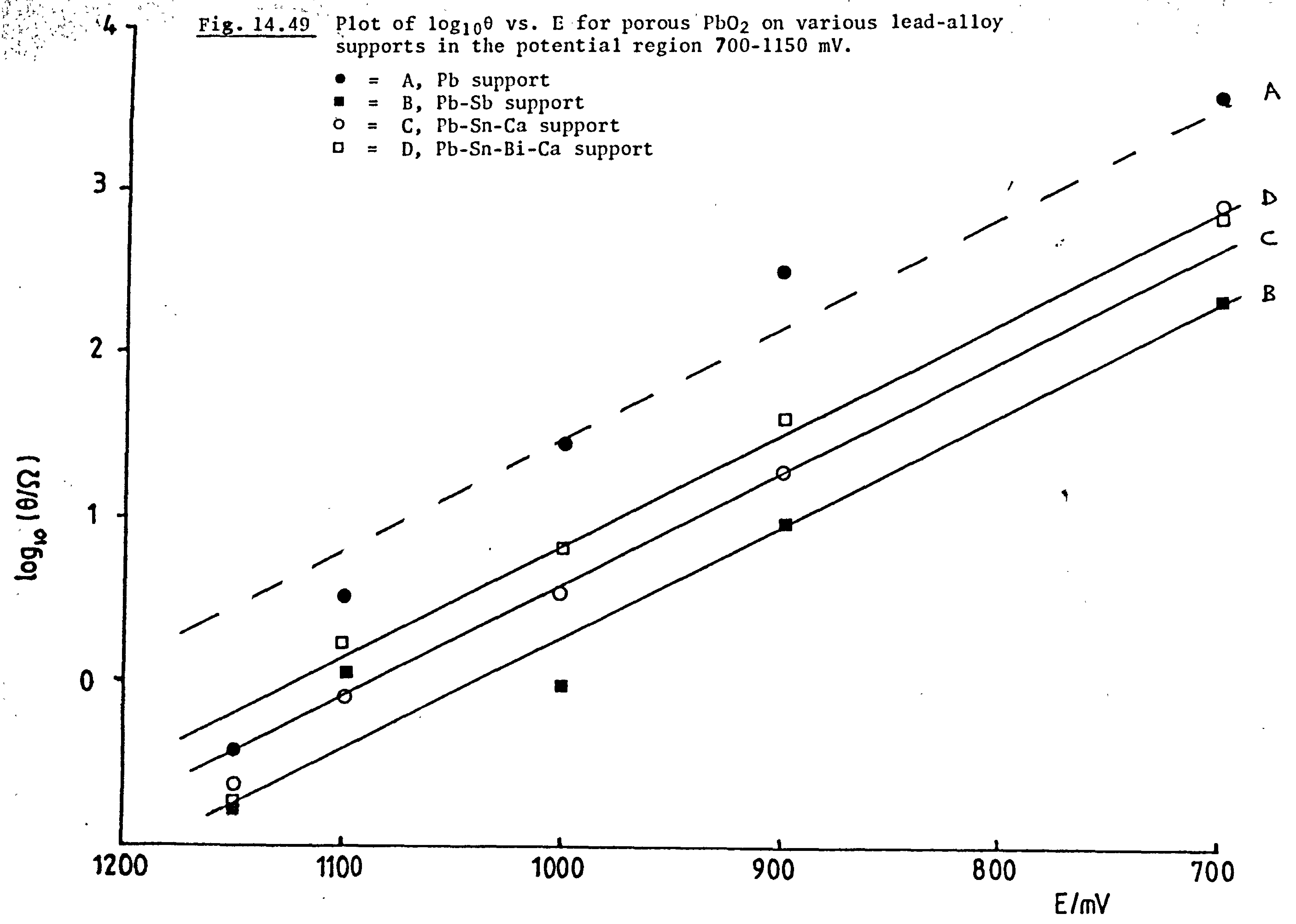

Fig. 14.49 Plot of $\log_{10}\theta$ vs. E for porous PbO_2 on various lead-alloy supports in the potential region 700-1150 mV.

● = A, Pb support
■ = B, Pb-Sb support
○ = C, Pb-Sn-Ca support
□ = D, Pb-Sn-Bi-Ca support

Fig. 14.50 Plot of $\log_{10} R_{ads}$ vs. E for various positives.

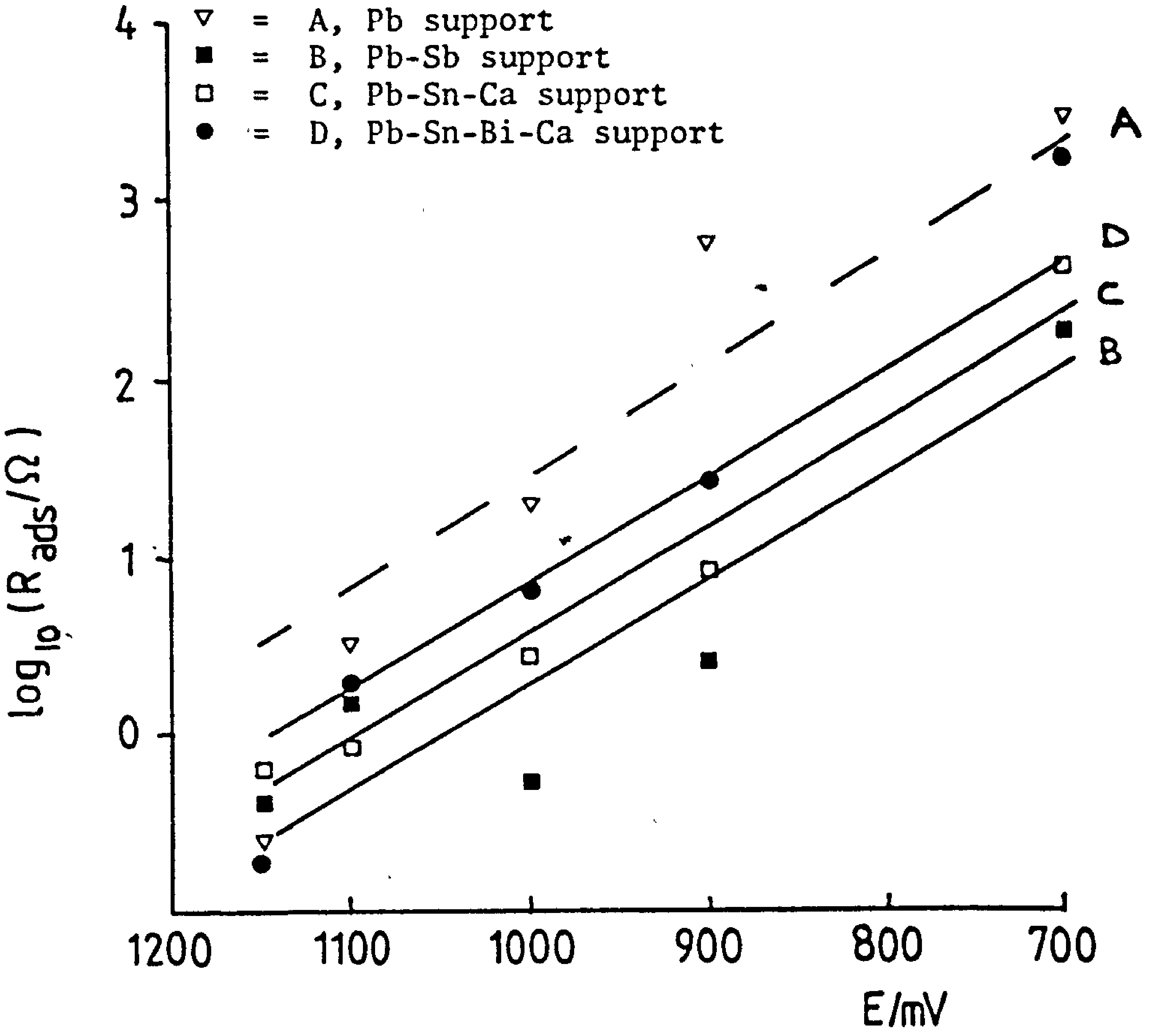

Fig. 14.51 Plot of $\log_{10} R_{ext}$ vs. E for various positives.

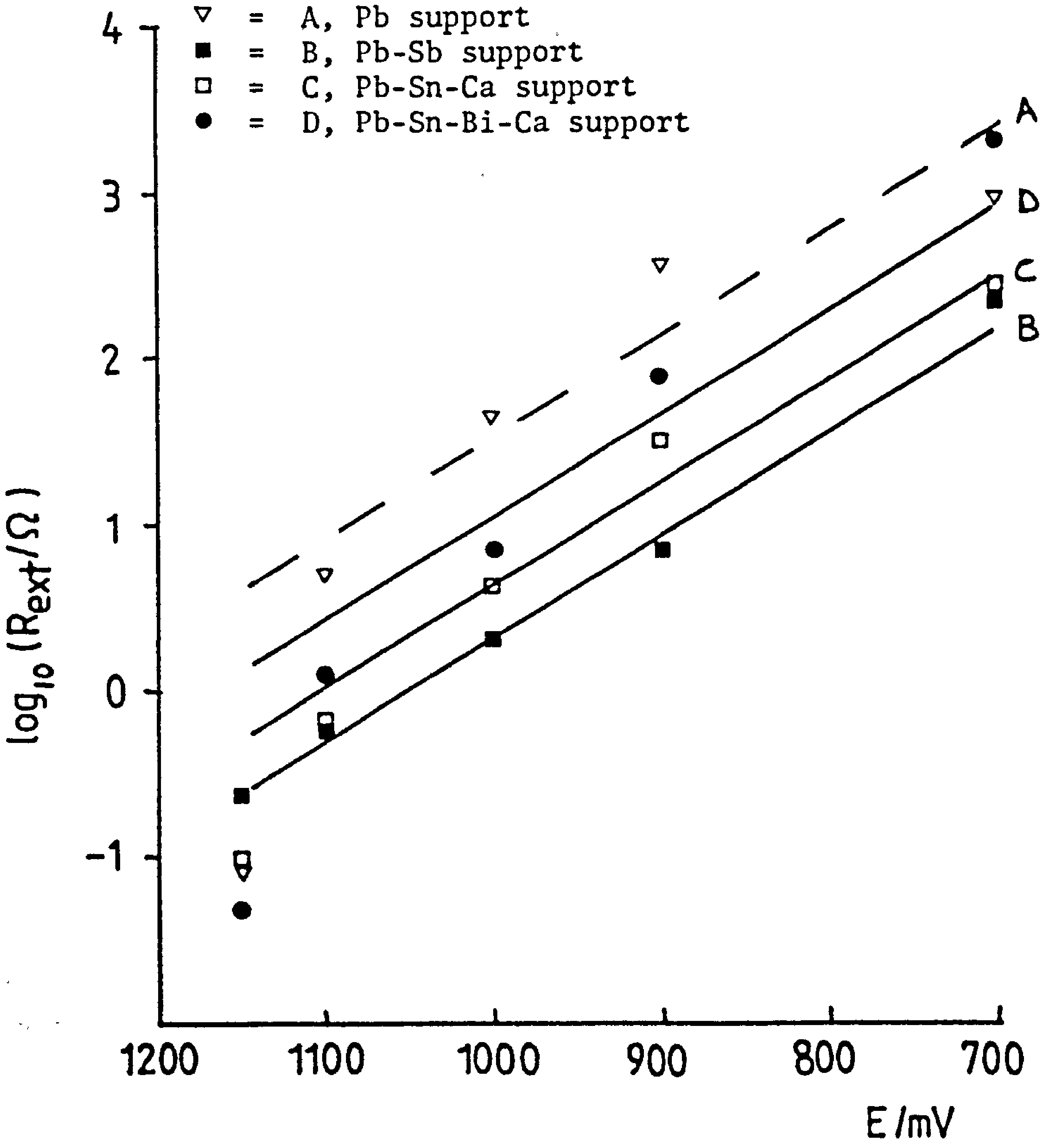

represent the Sluyters and Randles plots respectively for the above electrode at 700 mV. As can be seen, the analogue in Fig. 13.17 fits the data very well. The Sluyters and Randles plots in Figs. 14.56 and 14.57 respectively refer to 4.85 gcm^{-3} pasted (porous) PbO_2 on a Pb-Sb (1.88%) support at 1190 mV; consequently Figs. 14.58 and 14.59 correspond to the latter but at 700 mV. As shown there is hardly any difference among the two different paste density positives. The analogue in Fig. 13.17 matches the data in these figures (Figs. 14.56-14.59). Table 14.4 shows the kinetic parameter values which make up the analogue. With the 4.55 gcm^{-3} positive at 700 mV the value for R_{ext} is very high compared with the corresponding R_{ext} value for the 4.85 gcm^{-3} positive at the same potential. This suggests that a thicker $PbSO_4$ film is produced with the former.

Figs. 14.60 and 14.61 correspond to 4.55 gcm^{-3} pasted (porous) PbO_2 on a Pb-Sn (0.34%) - Ca (0.086%) support at 1190 mV whilst Figs. 14.62 and 14.63 represent the above respectively but at 700 mV. Figs. 14.64-14.67 relate to the data obtained for 4.85 gcm^{-3} pasted (porous) PbO_2 on the Pb-Sn-Ca support. The analogue still matches the experimental data quite well. Table 14.4 shows that the 4.55 gcm^{-3} Pb-Sn-Ca positive at 1190 mV has a very high external film resistance, $R_{ext} = 1\times10^{12}\Omega$. This is similar to what was obtained earlier with the 4.25 gcm^{-3} Pb-Sn-Ca positive at 1190 mV. Hence the high value obtained for R_{ext} indicates that the 4.55 gcm^{-3} positive is acting as a perfect capacitor. Also the θ, σ, R_{ads} and R_{ext} values for the 4.85 gcm^{-3} Pb-Sn-Ca positive at 700 mV are very high. This highlights the formation of a very thick $PbSO_4$ layer.

14.4 Conclusions

1. The analogue put forward in the previous chapter for the discharge

Fig. 14.52 Sluyters plot for 4.55 gcm^{-3} pasted (porous) PbO_2 on a Pb-Sb (1.88%) support (nominal surface area = 0.07 cm^2) in 5M H_2SO_4 at 23°C; 1190 mV; frequencies in hertz are given on the plot. The crosses (+) show experimental data and the line shows the computer match.

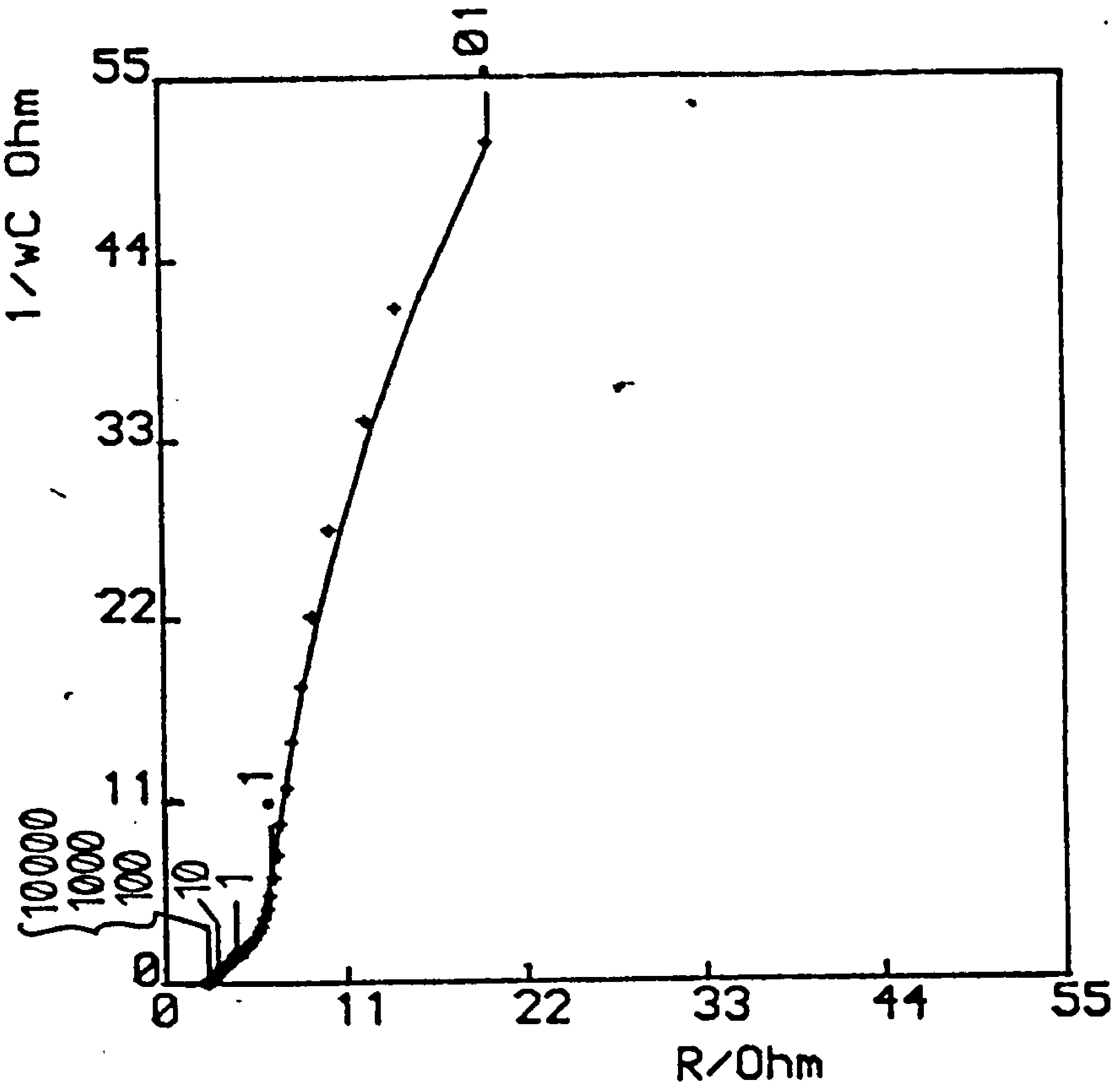

Fig. 14.53 The Randles plot corresponding to the system of Fig. 14.52 at 1190 mV. + and x correspond to experimental data (R and 1/ωC respectively) and the lines show the computer matches.

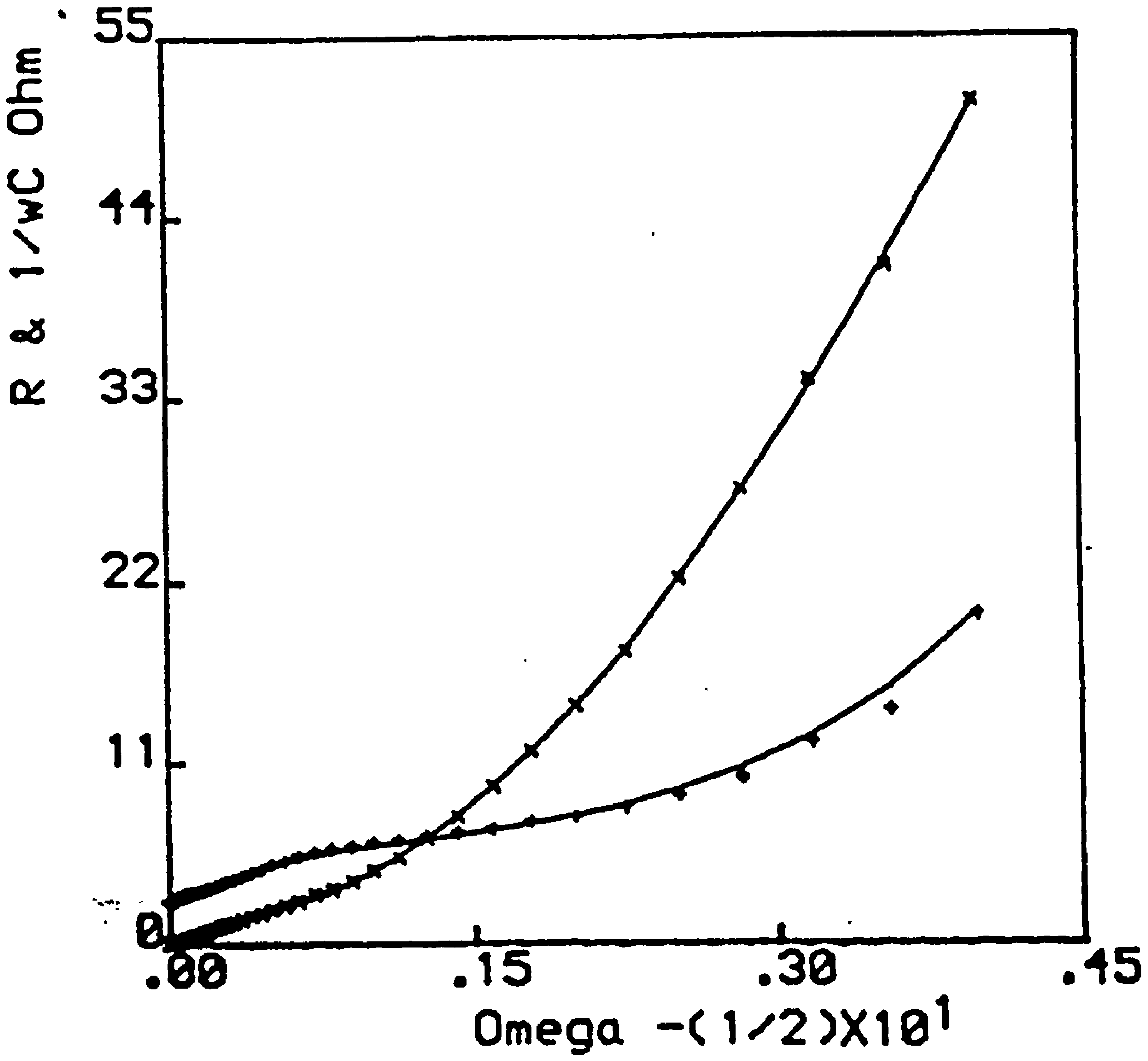

Fig. 14.54 Details as in Fig. 14.52 but at 700 mV.

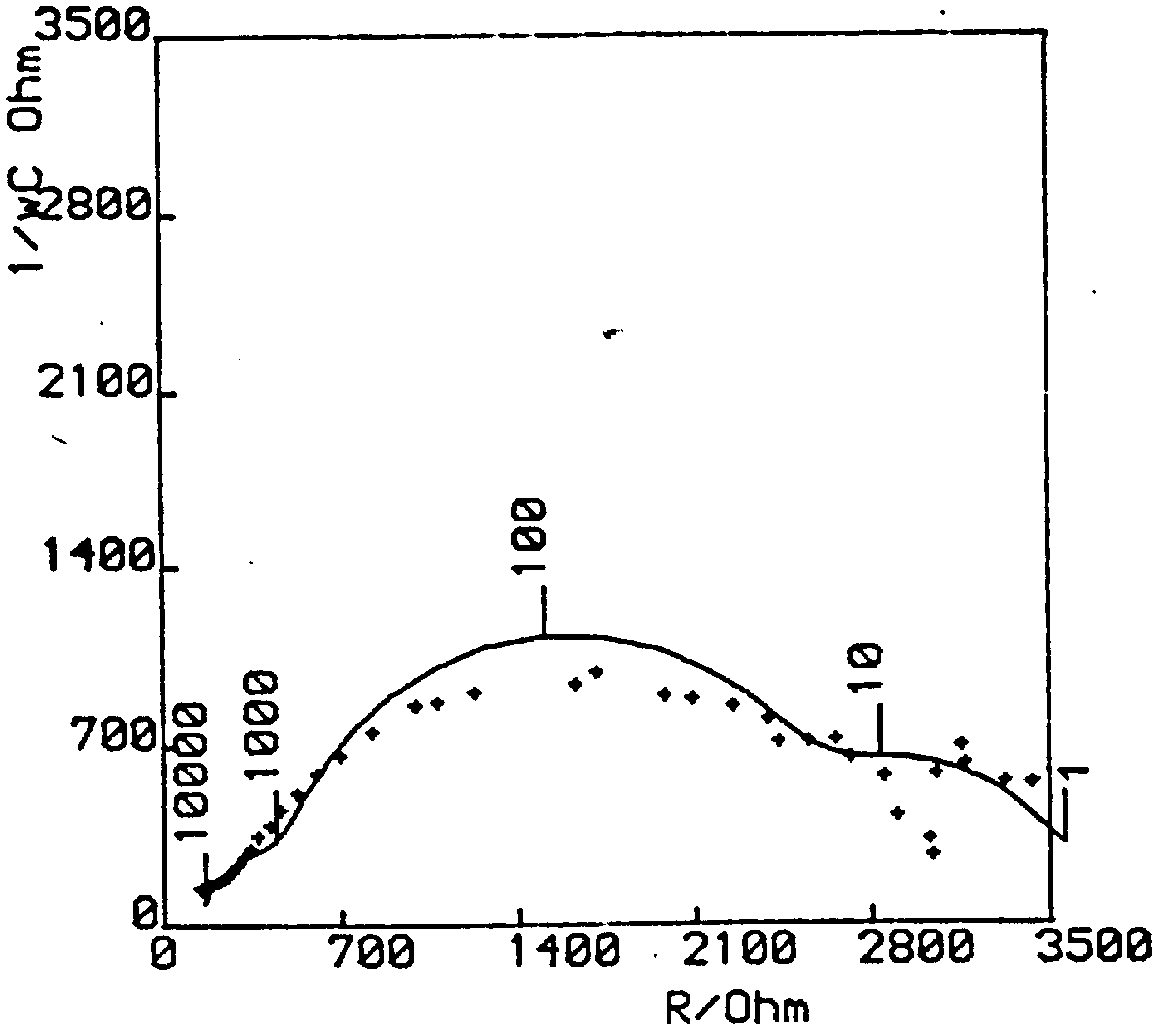

Fig. 14.55 Details as in Fig. 14.53 but at 700 mV.

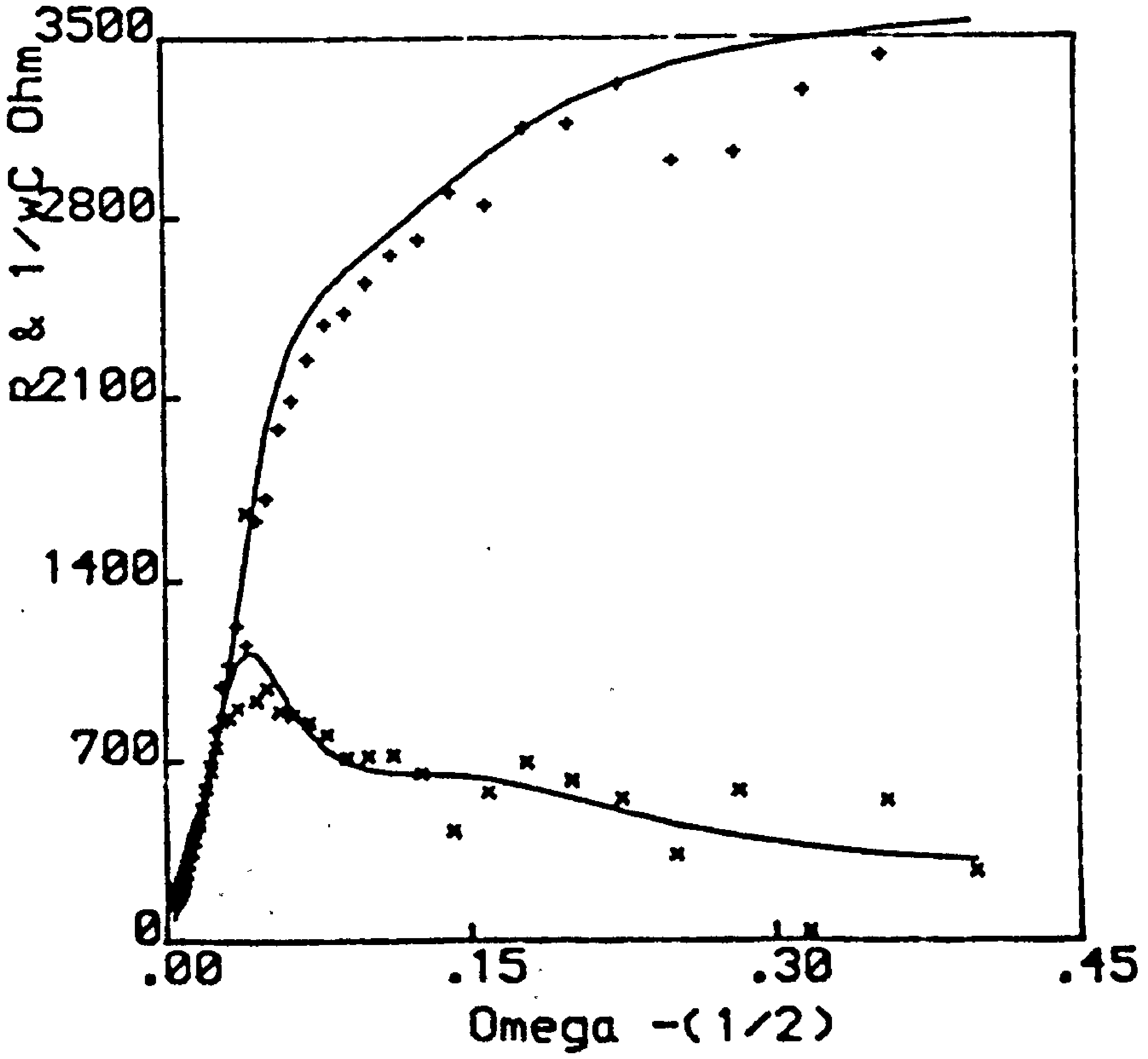

Fig. 14.56 Details as in Fig. 14.52 but for 4.85 gcm^{-3} pasted (porous) PbO_2 on a Pb-Sb (1.88%) support at 1190 mV.

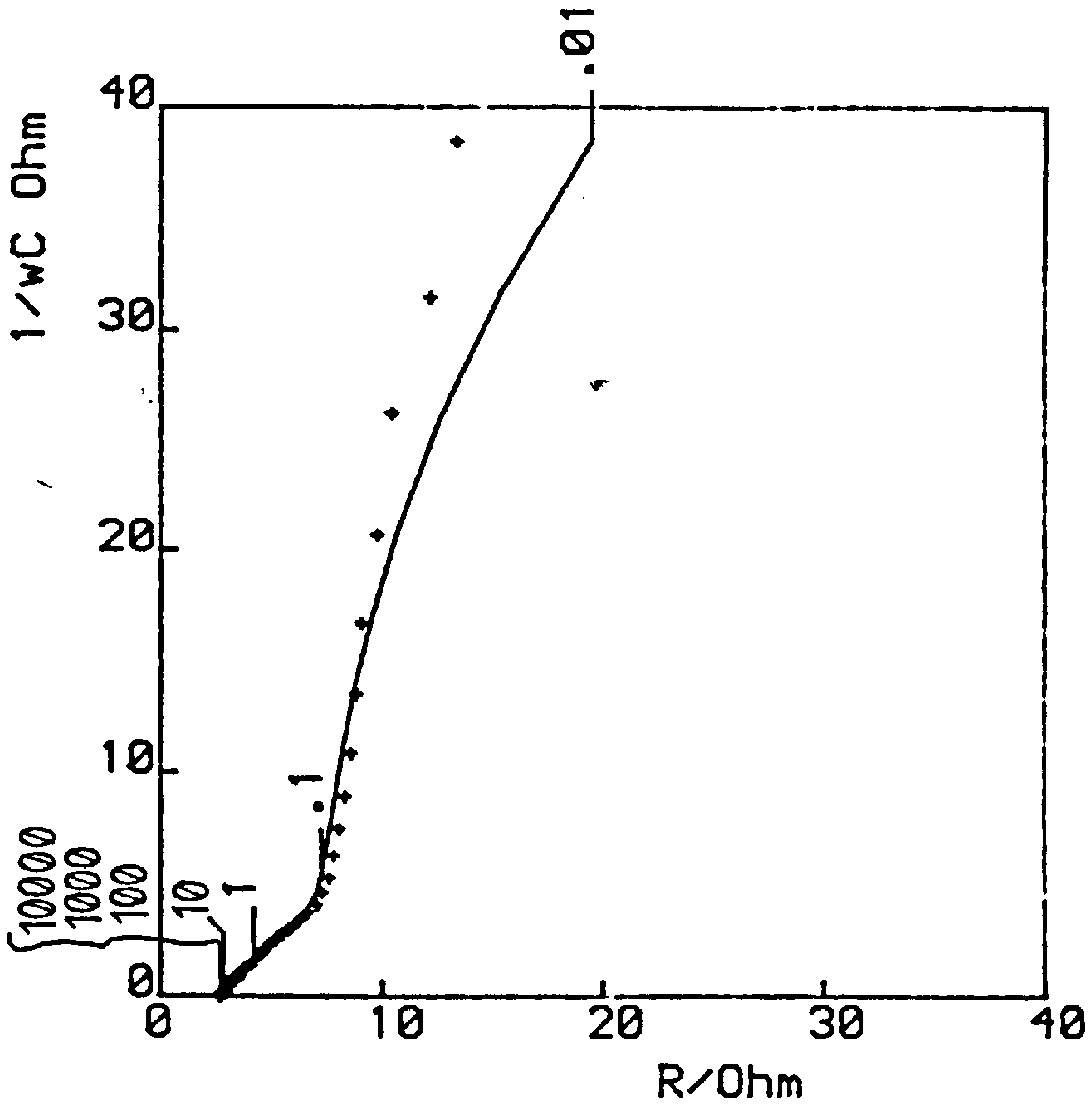

Fig. 14.57 Details as in Fig. 14.53 but for 4.85 gcm^{-3} pasted Pb-Sb positive.

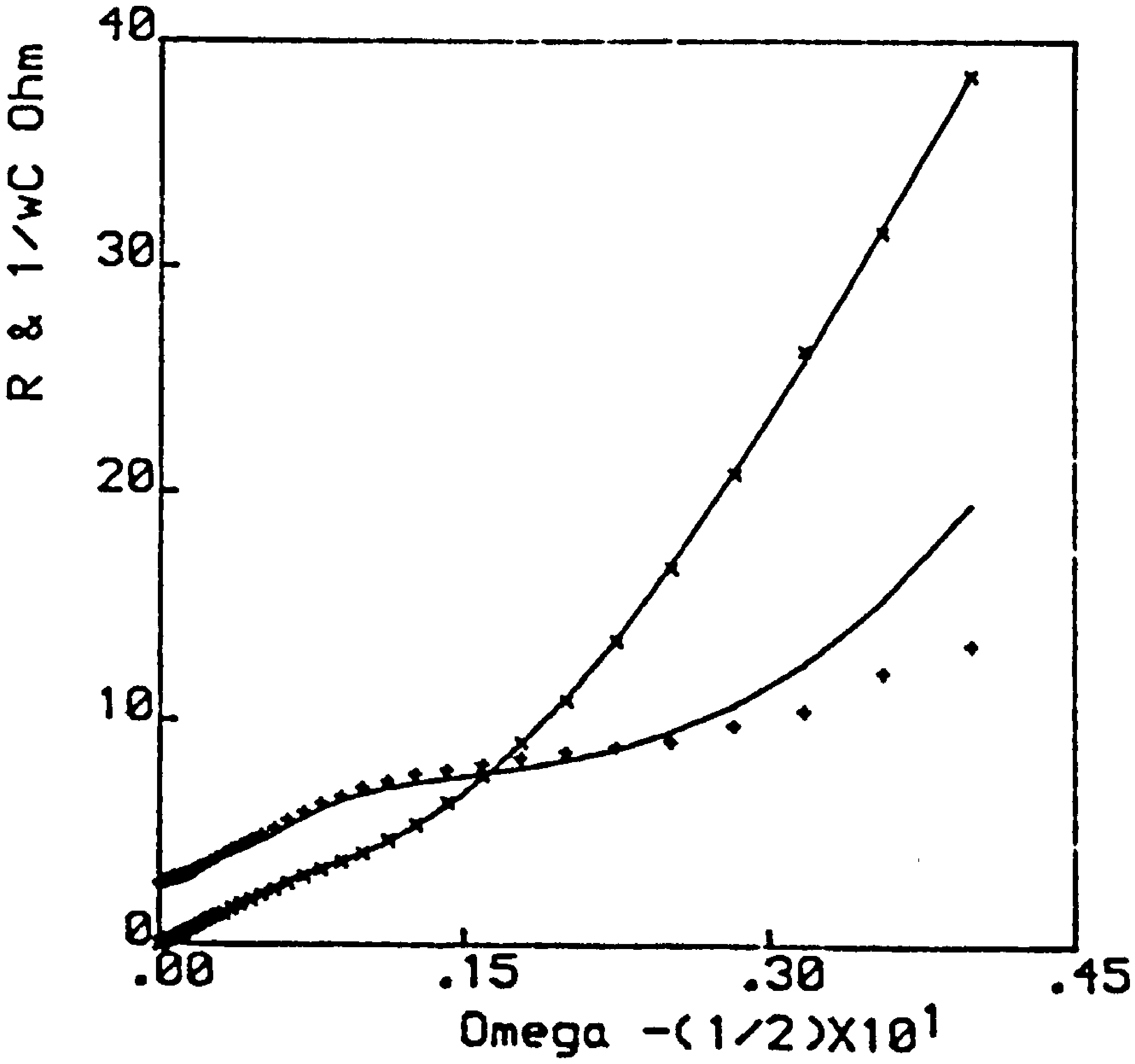

Fig. 14.58 Details as in Fig. 14.56 but at 700 mV.

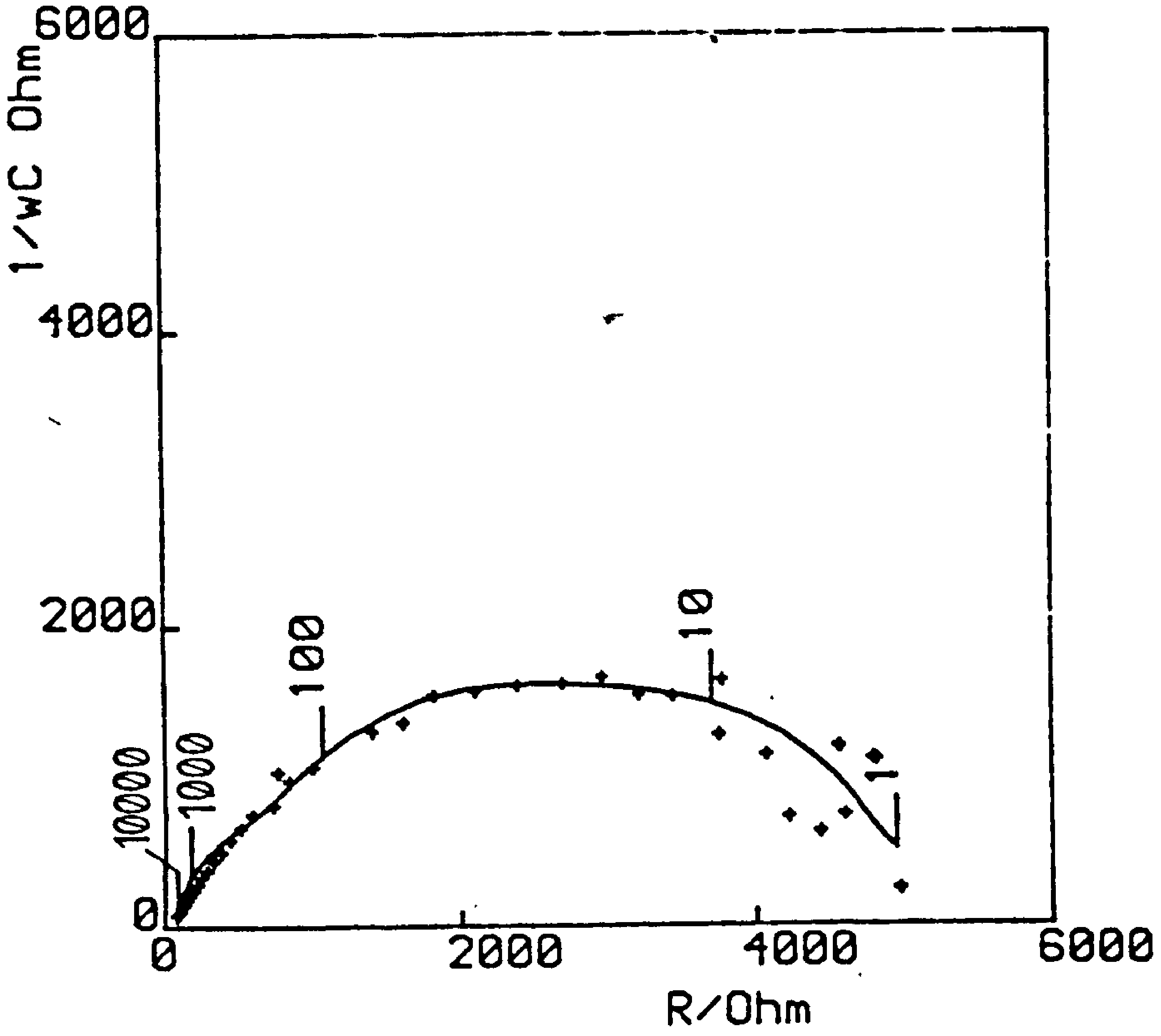

Fig. 14.59 Details as in Fig. 14.57 but at 700 mV.

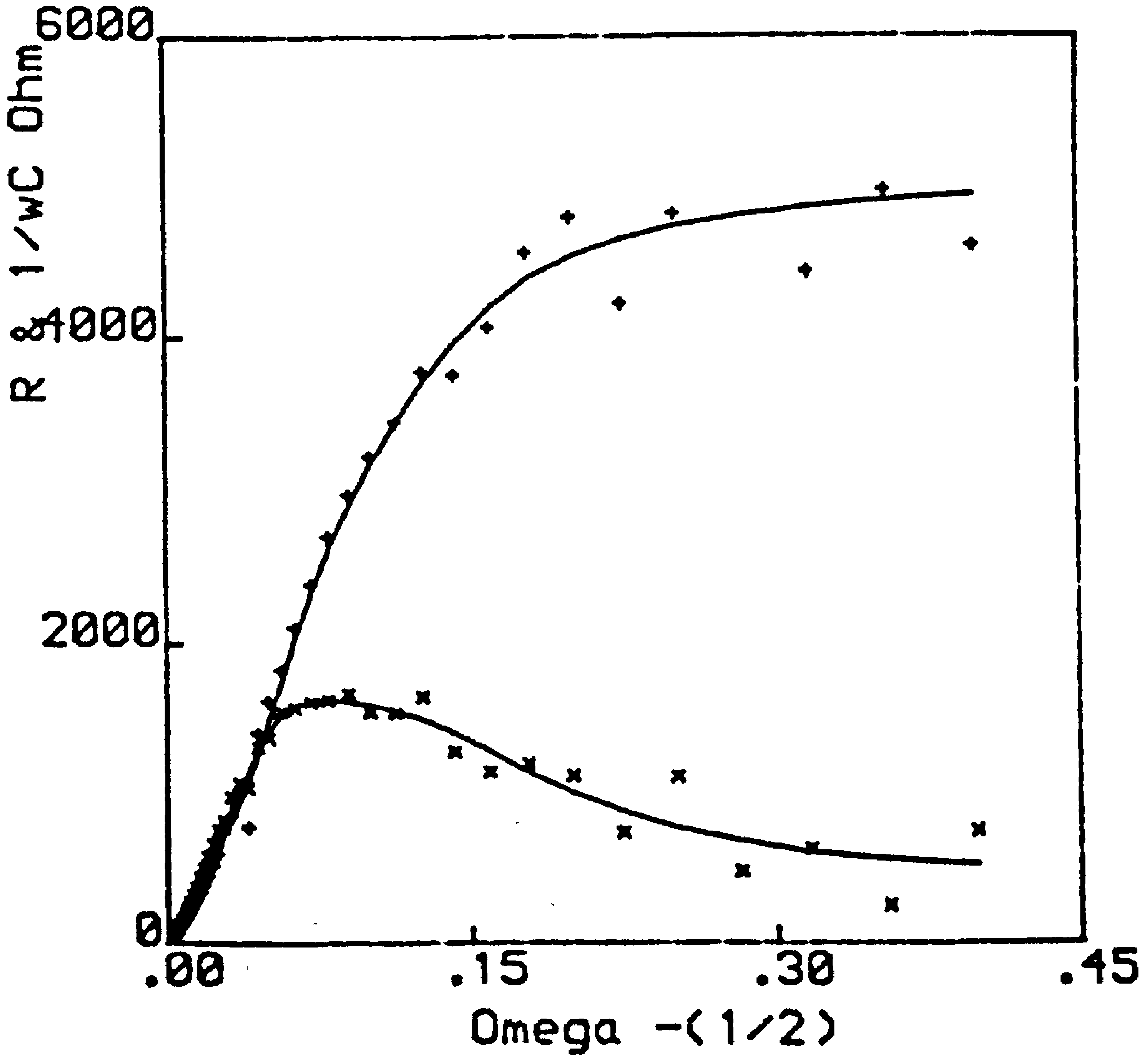

Fig. 14.60 Details as in Fig. 14.52 but for 4.55 gcm^{-3} pasted (porous) PbO_2 on a Pb-Sn (0.34%) - Ca (0.086%) support at 1190 mV.

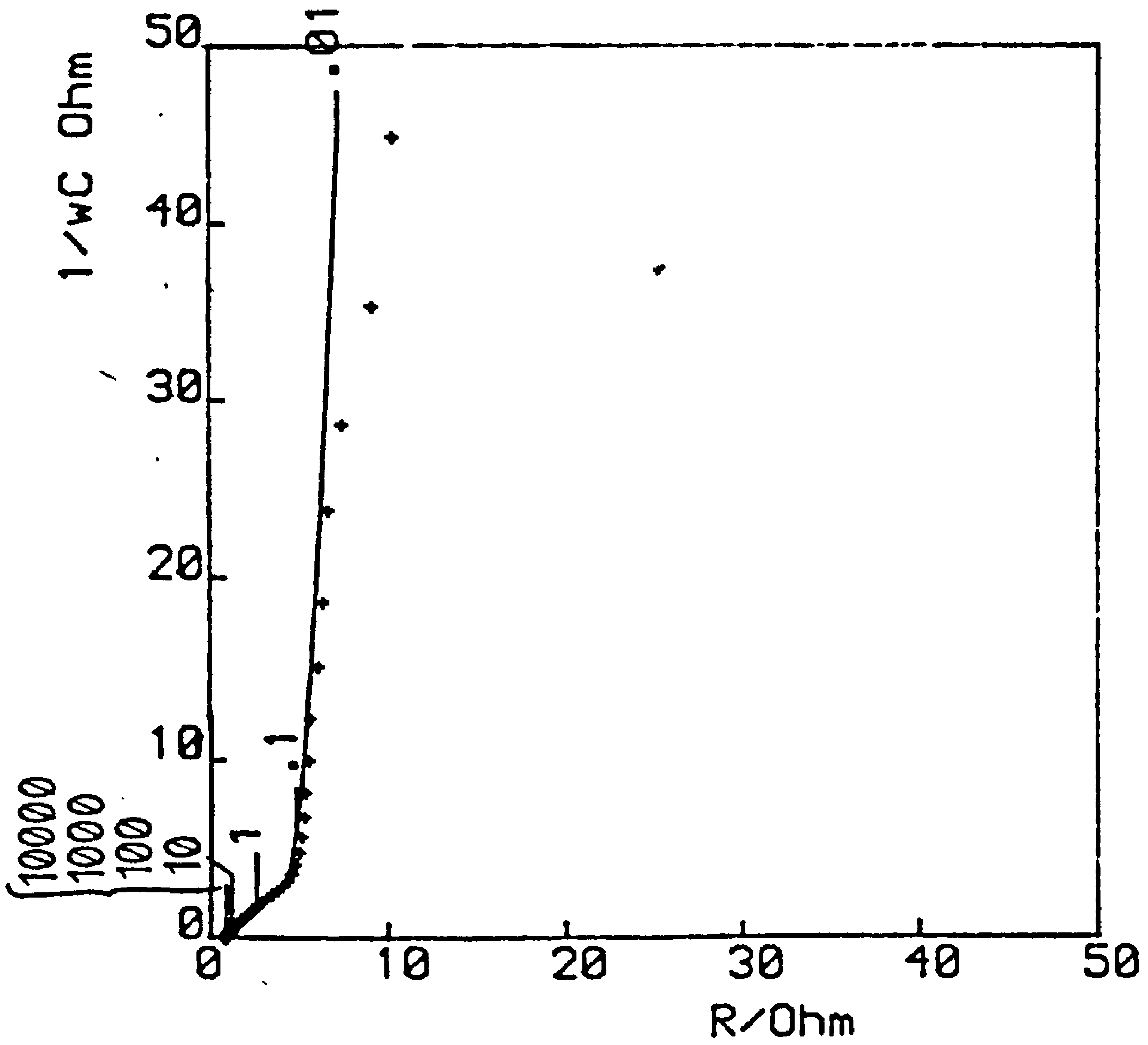

Fig. 14.61 Details as in Fig. 14.53 but for 4.55 gcm^{-3} pasted Pb-Sn-Ca positive.

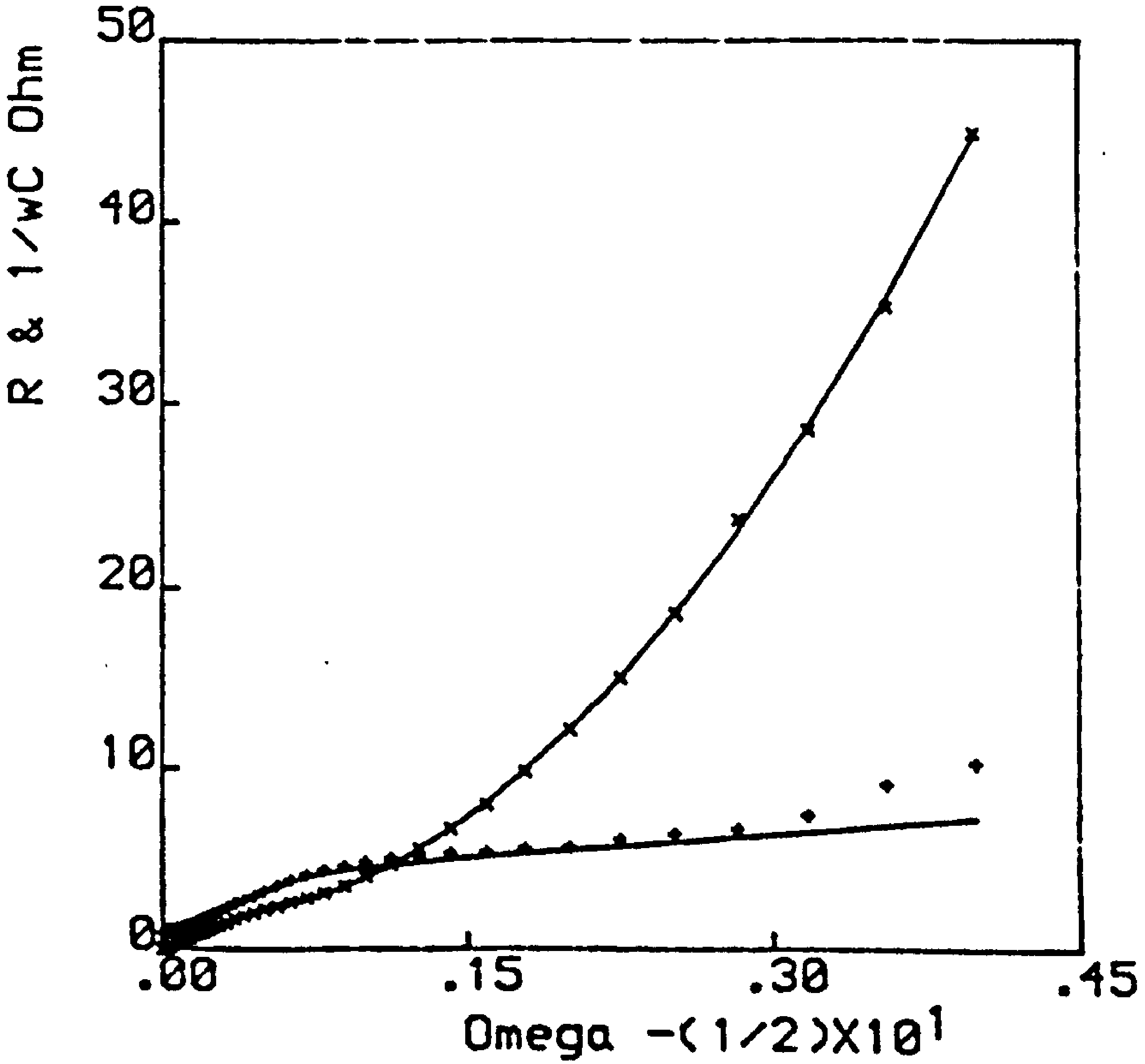

Fig. 14.62 Details as in Fig. 14.60 but at 700 mV.

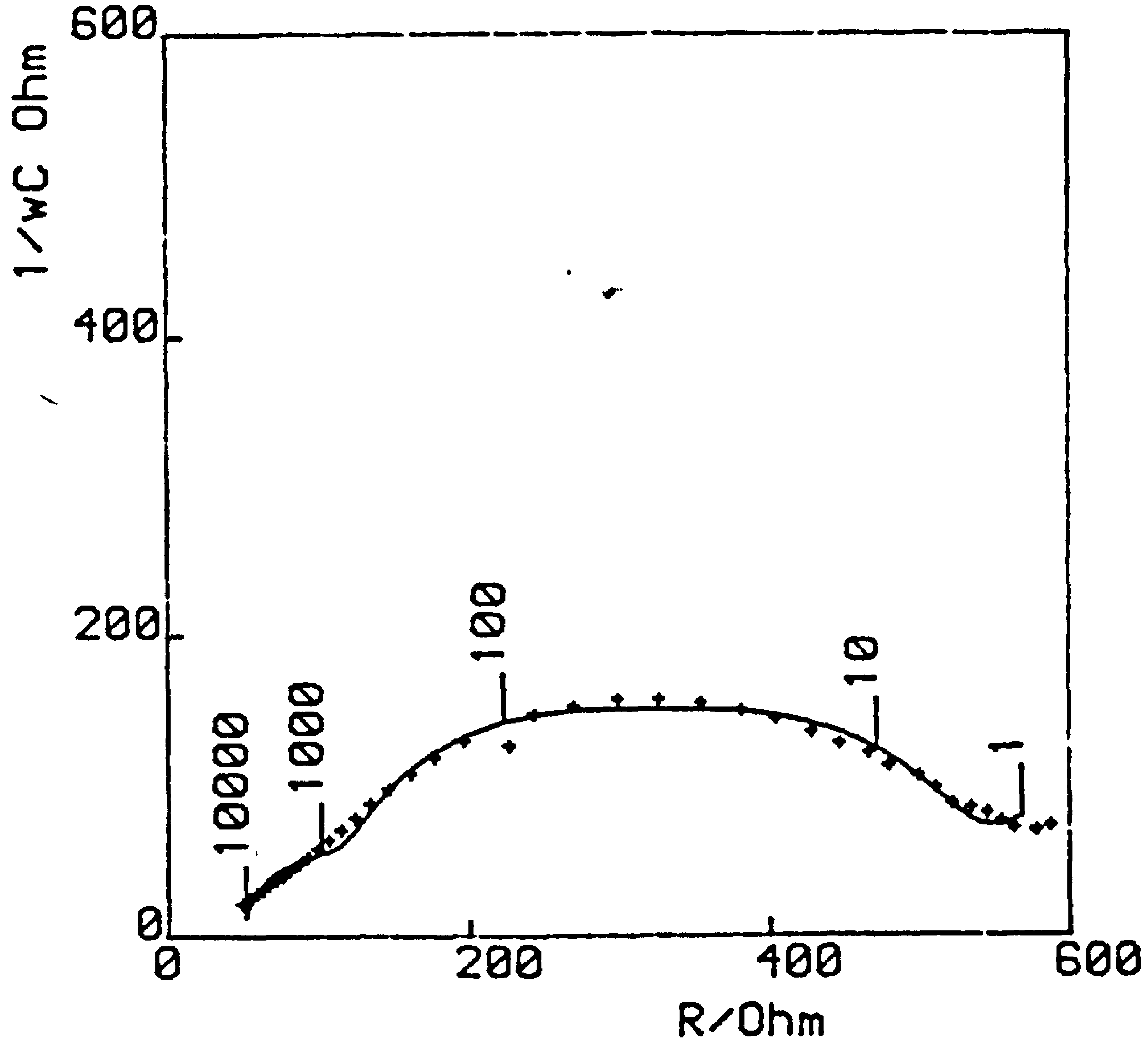

Fig. 14.63 Details as in Fig. 14.61 but at 700 mV.

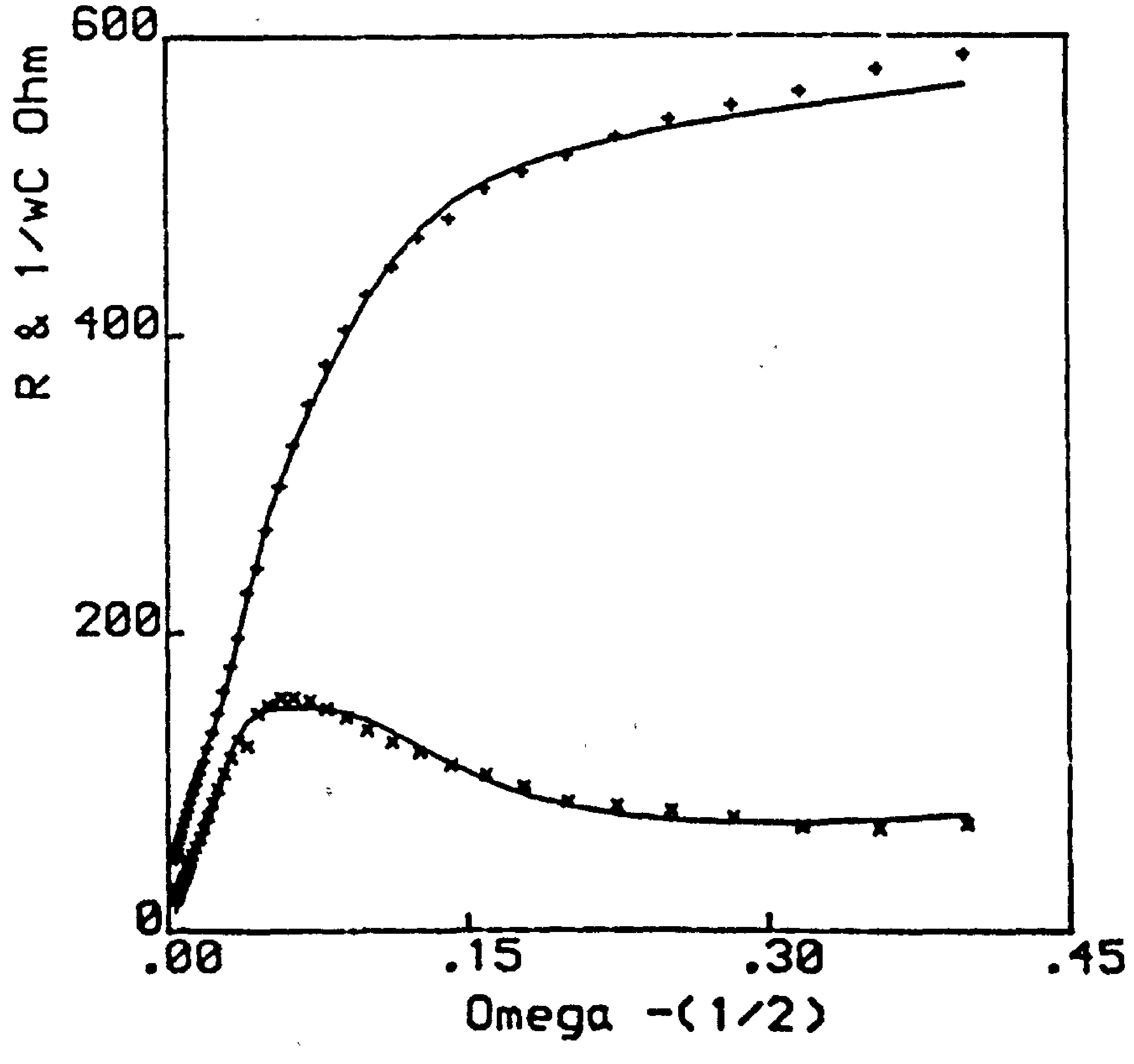

Fig. 14.64 Details as in Fig. 14.52 but for 4.85 gcm^{-3} pasted (porous) PbO_2 on a Pb-Sn (0.34%) - Ca (0.086%) support at 1190 mV.

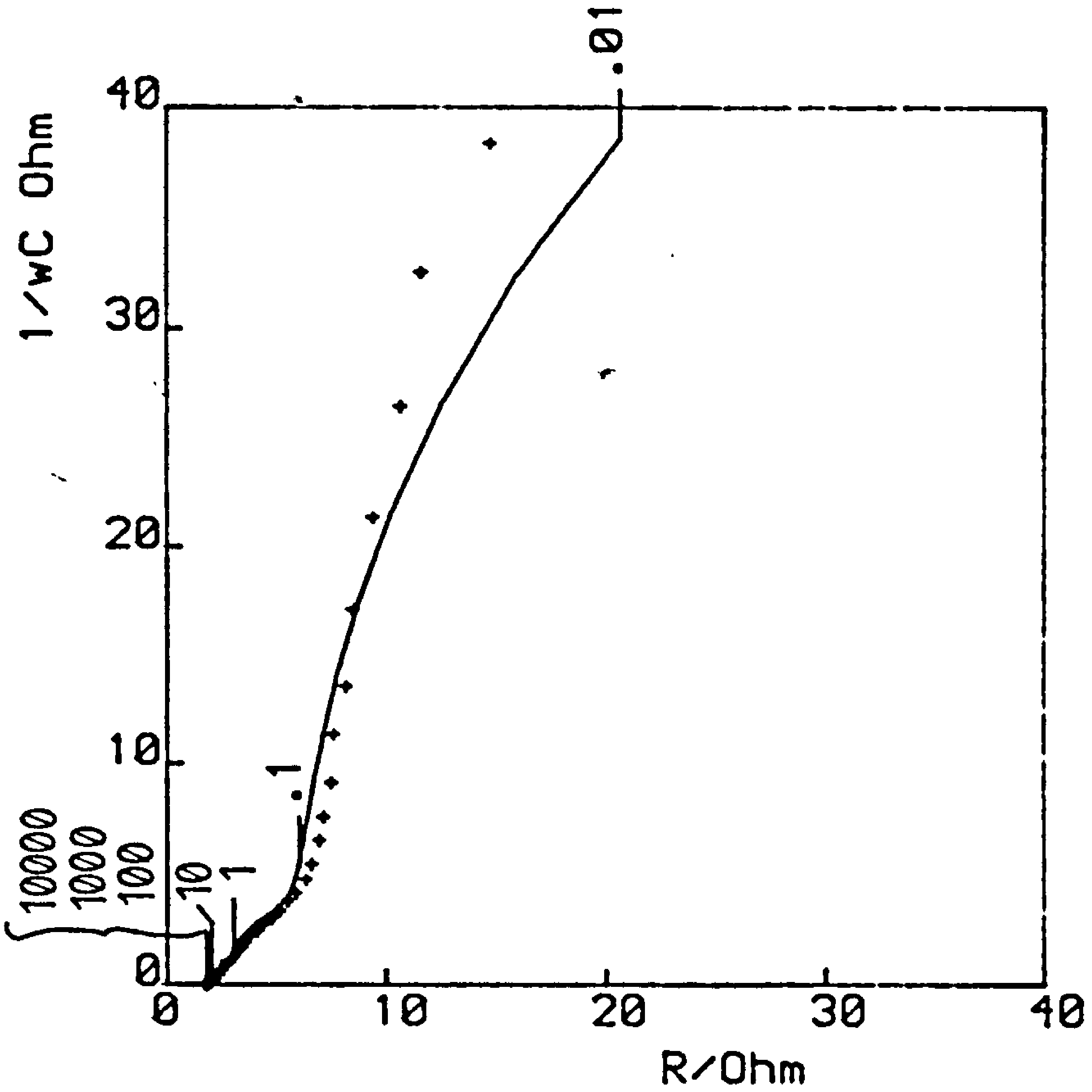

Fig. 14.65 Details as in Fig. 14.53 but for 4.85 gcm^{-3} pasted Pb-Sn-Ca positive.

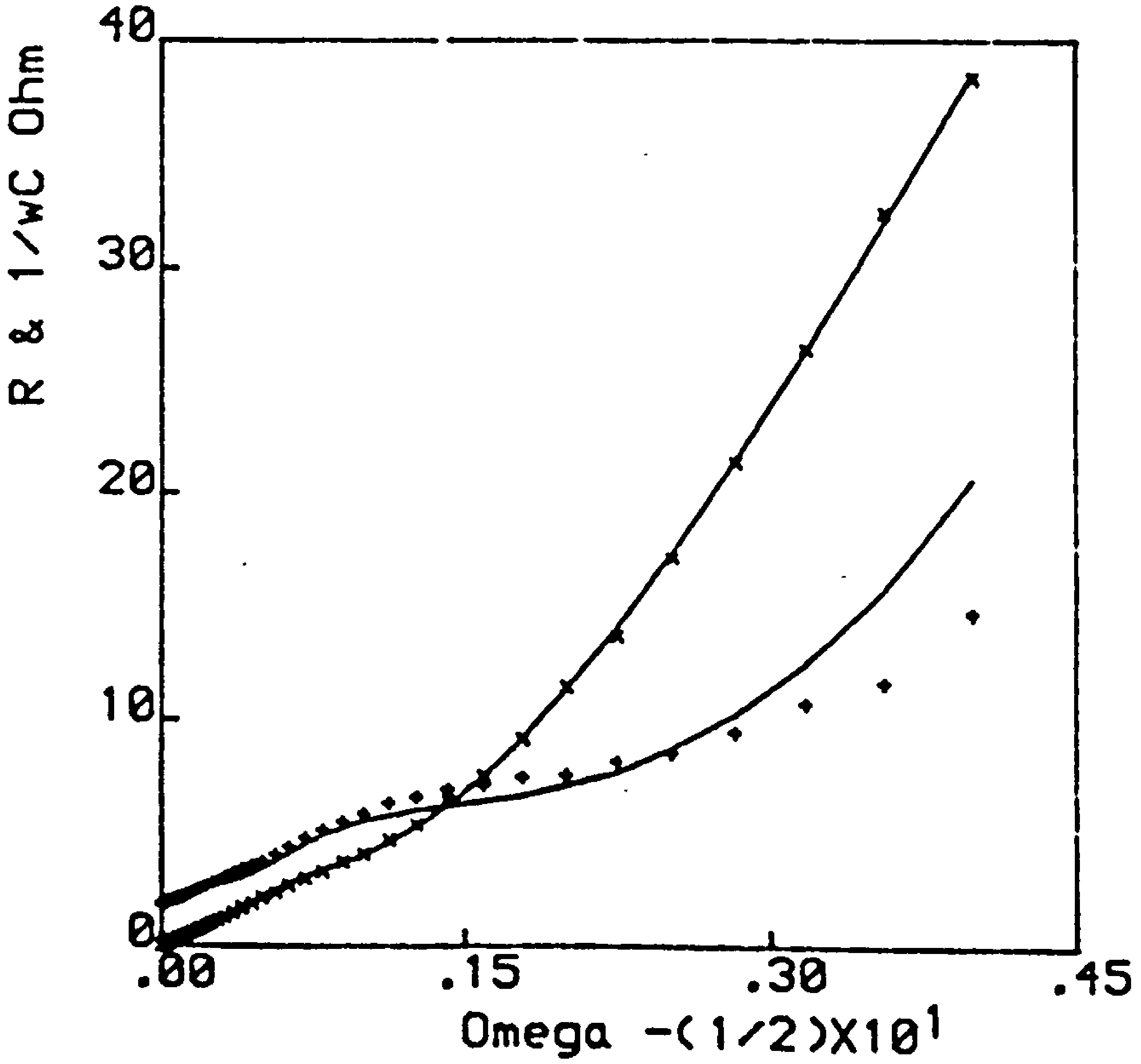

Fig. 14.66 Details as in Fig. 14.60 but at 700 mV.

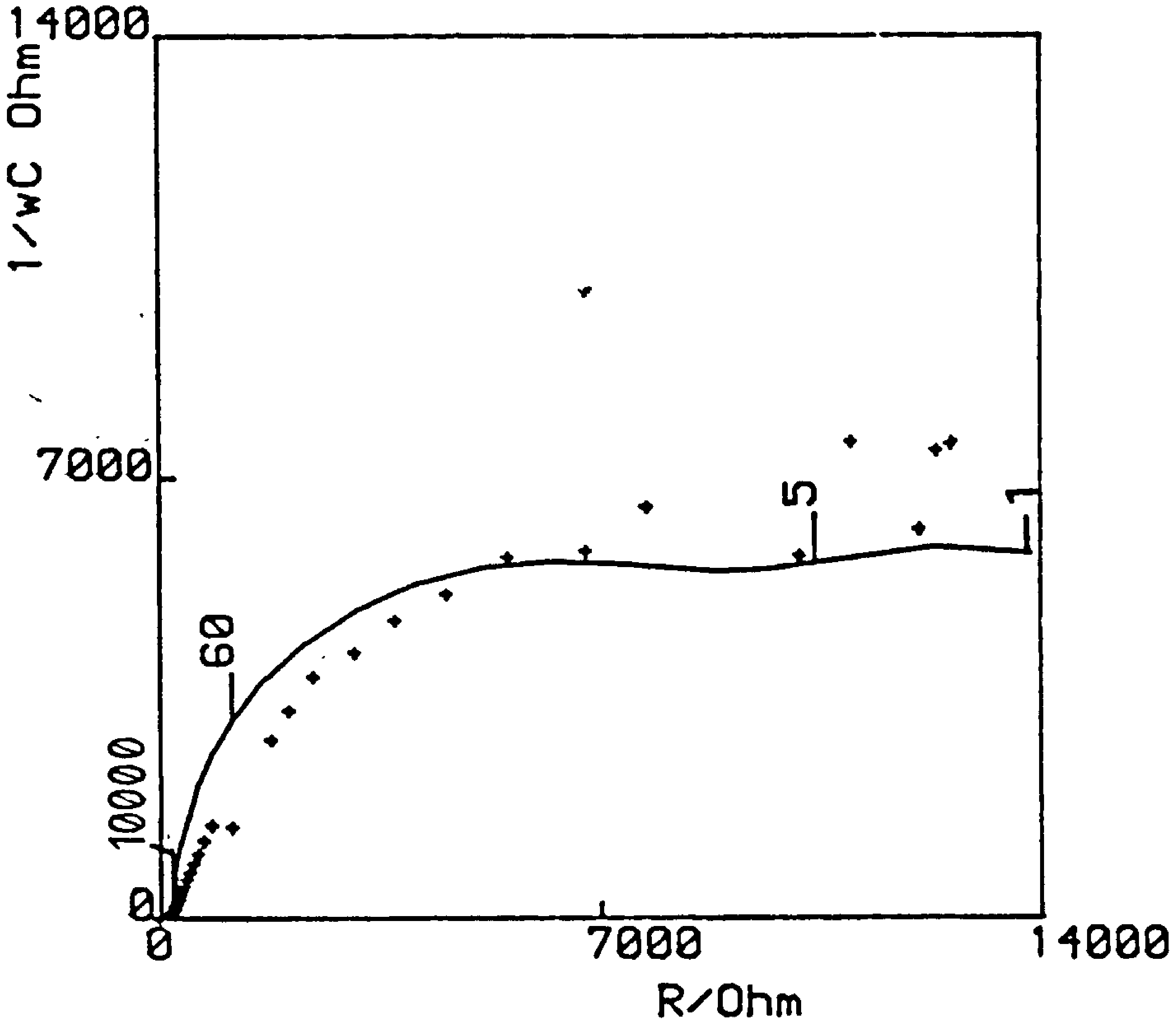

Fig. 14.67 Details as in Fig. 14.61 but at 700 mV.

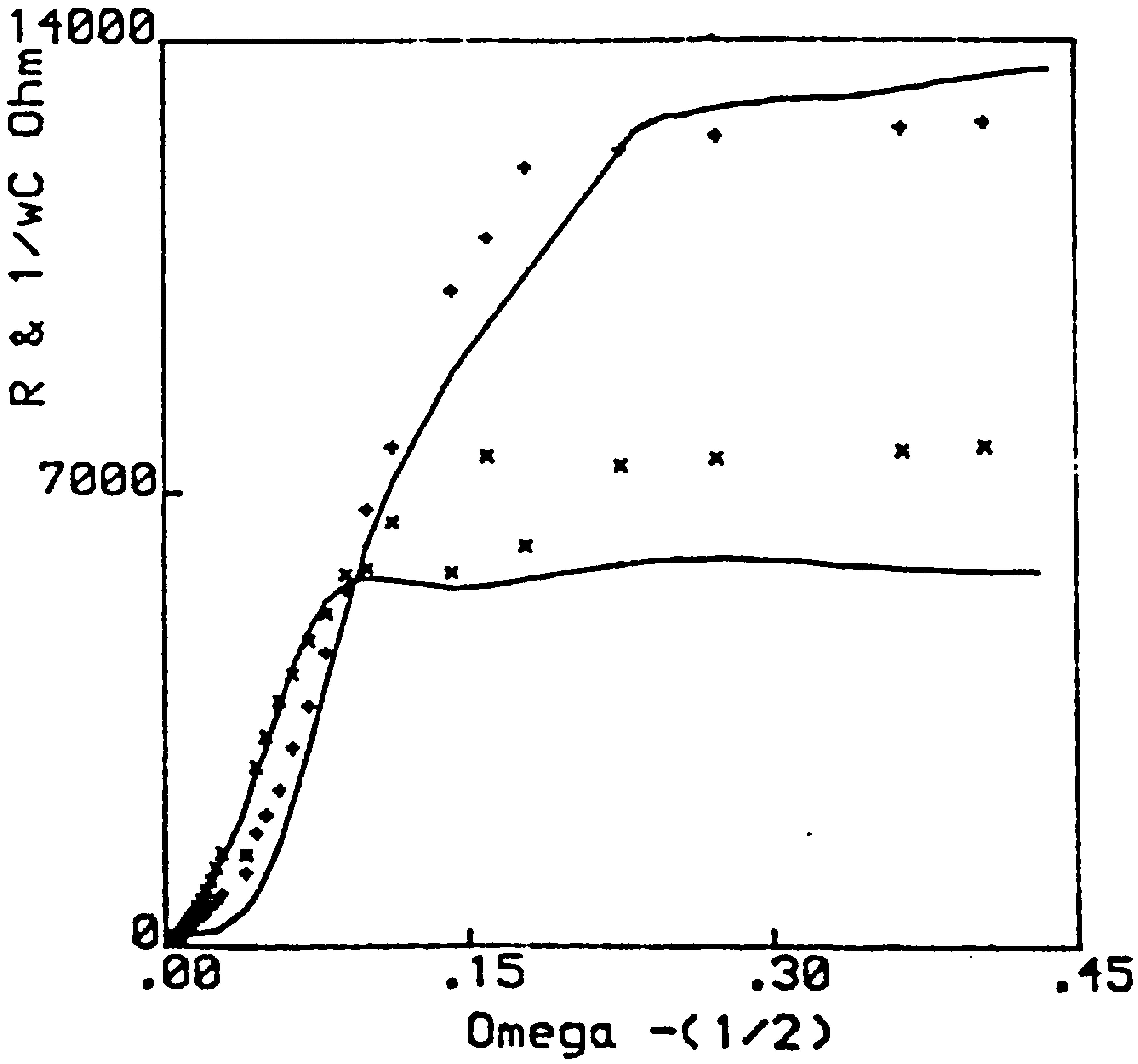

TABLE 14.4

Electrode characteristics obtained from computer match for various porous (pasted) PbO_2 electrodes (nominal surface area = 0.07 cm^2).

Electrodes / Kinetic Parameters	4.55 gcm^{-3} pasted Pb-Sb electrode at E = 1.190V	4.55 gcm^{-3} pasted Pb-Sb electrode at E = 0.700V	4.85 gcm^{-3} pasted Pb-Sb electrode at E = 1.190V	4.85 gcm^{-3} pasted Pb-Sb electrode at E = 0.700V	4.55 gcm^{-3} pasted Pb-Sn-Ca electrode at E = 1.190V	4.55 gcm^{-3} pasted Pb-Sn-Ca electrode at E = 0.700V	4.85 gcm^{-3} pasted Pb-Sn-Ca electrode at E = 1.190V	4.85 gcm^{-3} pasted Pb-Sn-Ca electrode at E = 0.700V
R_Ω/Ω	2.544	146.2	2.691	88.34	0.9073	49.44	1.816	187.8
θ/Ω	0.7601	338.0	1.953	2921	1.234	270.0	1.345	5636
C_{dL}/F	8.5389E-3	2.0946E-7	2.8564E-2	1.3652E-6	1.7874E-2	6.7641E-6	2.3943E-2	1.592E-6
$\sigma/\Omega s^{-\frac{1}{2}}$	1.058	395.1	9.7908E-2	668.1	0.836	157.7	9.0413E-3	1000
C_{ads}/F	9.8413E-2	2.9671E-5	0.1617	1.3335E-5	0.1071	7.0376E-5	0.132	7.7607E-6
R_{ads}/Ω	1.733	853.3	2.616	1091	1.782	119.6	2.968	7158
C_{ext}/F	0.3235	7.8812E-7	0.332	6.1917E-7	0.3858	1.4295E-6	0.3626	1.3754E-6
R_{ext}/Ω	212.5	2087	134.3	630.1	(1E12)	68.29	116.4	5434

behaviour of porous PbO_2 fits the experimental data obtained for the various porous PbO_2 electrodes very well.

2. The model was tested successfully on other porous PbO_2 matrices on the same Pb-alloy supports.
3. Of all the electrodes investigated the charge transfer resistance values show that the antimonial positive discharges more efficiently.
4. The porous PbO_2 on Pb-Sn-Ca support (produced from 4.25 gcm^{-3} and 4.55 gcm^{-3} positive pastes), at the open circuit potential (1190 mV) acted as pure capacitors.

CHAPTER 15

FINAL DISCUSSION

Cyclic voltammetry has shown that the charge output from the planar PbO_2 electrode decreases with increasing sulphuric acid concentration (that is, greater than 5 mol dm^{-3}) and using scanning electron microscopy it was found that the lead sulphate crystals, in H_2SO_4 concentrations greater than 5 mol dm^{-3}, became much smaller forming a tighter and passivating film. Different acid concentrations affected the electrochemistry of the various lead alloys employed, for example, in 5 mol dm^{-3} sulphuric acid the lead-tin-calcium alloys were more susceptible to anodic attack than either pure lead or the various antimonial lead alloys. Further work could be carried out using more combinations of lead alloys in different H_2SO_4 concentrations greater than 5 mol dm^{-3}, as well as concentrations less than 5 mol dm^{-3}. Various additives, such as, antimonial salts could be introduced into the H_2SO_4 solution to see if they have any effect on the electrochemical behaviour of the PbO_2 formed on the lead alloys. Porous PbO_2 (originally formed from positive paste containing 14.3% red lead) produced on various lead alloys, which when subjected to cyclic voltammetry, was not only affected by acid concentration but also by the alloy support.

The potentiostatic step experiments on the porous PbO_2 electrodes (as mentioned above) showed that the electrodes with Pb-Sn-Ca backing discharged ($PbO_2 \rightarrow PbSO_4$) at a faster rate than the electrodes with the antimonial lead support. After a potentiostatic discharge all the electrodes accepted charge very slowly when stepped back into the PbO_2 region. This shows clearly that galvanostatic charging conditions, rather than potentiostatic ones, are needed to charge a lead-acid cell effectively.

Scanning electron microscopy has shown that when the porous electrodes were subjected to the various potentiostatic pulse experiments a difference could be seen between the Pb-Sb and Pb-Sn-Ca positives. In particular, dendritic growths only appeared on the porous PbO_2 surface on a Pb-Sb support after a potentiostatic oxidation was carried out. With X-ray diffraction the dendrites were found to be α-PbO_2. Hence more work could be done using various other techniques, such as, electron spectroscopy for chemical analysis (ESCA), neutron diffraction and Auger spectroscopy to actually determine the exact nature of the dendritic crystals.

The porous electrodes have been subjected to linear sweep cycling and potentiostatic step experiments, and scanning electron microscopy can again be utilised to see what effect the above techniques have on the electrodes. As described earlier, established current-time relationships for electrocrystallisation processes were used to match parts of the transients obtained for the porous electrodes. However, these transients are of a complex nature representing various processes which occur and hence a computer is required to deconvolute the i-t curves to find out what reactions do occur within the porous PbO_2 matrix.

Varying the positive paste (100% grey oxide) density provided some interesting results. Electrodes which originally had the least dense paste (4.25 gcm^{-3}) discharged the most as a result of a potentiostatic reduction pulse (1240 → 700 mV). However, after 100 potentiodynamic cycles (1240-700 mV) followed by a potentiostatic reduction it was found by statistical analysis on the pulse data that the Pb alloy support had little effect on the paste densities used.

More pulse work could be done using different H_2SO_4 concentrations and different lead alloys. Addition of bismuth to the lead-tin-calcium alloy seems to improve the charge acceptance (700 → 1240 mV) compared with the other electrodes. Hence further scanning electron microscopy can be carried out on the positives to see what changes occur at the electrode surface.

The a.c. impedance technique has been used successfully to determine the nature of the discharge behaviour of porous PbO_2. The model described in this thesis fits the experimental data obtained for the various porous PbO_2 electrodes (previously produced from 100% grey oxide paste) quite well over a large potential range. It was interesting to note that the kinetic parameter values reflected the fact that the antimonial positive discharges more efficiently. However, the analogue does have limitations because it does not take into account crystallisation and nucleation reactions. If the theory for crystallisation and nucleation which occur during the formation of $PbSO_4$ was available the present model would be further improved. Future a.c. work could involve carrying out impedance measurements on the porous PbO_2 electrodes as they are stepped back into the PbO_2 region after a complete discharge. A.C. studies on porous PbO_2 electrodes in starved H_2SO_4 electrolyte, for example, H_2SO_4 absorbed onto glass wool fibre material would be another interesting research topic.

APPENDIX 1

Growth of dendrites

Barton and Bockris [122] have explained that with dendritic formation growth occurs mainly at the tip of the dendrite. The tip in turn can be approximated to having a spherical nature as is shown in Fig. 1.

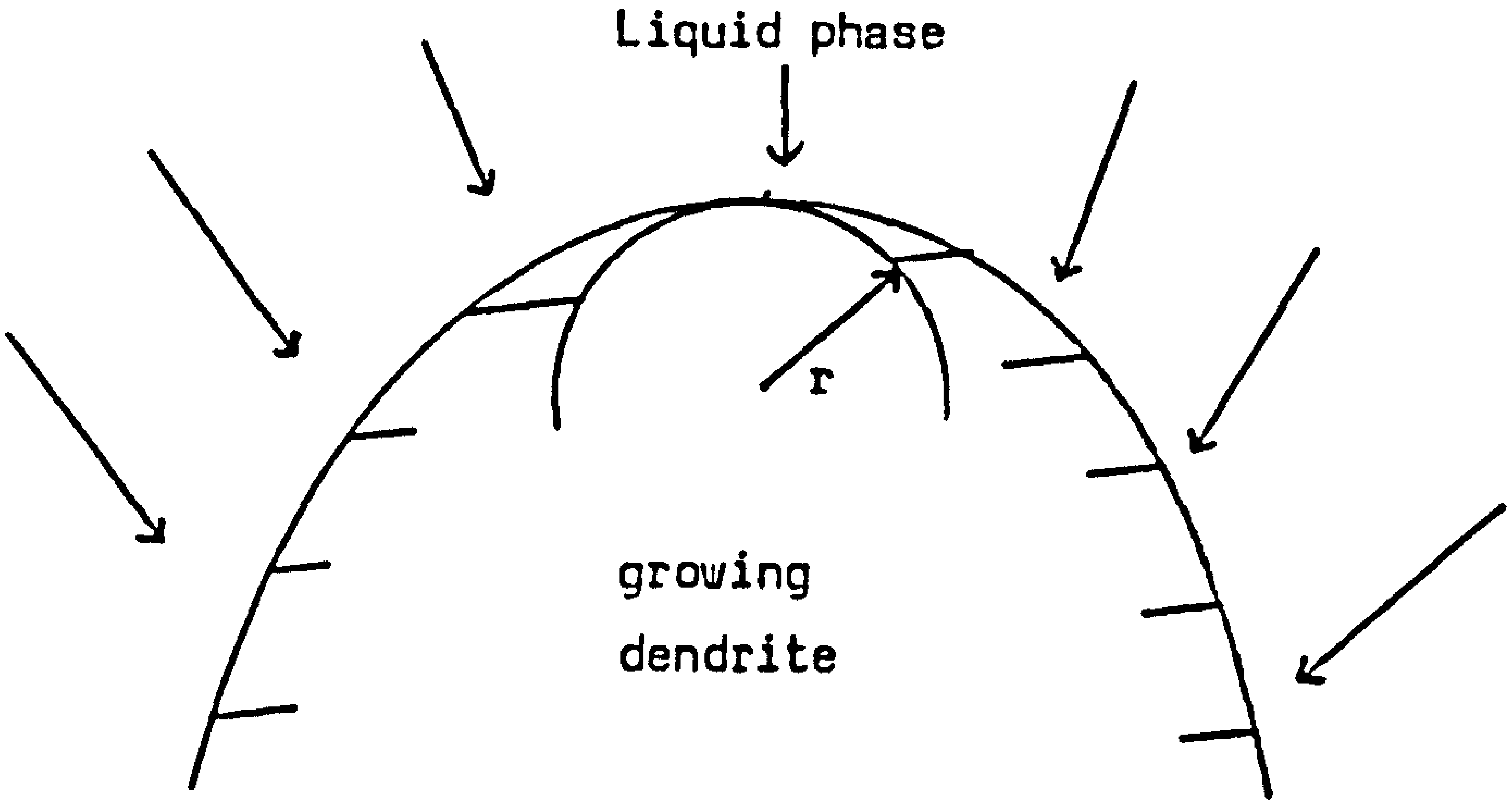

Fig. 1 Parabolic and spherical models of a dendrite tip.

Hence simple equations can be derived relating the radius of curvature at the tip r, the observed local current density i, and the different kinds of overpotentials.

$$\eta_d = \frac{RT}{(zF)^2 \, DC^b} \cdot ir = K_d \, i \, r \qquad (1)$$

$$\eta_a = \frac{RT}{i_o zF} \cdot i = K_a \, i \qquad (2)$$

$$\eta_k = \frac{2\gamma V}{zF} \cdot \frac{1}{r} = \frac{K_k}{r} \qquad (3)$$

where η_d is the diffusion (concentration) overpotential,

η_a is the activation overpotential,

η_k is a 'curvature' overpotential arising from the shift of the reversible potential of a curved surface towards cathodic values with respect to a flat electrode ($r = \infty$),

and γ is the surface tension of the metal-electrolyte interface.

The total (applied) overpotential is

$$\eta = \text{constant} = \eta_d + \eta_a + \eta_k$$
$$= K_d . r\, i + K_a . i + K_k . \frac{1}{r} \qquad (4)$$

It can be seen from equation (4) that the first term will result in an increase of the local current density with decreasing radius of curvature while the third term will have the opposite effect; a maximum rate of growth should be obtained for some intermediate values of r. Through experiments it was found that the radius for maximum rate of growth increases sharply with decreasing overpotential.

Growth is preferential at the tip because diffusion conditions are enhanced due to the onset of spherical rather than linear diffusion. However, this process cannot become effective while the growing surface remains in a region in which the concentration gradient is controlled by the diffusion layer of the larger electrode.

Hamilton [123] marginally improved on the theory put forward by Barton and Bockris. The main points of Hamilton's theory are:

a) the dendrite surface has a parabolic shape rather than a spherical one,

b) allowance is made for the fact that the boundary conditions apply on a moving surface (that is, the advancing dendrite tip),

and c) it assumes that the shape of the growing dendrite is conserved.

However, an abnormally low value of γ has to be assumed together with a high value for the exchange current density in order for the experimental data, obtained by Barton and Bockris, to fit Hamilton's theory.

Price et al [124] postulated a theory for electrolytic whisker growth which is based on adsorbed impurities inhibiting crystal growth. It takes into account the kinetic aspect of adsorption and it assumes that growth (once nucleation has started) proceeds through the lateral propagation of layers.

The theory put forward by Barton and Bockris is more realistic for dendritic growth in pure solutions or melts whereas under heavy poisoning conditions, a mechanism qualitatively similar to that proposed by Price et al is a viable prospect.

In conclusion, when Price et al compared the experimental data (obtained for Ag dendrites) with the prediction of their theory, it was found that the growing crystal "adjusts itself" in such a way that the rate of growth corresponds exactly to a 'critical' current density, rather than the latter being a lower limit for that rate. As yet the mechanism by which this adjustment occurs cannot be explained by this theory.

REFERENCES

1. G. Planté, Compt. Rend., 50 (1860) 640.
2. J.H. Gladstone and A. Tribe, Nature, 25, 221, 461; 26, 251, 342, 602; 27, 583 (1882-1883).
3. D.N. Craig and G.W. Vinal, J. Res. Nat. Bur. Stand., 24 (1940) 475.
4. G.W. Vinal, "Storage Batteries", 4th Ed, John Wiley, 1955.
5. J. Burbank, A.C. Simon aud E. Willihnganz. Advan. Electrochem. Electrochem. Eng., Vol. 8 (P. Delahay and C.W. Tobias, eds) Wiley-Interscience, New York (1971) p.157.
6. P. Ness, Electrochim. Acta. 12 (1967) 161.
7. J. Burbank, NRL Reports 6859 (1969)and 7256 (1971), U.S. Naval Research Laboratory, Washington, D.C.
8. E. Willihnganz, Power Sources 5, 9th International Symposium, Brighton 1974 (D.H. Collins, ed.), Academic Press, New York, 1975, p.43.
9. J.P. Carr and N.A. Hampson, Chem. Rev., 72 (1972) 679.
10. P. Ruetschi, R.T. Angstadt and B.D. Cahan, J. Electrochem. Soc., 106 (1959) 547.
11. S. Hattori, M. Yamaura, M. Kono, M. Yamone, H. Nakashima and J. Yamashita, ILZRO project LE - 197, Semi-annual report (1974).
12. I.K. Gibson, Chloride Technical Ltd., (CTL) Project Report No. 4280, (1981).
13. H. Helmholtz, Weid. Ann., 7 (1879) 377.
14. A. Gouy, J. Phys., 9 (1910) 457.
15. D.L. Chapman, Phil. Mag., 25 (1913) 475.
16. O. Stern, Z. Elektrochem., 30 (1924) 508.
17. D.C. Grahame, Chem. Rev., 41 (1947)441.
18. M.A. Devanathan, J. O'M.Bockris and K. Müller, Proc. Roy. Soc., London, A274 (1963) 55.
19. A.N. Frumkin, J. Electrochem. Soc., 107 (1960) 461.
20. Idem, Svensk Komisk Tichschoift, 77 (1965) 300.

21. S. Levine, G.M. Bell and A.L. Smith, J. Phys. Chem., 73 (1969) 3534.

22. B.B. Damaskin and A.N. Frumkin, Electrochim. Acta. 19 (1974) 173.

23. R. Parsons, J. Electroanal. Chem., 59 (1975) 229.

24. I.L. Cooper, J.A. Harrison, J. Electroanal. Chem., 66 (1975) 85.

25. Idem, Electrochim. Acta. 22 (1977) 519.

26. Idem, ibid., 22 (1977) 1361.

27. Idem, ibid., 22 (1977 1365.

28. I.L. Cooper and J.A. Harrison, Electrochim. Acta. 23 (1978) 545.

29. W.A. Caspari, Z. Physik. Chem., 30 (1899) 89.

30. T. Erdey-Gruz and M. Volmer, Z. Physik. Chem., 105A, (1930) 203.

31. K.J. Vetter, Z. Physik. Chem., 194 (1950) 284.

32. K.J. Vetter, Z. Electrochem., 56 (1952) 931.

33. J. Tafel, Z. Physik. Chem., 50 (1905) 641.

34. K.J. Vetter, ibid., 194 (1956) 284.

35. J.E.B. Randles, Trans. Faraday Soc., 48 (1952) 828.

36. V.V. Losev, "Modern Aspects of Electrochemistry", Vol. 7, Ed. B.E. Conway and J. O'M. Bockris, Butterworths (1972) 314.

37. V.G. Levich, Advan. Electrochem. Electrochem. Eng., 4 (1966) 249.

38. R.A. Marcus, Electrochim. Acta. 13 (1968) 995.

39. R.R. Dogonadze, "Reactions of molecules at electrodes", Wiley (1971) 135.

40. V.G. Levich, "Physico - Chemical Hydrodynamics", Prentice Hall, Englewood Cliffs, (1962).

41. R. de Levie (edited by Delahay and Tobias), Advan. Electrochem. Electrochem. Eng., Vol. 6, Interscience, New York, (1967) p. 329.

42. A. Winsel, Z. Electrochem. 66 (1962) 287.

43. L.G. Austin, Trans. Faraday. Soc., 60 (1964) 1319.

44. F. Dolezaek, 'Die Theorie des Bleiaccumulators', Verlag von Wilhelm Knapp, Halle a/s., 1901.

45. J. Euler and W. Nonnenmacher, Electrochim. Acta. 2 (1960) 268.

46. J. Euler, Electrochim. Acta. 8 (1963) 409.

47. J.S. Newman and C.W. Tobias, J. Electrochem. Soc., 109 (1962) 1183.
48. R.C. Alkire, E.A. Grens II and C.W. Tobias, ibid., 116 (1969 1328.
49. R.C. Alkire and B. Place, ibid., 119 (1972) 1687.
50. J.S. Dunning, D.N. Bennion and J. Newman, ibid., 118 (1971) 1251.
51. K. Micka and I. Rousar, Electrochim. Acta. 19 (1974) 499.
52. Idem, ibid., 18 (1973) 629.
53. Idem, ibid., 21 (1976) 599.
54. D. Simonsson, J. Electrochem. Soc., 120 (1973) 151.
55. Idem, J. Appl. Electrochem., 3 (1973) 261.
56. Idem, ibid., 4 (1974) 109.
57. D. Simonsson, Kungl. Tekniska. Högskolan, Inst. för Kemisk Teknologi, Stockholm, 1973.
58. J. Lehning, Elektrotech. Z., 93A (1972) 62.
59. W. Runge, Elektrotech. Z., 93A (1972) 67.
60. A.D. Turner, A.E.R.E. Report No. R8931, 1978.
61. L.A. Matheson and N. Nichols, Trans. Electrochem. Soc., 73 (1938) 193.
62. P. Delahay, "New Instrumental Methods in Electrochemistry", Interscience Publishers Inc., New York (1966) Chapter 6.
63. R.S. Nicholson and J. Shain, Anal. Chem.,36 (1964) 706.
64. W.M. Schwarz and J. Shain, J. Phys. Chem., 69 (1965) 30.
65. A. Sevick, Coll. Czech. Chem. Comm., 13 (1948) 349.
66. W. Kemula and Z. Kublik, Anal. Chim. Acta., 18 (1958) 104.
67. H. Matsuda and Y. Ayabe, Z. Elektrochem., 59 (1955) 494.
68. J.E.B. Randles, Trans. Faraday Soc., 44 (1948) 322, 327.
69. L. Gierst, "Trans. Symp. Electrode Proc.", Philadelphia, Wiley, New York, 1959, p.109.
70. M. Fleischmann and H.R. Thirsk, Electrochim. Acta. 1 (1959) 146.
71. J.A. Harrison and H.R. Thirsk, "Electroanalytical Chemistry", Vol. 5 (Ed. A.J. Bard), Marcel Dekker, New York (1971).

72. M. Avrami, J. Chem. Phys., 7 (1939) 1103; 8 (1940) 212; 9 (1941) 177.

73. S.K. Rangarajan, J. Electroanal. Chem., 46 (1973) 125.

74. U. Bertocci, J. Electrochem. Soc., 119 (1972) 822.

75. V. Bostanov, R. Roussinova and E. Budevski, J. Electrochem. Soc., 119 (1972) 1346.

76. R.D. Armstrong and A.A. Metcalfe, J. Electroanal. Chem., 63 (1975) 19.

77. F.C. Frank, Proc. Roy. Soc., A201 (1950) 586.

78. R.D. Armstrong, M. Fleischmann and H.R. Thirsk, J. Electroanal. Chem., 11 (1966) 208.

79. E. Warburg, Ann. Physik., 67 (1899) 493; 6 (1901) 125.

80. J.E.B. Randles, Discussion Faraday Soc., 1 (1947) 11.

81. B.V. Ershler, ibid., 1 (1947) 269.

82. H. Gerischer, Z. Physik. Chem., 198 (1951) 286; 201 (1952) 55.

83. M. Sluyters-Rehback, D.J. Kooyam and J.H. Sluyters, "Polarography", Ed. G.J. Hills, Macmillan Press, (1964) 143.

84. J.H. Sluyters, Rec. Trad. Chim., 79 (1960) 1092.

85. M. Sluyters-Rehback and J.H. Sluyters, "Electroanalytical Chemistry", Vol. 4, (ed. Bard), Dekker, New York, (1970) p.1.

86. D.C. Grahame, J. Electrochem. Soc., 99 (1952) 370C.

87. H.A. Laitinen and J.E.B. Randles, Trans. Faraday Soc., 51 (1955) 54.

88. R.D. Armstrong and A.A. Metcalfe, J. Electroanal. Chem., 71 (1976) 5.

89. M. Keddam, Z. Stoynov and H. Takenouti, J. Appl. Electrochem., 7 (1977) 539.

90. S.A.G.R. Karunathilaka, N.A. Hampson, R. Leek, T.J. Sinclair, J. Appl. Electrochem., 10 (1980) 799.

91. R. Darby, J. Electrochem. Soc., 113 (1966) 392, 496.

92. F. Gutmann, J. Electrochem. Soc., 112 (1965) 94.

93. P.J. Mitchell, Ph.D. Thesis, Loughborough University (1983).

94. N.A. Hampson, S. Kelly and K. Peters, J. Appl. Electrochem., 10 (1980) 91.

95. M. Abramowitz and I.A. Stigun (Eds), "Handbook of Mathematical Functions", Dover publications Inc., New York, (1970) p.886.

96. C. Lazarides and N.A. Hampson, J. Appl. Electrochem., 12 (1982) 469.

97. N.A. Hampson, S. Kelly, K. Peters and P. Whyatt, J. Appl. Electrochem., 10 (1980) 597.

98. M. Fleischmann and H.R. Thirsk, Trans. Faraday. Soc., 51 (1955) 71.

99. S.G. Canagaratna, P. Casson, N.A. Hampson and K. Peters, J. Electroanal. Chem., 79 (1977) 273.

100. H.E. Haring and U.B. Thomas, Trans. Electrochem. Soc., 68 (1935) 293.

101. E.E. Schumacher and G.S. Phipps, ibid., 68 (1935) 309.

102. U.B. Thomas, F.T. Forster and H.E. Haring, ibid., 92 (1947) 313.

103. N.A. Hampson, S. Kelly and K. Peters, J. Appl. Electrochem., 11 (1981) 595.

104. P. Casson, Ph.D. Thesis, Loughborough University (1978)

105. H.R. Thirsk and J.A. Harrison,"A Guide to the Study of Electrode Kinetics", Academic Press, London and New York, p. 115.

106. J.L. Dawson, M.E. Rana, B. Munasiri and J. McWhinnie, Power Sources 7 (ed. J. Thompson), Academic Press Inc., 1979 (p.1).

107. P. Casson, N.A. Hampson, K. Peters and P. Whyatt, J. Electroanal. Chem., 93 (1978) 1.

108. R.G. Acton, in D.H. Collins (ed.), 'Proc. Symp. on Power Sources, Brighton, 1966,' Pergamon, New York, 1967, p.133.

109. J.L. Devitt and M. Myers, J. Electrochem. Soc., 123 (1976) 1769.

110. M. Fleischmann and H.R. Thirsk, Adv. Electrochem. Electrochem. Eng., Vol. 3 (1963) p.123.

111. D.D. Macdonald, "Transient Techniques in Electrochemistry", Plenum Press, New York and London, p.277.

112. S.G. Canagaratna and N.A. Hampson, Surface Technology, 5 (1977) 163.

113. S.G. Canagaratna and N.A. Hampson, J. Electroanal. Chem., 86 (1978) 361.

114. P. Casson, N.A. Hampson and M.J. Willars, J. Electroanal. Chem., 97 (1979) 21.

115. C. Lazarides and N.A. Hampson, Surface Technology, 16 (1982) 255; 17 (1982) 139.

116. N.A. Hampson and C. Lazarides, Surface Technology, 17 (1982) 205.

117. S. Kelly, N.A. Hampson, S.A.G.R. Karunathilaka and R. Leek, Surface Technology, 13 (1981) 349.

118. N.A. Hampson, S. Kelly and K. Peters, J. Appl. Electrochem., 11 (1981) 751.

119. S. Kelly, N.A. Hampson and K. Peters, J. Appl. Electrochem., 11 (1981) 765.

120. N.A. Hampson, P.C. Jones and R.F. Phillips, Can. J. Chem., 45 (1967) 2045; 46 (1968) 1325.

121. S.A.G.R. Karunathilaka, N.A. Hampson, R. Leek and T.J. Sinclair, J. Appl. Electrochem., 10 (1980) 357.

122. J.L. Barton and J. Bockris, 'Proc. Roy. Soc. London', Ser. A 268 (1962) 485.

123. D.R. Hamilton, Electrochim. Acta. 8 (1963) 731.

124. L. Price, D.A. Vermilyea, and D. Webb, Acta. Met., 6 (1958) 524.